THERMOMECHANICAL BEHAVIOR OF A DIRECTIONALLY SOLIDIFIED NICKEL-BASE SUPERALLOY IN THE AGED STATE

A Dissertation
Presented to
The Academic Faculty

by

Michael M. Kirka

In Partial Fulfillment
of the Requirements for the Degree
Doctor of Philosophy in the
George W. Woodruff School of Mechanical Engineering

Georgia Institute of Technology
May 2014

THERMOMECHANICAL BEHAVIOR OF A DIRECTIONALLY SOLIDIFIED NICKEL-BASE SUPERALLOY IN THE AGED STATE

Approved by:

Dr. Richard W. Neu, Advisor
Woodruff School of Mechanical Engineering
School of Materials Science and Engineering
Georgia Institute of Technology

Dr. Rosario Gerhardt
School of Materials Science and Engineering
Georgia Institute of Technology

Dr. David L. McDowell
Woodruff School of Mechanical Engineering
School of Materials Science and Engineering
Georgia Institute of Technology

Dr. Stephen D. Antolovich
Woodruff School of Mechanical Engineering
School of Materials Science and Engineering
Georgia Institute of Technology

Dr. Thomas H. Sanders Jr.
School of Materials Science and Engineering
Georgia Institute of Technology

Dr. Surya Kalidindi
Woodruff School of Mechanical Engineering
School of Materials Science and Engineering
Georgia Institute of Technology

Date Approved: February 27, 2014

ACKNOWLEDGEMENTS

The work presented in this thesis was the culmination of the collective encouragement, guidance, and thoughts of many people I have had the privilege of knowing.

I am extremely grateful to my thesis advisor Dr. Richard Neu for his support, encouragement, and criticism throughout my Ph.D. process; Dr. Neu was an indispensible teacher and mentor, and perhaps endured more than his fare share of rough drafts from me. Further, I would like to thank Dr. Stephen Antolovich and Dr. Thomas Sanders for their invaluable advice and discussions that interjected reality and comedy into my graduate studies. Further, I would like to recognize the members of my reading committee, Dr. Surya Kalidindi, Dr. David McDowell, and Dr. Rosario Gerhardt for their time and contributions.

I would like to recognize those whom I have had the opportunity to work and interact with in the course of my research, James Huggins, Patxi Fernandez-Zelaia, Matthew Priddy, Ben Smith, Sean Neal, Matthew Siopis, Kyle Brindley, Brian Clark, Ashley Nelson, Siddharth Avachat, Rohan Bansal, Anirudh Rudraraju, Shaun Eshraghi, Jeffery Llyod, Bill Musinski, Robert Amao, Andy Radzicki, and Ben Adair.

While my involvement in the Graduate Student Government at Georgia Tech probably increased my time as a graduate student, I considered it an honor and pleasure to have had the opportunity to meet and work with so many great students and administrators, Gareth Guvanasen, Jeffery Fisher, Arren Washington, Eran Mordel, James Black, Michael Ellis, Yogi Patel, Dr. Kim Harrington, Dr. Carol Moore, Ninh Tran, and Dean John Stein.

Lastly, I would like to thank my corporate sponsors. Without the financial support of Siemens Energy, this research would not have been possible.

TABLE OF CONTENTS

LIST OF TABLES

LIST OF FIGURES

SUMMARY

Understanding the effects of aged microstructures on the thermomechanical fatigue (TMF) properties of nickel-base (Ni-base) superalloys remains unclear. Few experimental results are currently available in this area, and of the limited results available, some promote aged microstructures as beneficial, while others as detrimental. The importance of these aged structures arises from the fact that when components used in the hot sections of gas turbine engines remain in service for extended periods of time, the local temperature and stress provides the catalyst for the evolution of the microstructure.

An experimental assessment of a negative misfit directionally solidified (DS) Ni-base superalloy was undertaken to characterize the aging kinetics and understand the influence of the TMF cycle temperature extremum, temperature-load phasing, mean strain, creep-fatigue, orientation effects, and microstructure on TMF fatigue crack initiation. To determine the effects of aging on the TMF response, the as-heat-treated alloy was artificially aged to three unique microstructures identified in the aging kinetics study. The experiments revealed that not all aged microstructures are detrimental to the fatigue life behavior. Specifically, when the γ' precipitates age in a manner to align themselves parallel to the axis of the applied stress, an increase in the fatigue life over that of the as-heat-treated microstructure is observed for out-of-phase TMF with dwells.

To extend the experimental understanding of the aged microstructures into service component design and life analysis, a temperature-dependent crystal viscoplasticity (CVP) constitutive model is developed to capture the sensitivity of the aged microstructure through embedding additional variables associated with the current

state of the γ' particles. As a result of the adaptations, the CVP model has the ability to describe the long-term aging effects of directional coarsening relevant to the analysis industrial gas turbine hot section components.

CHAPTER I

INTRODUCTION

1.1 Motivation

Nickel-base (Ni-base) superalloys are often the choice material for hot section components of gas turbine engines (GTE) and are responsible for the high efficiency that GTEs exhibit over all other power generation methods. Gas turbines can be placed into one of two classifications, industrial gas turbine engines (IGTE) and aerospace engines (aero). Regardless of classification, the ranges in size of the engines can be drastic, with industrial units being able to output anywhere from 10 to 450 MW per unit, and the largest aero engines outputting 140 MW [1].

With the different engine classifications arise differences in the demands and requirements of the materials of which they are comprised. IGT engines are often exposed to natural gas fuels containing chemical impurities such as sulfides and phosphides, which result in highly corrosive operating environments. Additionally, operators of IGTs have a desire to operate the units at higher firing temperatures to encumber increased efficiencies while continuously operating the engine for months between shutdowns. On the aerospace side, operators burn high-grade aviation fuels, require the engines to be as lightweight as possible, and endure thousands of start-up and shutdown cycles, while also demanding ever increased operating temperatures. Because of these demands Ni-base superalloys remain the only material class capable of withstanding the operating conditions.

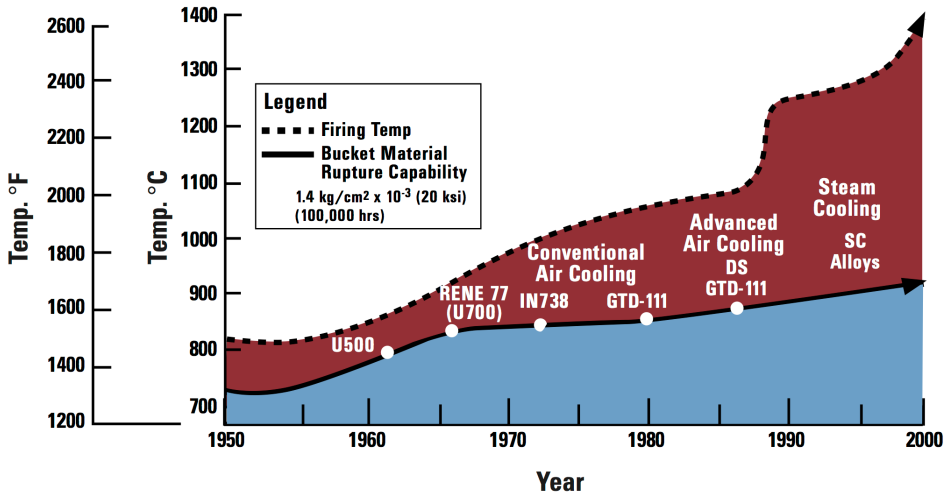

Figure 1.1: Progress in engine firing temperature and maximum exposure temperature of the airfoil material [2].

In the materials design realm, the creep performance has traditionally been the driving factor and measure of improvement of Ni-base superalloys [3]. However, so great have the creep properties been enhanced, that thermomechanical fatigue (TMF) cracking in localized regions have become the main factor of component failure or removal from service [4–6]. Further highlighting the importance of TMF occurring in Ni-base superalloys is that a 300°C drop in the minimum temperature of the TMF cycle results in a two third decrease in the fatigue life [7]. Additionally, fatigue evaluation of new alloys only considers laboratory tests on the as-heat-treated material, which in real materials used in hot section components is short lived.

In developing the next generation of Ni-base superalloys, the experimental efforts required to determine the proper alloy chemistry, solidification conditions and heat-treatment is an extensively involved process aside from being extremely costly [8]. As the design tools for engineers have increased, the development cycle for new components has dropped to a quarter of that of a new material. As such, material development has not kept pace with the engine development cycle. In regards to materials, modification of a current alloy requires four years, new materials within

an existing alloy class ten years, with new alloys twenty years and up [8]. With this disparity, the concept of integrated computational materials engineering (ICME) has become increasingly embraced by industry and government as a means to tie together the alloy design and evaluation phase to that of the component design phase, alloying turbine engine manufactures to more rapidly develop and optimize alloys and heat-treats [9–12]. Among the great challenges facing wide spread acceptance of the ICME concept are cases of successful application of the method to trusted alloys [13].

1.2 Research Objectives

Inevitability, the day from which a GTE begins operation, the materials within the engine undergo thermal and load exposure that ultimately lead evolution of the microstructure. Per current material and engine component design methodologies, the mechanical properties of the as-heat-treated material have traditionally been assumed applicable to the entire life of a service component. Generally, this assumption is not valid. Ultimately, the combination of materials design and component design has slowed overall advancements in GTE technology. Through this work questions and ideas prevalent in alloy and component design will be discussed. Further, a framework for coupling experimental with computational techniques to decrease the gap that currently exists will be presented. The specific topics addressed here:

1. **Fully understand and characterize the kinetics of directional coarsening in the heterogeneous microstructure of a Ni-base superalloy and develop artificially aging profiles that capture long-term aging of the alloy in service.** From the day a service component begins operation, the microstructure evolves according to thermomechanical exposure. To characterize this evolution, experiments were be preformed on CM247LC-DS to determine and understand the kinetics of isotropic coarsening and directional coarsening formation within the material.

2. **Determine the effects of TMF loading conditions on the crack initiation in a Ni-base superalloy in the as-heat-treated state.** During normal operation a service component is exposed to a variety of TMF loading conditions, each with varying impacts on the material's fatigue life. To understand the effects of TMF loading conditions, experiments will be preformed on CM247LC-DS where the TMF cycle temperature extremum, temperature strain phasing, mean strain, creep-fatigue interactions, and orientation effects on the crack initiation are investigated.

3. **Establish an understanding of the effect of thermally induced microstructure changes on the monotonic and cyclic deformation response of a Ni-base superalloy.** Currently, the understanding of the benefits or determinants of aged microstructures under relevant IGTE TMF conditions is unclear. To provide clarity, experiments on CM247LC-DS in the isotropic coarsened and directionally coarsened microstructure states under IGTE relevant TMF conditions will be conducted.

4. **Establish a crystal viscoplastic model that captures the influences of aging on the cyclic behavior of a Ni-base superalloy.** In most crystal viscoplasticity models, the microstructure morphology is assumed to be static and the softening effects associated with the aging of Ni-base superalloys are neglected. An analytically derived kinetics model is embedded within the CVP model framework to account for microstructural evolution, which allows updating of the material parameters for the current state of the microstructure.

1.3 Thesis Overview

The work to be discussed is done so in a logical manner, such that the topic of current discussion provides the basis for the subject of the succeeding chapters. Firstly, Chapter 2 provides a general review of Ni-base superalloys and gives insight into the

complexities of their design, and where the current state-of-the-art stands. Presented in Chapter 3 are the experimental methods utilized in this study and how the microstructure of CM247LC-DS was artificially aged. Proceeding into Chapter 4 is a discussion on the techniques used to characterize the microstructure of a Ni-base superalloy in the aged state. Chapter 5 transitions into discussing the fatigue properties of CM247LC-DS and how TMF conditions influence the alloy's resistance to fatigue crack nucleation. Extending the results of Chapter 5, Chapter 6 examines the influences of the aged microstructures on the TMF behavior of CM247LC-DS. In Chapter 7 modifications to a crystal viscoplasticity model will be presented that allow for the model to become microstructure sensitive. Closing, Chapters 8 and 9 provide the conclusions and recommendations for continuation of this work into the next phase of development.

CHAPTER II

BACKGROUND

2.1 Chemistry, Solidification, and Crystallography of Ni-base Superalloys

2.1.1 Alloy Chemistry

In all forms, Ni-base superalloys are composed of two primary phases, an A1 matrix phase termed γ and a $L1_2$ precipitate phase denoted by γ'. The γ matrix is a disordered FCC like structure, where the alloying elements are allowed to occupy any of the atomic positions. In contrast, the γ' phase is an ordered intermetallic phase with a stoichiometric composition of Ni_3Al, where alloying elements of similar atomic and electronic structure may substitute with Ni in the lattice. Aside from the γ and γ' phases, secondary phases such as carbides, borides, and topologically closed packed (TCP) phases also have the possibility of occurring; however, their presence is highly dependent on alloy chemistry, solidification conditions, heat-treatment, and service temperature exposure of the material [14]. Typically modern alloy compositions are engineered to avoid all but the γ, γ', and carbide phases, as the other potential phases often detract from the desired mechanical performance of Ni-base superalloys [14–16].

The chemistries of modern Ni-base superalloys typically contain ten or more alloying elements, where the elements can be classified into one of the following three categories [14, 16]:

1) Solid-Solution Strengtheners: Elements such as cobalt, chromium, molybdenum, ruthenium, and rhenium segregate to the γ phase and provide solid solution strengthening to the matrix through their higher melting temperature when compared with nickel.

2) Precipitate Strengtheners: Aluminum, titanium, and tantalum form the $(Ni, Co)_3$ (Al,Ti) line compound or γ' phase [17].

3) Grain Boundary Strengtheners: Carbon and boron are added to allow for the formation of carbides and borides to strengthen the grain boundaries which is relevant to polycrystalline and directionally-solidified (DS) materials.

Shown in Table 2.1 is the chemical compositions of DS and SX Ni-base superalloys currently in common use in aero and IGT engines. In most cases, the chemical compositions of these alloys were derived from Mar-M247 with the intention of increasing the fatigue resistance in the intermediate temperature range, enhancing carbide stability, decreasing the amount of $\gamma - \gamma'$ eutectic, and in the case of DS alloys decreasing grain boundary cracking in the case of DS alloys [18].

Table 2.1: Chemical Compositions of commonly used Ni-base superalloys [16, 18].

Alloy	Cr	Co	Mo	W	Al	Ti	Ta	Hf	C	B	Zr	Re	Nb	Ni
Mar-M247LC-DS	8.4	10.0	0.7	10.0	5.5	1.0	3.0	1.5	0.07	0.015	0.05	-	-	Bal
CM247LC-DS	8.1	9.2	0.5	9.5	5.6	0.7	3.2	1.4	0.07	0.015	0.01	-	-	Bal
CMSX-4	6.5	9.0	0.6	6.0	5.6	1.0	6.0	-	-	-	-	3.0	-	Bal
CMSX-10	2.0	3.0	0.4	5.0	5.7	0.2	8.0	0.03	-	-	-	6.0	0.1	Bal

2.1.2 Solidification

Through various casting techniques, Ni-base superalloy components can be made in polycrystalline, DS, and single crystal (SX) forms as shown in Figure 2.1 [16, 19, 20]. Amongst the variants, each have their own defining microstructural characteristics. With conventionally cast superalloys, no effort is made to control the orientation of the individual grains through heat removal and the resultant is a randomly oriented microstructure. Directionally-solidified materials are typically oriented such that all grains have a common principle axis and no attempt to control the secondary orientations. In the case of SX materials, both the primary and secondary crystal orientations are controlled [19].

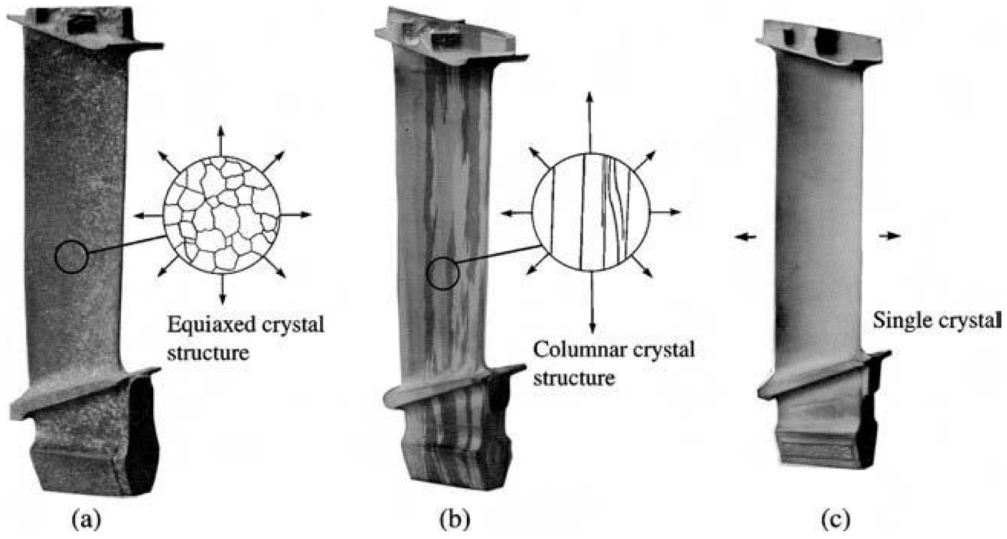

Figure 2.1: Cast airfoils with a) Equiaxed crystal structure b) Directionally solidified structure and c) Single crystal structure [16].

While great control over grain orientation has been introduced into the casting of Ni-base superalloys, solidification of alloys results in dendritic structure, which possess unwanted inhomogeneities within the structure on a macro and micro-scale. On the macroscale, are the primary, secondary, and tertiary dendrite arms, along with the interdendritic regions, i.e. the regions between neighboring dendrites as depicted in Figure 2.2. On the micro-scale, the solidification conditions influence the amount of elemental segregation in such a manner that the solidification front rejects alloying elements from the solid/liquid interface that have different atomic properties from that of the bulk element nickel. Ultimately, once solidification is complete, the net resultant is that the majority of the heavy elements reside in the interdentritic regions and the dendritic core is rich in nickel and aluminum [14].

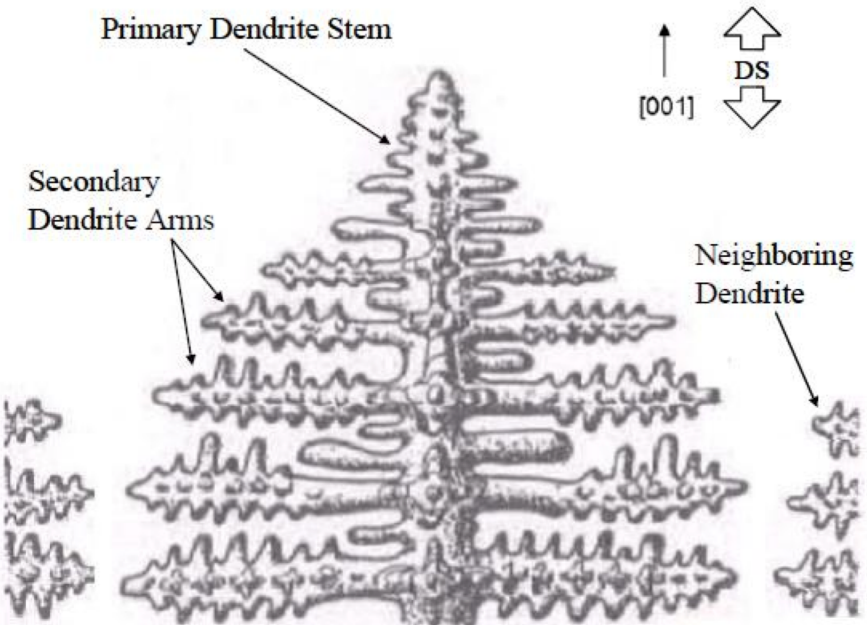

Figure 2.2: Generic dendritic structure of a cast alloy [21]

To a degree, the macro-scale inhomogeneities can be controlled through rate of solidification of the alloy. Experimentally, the spacing of the primary and secondary arms have been found to follow the linear relationship,

$$\lambda = \frac{V}{R} \tag{2.1}$$

where, λ is the primary dendrite spacing, V is the solidification velocity and R the thermal gradient [19,22,23]. The factor V/R is also known as the local rate of cooling within the casting [21]. Ultimately, to make the casting process feasible for industry use, practical solidification rates must be used.

2.1.3 Heat Treatment

As a balance in choosing feasible casting conditions and promoting desirable mechanical properties, all Ni-base superalloys are given multi-step heat-treatments. Although the complexity of the heat-treatment can vary by alloy, the steps can generally be

classified into two categories, solutioning and aging. A representative heat-treatment for the DS Ni-base superalloy Rene 80 is shown in Figure 2.3. During the solutioning stage, the γ' is dissolved into solution in an attempt to remove compositional spatial differences within the alloy which ultimately controls the lattice misfit

$$\delta = 2\frac{a'_\gamma - a_\gamma}{a'_\gamma + a_\gamma} \tag{2.2}$$

between the γ and γ' phases. Although solution treatments are effective in aiding removal of compositional gradients in Ni-base superalloys, there are still practical limits of this homogenization step and achieving true compositional homogenization is impossible [**?**]. As an example of the dependence of δ on the local chemical composition, is the X-ray diffraction derived empirical relation,

$$\Delta\delta = 10 - 3\left(4.6Al + 1.7Mo + 2Ti + 0.9W + Cr\right) + 0.5Ta \tag{2.3}$$

where Δ is the difference from the ideal γ and γ' phases and the elements are given in atomic percent [14].

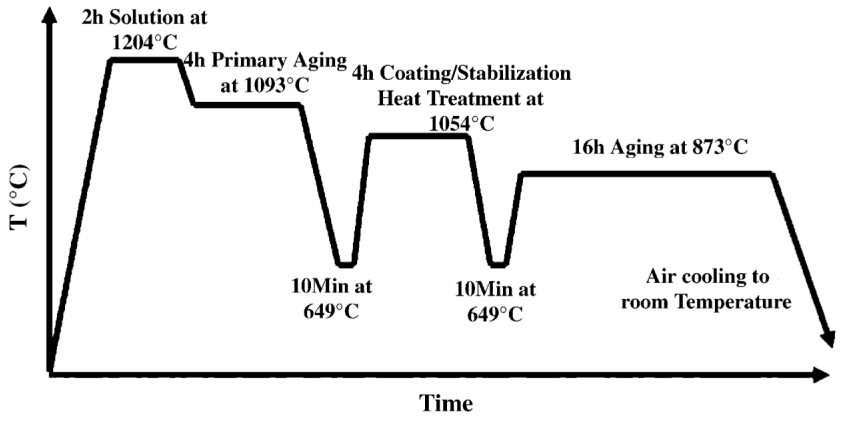

Figure 2.3: Example multi-step heat-treatment given to Rene 80 [24].

Upon the cooling from the solution temperature, the γ' precipitates according to traditional nucleation and growth mechanism. Initially the γ' nucleate as spheres

from the super saturated solution, but with continued aging the spheres eventually undergo a morphological transformation into cubes and ripen according to the Oswald coarsening mechanism [19]. Shown in Figure 2.4 is a representative micrograph of the $\gamma - \gamma'$ microstructure obtained after heat-treatment for the SX Ni-base superalloy CMSX-4

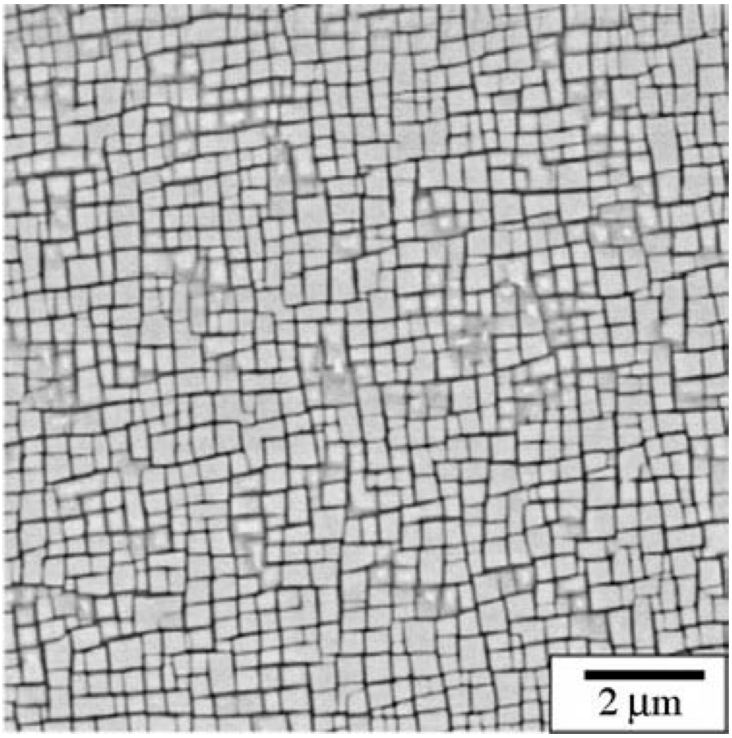

Figure 2.4: Resultant microstructure for SX CMSX-4 after multi-step heat-treatment [16]. White is γ' and black γ.

2.1.4 Carbides and TCPs

The precipitation of certain carbides is often promoted within Ni-base superalloys as carbides can provide additional strength, particularly in the case of polycrystalline and DS alloys. Most often, carbides are relegated to the grain boundaries and the interdendritic regions of the microstructure. The commonly encountered carbides are of the MC, M_6C, and $M_{23}C_6$ type, where, M represents Ti, Cr, or a refractory element in within the alloy [14]. The typical morphology of the carbides is a random Chinese script or blocky morphology as shown in Figure 2.5.

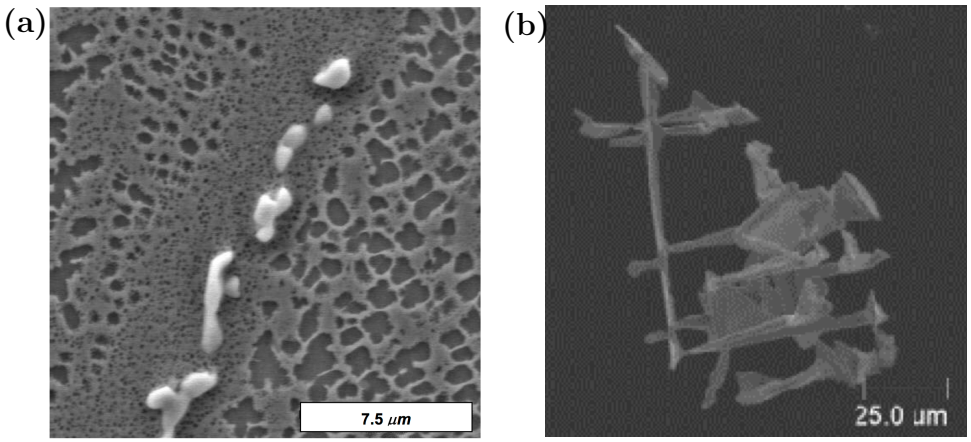

Figure 2.5: Chinese script morphology of carbides within Ni-base superalloys (a) Along a grain boundary in DS GTD-111 [25] (b) Carbide extracted from a GTD-111 matrix [26].

The primary MC-type carbides normally form during the solidification process at temperatures near the liquids temperature of the alloy and float in the molten liquid until becoming trapped in the last liquid to solidify in the interdendritic areas. Like the γ' phase, MC carbides also take on a FCC structure [15]. Although they are extremely stable, MC carbides are the primary source of carbon for the formation of the other carbide types which are formed through high temperature decomposition reactions [15].

One of the primary solid state reactions occurring within Ni-base superalloys involves MC carbides and the γ matrix, in the 870-950°C temperature range, and can be written as,

$$MC + \gamma \rightarrow M_{23}C_6 + \gamma' \tag{2.4}$$

The reaction equation is the result of experimental observations that both $M_{23}C_6$ and γ' form in the same areas as the degenerated MC carbides [14,15,27,28]. Below 871°C the decomposition of the primary MC carbides can not occur [29].

M_6C carbides typically form in the 815-980°C temperature range and form in regions of high refractory element content. The formation of the carbides occurs

through the replacement of chromium in other carbide types with molybdenum or tungsten. As a grain boundary strengthener, M_6C carbides remain stable above temperatures that cause $M_{23}C_6$ to breakdown. Like $M_{23}C_6$, M_6C is formed via reaction between MC carbides and γ according to

$$MC + \gamma \rightarrow M_6C + \gamma' \tag{2.5}$$

Further, M_6C and $M_{23}C_6$ have the ability to react to form one another by the following,

$$M_6C + M' \rightarrow M_{23}C_6 + M'' \tag{2.6}$$

where M' and M" represent metal species exchanging positions in the carbide reaction. However, the above reaction is highly dependent on the alloy chemistry, and the local refractory element concentrations. Of the possible reactions, the reaction presented in Equation 2.4 is typically the most observed in modern Ni-base superalloys and is the result of the heat-treatment processes used on the alloys [15].

2.2 Aging of Ni-base Superalloys

2.2.1 Stress-free Coarsening

Coarsening is the process of solute redistribution between particles of different sizes, where small particles dissolve at the expense of the larger growing particles. Overall, the driving force for coarsening is the reduction in free energy associated with the precipitate-matrix interface. The difference in local composition surrounding the precipitates of different sizes provides the diffusion mechanism for coarsening to occur. During the coarsening process, the volume fraction of the precipitate phase remains relatively constant. Typically studied is the case of spherical particle coarsening, which can be linked with the heat-treatment process. However, over the course of service exposure the coarsening processes of the optimized γ' cubes play a crucial role

in controlling the mechanical performance of the material.

The γ' coarsen according to a cubic rate law which is associated with the diffusion-controlled Ostwald ripening process. However, for long term coarsening, the cubic law is assumed valid; however, there are a lack of long-term studies reported in the literature. Of the commercial alloys studied under long-term coarsening conditions have been experimental Ni-Al-Ti-Mo alloys, Nimonic 80A, IN939, and Rene 80. In each of these studies is observed that a γ' size saturation occurs. The exposure time at which the size saturation occurs has been reported to be temperature sensitive. Some reports have placed the particle size stabilization occurrence on the development of interfacial $\gamma - \gamma'$ dislocation networks. Further, at extremely long coarsening times, decreases in the average particle size have been observed. This is attributed to formation of γ' octets and platelets which are lower in energy than a single large γ' cube [30–37]. The activation energy for coarsening processes in Ni-base superalloys is in the neighborhood of 100-200 kJ/mol [36].

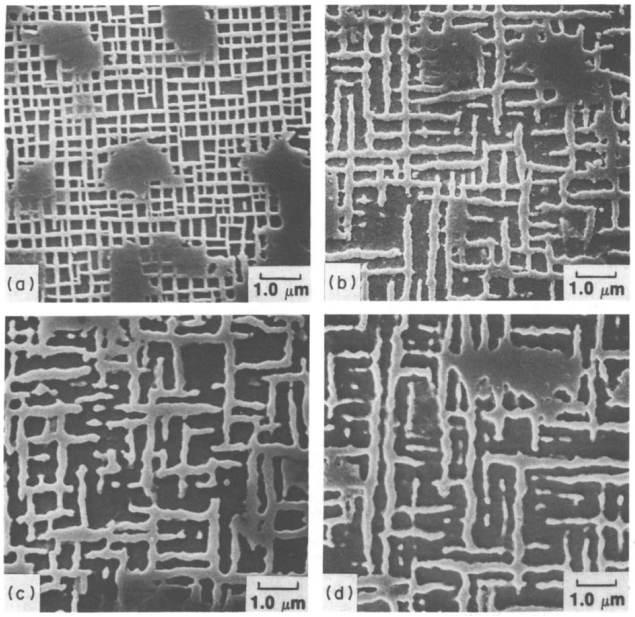

Figure 2.6: Coarsening of γ' in an experimental Ni-Al-Ti-Mo Ni-base superalloy after thermal exposure at 982°C for (a)25 hrs (b)50 hrs (c)1500 hrs and (d) 5000 hrs [32].

Early amongst the attempts to predict precipitate growth was the LSW model, developed by Lifshitz, Slyozov, and Wagner [38]. The LSW model assumes that the precipitate volume fraction is sufficiently small such that neighboring particles have great enough separation such that no elastic interactions occur between the particles. From this, the LSW theory predicts that the variation of the average radius of coarsening particles as a function of time is given by,

$$\overline{r}^3 - \overline{r}_o^3 = \frac{8 D_\sigma V_m t}{9 R T} \tag{2.7}$$

where D_σ is the diffusion coefficient of the solute in the matrix, V_m is the molar volume of the precipitate, R is the ideal gas constant, T is temperature in Kelvin, r_o the initial particle size, and t is time. While, the LSW model was found to provide predictive capability for dilute alloy with no particle interaction, the assumption that neighboring particles do not influence the growth of other particles greatly inhibits the direct extension to engineering alloys.

As a result of the shortcoming of the LSW model, modifications have been proposed that account for the effects of large precipitate volume fractions found in modern engineering alloys. Amongst them are the LSW modified and the LSW Encounter Modified theories that have been developed to include such influences as that of diffusion fields around individual particles and that of particle coalescence [39–41]. The primary modifications have been towards accounting for the volume fraction of the precipitates through the addition of modifying parameters in the rate constant. In general, the modified theories have been met by limited success, with the encounter type models achieving the best results on average [32, 36, 42].

2.2.2 Stress-Assisted Coarsening

In the heat-treated state, the stresses within the γ-γ' microstructure reaches magnitudes within the ranges of what one expect the materials to bear under external

loads. FEM results similar to those in Figure 2.7 show the distribution of the stresses within the γ channels and the γ' precipitate. The FEM results have also indicated that these internal stresses are largely unaffected by changes in the temperature [43].

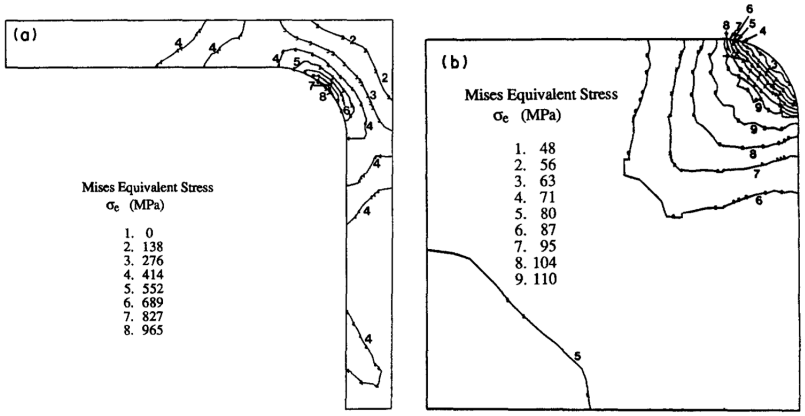

Figure 2.7: Contours of Mises equivalent stress associated with the initial misfit in CMSX-3 at 1050°C in (a) the γ matrix and (b) the γ' precipitate [43].

With the addition of an external stress to the highly stressed microstructure at temperatures above 850°C [44], sufficient energy is available to the composite $\gamma - \gamma'$ system such that the highly optimized γ' precipitates can undergo a process termed directional coarsening (DC) or rafting. DC is best characterized by the narrowing and subsequent widening of certain γ matrix channels. From Udmit-700, a positive misfit alloy, came some of the first studies of the effects of stress induced directional coarsening [45, 46]. Ultimately the actual direction in which the γ' coarsens depends on both the sign and magnitude of the lattice misfit of the alloy under question and the sign of the applied stress [43, 47]. For classification purposes (Figure 2.8),

> N-type rafts are those that coarsen with the long side normal to the axis of the applied load and require a tensile stress and negative misfit or a compressive stress and positive misfit
>
> P-type rafts are those that coarsen with the long side parallel to the axis of the applied load and require a tensile stress and positive misfit or a compressive

stress and negative misfit

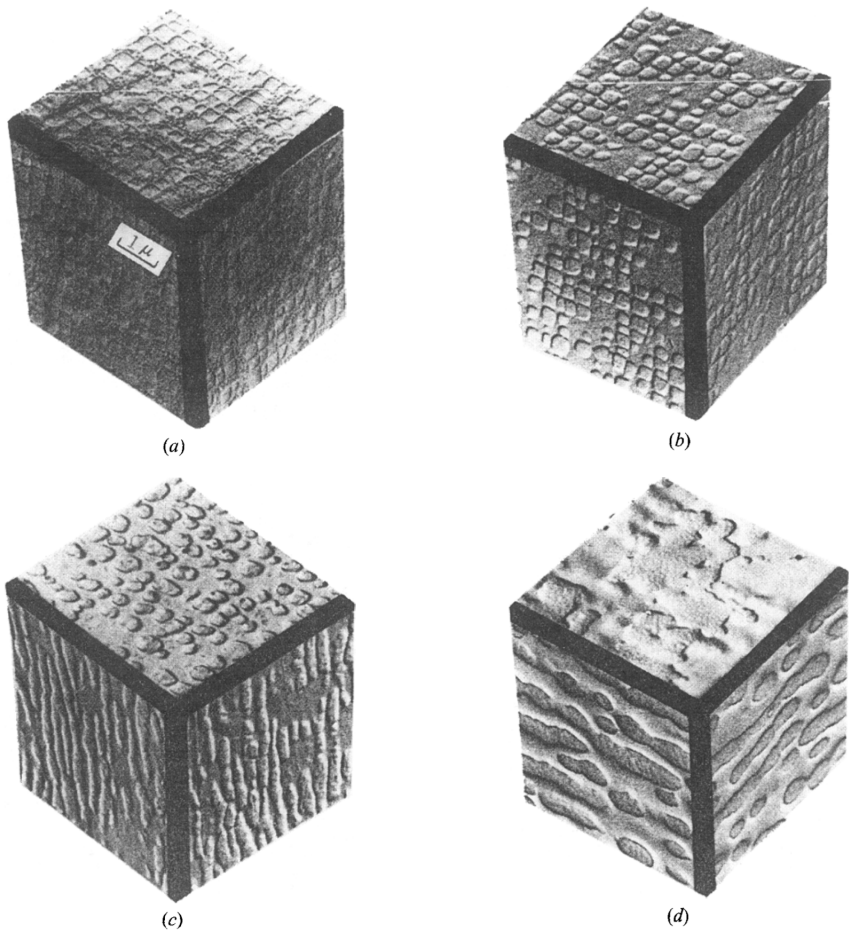

Figure 2.8: Microstructure states of Udmiet-700 with a positive lattice misfit (a) As-heat-treated state (b) Stress-free high temperature exposure resulting in coarsening (c) Tensile creep exposure resulting in P-rafts (d) Compressive creep exposure resulting in N-rafts [45].

From the perspective of precipitate evolution kinetics, rafting can be considered a two-step process. Early on the kinetics are dominated by the morphology change kinetics, later in the process, the dominant mechanism in the kinetics is that of coarsening as shown in Figure 2.9 [48]. The transition between rafting and coarsening, has been found to be roughly independent of temperature and stress, with a value of three times the initial γ channel width. Further, experimental observation have

determined that during the rafting process, the γ' volume fraction and precipitate periodicity remain nearly constant [48, 49].

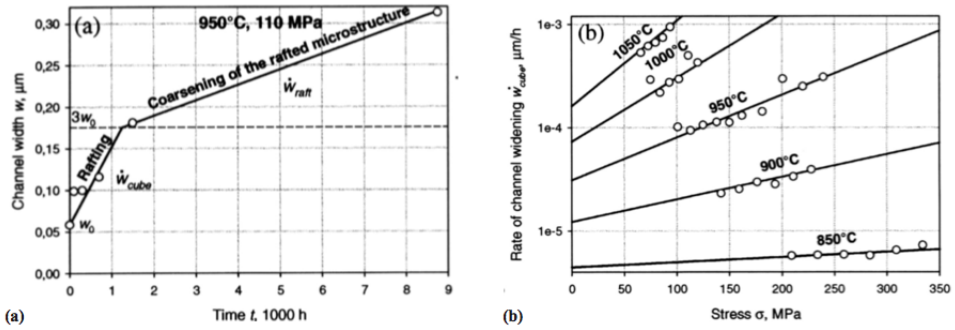

Figure 2.9: The kinetics of widening of γ-channels in [001] single-crystals of CMSX-4. (a) Increase of the channel width w during load annealing at 950°C, 110MPa. (b) Widening rate during rafting $\dot{w}_{cube}$ as a function of temperature and stress. [48]

As for explanations for the occurrence of rafting, much debate has been made as to whether the process arises from purely elastic strains or plastic strain. Generally, the basis that rafting occurs through plastic deformation within the γ channels is now widely accepted [50]. Through TEM analysis, the distribution of dislocations within the γ channels has been found to be nonuniform, such that there are preferential $\gamma - \gamma'$ interfaces where dislocations will collect depending on the sign on the applied creep stress [35, 43, 51]. Additionally, within the γ channels has been shown that stresses of magnitude to those that would be externally applied are present as result of the lattice misfit between the phases. In a theoretical sense, work has shown that elemental concentration gradients exist along the surface of the precipitates and are influenced by the applied stress and are a function of position on that surface. Further, the stress field has been found to alter the local growth kinetics, that results in a theoretical preferential direction to the coarsening [50, 52].

2.3 Precipitate Strengthening

In the standalone forms, neither pure γ or γ' present the necessary properties required of materials for high temperature service; however, when combined they exhibit unparalleled properties amongst all material classes (Figure 2.10). In the pure form Ni_3Al deforms through $\{111\}\langle 110\rangle$ slip at all temperatures until the structures disorder temperature at 1385°C. At temperatures below 800°C, $\{111\}$ slip has been observed to be heterogeneous, while above the slip is homogeneous or in other words all possible slip planes are active. Occurring with the Ni_3Al structure, are three distinct types of stacking faults:

1) Superlattice (intrinsic (SI) or extrinsic (SE)) faults which are shear displacements of $\frac{1}{3}\{111\}\langle 112\rangle$

2) Antiphase boundary (APB) faults which are produced via $\frac{a}{2}\{111\}\langle 110\rangle$ shear

3) Complex faults (CF) which are a superposition of the prior two and result in a shear of $\frac{a}{6}\{111\}\langle 112\rangle$.

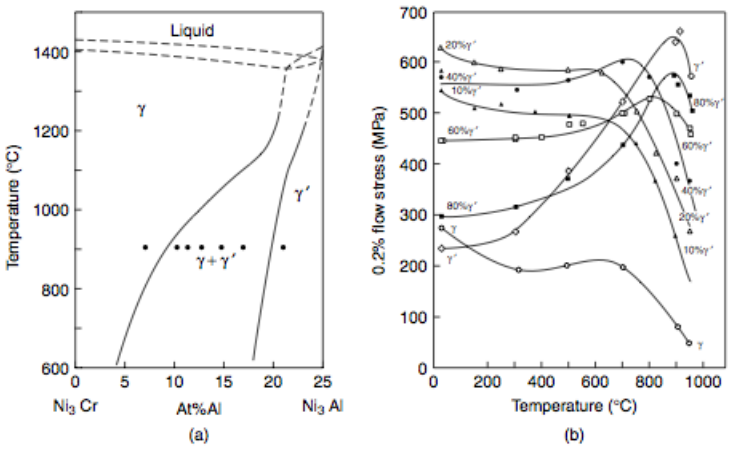

Figure 2.10: a) Section through the NiCrAl ternary phase diagram at 75 at% Ni b) Variance of the 0.2% flow stress of a Ni-base superalloy as function of γ' phase fraction [53].

Within the larger context of the composite $\gamma - \gamma'$ structure, the γ' particles have the ability to influence the mechanical behavior of Ni-base superalloys in many manners; however amongst them all, order strengthening is the dominant mechanism [16, 54, 55]. This was first evidenced through TEM work on the Ni-base superalloy Mar-M200 which revealed dislocations of the type $\frac{a}{2}\langle 1\bar{1}0\rangle\{111\}$ are unable to enter γ' precipitates without a trailing dislocation to reset the APB formed as a result of the passage of the first dislocation. Ultimately, the energy associated with the formation of the APB is the resistance that must be overcome if plastic deformation is to occur [54–57]. And such, the rate controlling step for plastic deformation to occur in Ni-base superalloys is the movement of a dislocation from the γ matrix to the γ' phase.

Depending on the size and spacing (volume fraction) of the γ' precipitates, the dislocation-precipitate interaction can be classified as either weak or strong [58, 59]. Specifically, weakly coupled dislocations is when the spacing of the dislocation is large compared to the diameter of the γ' particles as shown in Figure 2.11. Typically, the weak association is connected with Ni-base superalloys with low volume fractions of γ' which occurs in the early Niomic type superalloys or in the underaged (pre-heat-treatment) state [60].

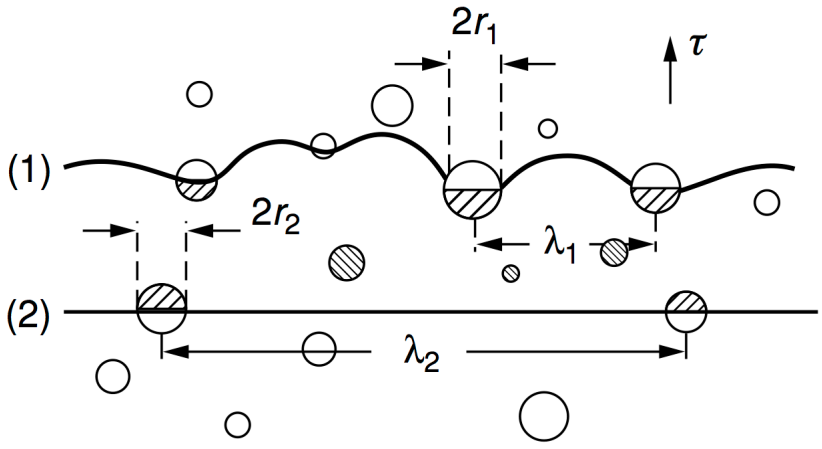

Figure 2.11: Weak pair-coupling of ordered γ' being sheared by dislocation pairs [16].

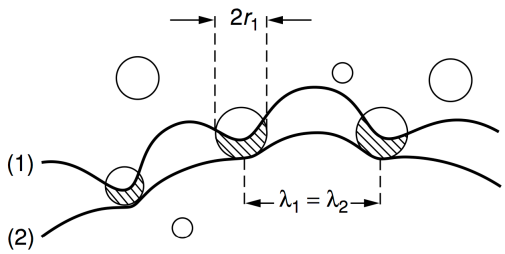

Figure 2.12: Strong pair-coupling of ordered γ' being sheared by dislocation pairs [16].

In the aged and over-aged states, weak dislocation mechanics are no longer applicable, and gives rise to strongly coupled dislocations where the spacing between γ' particles is on the same order as the spacing of the dislocation pairings as shown in Figure 2.12. In contrast to weak dislocations, each particle can have a dislocation pair association. Ultimately the applied shear stress required to pass a dislocation through a γ' particle must balance the net repulsive force between the dislocation for each dislocation. The critical shear stress is given by [16],

$$\tau_c = \sqrt{\frac{3}{2}} \left(\frac{Gb}{r} \right) f^{1/2} \frac{o}{\pi^{3/2}} \left(\frac{2\pi\gamma_{APB} r}{wGb^2} - 1 \right)^{1/2} \tag{2.8}$$

where G, b, f, and γ_{APB} have the same definitions as prior, o is a small dimensionless constant to account for numerical uncertainties, and r is the radius of the γ' particle.

Resulting from the γ'-dislocation interaction in the heat-treated state, is perhaps the most novel aspect of Ni-base superalloys; Ni-base superalloys exhibit a positive temperature dependence of the yield strength through the 700-800°C temperature range. This is directly attributable to the highly anisotropic energy associated with anti-phase boundaries in the γ' precipitates which results in the cross slip of dislocations from the {111} to {001} forming entanglements known as Kear-Wilsdorf locks [61].

2.4 Creep Behavior of Ni-base Superalloys

Between the three classes of cast Ni-base superalloys, all exhibit identical behavior in the early stages of creep as shown in Figure 2.13; however, conventionally cast materials fail after a creep strain of 2-3%, while DS and single crystal versions of identical alloy chemistry fail after creep strains of 20-30% while being exposed to identical loads and temperatures. In the conventionally cast state, the boundaries between neighboring grains become regions for concentration of significant amounts of inelastic strain and as a result, fracturing of the grain boundaries transverse to the applied load occurs [62].

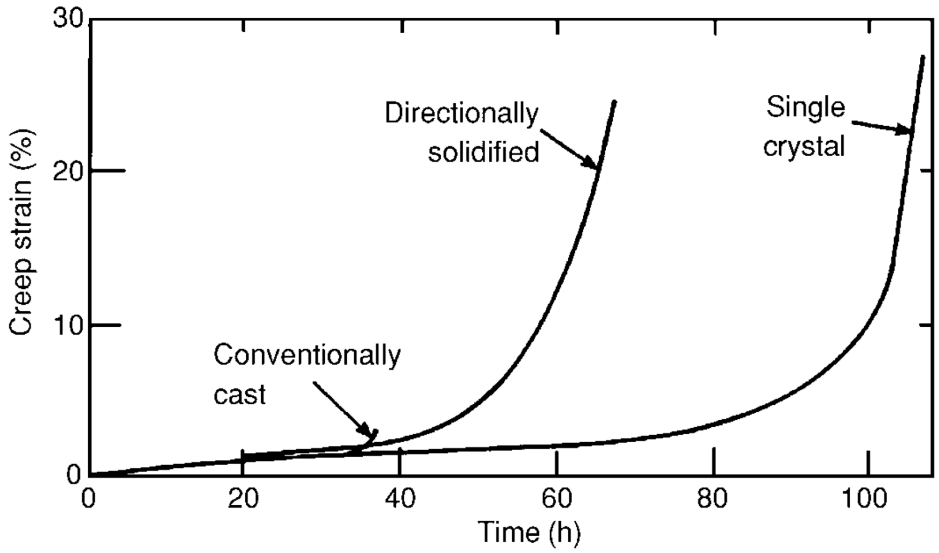

Figure 2.13: Creep testing of Mar-M200 in conventionally cast, directionally solidified, and single crystal forms at 206 MPa and 982°C [61]

In discussing the deformation mechanisms associated with the stages of creep in the context of Ni-base superaloys, the temperature and applied stress must be taken into consideration. This is because, with variation in temperature, arises a variation in the deformation phenomena; as a result a pairing of temperature ranges (temperature in °K) in relation to the melting temperature of the alloy and creep deformation mechanisms for Ni-base superalloys is required and can be classified in

the following manner [63]:

- Low temperatures $\frac{T}{T_m} < 0.6$
- Intermediate temperatures, $\frac{T}{T_m} \approx 0.6 - 0.7$
- High temperature, $\frac{T}{T_m} \geq 0.7$

2.4.1 Low Temperature Creep

The low temperature regime is dominated by high stresses and γ' shearing. Primary creep occurs through $\langle 112 \rangle$ slip on $\{111\}$ [64]. The slip is thought to occur through the reactions of Schokey partials of the $\frac{1}{2}\langle 110 \rangle$ at the $\gamma \backslash \gamma'$ interface. Overall, a $\frac{1}{3}[\bar{1}12]$ dislocation enters the γ' precipitate, while leaving behind a superlattice intrinsic stacking fault (SISF) and a $\frac{1}{6}[\bar{1}12]$ at the precipitate interface. With further reactions occurring and passage of similar dislocations through the γ' precipitates, the SISFs are eliminated and the precipitates are sheared. The transition to secondary creep occurs once a duplex slip orientation is reached. Once activated, this multi-slip condition prevents slip from occurring on the $\langle 112 \rangle$ and slip then occurs through on the $\langle 110 \rangle$ system.

2.4.2 Intermediate Temperature Creep

The intermediate temperature range, cutting of the γ' particles becomes difficult as a result of lower creep stress, and as a result the γ channels sustain significant inelastic deformation. Before the start of primary creep, a incubation period is often observed where no measurable macroscopic strains occur. During this incubation period grown-in networks of dislocations serve as sources for $\frac{a}{2}\langle 110 \rangle$ dislocations that when gliding through the γ channels deposit mixed or pure screw dislocations at the $\gamma \backslash \gamma'$ interfaces. During the incubation period, the dislocations glide almost exclusively through the channels that are horizontal to the applied load in a manner to relieve the stresses that result from the lattice misfit. In the case of compressive creep, the dislocations glide

through the vertical channels. Ultimately, the incubation stage sets-up a dislocation network that is highly inhomogeneous in nature and further, primary creep can not progress until the density of dislocations has reached a critical state. [51, 63]

With the passage into the primary creep regime, the dislocation density continues to increase until all the γ channels are filled [63]. Typically, dislocations of a single Burgers vector are present due to the limited sources of dislocations and react to deposit dislocation segments on γ' precipitate faces at 45° to the cube face. In cases where dislocation reactions do not occur, dislocation climb along the cube faces occurs resulting in a misfit relief. As observed by Pollock et al. [51], the strain accumulated during primary creep is often of the same magnitude required to relieve the internal stresses in the microstructure that result from the lattice misfit. This strain accumulation during primary creep corresponds to a decrease in the overall creep strain rate towards the end of primary creep. This is a result of the reduction of the internal stresses of the material, that are initially of the same order as the applied stress [65].

Only in the secondary creep regime has shearing of γ' particles been observed, and this only after strain accumulations of 2-3% [51]. The shearing phenomena, is the result of increases in stress within the precipitates while the surrounding matrix accumulates strain according to power law creep. In the case of high γ' volume fraction containing alloys, the shearing of the precipitates occurs through the passage of pairs of $\frac{a}{2}\langle 110\rangle$ matrix dislocations coupled with an APB [51, 66]

2.4.3 High Temperature Creep

The ultimate defining characteristics for the high temperature creep regime is the rapid development of equilibrium interfacial dislocation networks and the other being the directional coarsening of the γ' precipitates. Similar to the intermediate temperature regime, the early stages of primary creep are marked by inhomogeneous dislocation distributions from the limited number of dislocation sources. However, as

a result of the higher temperatures, dislocations can more rapidly diffuse through the γ channels, alleviating the misfit stresses. From a mechanical behavior point of view, the transition from that of primary creep to that of secondary or steady state creep is that of a plateau in the creep curve, this is normally correspondent to the evolution of the γ' structure from cubes to rafts.

The appearance of the constant strain rate is the direct result of a climb and dynamic recovery process occurring within the alloy. A defining characteristic of solid solutioned strengthened alloys, is that in the steady state creep regime is that a viscous glide mechanism operates at the beginning and end of the regime [67]. Macroscopically this is seen as the formation of voids and porosity through the coalescence of dislocations to localized regions within the material. In the case of high stress and temperature, the deformation mechanism that dominates is that of shearing of the γ' phase by couples of $\frac{a}{2}\langle 001\rangle$ dislocation [16, 68]. In the temperatures range of 650-750°C, and for low stress, there is not enough energy to push the dislocations through the γ' precipitates due to the high energy associated with the anti-phase boundaries in γ', and as a result the dislocations must loop around the precipitates [69–71].

The transition into the tertiary creep regime is normally marked by topological inversion of the phases, so that the γ' becomes the matrix and an acceleration in the creep rate as a result of the ease in which a$\langle 100\rangle$ dislocations can move through the interconnecting γ' matrix [71]. In the tertiary creep regime, the dominant dislocation mechanism is $\langle 1\bar{1}0\rangle\{111\}$ with these dislocations primarily being screw in nature. Further the deformation that occurs is homogeneous in nature, generally with more than two slip systems active [51, 72–74].

2.5 Fatigue Behavior of Ni-base Superalloys

In the operation of GTE, the start-up and shutdown of the engines is dominated by low cycle fatigue (LCF) interactions. Under these cyclic LCF conditions, Ni-base superalloys exhibit both temperature and strain rate dependent phenomena. However, a standard feature of Ni-base superalloys is that they rapidly achieve cyclic stability early in life at all temperatures and strain rates. In the case of isothermal LCF exposure, Ni-base superalloys exhibit a hardening effect that is the result of an increase in the dislocation density until a sustained state has occurred [68]. However, depending on the TMF load conditions either hardening or softening can occur.

For temperatures below 750°C, the cyclic defromation of Ni-base superalloys is dominated by inhomogeneous slip and shearing of the γ' precipitates by $\frac{a}{2}\langle 110\rangle$ on $\{111\}$ slip planes. Due to this shearing mechanism, Ni-base superalloys are largely strain rate independent at temperatures where the alloys strength is derived from that of the γ matrix phase which is generally below $750°C$. At lower temperatures, Ni-base superalloys are restricted to slip along the $\{111\}$ planes due to the limited amount of cross slip. A characteristic of low temperature fatigue is the formation of slip bands, which accommodates the plastic deformation, the ultimate spacing of which is an indication of the heterogeneity of the plastic deformation. However, increased plastic strain leads to more homogeneous deformation, i.e. decreased slip band spacings which is anomalous to multi slip [75].

At temperatures in the 750-900°C range, thermally-assisted processes begin to become possible and as a result cross-slip of dislocations is feasible. Further, for superalloys tested at low strain ranges under TMF conditions, localized recrystallization of material heavily deformed in slip bands has been observed, and attributed to the non-crystallographic fracture of superalloys [76]. Additionally, slip bands have been found to be precipitation sites for TCP phases [76].

In increasing the exposure temperatures of the cyclic loading further, ($> 900°C$)

and low stress levels, the deformation of Ni-base superalloys becomes more or less homogeneous as a result of deformation being localized to the γ channels and thermal sources providing the necessary energy for dislocations to easily cross-slip on the most highly stressed {111} planes [77]. Additionally, the increased thermal energy allows for the rapid formation of equilibrium dislocation networks similar to high temperature creep. At high temperatures, transmission electron microscopy (TEM) observations indicate that the dislocations are stored at the $\gamma - \gamma'$ interfaces and are typically nearly edge in character. Further, slip bands are found to be non-existent as a result of fewer dislocations being required to accommodate the plastic strain introduced into the material [68].

Orientation of DS and SX material has been observed to play a strong role in the fatigue life of the material [16, 78–82]. Typically, the greatest life for a Ni-base superalloy occurs when loaded along the [001] crystallographic axis. Much of the reduction in life observed for non-[001] fatigue lives can be attributed to the higher stresses for identical strains and the reduction in the number of available slip systems to accommodate the inelastic deformation of the material. While the differences in life are alloy and load dependent, differences as great as factors of ten have been reported. With the greatest differences in life occurring for small mechanical strain ranges.

In an effort to better simulate the fatigue conditions of hot section components, TMF conditions where a temperature waveform is imposed on a load waveform are often used. The most common TMF test types are out-of-phase (OP) and in-phase (IP) waveforms as shown in Figure 2.14. In OP loadings, the temperature and loading waveforms are 180° out of phase, while for IP loadings the waveforms are in phase (0°). In Figure 2.14 the loading can be of the form of an applied force, axial strain, displacement, etc. Of the two TMF cycle types, OP TMF is often considered to be the life limiting cycle [83, 84].

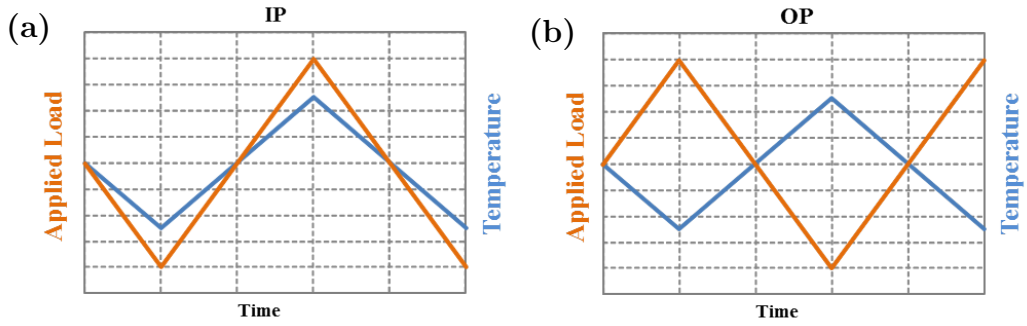

Figure 2.14: Thermomechanical fatigue waveforms for (a) Out-of-phase (b) and In-phase.

Resulting from the temperature-load phasing are differences in the damage mechanisms that lead to ultimate material failure. IP TMF of Ni-base superalloys is often considered the less damaging cycle definition as thermal exposure occurs during tensile stresses and the stresses at lower temperature are reduced which limits the slip band interaction in the materials [84]. Ultimately, the failure of the material is the result of fatigue crack propagation originating from damage that the γ matrix sustains under low temperature high stress conditions [7, 85]. In the case of OP TMF, oxides brittle oxides form on the material surfaces, and when undergoing strain reversals often crack or spall causing the oxidation of fresh material. In the case of continued oxide cracking the net result are oxidation spikes into the bulk material that become prime locations for fatigue crack nucleation as shown in Figure 2.15 [84]

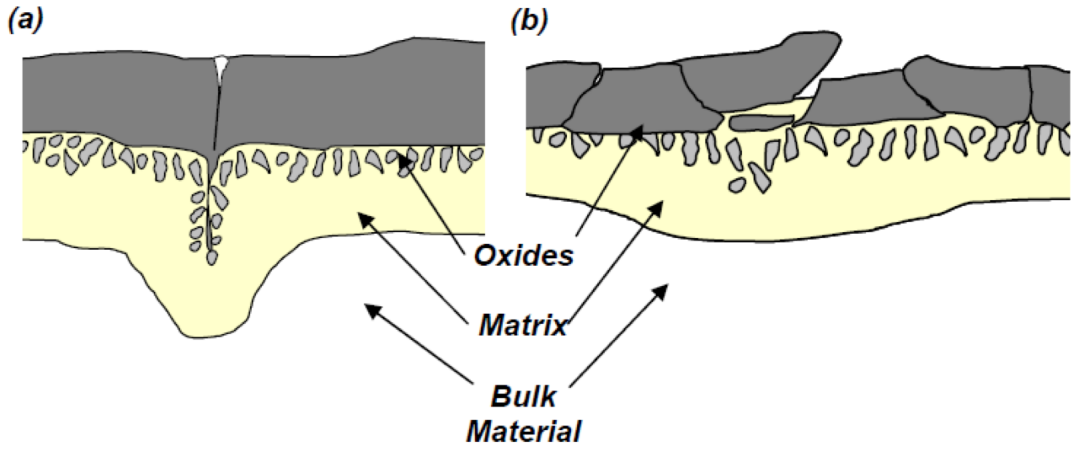

Figure 2.15: Surface oxidation and mechanical interaction illustrating (a) oxide spiking and (b) oxide spallation schematic [25].

From the results of transmission electron microscopy on Ni-base superalloys exposed to TMF deformation has been reported that dislocation arrangements are the net result of dynamic recovery processes taking place during the high temperature portion of the TMF cycles. At the $\gamma - \gamma'$ interfaces, hexagonal dislocation networks are observed to have formed as a result of high temperature climb. In view of the fact that in strain-controlled fatigue the net strain per cycle is zero, it is proposed that the sign of the dislocations in the networks is such that the internal stresses due to the lattice mismatch are reduced, in contrast to the case of monotonic deformation where the sign of the dislocations is governed by the sense of deformation [85]. Typically, in TMF the density of dislocations observed within the γ' precipitates is extremely low [86].

Unlike service components where microstructure evolution readily occurs, laboratory fatigue experiments are often too short to allow for significant microstructural evolution. As a result, efforts to artificially produce aged microstructures and investigate their fatigue properties has been considered [6,87]. In the case of polycrystalline Rene 80 given a tensile pre-creep treatment and tested at $871°C$ [88], the resulting N-raft microstructure was observed to reduce the fatigue life by a factor of five. However,

CMSX-4 given a compressive pre-creep treatment resulting in a P-raft microstructure and tested under CC isothermal conditions at 950 and 1050°C resulted in a 100% increase in the fatigue [89]. Interestingly, when CMSX-4 with a P-raft microstructure was tested under OP TMF conditions, a 50% life reduction was reported [90].

2.6 Creep-Fatigue Behavior of Superalloys

Generally speaking, the service conditions that Ni-base superalloys experience can be classified as neither as neither creep nor fatigue. As a result, cycles that include strain or load holds at peak cycle temperature are often used. These cycles are termed creep-fatigue (CF) cycles [68] and are for IP and OP TMF cases are shown in Figure 2.16. In absolute terms, neither tensile nor compressive dwells can be assigned a higher severity over the other as the severity is alloy dependent [68]. Overall, the net effect of dwell periods are the conversion of elastic strains into inelastic, while stress relaxation concurrently occurs.

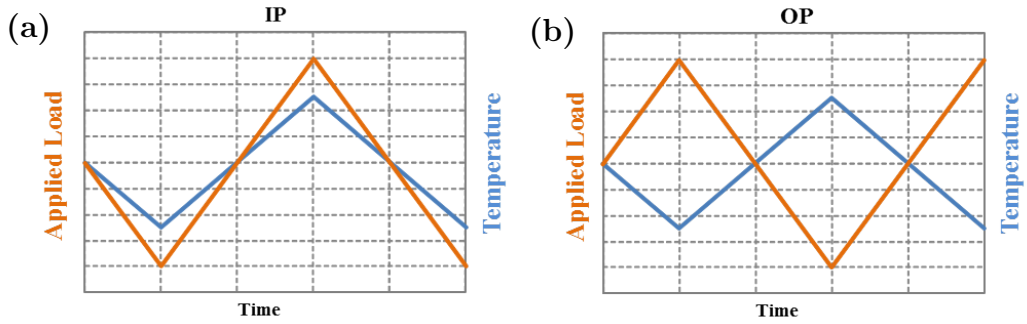

Figure 2.16: Creep-fatigue waveforms for (a) Out-of-phase (b) and In-phase.

In the case of tensile strain holds, the stress relaxation is the result of the formation of cavities and voids internal to the material [86]. Further, compressive holds generally promote the formation of larger oxidation spikes into the material, that upon the tensile reversal the oxide spikes are cracked and result in an elevated crack growth rate (Okazaki and Yamazaki, 1999). In addition, compressive holds lead to the development of tensile mean stresses [86, 91]. For the hold times 20 minutes was

determined sufficient to reach a saturated relaxation state, previously reported results on other Ni-base superalloys have indicated that the beyond a threshold, hold periods have no net influence on the stress relaxation and fatigue life [68].

For TMF CF cycles, neither tensile or compressive holds times can generally be classified as life limiting on the life of the material [68]. Generally, when compared to CC material life results, life reductions resulting from CF interactions can be in the 50-90% range depending on the loading conditions considered. While under CC conditions, aging of the γ' microstructure is nonexistent, there have been many documented cases of rafted microstructures observed in the failed material exposed to CF conditions [7, 91, 92].

CHAPTER III

EXPERIMENTAL METHODS

3.1 Specimen Geometries

In this study, all specimens were machined from CM247LC-DS slabs similar to the one shown in Figure 3.1. The slabs had approximate dimensions of 127x228x24 mm and were given proprietary heat-treatments identical to service components. Two types of specimen geometries were utilized: cylindrically smooth dogbone specimens (Figure 3.2) for low cycle fatigue experiments and specimens with a tapered gage section (Figure 3.3) to study the evolution kinetics of the γ' precipitates as a function of stress for a given temperature and time. All specimens were prepared by Cincinnati Test Labs (Cincinnati, OH). In the case of the smooth dogbone specimens, all had a gage length of 12.7 mm (0.55 in), gage diameter of 6.4 mm (0.25 in) and shank diameter of 12.7 mm (0.5 in). The surface finish for these specimens was specified as 32 RMS. These design specifications follow that as laid out by the ASTM standard E606-04 [93]. In the case of the tapered kinetics specimens, no testing standard exists. As a result machining tolerances and surface finish similar to those prescribed for the smooth bar specimens were adopted. The overall length of the specimens was 95.25 mm (4 in), with a 12.7 mm (0.5 in) shank length. The major and minor diameter of the kinetics specimens was 12.8 mm (0.5 in) and 6.4 mm (0.25 in) respectively, with the tapering occurring over a length of 41 mm (1.5 in).

For the smooth dogbone specimens given tensile pre-creep treatments and kinetics specimens used in tensile creep, an extra 12.4 mm of material was included on each end of the specimens. The additional material was used for machining of $\frac{1}{2}$in-13 UNC threads to allow for specimen installation in the tensile creep frame assemblies.

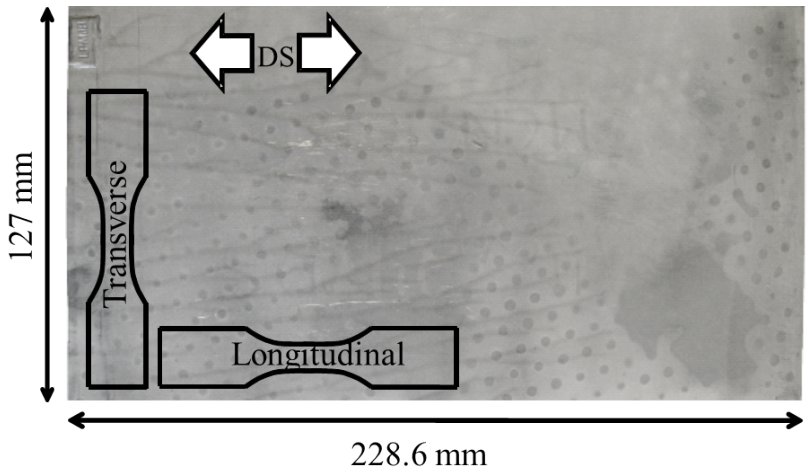

Figure 3.1: Directionally solidified CM247LC-DS slab in the as-cast and heat treated condition.

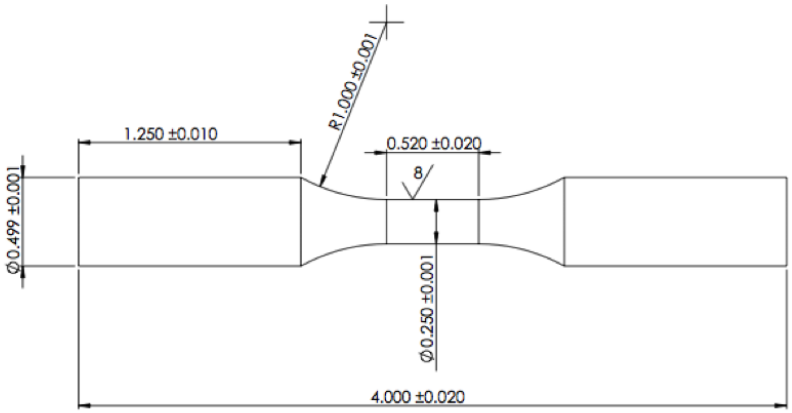

Figure 3.2: Geometry of standard smooth cylindrical dogbone specimen. Units are in inches.

After the addition of the threaded creep adapters, the smooth dogbone and kinetics specimens had length of 127 (5 in) and 120.6 mm (4.75 in) respectively.

3.2 Aging Experiments

3.2.1 Isotropic Coarsening

To provide the thermal exposure for isotropic coarsening of the microstructure, a 3-zone Lindberg 240 V (Model 59744-A) electric-resistance tube furnace was utilized (Figure 3.4). While in the furnace the specimens were exposed to static laboratory

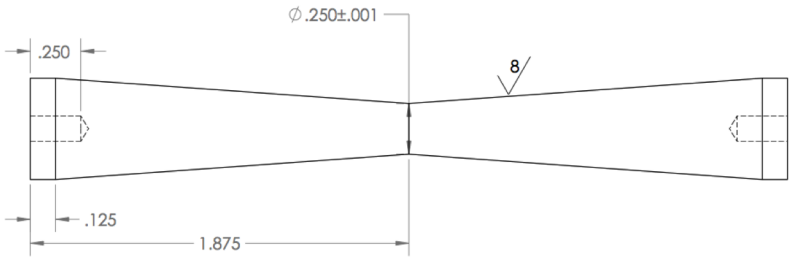

Figure 3.3: Geometry of kinetics specimen used to obtain a variation in stress to study microstructure evolution kinetics dependence on stress. Units are in inches.

Figure 3.4: Lindbergh tube furnace used for isotropic coarsening.

air for the duration of the exposure. Upon shutdown, the specimens were allowed to air cool inside of the furnace. Afterwards, the oxidation scale that formed during the thermal exposure was removed from the specimens gage section. This was done through sanding the gauge section beginning 240 grit SiC paper and successively decreasing the grit size to 2400 grit SiC sand paper. As a result, the diameter after thermal exposure and polishing was 0.25 in.

3.2.2 Aging in Tension

Tensile pre-creep treatments were given to the group of specimens with the threaded creep adapters. The specimens were screwed into the specimen adapters, which were then attached to pull rods of 19.05 mm (0.75) diameter. The specimen adaptors

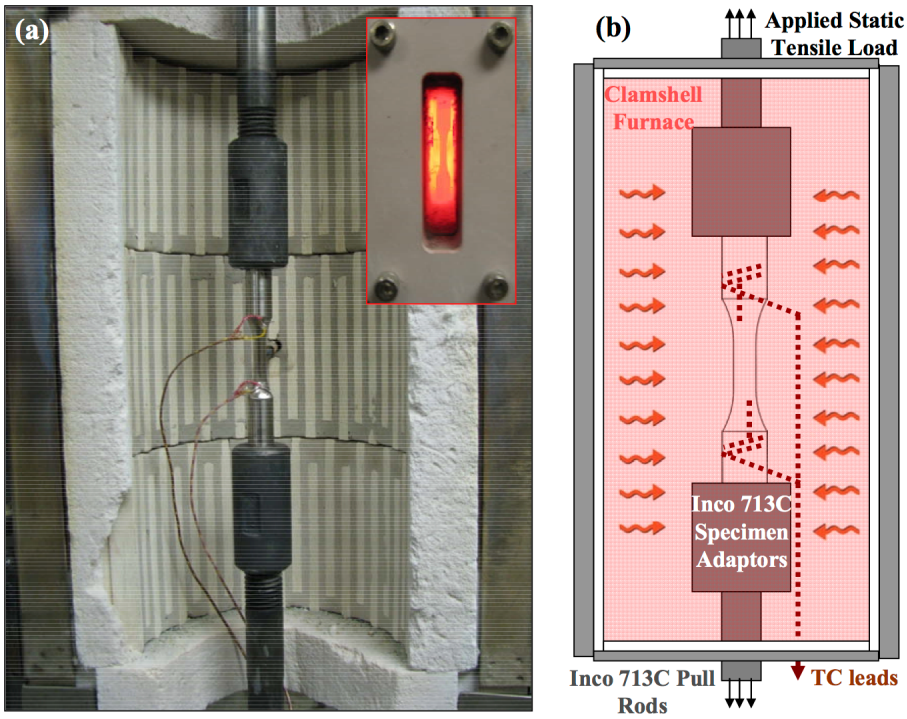

Figure 3.5: Tensile creep set-up depicting the specimen/pull rod linkages.

and pull rods were manufactured from either Mar-M246 or IN713. For providing the tensile pre-creep treatment, SATEC tensile creep frames (Model 1156) were used. The frames were outfitted with three zone ATS clamshell furnaces that utilized super kanthal heating elements and were collectively controlled by a Omega temperature controller (Model: CN5001K2).

The temperature distribution across the length of the specimen was determined through K-type thermocouples spot welded on each of the specimen shoulders as shown in Figure 3.5. Through adjusting the specimens position within the furnace, the temperature gradient across the specimen was maintained within +/-1% of the desired temperature in compliance with ASTM standard E139-11 [94]. Heat within the furnace was allowed to stabilize for two hours prior to the application of the load. Once the pre-creep treatment was completed, the specimens were allowed to air cool to room temperature. Removal of the accumulated oxide layer was done in

the manner described earlier.

3.2.3 Aging in Compression

Compressive pre-creep treatments were given to a group of standard fatigue specimens using the custom built compressive creep frame shown in Figure 3.6. The design details of the compressive creep frame as provided in Appendix A. To install the specimens within the compressive creep frame, the specimens were placed within the specimen centering pocket on the lower specimen support cylinder with the upper specimen support cylinder then being placed atop the specimen resulting in the configuration shown in Figure 3.7. To provide rigidity to the specimen assembly during heating, the hydraulic cylinder assembly was extended until contact was made between the specimen assembly and hydraulic cylinder assembly. To prevent the build-up of stress in the hydraulic system during heating of the specimen assembly from constrained thermal expansion, the hydraulic valve on the pump was left open. This allowed free thermal expansion to occur. As a note, in the current design implementation, the maximum testing temperature is 950°C. Above 950°C, oxidation of the 316 stainless steel support cylinders is too great.

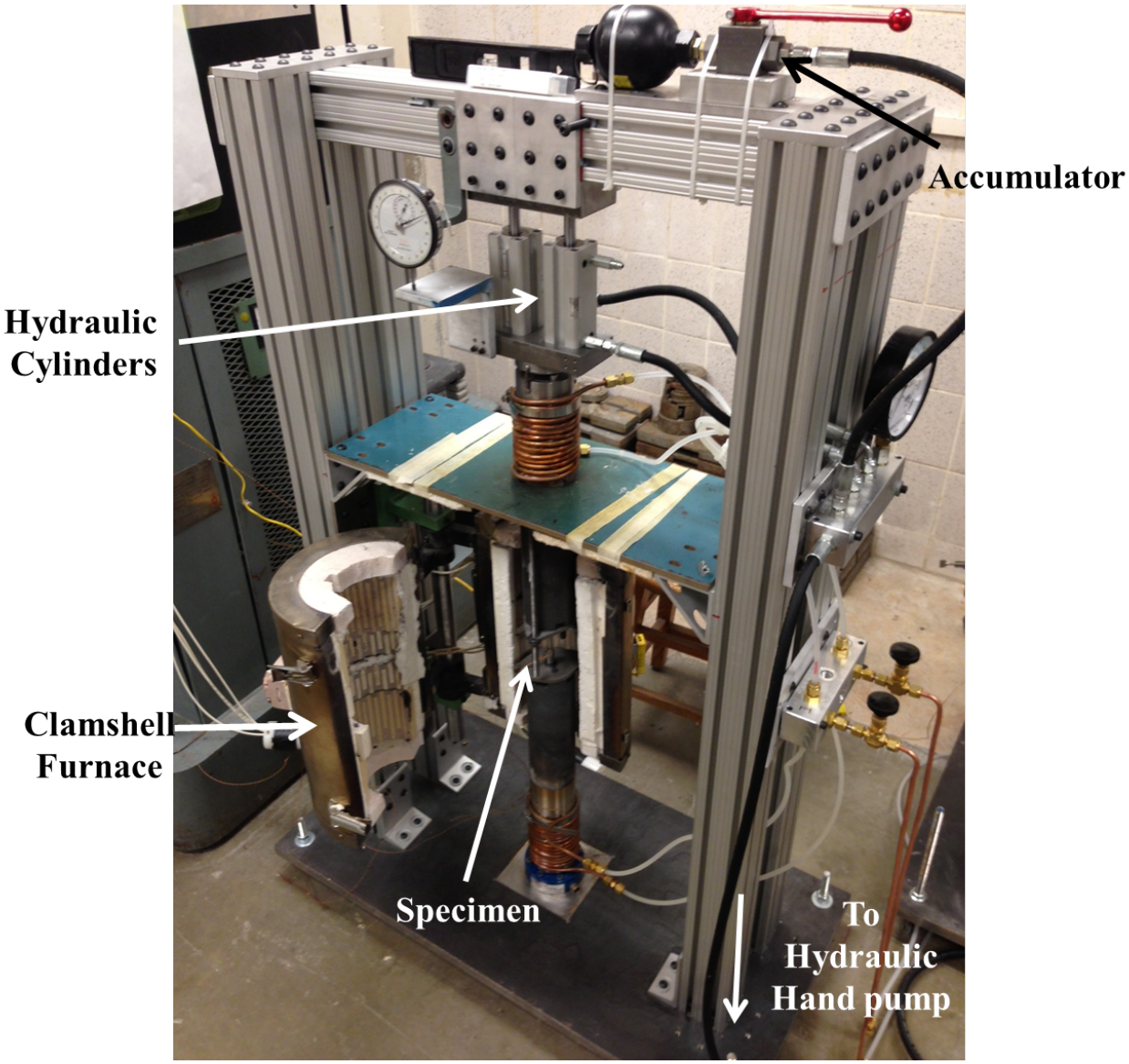

Figure 3.6: Overview of the compression creep frame.

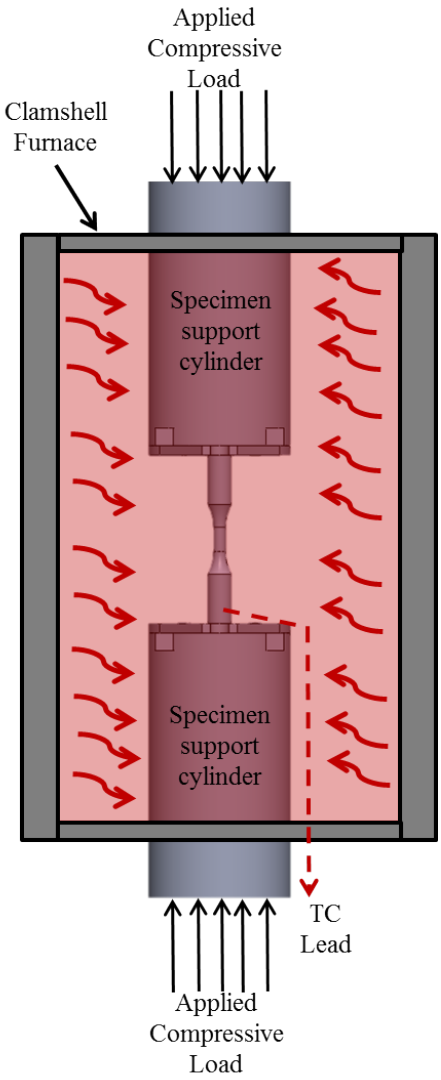

Figure 3.7: Compressive creep schematic depicting the specimen specimen assembly.

The temperature distribution across the length of the specimen was determined through K-type thermocouples spot welded on each of the specimen shoulders as shown in Figure 3.5. The temperature gradient across the specimen was monitored to ensure a +/-1% variation was maintained. As no ASTM standard for compressive creep of metals at high temperature exists, applicable best practices were borrowed from ASTM standard E139-11 for high temperature tensile creep [94]. Once at temperature, the furnace was allowed to stabilize for two hours prior to the application of

the compressive load. Once the compressive pre-creep treatment was completed, the specimens were allowed to air cool to room temperature. Removal of the accumulated oxide layer was done in the manner described earlier.

3.3 Low Cycle Fatigue

3.3.1 Servohydraulic Test System

For all LCF experiments, either a 44.5 kN (10 kip) MTS axial servohydraulic testing machine with load cell resolution of +/-0.5kN (+/-100 lbf) or 100kN (22 kip) MTS axial torsional servohydraulic testing machine with a load cell resolution of +/-1.25 kN (+/-250 lbf) was utilized for all testing. The load frames were equipped with water-cooled MTS model 646 collet grips to grip the cylindrically smooth dogbone specimens and provide conductive cooling for TMF testing. FlexTest40 digital controllers in conjunction with MTS TestSuite Multipurpose Elite Software were used to control the servohydraulic machines. An analog temperature command signal was output by the digital controller to a Watlow 945A-2FK5-A000 PID temperature controller on the 44.5 kN machine. Later a Eurotherm model 3204 temperature controller replaced the Watlow temperature controller. An identical Eurotherm temperature controller was used on the 100 kN machine. In either case, the input analog signal to the temperature controller served as a remote set point necessary to determine the error signal for PID control. Ameritherm 2kW induction heaters were used on both systems, which induced the desired temperatures in each specimen. Temperature feedback was provided by a K-type thermocouple. The nominal hydraulic pressure applied to grip the specimens was 29 MPa (4200 psi).

Axial displacement within the gage section were measured using a high temperature extensometer (MTS model 632.52E-14), with the nominal gage length between extensometer tips being 12.7 mm (0.5 in) as shown in Figure 3.8. Alumina rods with v-chisel points extended from the extensometer, passed between induction coil turns

and pressed against the gage section of the specimen. The 5.0 mm diameter alumina rods had v-wedge ends, which were held against the specimen by a spring mechanism mounted in the support brackets.

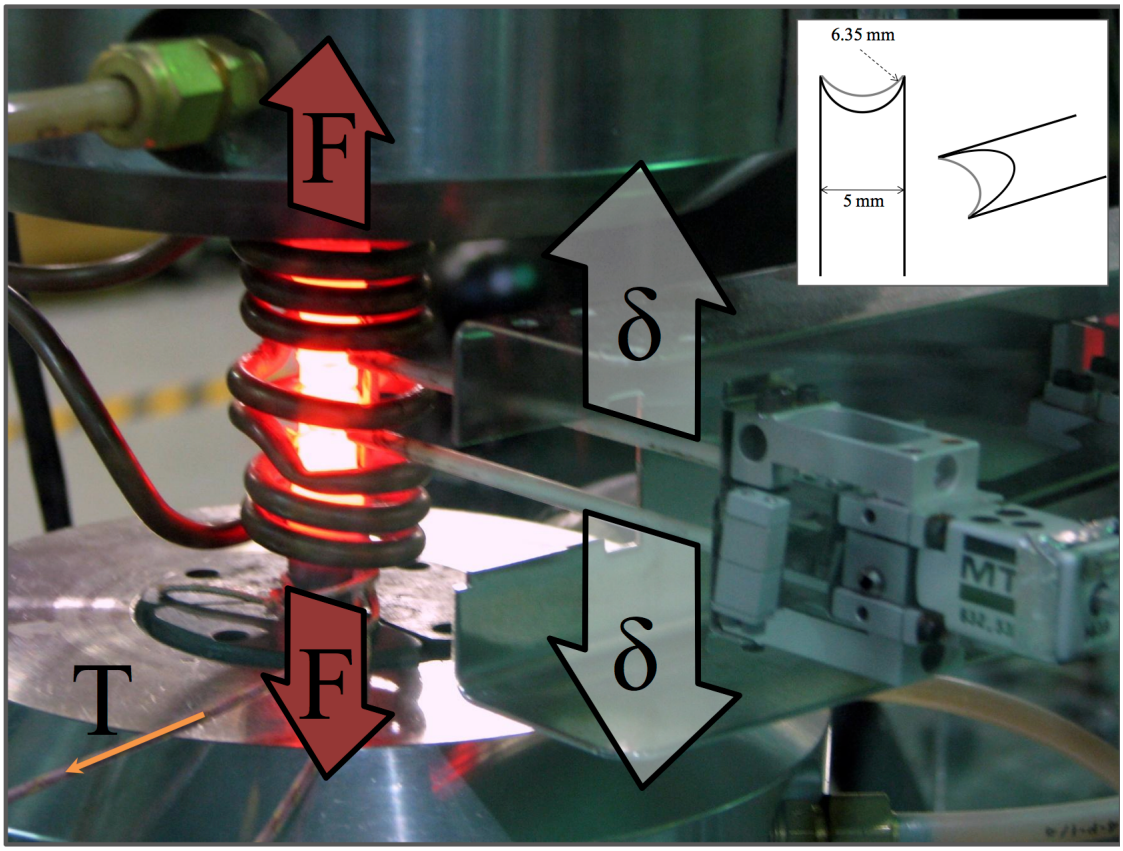

Figure 3.8: Servohydraulic setup depicting the temperature (T) measurement, controlled force (F) and the measured displacement (δ).

Each specimen had a single thermocouple (TC) spot welded onto the gage section slightly outside of the extensometer rod seating position as shown in Figure 3.9. This TC placement was chosen as to minimize the possibility of introducing flaws into the gage section at which the fatigue crack would nucleate. The induction coils were made from copper tubing having 4.7 mm ($\frac{3}{16}$ in) outer diameter. For the induction coil, seven turns were utilized in the coil including a middle turn between the extensometer rods. The middle turn had a inner diameter of 28 mm while the other turns had inner diameters of 23 mm.

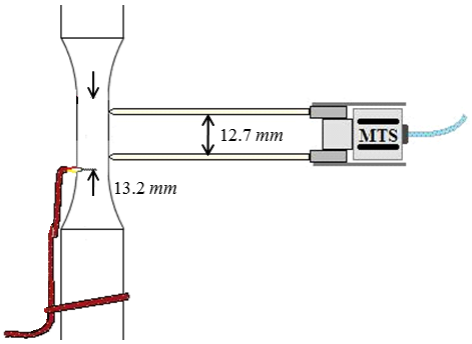

Figure 3.9: Depiction of TC spot weld location in relation to the extensometer seating location on the gauge section of round dogbone specimen.

3.3.2 Thermal Expansion Compensation in TMF

In the case of the cylindrical smooth dogbone specimens, the deformation can be assumed to uniform throughout the specimen's gage section and the extensometer displacement measurement at the specimen surface is a measure of the total strain occurring in the specimen,

$$\epsilon = \epsilon_\theta + \epsilon_{mech} \tag{3.1}$$

where ϵ_Θ is the thermal strain, and ϵ_{mech} is the mechanical strain. To properly determine the mechanical strain during a TMF experiments, the strain associated with the thermal expansion must be determined a priori. Experimentally, thermal strain can be calculated as either a function of temperature or time. Defining the thermal strain or thermal displacement as a function of temperature corresponds to temperature-based thermal strain compensation as described in ASTM E2368-10 [95].

3.3.2.1 Temperature-Based Compensation

For temperature-based compensation, the secant method is traditionally utilized assuming a linear relationship between thermal expansion and temperature,

$$\epsilon_\theta = \alpha\,(T - T_o) \tag{3.2}$$

where α is the coefficient of thermal expansion and T_o is taken as the reference temperature for zero thermal strain. In the case of Ni-base superalloys, particularly with a large temperature range, a nonlinear function is often required to account for the nonlinearity of the material's thermal expansion. The relationship can be made nonlinear by either introducing a nonlinear temperature dependent thermal expansion coefficient,

$$\epsilon_\theta = \alpha\left(T\right)\left(T - T_o\right) \tag{3.3}$$

or through the introduction of higher order polynomial terms,

$$\epsilon_\theta = \sum_{n}^{i=0} \alpha_i T^i \tag{3.4}$$

Within the MTS Multipurpose Elite software the temperature dependent compensation can be implemented through the fitting of a polynomial to free expansion data. In prescribing free expansion, a null force and cycle temperature at a mean value and amplitude, and a cycle time identical to the TMF experiment. For capturing the nonlinearity of the thermal expansion, typically a second order polynomial is sufficient as shown in Figure 3.10.

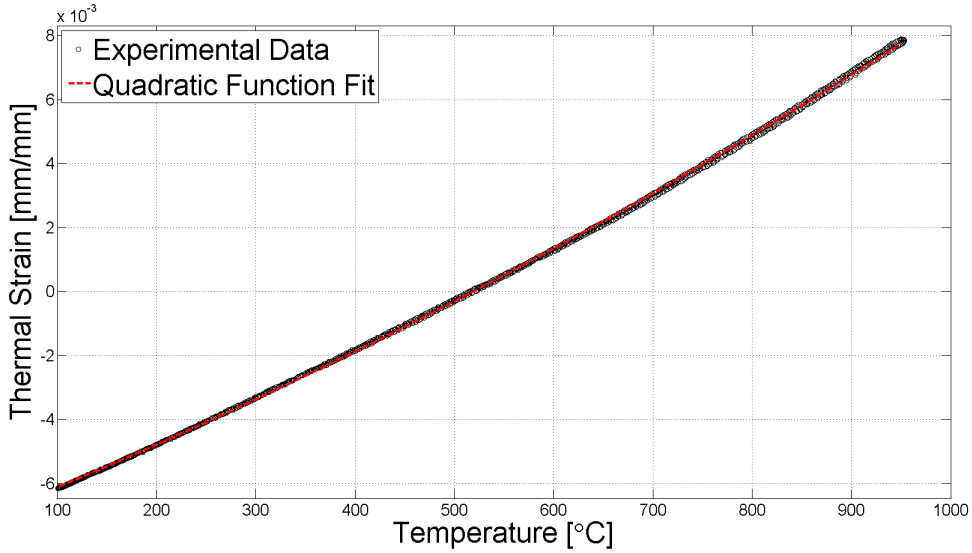

Figure 3.10: Measured strain under free expansion shown with temperature-based thermal strain fit.

The deterrent of the temperature dependent method is that the cyclic hysteresis of the thermal expansion loop is not adequately captured and the net polynomial fit results in the approximation of the average thermal strain at a given temperature (Figure 3.10). This cyclic hysteresis is dependent on the combined effects of differences in the heating and cooling of the material and temporal lags in the electronic signals being processed by the temperature controller and the servohydraulic controller. To provide allowance for this, the ASTM E2368-10 provides limits on the error between measured and calculated thermal expansion to a maximum hysteresis width to within 5% of the expansion range [95].

3.3.2.2 Time-Based Compensation

The alternative to the temperature-based compensation method is that of time-based thermal expansion compensation; this method allows for the accounting of the cyclic hysteresis and non linearity in the cooling or heating cycle. In the case of TMF experiments, the applied temperature can be considered a constant periodic function in the time domain, regardless if the experiment is IP, OP, or either IP/OP with

a dwell. Acknowledging this periodicity, a Fourier series can be readily applied to represent the time based thermal strain function. In the finite form, the Fourier series can be represented by

$$\epsilon_\theta(t) = \frac{1}{2}a_o + \sum_{n=1}^{N}(a_n cos(nt) + b_n sin(nt)) \tag{3.5}$$

where the Fourier coefficients a_n and b_n are numerically determined from the experimental thermal strain data. In the case of constant thermal cycling 10-20 Fourier coefficients are sufficient to capture the cyclic hysteresis as shown in Figure 3.11.

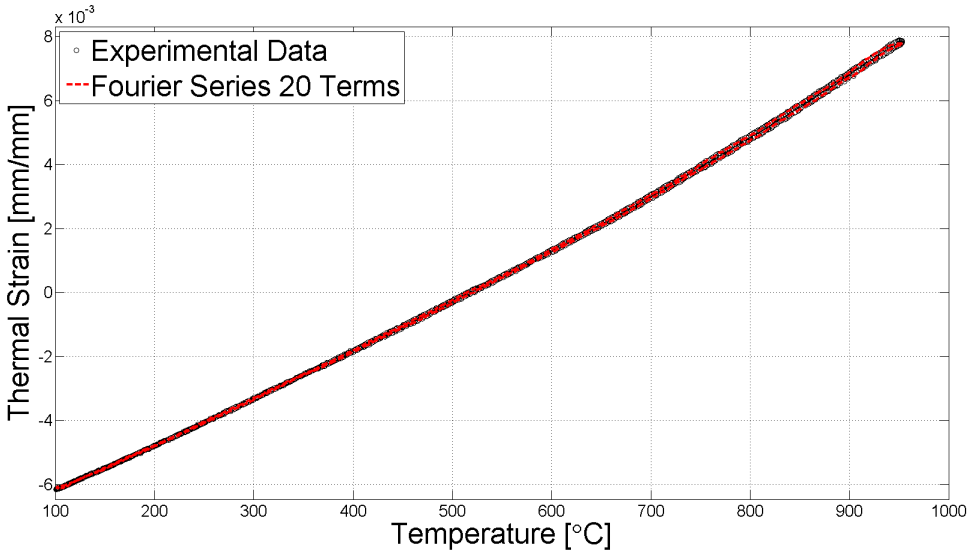

Figure 3.11: Measured strain under free expansion shown with time based thermal strain fit.

Although a powerful method for the fitting of the thermal strain history, the time based Fourier Series approach does have limitations. Direct extension of the methodology to TMF cycles that includes strain dwell periods requires accounting of the Gibbs Phenomena. The Gibbs Phenomena is where the periodic function overshoots the true function at jump discontinuities [96], which in the case of continuous thermal cycling with a dwell, a natural overshoot in the fit of the thermal strain will occur and the beginning and ending of the dwell period.

To compensate for the Gibbs Phenomena in the thermal strain fit, the temperature control signal is programed to overshoot the dwell temperature by 5-10°C and then drop back to the dwell temperature within a second. To account for the Gibbs phenomena prior to cool down, the temperature control signal is directed to increase the temperature by 5-10°C during the final few seconds of the dwell. The net effects of including these small temperature overshoots is that they mimic the Gibbs phenomena, but in a controllable and predictable manner, such that the thermal strain calculations are repeatable (Figure 3.12).

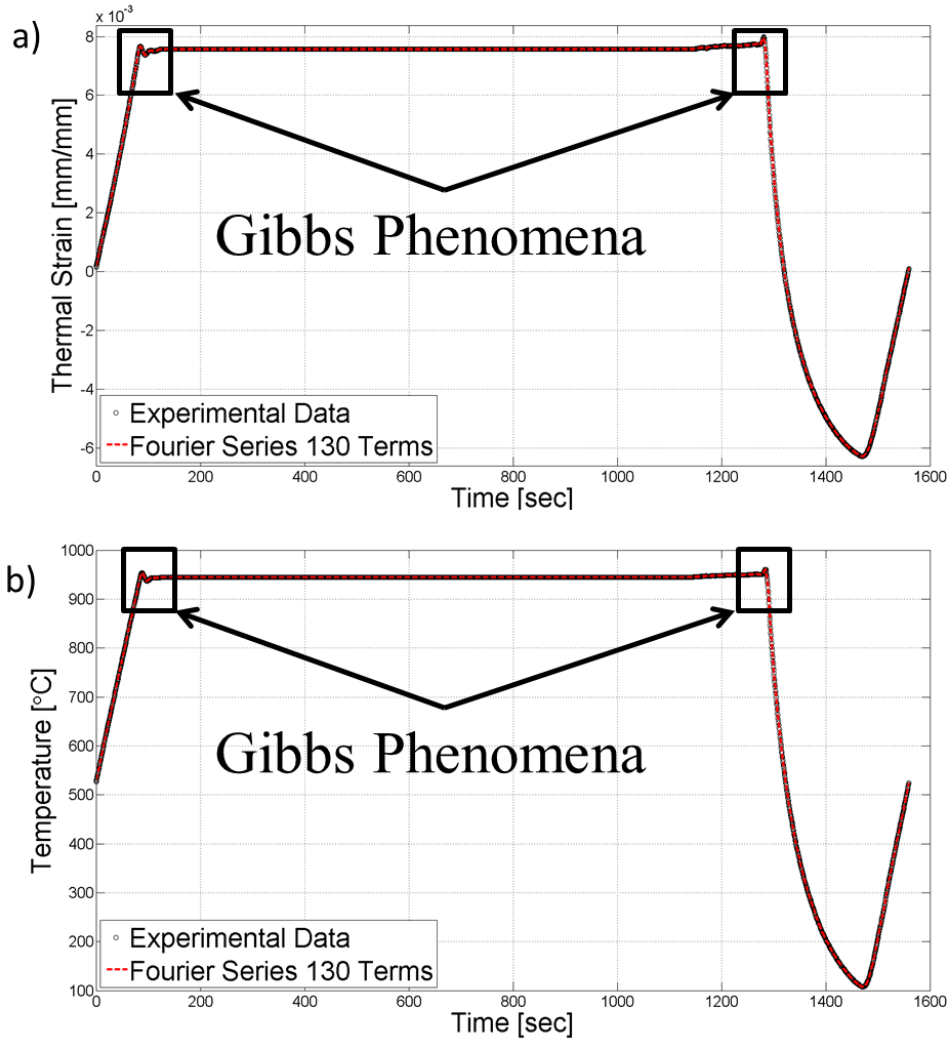

Figure 3.12: Time based thermal strain compensation accounting for the Gibbs phenomena a) Thermal strain vs. time b) Temperature vs. time.

3.3.3 Fatigue Testing Methodology

All TMF tests were performed while adhering to ASTM E2368-10 and ASTM E606-12 in the case of isothermal experiments. Dictated by the ASTM standard E2368-10 is the following testing requirements related to the experiment temperature, with the first requirement being common with E606-12:

1) The maximum allowed temperature differential over the length of the gage section at any time during cycling shall not be greater than $+\backslash -1\%$ of T_{max} in °K or $+\backslash -3$°K, whichever is greatest.

2) During free expansion cycling, the thermal hysteresis shall be no more than 5% of the total thermal strain range.

3) Under mechanical strain control, the response may not deviate from the control signal by more than 2% of the range.

4) The phase shift shall not deviate by more than 5° of the desired value for all time.

Fulfillment of the first criterion is dependent on the design and quality the induction coil. A newly fabricated induction coil must be first thoroughly tested for temperature differentials prior to any TMF testing. For the coils used over the course of this research, validation of coil's ability to produce a uniform temperature distribution was determined by welding ten thermocouples to a smooth dogbone specimen and recording temperature at every 50°C between 100-1050°C. Of the ten thermocouples, six measured the temperature differential in the axial direction and four radially at the center of the gage section. In cases where temperature distributions outside of the standard were found, the spacing of the coils or shape would be altered until the temperature distribution was within the allowable tolerance.

In cases where temperature-dependent thermal strain compensation was used, the temperature control parameters (PID values) were varied during cycling until the hysteresis width was minimized so as to satisfy the second criteria. Instances where the time-based Fourier series thermal expansion compensation was utilized to capture steady-state thermal expansion behavior this criteria was automatically satisfied.

To satisfy the criterion on phase shift the time lag between temperature command and thermocouple feedback was quantified and incorporated so that phasing in the control program offset the time lag associated with temperature control error. Prior to the start of each TMF test, a few elastic TMF cycles were performed in mechanical strain control to ensure that phasing compensation adhered to the standards, and if not, the phase lag was modified until the ASTM E2368-10 was satisfied. For all tests the necessary phase lag needed to adhere to ASTM E2368-10 varied between -20 and -24° depending on the load frame being used.

3.3.4 Life Criteria

In fatigue testing, different thoughts exist through which the life of the material under given experimental conditions is determined. Generally speaking, complete fracture of a specimen is not necessarily the life of the material, as design specifications often consider the material to have failed prior to full fracture so as to avoid catastrophic failures that can lead to loss of life or significant capital loss. For all strain-controlled experiment conducted, a 5% load drop criteria from the stabilized hysteresis was used to determine the experiential life,

$$P_i(N_i) = 0.95 * P_o \tag{3.6}$$

where P_o is the stabilized peak tensile load.

3.4 Metallography Preparation

To prepare all specimens for microstructural analysis, a Buehler low speed Isomet saw was used for sectioning the specimens. Once sectioned, the specimens were cold mounted in epoxy to provide a workable geometry for the grinding and polishing process. To give the specimens an acceptable surface for etching a five step grinding and polishing process was used as detailed in Table 3.1. To reveal the $\gamma - \gamma'$ microstructure either Kallings Etchent II or a γ' etcher were used as given in Table 3.2. The Kallings II etchent is a general etchant that chemically attacks both the γ and γ' phases and relies on phase contrast between the phases to distinguish them. The etchant that specifically attacks the γ' is valuable in that localized plastic deformation in the form of slip bands is readily revealed within the microstructure. Unless specifically noted in the micrograph, Kallings II was used.

Table 3.1: Grinding and polishing procedure used for preparing CM247LC-DS specimens for microscopy [97]

Surface	Abrasive/Size	Load [N]	Platen Speed [rpm]	Time [min]
Si-carbide	P240 grit	27	240-300	Until Plane
Ultra-Pol Silk Cloth	9μ Diamond	27	100-150	5
Trident cloth	3μ Diamond	27	100-150	4
Trident cloth	1μ Diamond	27	100-150	3
Microcloth pad	0.05 Alumina μ diamond	27	80-150	2

Table 3.2: Ni-base superalloy etchants [97].

Etchant Name	Etchant Constituents	Notes
γ' Etchant	50ml HCL 50ml H_2O_2	Good grain boundary etch. Attacks γ' in Ni-base alloys. Sample immersion for 10-15 seconds.
Kallings II	HCL H_2O CuCl	General etchant. Attacks γ' in Ni-base alloys. Sample immersion for 30-45 seconds.

CHAPTER IV

CHARACTERIZATION OF AGED MICROSTRUCTURES

The microstructure states that occur in a GTE service components as a result of thermomechanical exposure can be considered anything but ideal; these microstructures arise as a result of coupled thermal and stress histories that vary spatially due to the intricate cooling passages and hot gas flows. To provide a link between the microstructure states encountered in service components at the end of its service life and those microstructure generated under controlled laboratory conditions, an airfoil removed from service after 32,000 hours of service was serial sectioned and examined. From this information, parameters for the aging of specimens to be tested under TMF were determined. Further, the results of artificial aging experiments conducted under controlled laboratory conditions will be discussed and their use in calibrating an analytical aging model that relates to how the γ' phase evolves. Lastly, the experimentally determined effects of aging on the elastic modulus, yield strength, and room temperature fatigue behavior of CM247LC-DS will be discussed.

4.1 As-Heat Treated Microstructure Quantification

The microstructure in the as-heat-treated form is coarse with columnar grains of an average diameter of 2 mm. The primary dendrite spacing is 0.5 to 1 mm, with the secondary dendrite arm spacing being 0.25 mm. Representative micrographs of the dendritic structure within from the perspective of the longitudinal orientation (direction of solidification) are shown in Figure 4.1a. Through the anisotropy of light diffraction, grains of different secondary orientations can be readily observed through the differences in contrast as shown in Figure 4.1b.

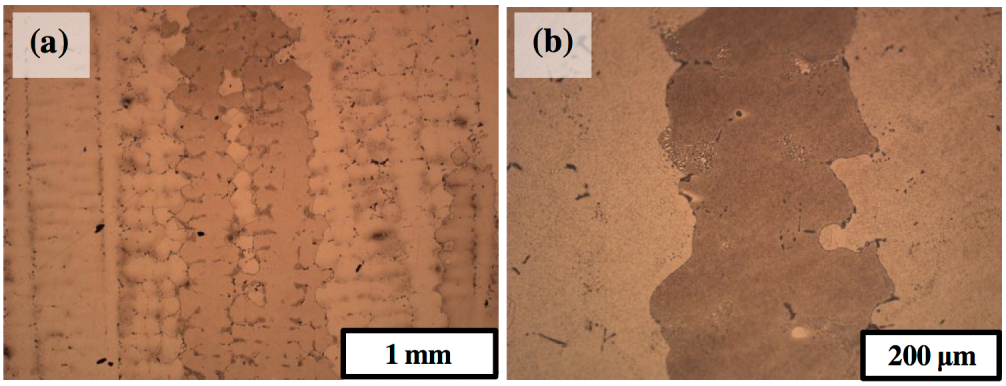

Figure 4.1: (a) Dendritic grain structure of CM247LC-DS in the longitudinal orientation (b) Magnified view of the dendritic grain structure.

In the standard heat-treated form, CM247LC-DS is a multi-phase material with a dendritic structure. Within the dendritic core consists of a austenitic FCC-like γ matrix, into which is dispersed a bimodal distribution of γ' precipitates throughout the matrix. Both the primary and secondary γ' found within the dendritic regions of the material take on a cuboidal geometry. The primary γ' is shown in Figure 4.2. The secondary γ' are located in the γ channels between the primary γ' precipitates. In the fully heat-treated state, the average primary γ' cube length (w_o) was determined to be 0.75 μm. Through scanning electron microscopy (SEM), the secondary γ' were not observed in the microstructure. Their lack of presence could be a consequence of the etching process. In previous studies on CM247LC-DS with the same heat-treatment as in this work, secondary γ' were reported to have a cube length of 70 nm on average [98]. Lastly, the average γ channel width (h_o) was measured to be $0.18\mu m$.

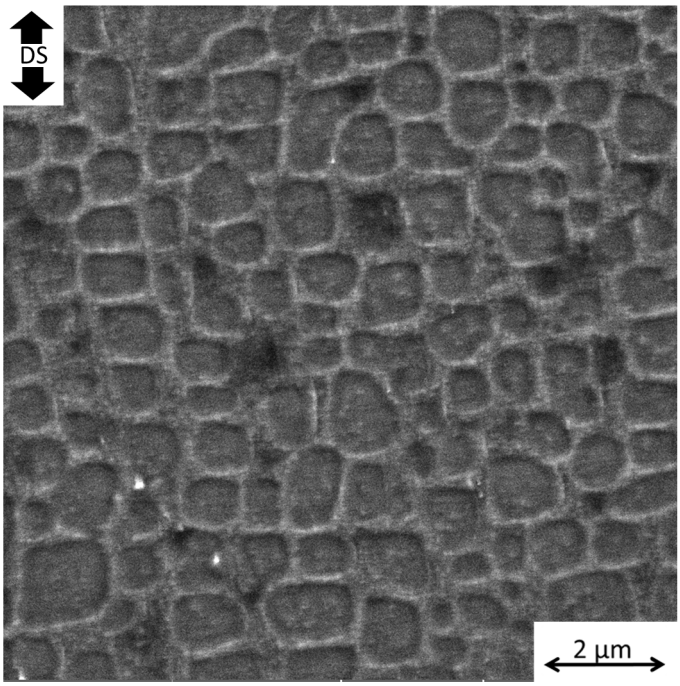

Figure 4.2: Initial cuboidal γ' microstructure within the dendritic core.

For the proprietary heat-treatment given to the alloy, γ-γ' lattice misfit in CM247LC-DS is negative over the entire temperature range of interest. The misfit defined by Equation 2.2 was determined through JMatPro and is shown in Figure 4.3 [99]. The implications are such that under pure tensile loading N-Rafts will be formed and under pure compressive loads P-Rafts.

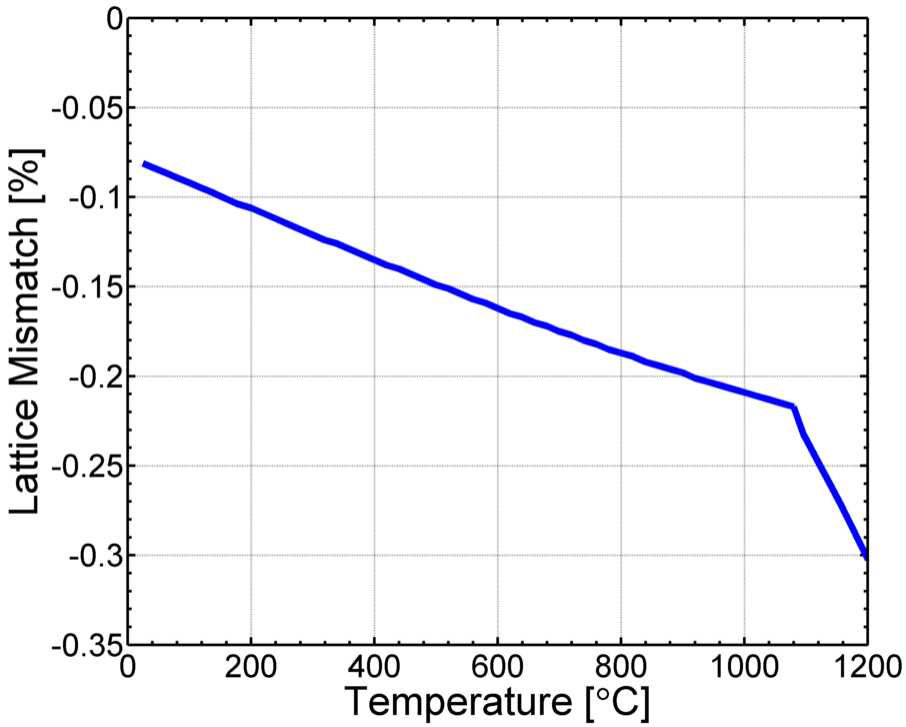

Figure 4.3: γ-γ' lattice misfit for CM247LC-DS in the as-heat-treated state calculated by JMatPro [99].

Within the interdendritic regions is found eutectic nodules of γ-γ' that can vary in size from about 20 μm up to 180 μm (Figure 4.4), as well as various carbide types intermixed with the eutectic nodules or along the grain boundaries (Figure 4.5). The presence of the eutectic γ' in the heat-treated structure indicates that the interdendritic γ' did not fully enter into solution during the solution treatment phase of the heat-treatment [15]. This can be attributed to the compositional differences that exists between the dendritic core and the interdendritic regions [14, 15, 21].

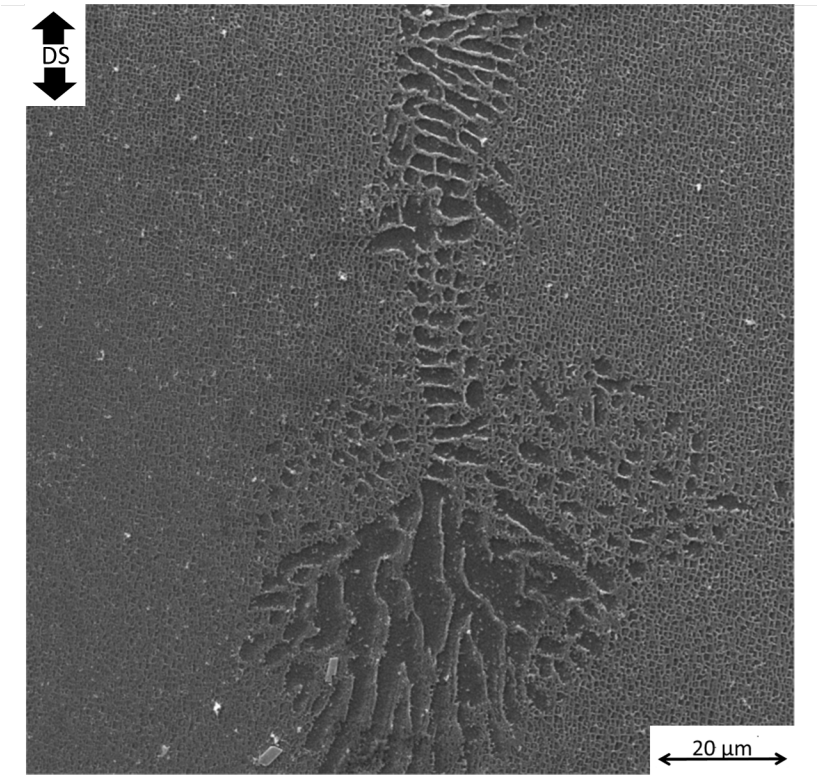

Figure 4.4: Eutectic nodule between dendrite arms within the as-heat-treated microstructure.

The carbides observed in the interdendritic regions and along the grain boundaries range in type and size with MC and $M_{23}C_6$ being the most abundant carbides. The MC-type have an irregular block-like or script morphology (Figure 4.5a) and appear along the grain boundaries. While the $M_{23}C_6$ carbides appear as small cubes measuring a few microns up through elongated plates of over 100 μm as shown in Figure 4.5b. The $M_{23}C_6$ type carbides can be identified through the γ' islands surrounding them. This is a result of the dissociation/precipitation reaction that occurs to generate the $M_{23}C_6$ carbides [15, 27]. Further, surrounding the MC carbides within the grain boundaries are regions denuded of γ'.

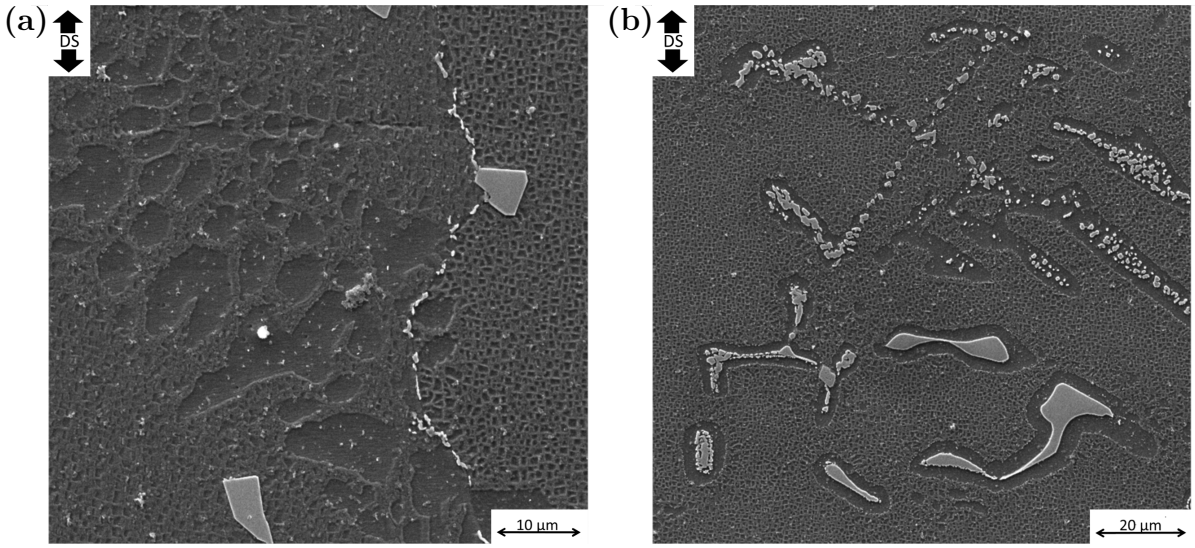

Figure 4.5: Examples of (a) MC grain boundary carbide (b) $M_{23}C_6$ eutectic carbides in the as-heat-treated microstructure.

4.2 Service Component Microstructure

Microstructural analysis was conducted on a airfoil removed from the second stage of a Siemens Energy SGT500 IGT (Figure 4.6) after 32,000 hours (3.5 years) of operation and experiencing 350 engine start/shutdown cycles. To make the airfoil manageable for metallographic analysis, the airfoil was cut into eight 25 mm thick horizontal slices via wire-EDM starting from the blade cap, subsequently each horizontal piece was sliced into four pieces. Rather than providing an exhaustive presentation of the microstructures within the airfoil, a summary of the collective observations from the airfoil microstructural analysis is presented.

Figure 4.6: Second stage airfoil from a Siemens Energy SGT500 IGT removed from service after 32,000 hrs.

For this study, a sample from an airfoil in the as-heat-treated conditions was unavailable. Therefore, the initial microstructure of the airfoil is assumed to be identical to that observed in the fatigue specimens in the as-heat-treated state for the purposes of comparison. At all locations investigated within the root and platform of the airfoil, no microstructure states directly correlating to the as-heat-treated microstructure were observed. Further, microstructures that could be classified strictly as directionally-coarsened or isotropically-coarsened were not observed. Rather, the micorstructures were observed to be in the late stages γ' coalescence. In spatial relation to the blade, the isotropically coarsened and N-raft like microstructures were observed to be in regions near cooling passages on the internal walls, while P-raft like

microstructures were found throughout the blade platform and the material near the surface of the blade root. This is depicted in the blade cut-away shown in Figure 4.7. Commonly reported in the analysis of failed aero turbine blades is the presence of TCP phases as a result of excess thermal exposure [100]; in the case of the IGT airfoil investigated none were observed. This can be attributed to the fact that IGTE components are designed such that the maximum material temperature does not exceed 1000°C [101].

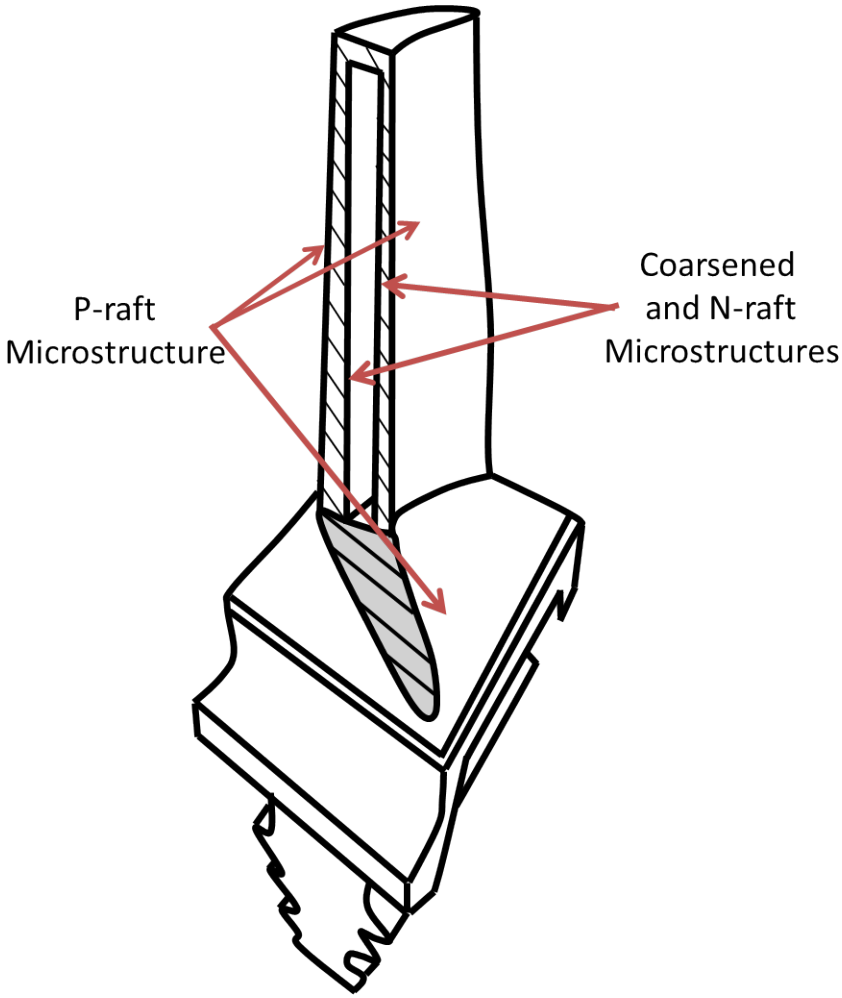

Figure 4.7: Airfoil cut-away indicating the locations where the specific aged microstructures were found upon metallographic analysis.

Within the material surrounding the cooling passages, the distinguishment between a isotropically coarsened like state and a N-raft like state were made based on

the aspect ratio of the γ' precipitates. Examples of the microstructures are shown in Figures 4.8 and 4.9. In both cases, the microstructures are in the late stages of coarsening, with the average γ' width being $1.8\mu m$ or four times the as-heat-treated γ' size. Further, in these microstructures is observed tertiary γ' have precipitated as a result of thermal exposure, solute homogenization conditions, or through the break-down of morphologically unstable primary γ' due to the loss of coherency [14, 102]. In the case of the tertiary γ', the average cube length was measured to be 0.2 μm. This is roughly half of the width of the primary γ' in the as-heat-treated state.

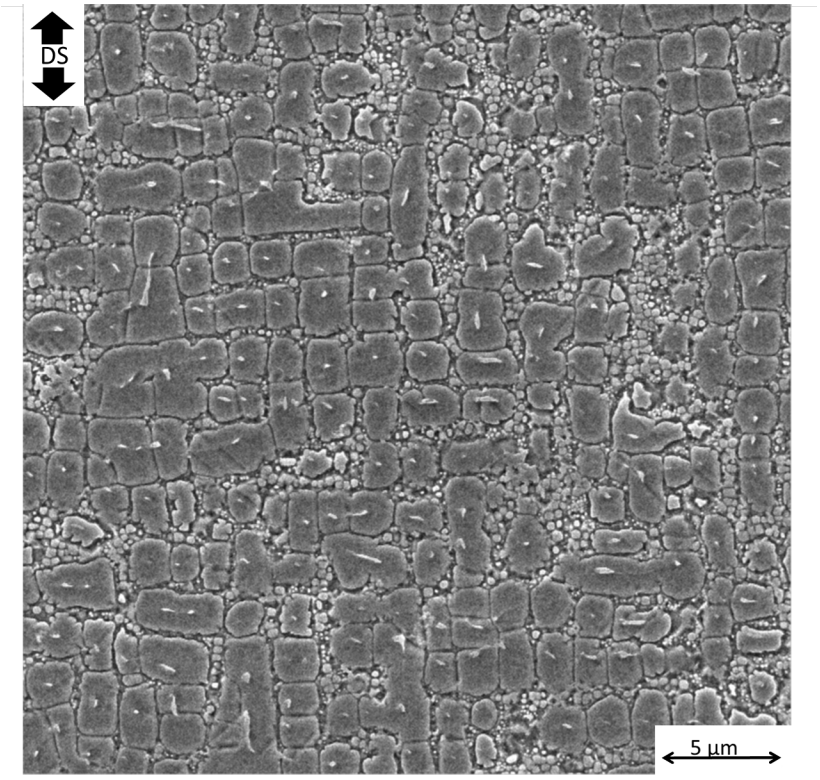

Figure 4.8: Isotropically coarsened microstructure state within the service component.

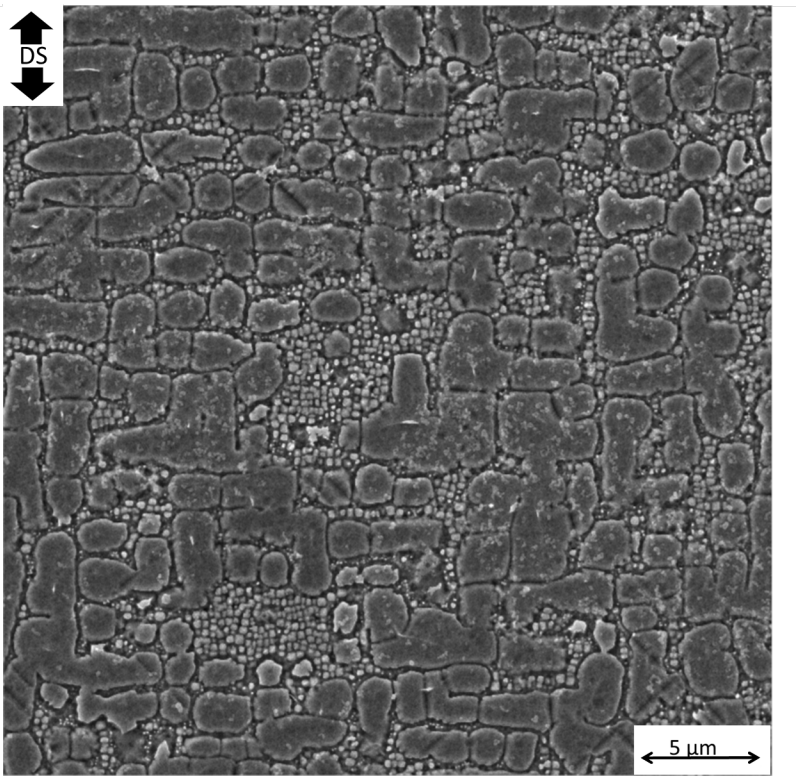

Figure 4.9: N-raft like microstructure state within the service component. The distinguishing feature from stress-free coarsened being the γ' aspect ratio.

In all cases, the observed P-raft microstructures were also found to be in a late state of coarsening as shown in Figure 4.10. The average P-raft width was determined to be $2\mu m$ while the length ranged from 3-8μm. Through a lateral translation of ≈250 μm from the location in Figure 4.10 towards the exterior surface of the blade a γ' depletion zone just below the thermal barrier coating was observed as shown in Figure 4.11.

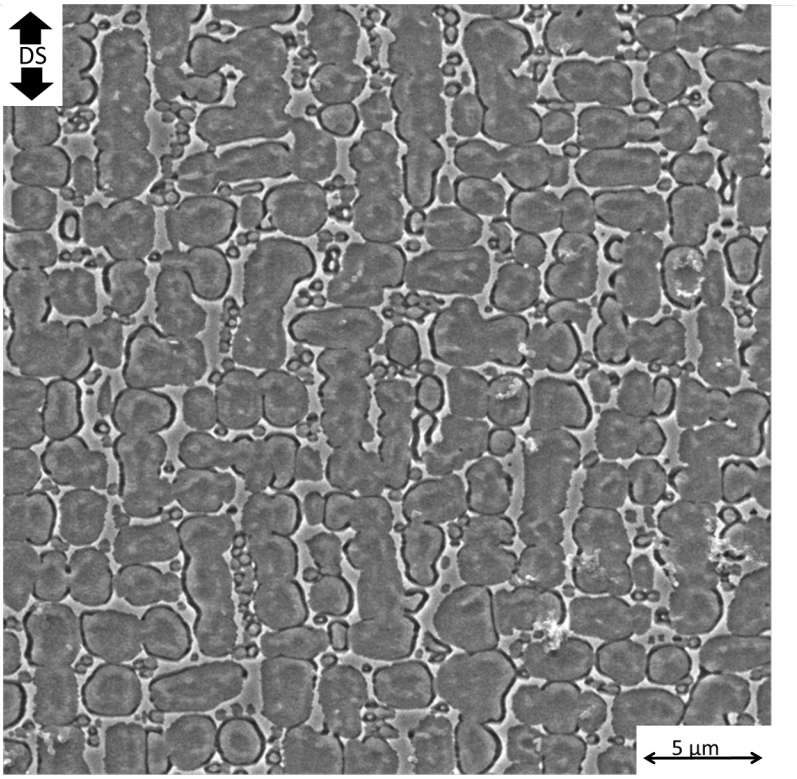

Figure 4.10: P-raft like microstructure state within the service component. The lighter color is the γ matrix.

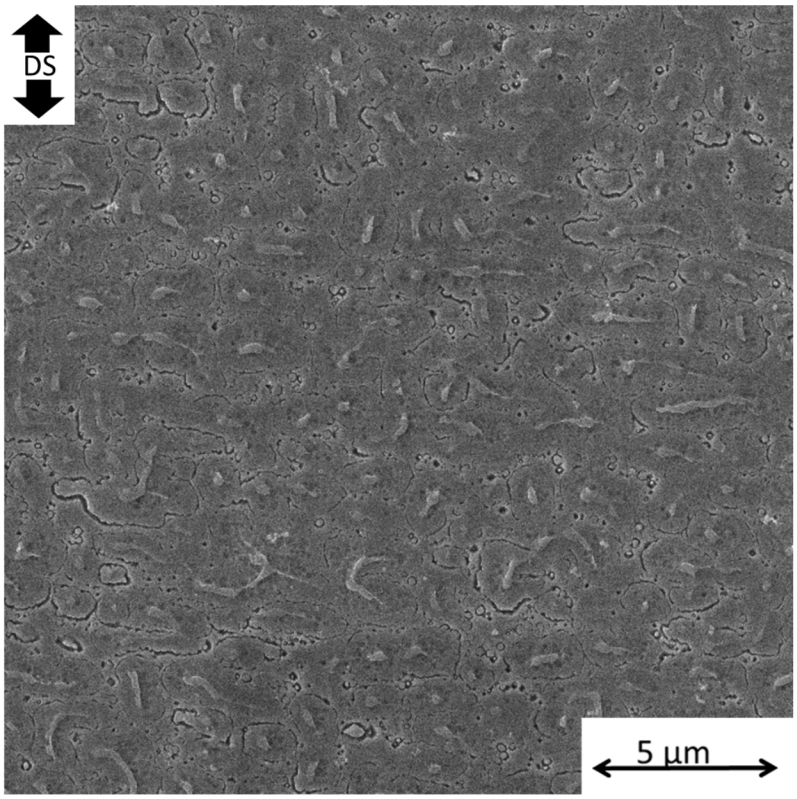

Figure 4.11: γ' depletion zone occurring just below the interface of the Ni-base superalloy with the thermal barrier coating.

4.3 Statistical Representation of Microstructure

Traditional methods for determining the microstructural attributes such as the linear intercept method for grain size provide only a magnitude measure of the microstructure [103, 104]. Advanced methods such as two-point correlation statistics have the ability to provide a magnitude measure in addition to the associated spatial correlation [104]. Physically, two-point correlation functions arise form the integration of a microstructure function $m(\mathbf{x}, h)$ at a point defined by $\boldsymbol{x}$. Specifically, $m(\mathbf{x}, h)$ defines the volume density of the local state h located at $\boldsymbol{x}$. Mathematically, the correlation functions are represented by [104],

$$f_2\left(h, h'|\mathbf{r}\right) = \frac{1}{Vol\left(\Omega|\mathbf{r}\right)} \iiint M\left(x, h\right) M\left(x + \mathbf{r}, h' dx\right) dx \tag{4.1}$$

where Ω is the microstructural volume of interest, $\boldsymbol{r}$ is a vector in the neighborhood of x, and h' is a local microstructure state neighboring h.

To apply the theory of two-point correlation functions in a computational framework, Equation 4.1 is discretized and transformed into the Fourier domain to separate the frequency of the microstructure phases resulting in [105],

$$ {}^{np}F_k = \mathscr{F}({}^{np}f_t) = \frac{1}{S}{}^{n}M_k^{*p}M_k = \frac{1}{S}\left|{}^{n}M_k\right|\left|{}^{p}M_k\right| e^{-i^{n}\Theta_k}e^{i^{p}\Theta_k} \tag{4.2} $$

where $|{}^{n}M_k|$ and ${}^{n}\Theta_k$ are the amplitude and phase of the Fourier transform, and S is the area of the microstructure grid. From Equation 4.2, two relations can be defined, the cross-correlation function and the auto-correlation function, where the autocorrelation function is defined by $f(h, h|\boldsymbol{r})$ and the cross-correlation by $f(h, h' \neq h|\boldsymbol{r})$ [104]. The cross-correlation function gives the probability that a random vector of length x can be found to start and end within the same phase. While the auto-correlation function provide the probability that a vector of length x will start in one phase and end in the other. In the case of a two-phase microstructure, the cross-correlation function and auto-correlation function are direct inverses of one another [106].

The key microstructure attributes observed within the $\gamma - \gamma'$ microstructure can be represented by an ideal unit cell as shown in Figure 4.12, where w_i is the width of the γ' precipitate, h_i the width of the γ channel, and i represents one of the three primary crystallographic directions, [001], [010], or [100].

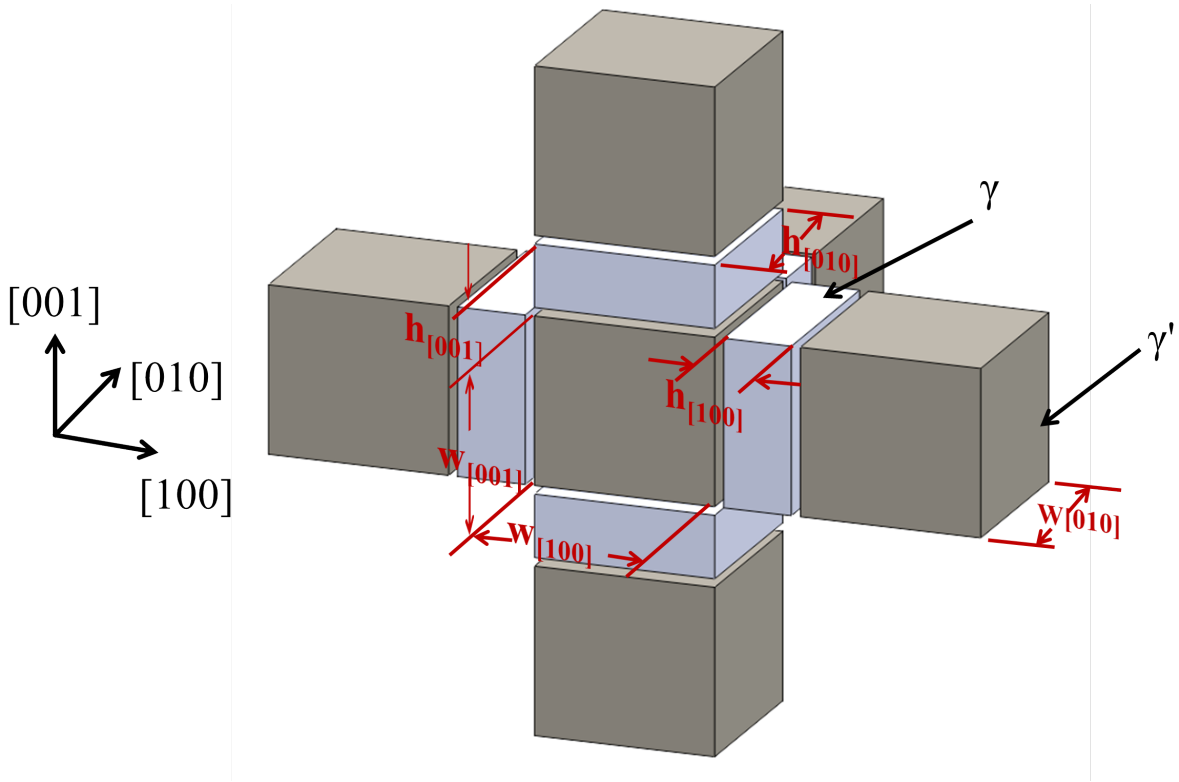

Figure 4.12: Representative $\gamma - \gamma'$ unit cell depicting the initial configuration with the neighboring γ' cubes.

Applying two-point correlation statistics to microstructure states within the dendritic regions of an Ni-base superalloy, the γ channel width and $\gamma - \gamma'$ periodicity can be determined. While, two-point correlation statistics can also be applied to the interdendritic regions of the microstructure, the pure randomness of the interdendritic regions does not provide any meaningful measure through which microstructure evolution can be measured. Specifically, the probabilistic distribution obtained from the cross-correlation function (Figure 4.13a) along the primary crystallographic orientations, e.g. [001] results in a decaying sinusoidal curve similar to that shown in Figure 4.13b for the as-heat-treated microstructure. Because of the cuboidal symmetry in the as-heat-treated state, the probabilistic distribution in the [100] crystallographic direction exhibits a similar decaying sinusoidal wave. The first maxima of the probabilistic curve corresponds to half of the width of a γ' precipitate, $\frac{1}{2}w_i$ in the noted

crystallographic direction, while the first minima is the sum of half of a γ' width and a the width of the γ channel, or $\frac{1}{2}w_i + h_i$. The secondary and tertiary maxima and minima (if they exist) provide the next highest frequency in integer multiples of $\frac{1}{2}w_i$ and h_i.

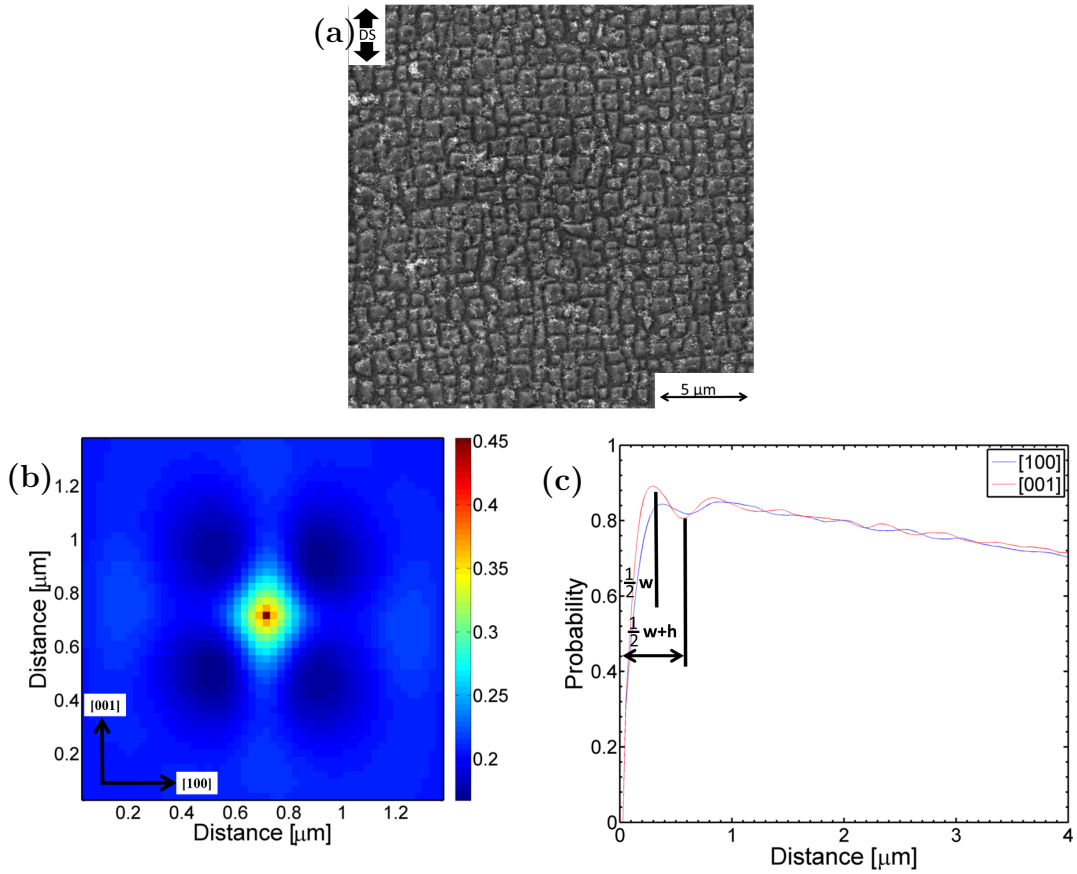

Figure 4.13: Cross-correlation for the γ' phase in the as-heat-treated microstructure given in (a) and (c) along the [001] and [100] crystallographic directions.

In the case of directionally-coarsened microstructures, the probabilistic distribution curves in the crystallographic direction in which the γ' precipitates elongate exhibits a heavily dampened response which typically results in a single maxima for that crystallographic direction. This is shown in Figures 4.14 and 4.15 for the N-raft and P-raft cases.

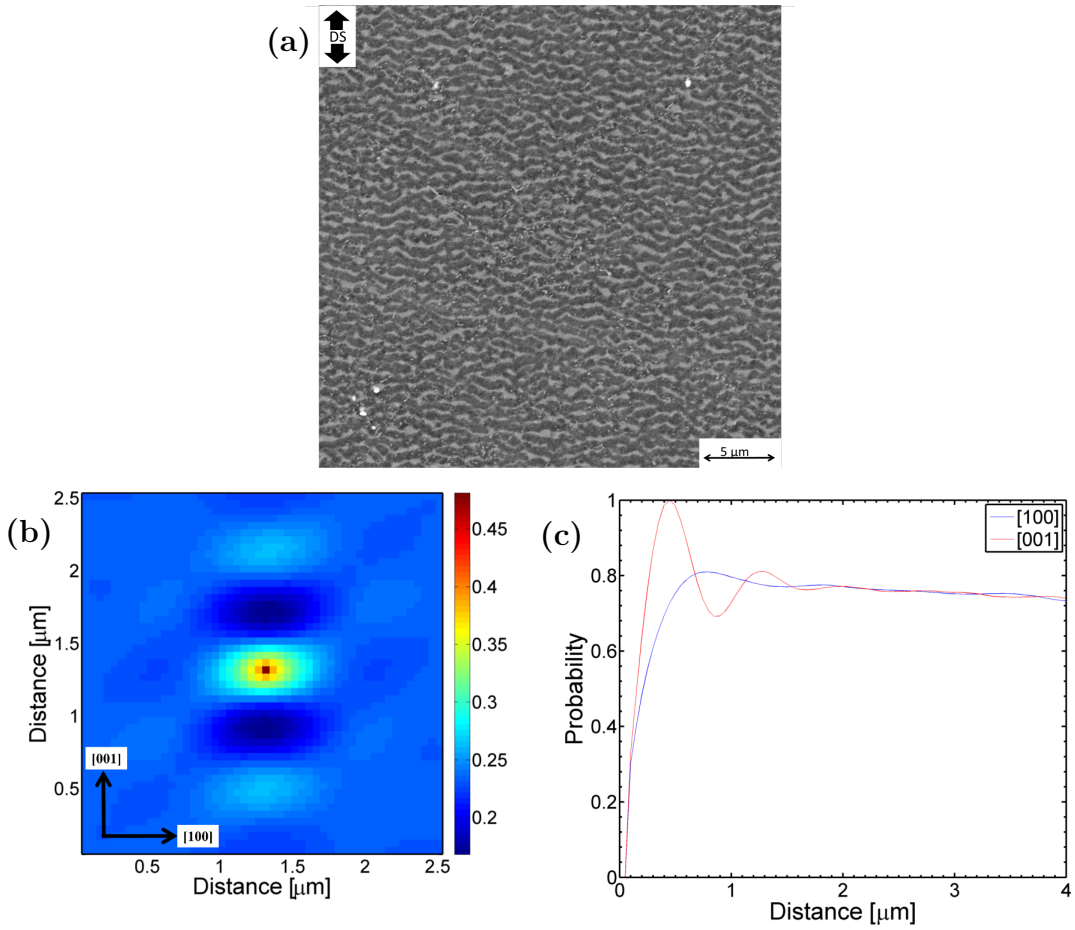

Figure 4.14: Cross-correlation for the γ' phase with an N-raft precipitate morphology as given in (a) and (c) along the [001] and [100] crystallographic directions.

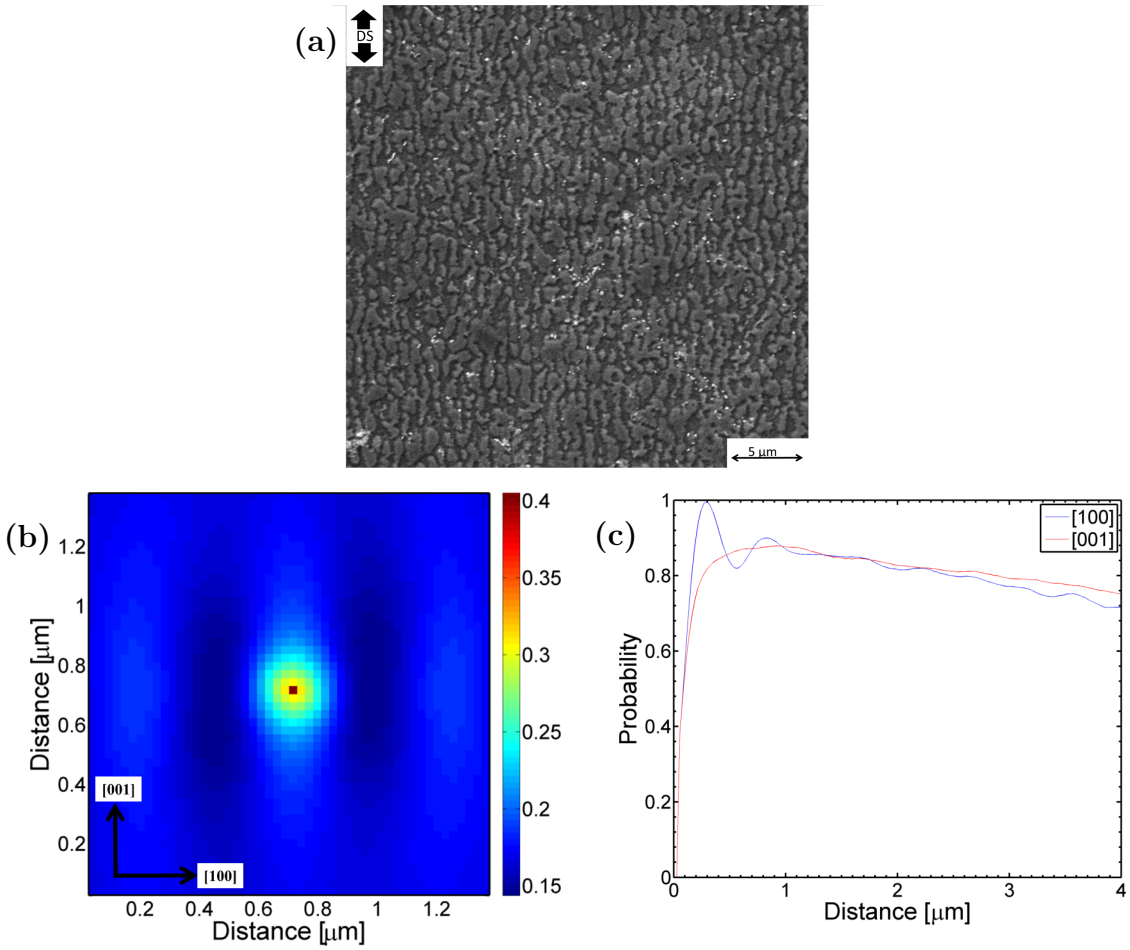

Figure 4.15: Cross-correlation for the γ' phase with an P-raft precipitate morphology as given in (a) and (c) along the [001] and [100] crystallographic directions.

4.4 Microstructure Evolution Analysis

To understand the effect of thermomechanical exposure on the as-heat-treated microstructure evolution, aging experiments were conducted utilizing specimen geometries and methods as discussed previously in Chapter 3. Presented first will be an analytical model that captures the combined effects of rafting and coarsening on the aging kinetics. Later this model will be placed within the CVP model framework. Following, the observations and quantifiable attributes of the aged microstructures and the subsequent parameters for the microstructure-aging model will be provided.

To model the kinetics of aging in a $\gamma - \gamma'$ microstructure, both isotropic coarsening and directional coarsening are assumed to occur simultaneously. Capturing both isotropic coarsening and rafting is important, since experimental results indicate that isotropic coarsening can account for up to 20% of the coarsening rate [107]. Under isotropic coarsening conditions, experimental studies have shown the γ' precipitates coarsen according to Ostwald ripening [32, 36, 49]. While few long term experimental studies on coarsening in Ni-base superalloys exist, those that have been conducted report that cubic rate laws better match the experimental results for isotropic coarsening of cuboidal γ' [32,36]. For a cubic γ' precipitate, the cubic rate law for isotropic coarsening can be formulated as [32],

$$\left(\frac{w_i}{2}\right)^3 - \left(\frac{w_o}{2}\right)^3 = Kt \tag{4.3}$$

or in rate form [49],

$$\dot{w}_i^{coar} = \frac{8K}{3}\left(w_o^3 + 8Kt\right)^{-\frac{2}{3}} \tag{4.4}$$

where $\dot{w}_i^{coar}$ is the isotropic rate of coarsening, w_o is the initial length of the γ' cube, t is time, and K is the rate constant for coarsening,

$$K = K_o exp\left(-\frac{Q_{coar}}{RT}\right) \tag{4.5}$$

where K_o is the coarsening constant, Q_{coar} the activation energy for coarsening, R the ideal gas constant, and T the temperature. Further, during isotropic coarsening a proportional growth relationship within the unit cell can be assumed maintained [107],

$$\frac{\dot{w}_i}{\dot{\lambda}_i} = \frac{w_o}{\lambda_o} \tag{4.6}$$

where λ is the periodicity of the $\gamma - \gamma'$ microstructure defined as $\lambda_i = w_i + h_i$.

To capture the kinetics of directional coarsening, an Arrhenius type relation, where the rate of rafting of the γ' precipitates under a multiaxial load is given by [48, 49],

$$\dot{w}_i^{raft}(T, \boldsymbol{\sigma}) = -\left(\frac{3Aw_i}{2w_o}\right)\left(\frac{\sigma_i^{dev}}{\sigma_{VM} + \delta}\right) exp\left(-\frac{Q_{raft} - \sigma_{VM}U(T)}{RT}\right) \tag{4.7}$$

where σ_{VM} is the von Mises stress, σ_i^{dev} the diagonal components of the deviatoric stress tensor, Q_{raft} the activation energy required for rafting, and U(T) the activation volume at a temperature T is used. The activation volume is given by,

$$U(T) = U_T\,(T - T_o)^n \tag{4.8}$$

where, T_o is the cutoff temperature below which rafting does not occur, and n and U_T are model parameters. Overall the rate of aging is given by the sum of the individual kinetics,

$$\dot{w}_i = \dot{w}_i^{coar} + \dot{w}_i^{raft} \tag{4.9}$$

A ramification of this simple model is that the length of the γ' in the direction of coalescence is not accurately accounted for due to that the model does not consider interactions amongst neighboring unit cell. However, the reduction in the width of the γ channel is captured through the model.

To provide the necessary information for determining the material parameters in Equations 4.3-4.5, isotropic coarsening was conducted at 850, 900, 950, and 100°C with exposure times ranging between 96 and 672 hrs. The resultant isotropically coarsened microstructure states for the shortest and longest exposure times for each exposure temperatures are shown in Figures 4.16. Isothermal exposure at 900-1000°C resulted in measurable microstructural changes, while the γ' were unchanged after 670 hrs of exposure at 850°C. If significantly longer exposure times ($\approx$ 30,000 hrs) were used, the expectation is that measurable isotropic coarsening would have been

observed as in long term coarsening studies at 850°C [32,36]. For the shortest exposure time at 1000°C, a 13% increase in the size of the γ' cubes was measured. And the longest exposure time at 1000°C yielded a 25% increase.

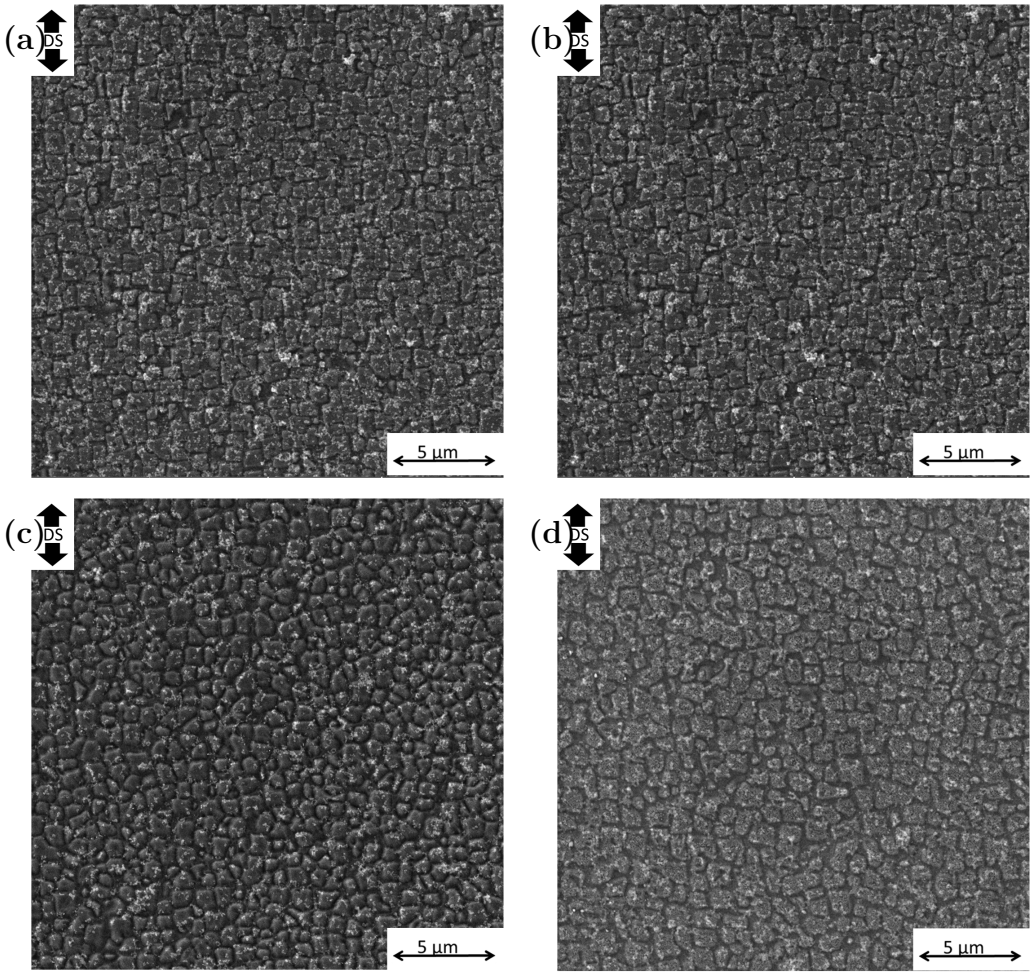

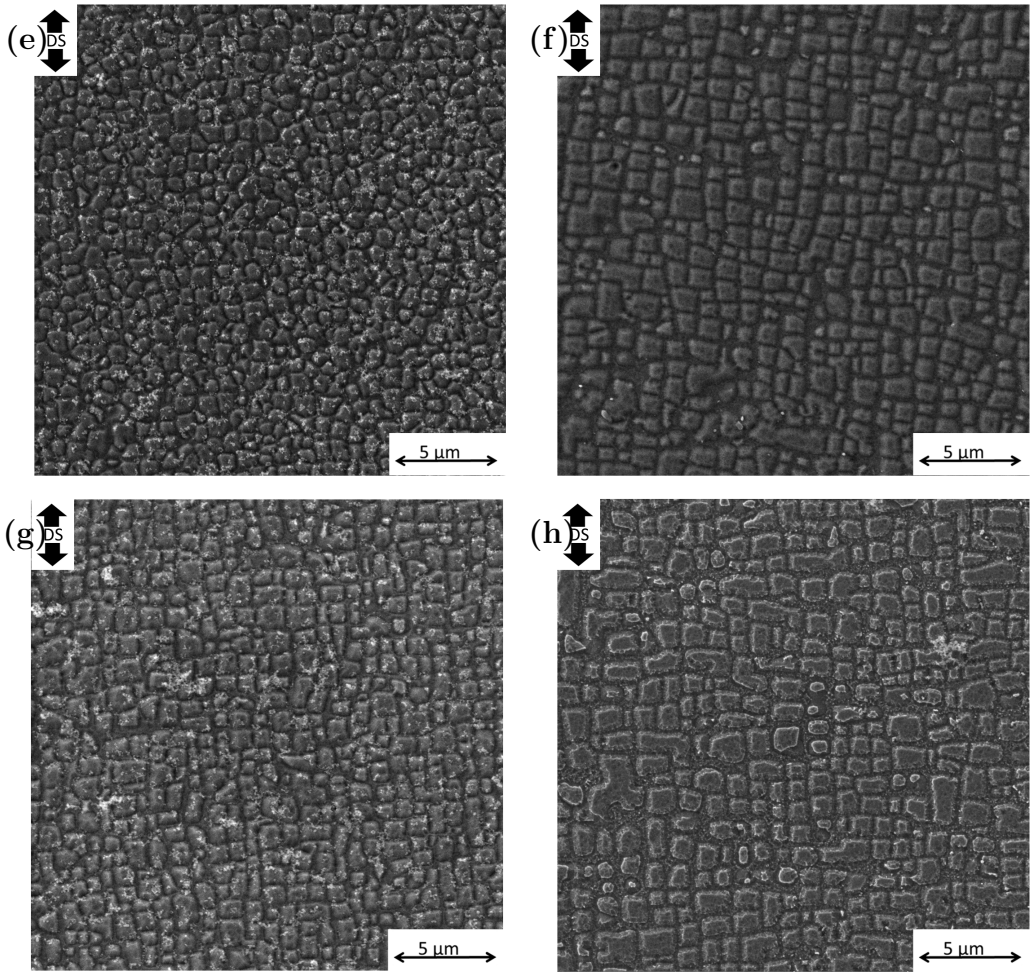

Figure 4.16: Resultant microstructures after isothermal exposure at (a) 850°C for 96hrs (b) 850°C for 672hrs (c) 900°C for 96hrs (d) 900°C for 672hrs (e) 950°C 96hrs (f) 950°C for 672 hrs (g) 1000°C for 96hrs and (h) 1000°C for 672hrs.

Shown in Figure 4.17 is the growth of the γ' for isothermal exposure times used in this study. The activation energy, Q_{coar}, for isotropic coarsening was calculated to be 105 $\frac{kJ}{kmol}$. This value being in-line with long-term coarsening of Rene 80, but 2x less than that determined for CMSX-4 for short term coarsening (<250 hrs) [36,108]. Also, this value is close to that for the activation energy for the self diffusion of aluminum in nickel [16]. In general, large variations in the activation energy for isotropic coarsening have been reported in the literature even when the studies consider the same alloy in the same heat-treated state [36]. Additionally, the coarsening constant, K_o, was

determined to be $1.1x10^{-3}\frac{\mu m^3}{hr}$ through a linear regression analysis. Summarized in Table 4.1 are the constants for predicting isotropic coarsening using Equations 4.3-4.6.

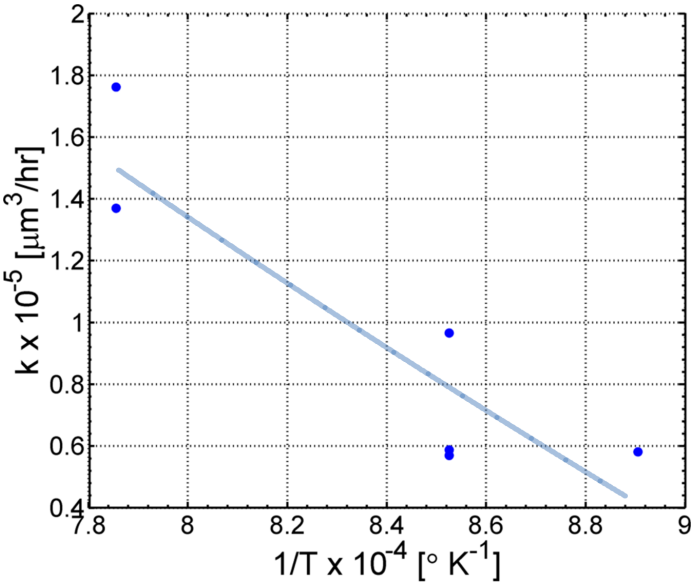

Figure 4.17: Temperature dependence of the coarsening rate k.

Table 4.1: Material constants for analytical isotropic coarsening model.

Parameter	CM247LC-DS	Units
$Q_{coarsen}$	110	$\frac{kJ}{K}$
L_o	0.75	μm
K_o	$1.1x10^{-3}$	$\frac{\mu m^3}{hr}$

In determining the size of the γ', the potential for error in the measurements can be great, this being attributable to the fact that the γ' precipitates can coalesce during isotropic coarsening to form L- and U-shaped particles. As a result when examining a 2D surface a single precipitate can appear as one large irregularly shaped precipitate or as multiple particles [36]. In addition, there is also an uncertainty if a micrograph is truly within the desired crystallographic plane.

Directional coarsening experiments were conducted under tensile creep conditions at temperatures of 850°C, 900°C, and 950°C and compressive creep at 900°C and 950°C. The specific loadings conditions are listed in Table 4.2 and representative aged

microstructures at each temperature are shown in Figures 4.18 and 4.19. Multiple exposure times and loads were used to better capture the rafting kinetics of the microstructure at different points in time under identical stresses.

At 850°C and exposure to a 360 MPa tensile stress for 250 hours the extreme early stages of rafting were observed in the form of a small number of γ' coalescing and a 10% increase in the γ channel. However, at 240 MPa no measurable changes in the width of the γ channel could be made. At 900°C low tensile stresses resulted in a partially rafted state, while fully rafted structures were obtained at the peak stresses within the specimens. At 950°C, all applied tensile loads were found to result in a N-raft structures. With the application of compressive creep stresses, the rate at which the rate of γ channel widening is found to be reduced in comparison to those formed under tensile creep conditions for the same stress as shown in Figure 4.20. This reduction can be attributed to the fact that movement of dislocations through the vertical γ channels occurs at a reduced rate compared to the horizontal γ channels [109, 110]. Through fitting the data to Equations 4.7-4.8, the activation energy necessary for rafting, Q_{raft}, was determined to be 225 $\frac{kJ}{molK}$ through linear regression analysis. In Table 4.3 are provided the material parameters for Equations 4.7-4.8.

Table 4.2: Tensile and compressive creep exposure conditions.

Temperature [°C]	Exposure Conditions
850	170 hours at 11 kN
	250 hours at 11.6 kN*
900	300 hours at 8 kN
	350 hours at 9.78 kN*
	630 hours at -9.78 kN
950	300 hours at 4.71 kN
	504 hours at 5.6 kN*
	410 hours at -5.6 kN
	630 hours at -5.6 kN

*Rupture

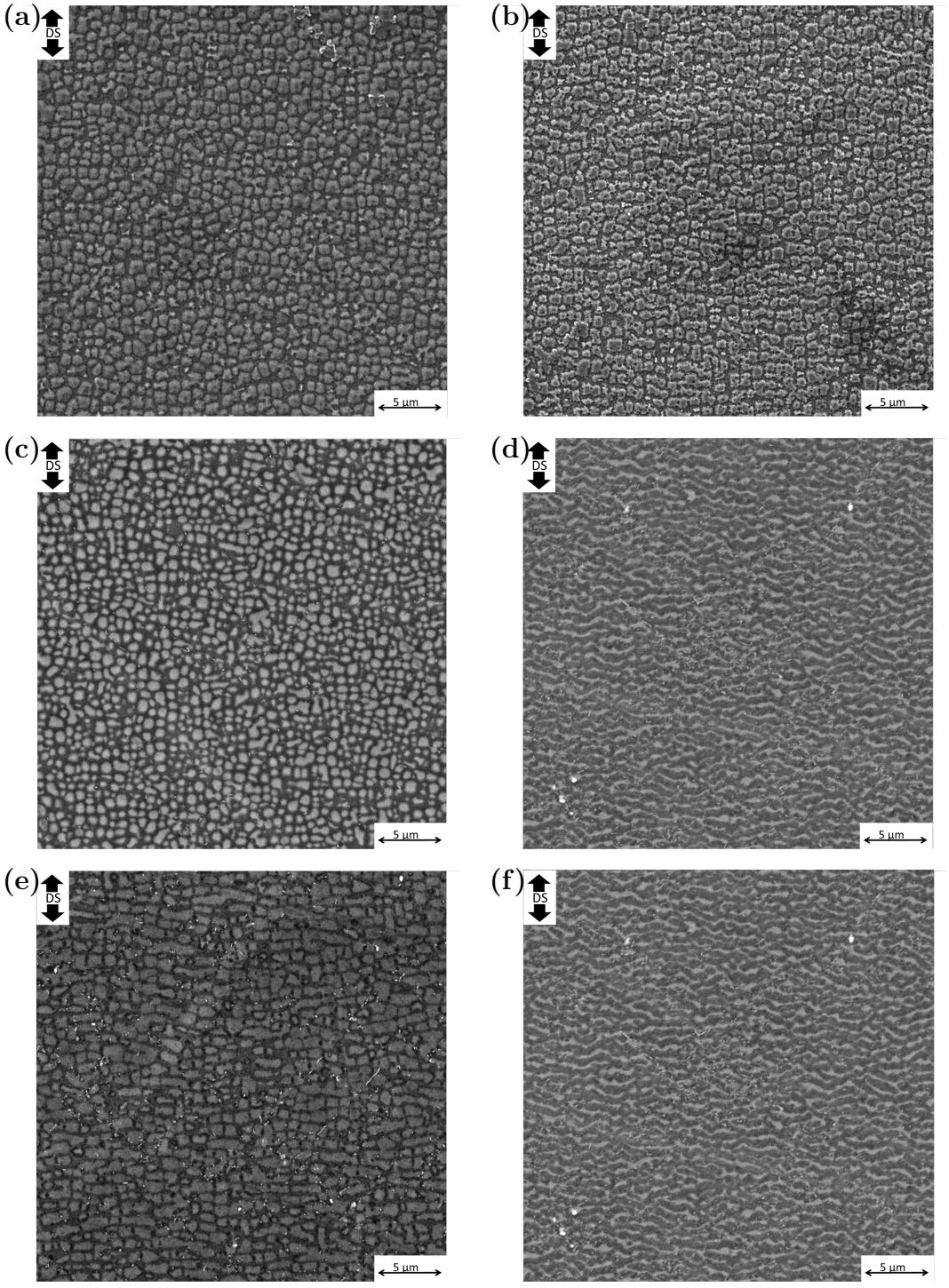

Figure 4.18: Resultant N-raft microstructure from exposure to (a) 850°C and 240 MPa for 250 hrs (b) 850°C and 258 MPa for 250 hrs (c) 900°C and 504 MPa for 300 hrs (d) 900°C and 250 MPa for 300 hrs (e) 950°C and 96 MPa for 504 hrs (f) 950°C 176 MPa for 504 hrs.

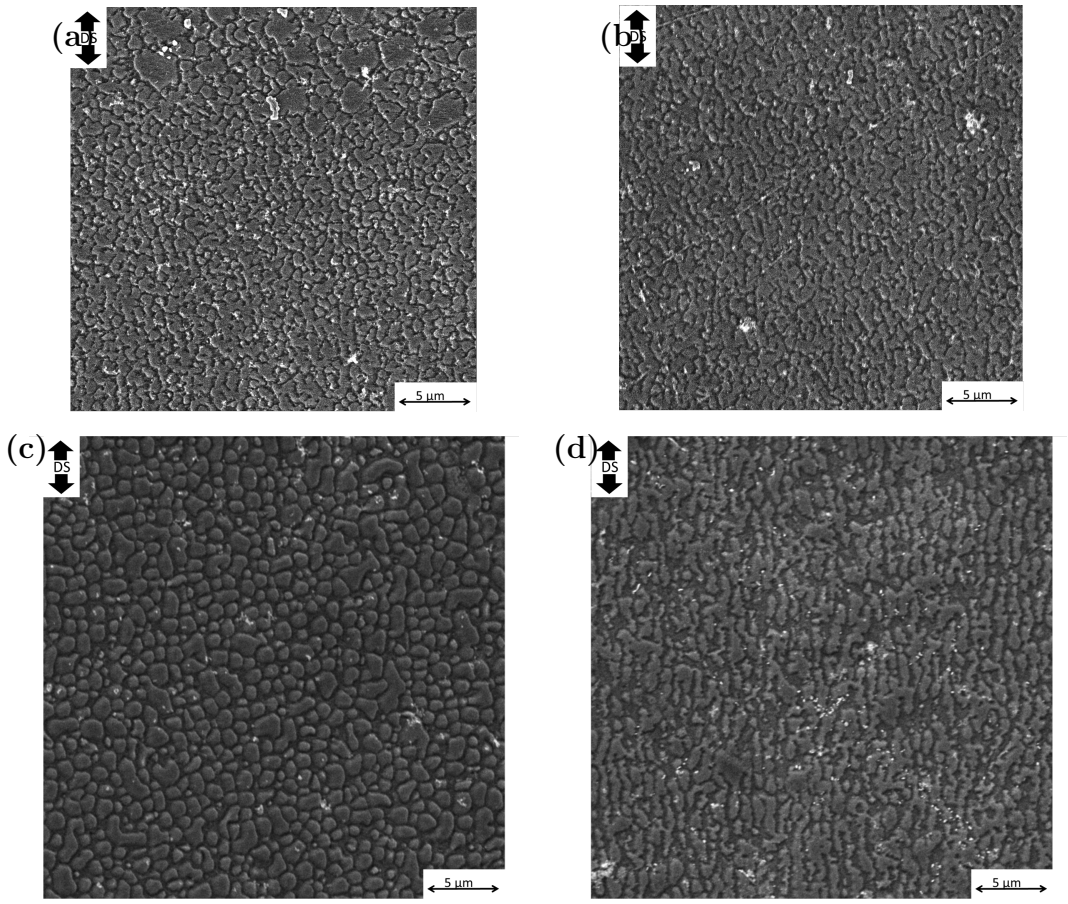

Figure 4.19: Resultant P-raft microstructure from exposure to (a) 900°C and -120 MPa for 630 hrs (b) 900°C and -240 MPa for 630 hrs (c) 950°C and -117 MPa for 410 hrs (d) 950°C -176 MPa for 410 hrs.

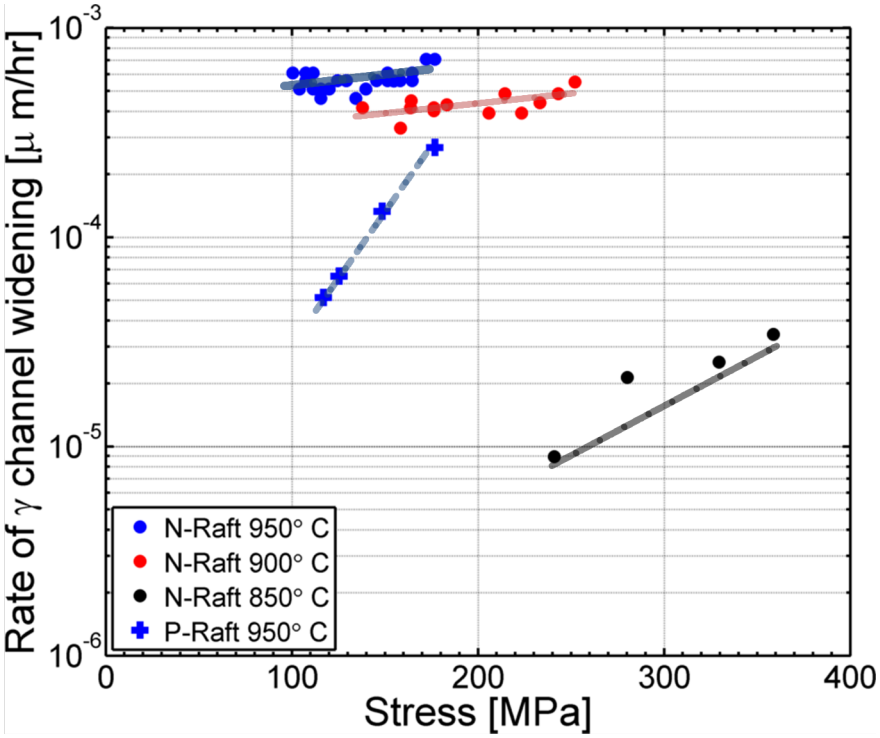

Figure 4.20: Rate of γ channel widening under uniaxial conditions as a function of stress and temperature.

Table 4.3: Material constants for rafting model.

Parameter	CM247LC-DS	Units
A	1.2x10^{-5}	$\frac{m}{s}$
Q_{raft}	290	$\frac{kJ}{K}$
h_o	0.18	μm
L_o	0.75	μm
U_T	0.14	$\frac{J}{molMPaK^n}$
T_o	1023	$^\circ K$
n	1.24	-

In this implementation of the model, isotopic coarsening data was used in the specific determination of the isotopic coarsening material parameters whereas in previous works only directional coarsening data was used for the determination of both the isotropic coarsening parameters and the directional coarsening aging parameters.

4.5 Quantification of the Mechanical Properties of Aged Microstructure

For the purposes of mechanical testing, a single set of conditions for each of the three unique microstructures was chosen and are described within this section. To induce an over aged precipitate state, virgin material in the standard heat-treated state was exposed to 1000°C for 720 hours in a laboratory air environment as discussed in Section 3.2.1. Shown in Figure 4.21a is the resultant microstructure in comparison to the virgin state. As a result of the thermal exposure the γ' cubes increased in size to a cube length of 0.85 μm on average from the initial average cube length of 0.75 μm. Additionally, the γ channels were observed to be devoid of secondary γ'. This can be attributed to the Ostwald ripening process through which the larger precipitates coarsen at the expense of the smaller ones [15, 16].

For the tensile pre-creep treatment, a stress of 150 MPa was applied for a period of 300 hours at 950°C via tensile creep as described in Section 3.2.2. As a result of this tensile pre-creep exposure, the material realized an inelastic creep strain of $\epsilon_{Creep} = 0.37\%$ based on available creep data for the alloy [101]. Shown in Figure 4.21c is the N-rafted microstructure in comparison to the initial virgin state. The tensile pre-creep resulted in a fully N-rafted structure, where the average width of the γ channels perpendicular to the applied load was increased from 0.18 μm to 0.3μm.

Utilizing the in-house compression frame and protocols discussed in Section 3.2.3, was conducted the aging of the material under compressive pre-creep conditions. To produce the P-raft microstructure, a pre-creep treatment of -130 MPa at 950°C over the course of 300 hours was given. The different stress used from that of the tensile pre-creep treatment was to avoid inducing too great of creep damage into the microstructure. CM247LC-DS exhibits a tension/compression creep asymmetry. As a result of the pre-creep exposure, the γ channels parallel to the applied load increased

to a width of 0.25 μm as depicted in Figure 4.21d.

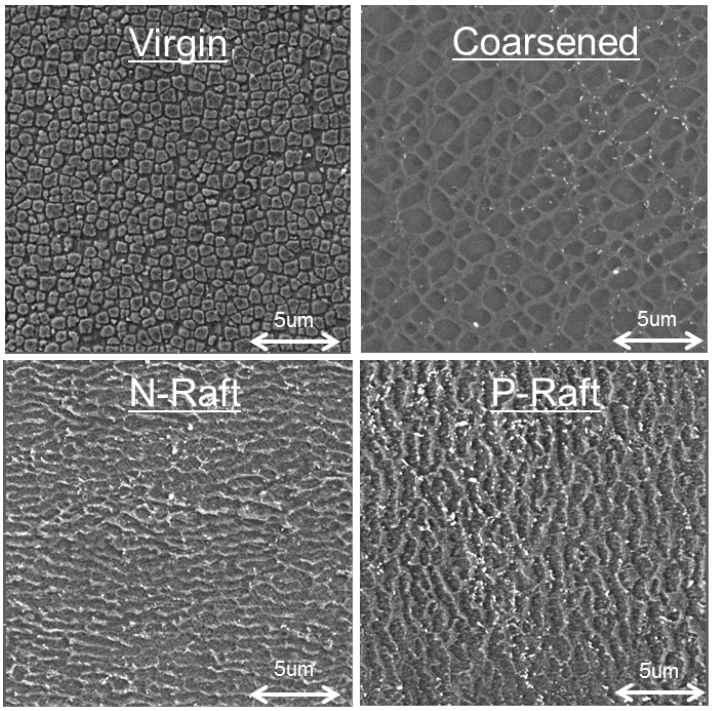

Figure 4.21: Comparison of the (a) Virgin microstructure to that of the resulting (b) Isotropically coarsened (c) N-raft and (d) P-raft microstructures.

In addition to coarsening and rafting, aging also alters the initial dislocation and internal stress state. In the virgin state, the matrix is nearly dislocation free, however large compressive stresses exist in the γ channels that are of the same magnitude of those applied in the course of creep or cyclic fatigue loadings as depicted in Figure 4.22a [50, 63, 92, 111, 112]. Through stress-free thermal exposure (annealing), the coherency stresses between the $\gamma - \gamma'$ relax in a near uniform manner through the generation of edge dislocations. These edge dislocations deposit themselves on all the $\gamma - \gamma'$ interfaces as shown in Figure 4.22b so as fully relieve the misfit stresses [32,92]. In contrast to the annealed case, the application of a tensile pre-creep generates preferential dislocation networks along the $\gamma - \gamma'$ interfaces perpendicular to the applied load, while leaving the vertical γ channels under a compressive coherency stress (Figure 4.22c); on the other hand compressive pre-creep causes stress relieving

dislocation networks to form along the cube faces parallel to the applied load as shown in Figure 4.22d [44, 51, 63, 111].

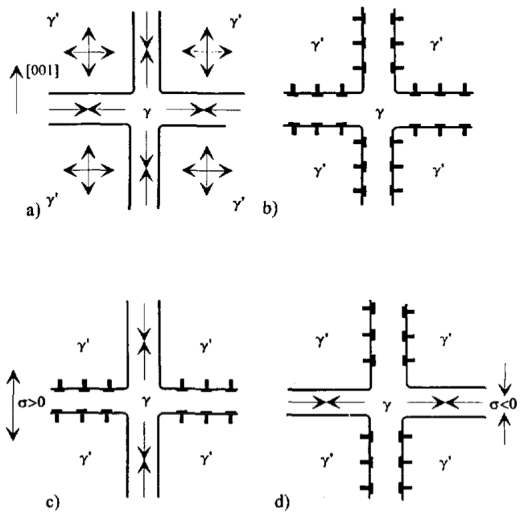

Figure 4.22: Dislocation state in a negative misfit alloy, the (a) Virgin state (b) Stress-free coarsened (c) Tensile pre-creep (d) Compressive pre-creep adapted from [111]

As a note, in selecting the aging parameters, the intent was not to provide a direct comparison between the aged microstructures, but rather a comparison back to the behavior of the virgin microstructure behavior under TMF conditions representative of those within a service component that would bring about the representative aged microstructure. As a result the aging parameters used were chosen to bring about the greatest possible degree of microstructural change that are similar to those found in a service component removed from service after 30,000 hrs without imparting to great of damage into the material that would otherwise skew the results.

4.5.1 Elastic and Yield Behavior in the Aged States

Aging of the γ' had a minimal effect on the temperature-dependent response of the elastic modulus in the longitudinal and transverse orientations as shown in Figure 4.23. The reported values represent the mean value, where a minimum of five data points were obtained at each temperature. In the longitudinal orientation all moduli

values at a given temperature were found to be within a 2-3% variation of the mean value. This can be considered reasonable given potential microstructural inhomogeneities occurring amongst the different cast slabs; specifically the allowed $+/-7.5°$ longitudinal grain misoreintation relative to the growth direction [16]. In the case of the transverse modulus, a variance of 10% was observed at a given temperature. The increased scatter over the longitudinal values can be attributed to the fact that a wholly random secondary grain orientation is present in the transverse specimens. Work on large grained polycrystalline alloys have shown that when randomness is introduced into the grain orientation, variations as high as $+/-50\%$ from the mean elastic moduli can occur [19].

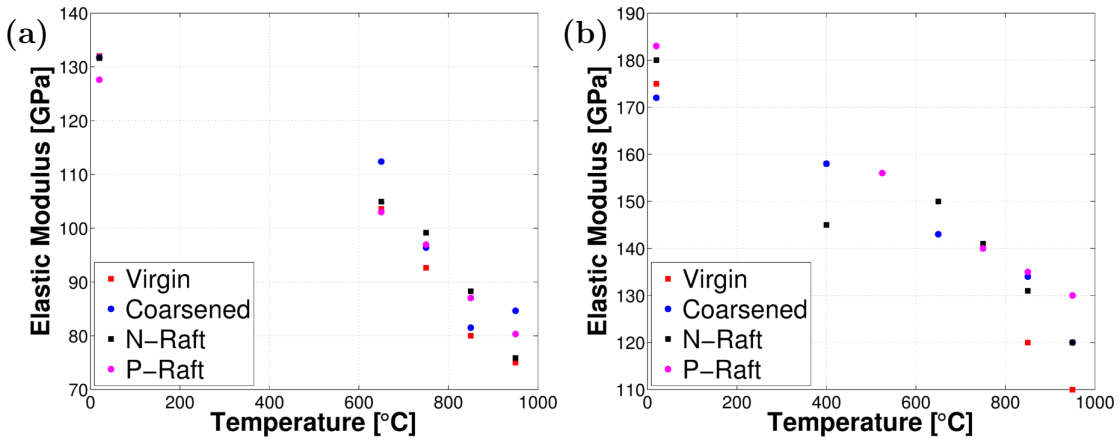

Figure 4.23: Elastic modulus comparison of CM247LC-DS in the Virgin, isotropically coarsened, N-raft and, P-raft states in the (a) longitudinal orientation (b) transverse orientation.

For both of the rafted structures, and isotropically coarsened, the yield strength curves behave similarly to the virgin material and exhibit nearly constant values between room temperature and 650°C as shown in Figure 4.24. Above 650°C, the drop-off in the yield strength of the aged microstructures is well pronounced in comparison to the virgin microstructure which peaks at 750°C. Bounding the measured yield strength is the virgin microstructure on the maximum and the virgin and the isotropically coarsened on the minimum. Generally, the aged microstructures exhibit

a 20% reduction in yield strength over that of the virgin microstructure. Though at 950°C and 1050°C all the microstructures exhibit similar yield strengths. This can be primarily attributed to the fact that above 950°C, the γ matrix is sustaining nearly all the inelastic deformation, as the passage of dislocations through the γ' precipitates becomes impossible [16]. Below 850°C aging of the γ' results in a lowering of the threshold stress required to shear the precipitates via dislocation pairs [68, 113–115]. These results are similar to those observed for IN-713LC and SX MC2 in coarsened states [116, 117].

In the as-heat-treated state little variation is typically observed between the 0.2% and 0.02% yield strengths of a Ni-base superalloy at temperatures below 750°C in the longitudinal orientation. While the aged microstructures indicate that some softening has occurred as a result of the aging processes, the 0.02% offset yield strength indicates that through aging, internal stresses within the alloy are greatly reduced. The implications of these results are such that thermomechanical loadings for which would be entirely elastic for the virgin material, result in plastic deformation in the aged microstructures.

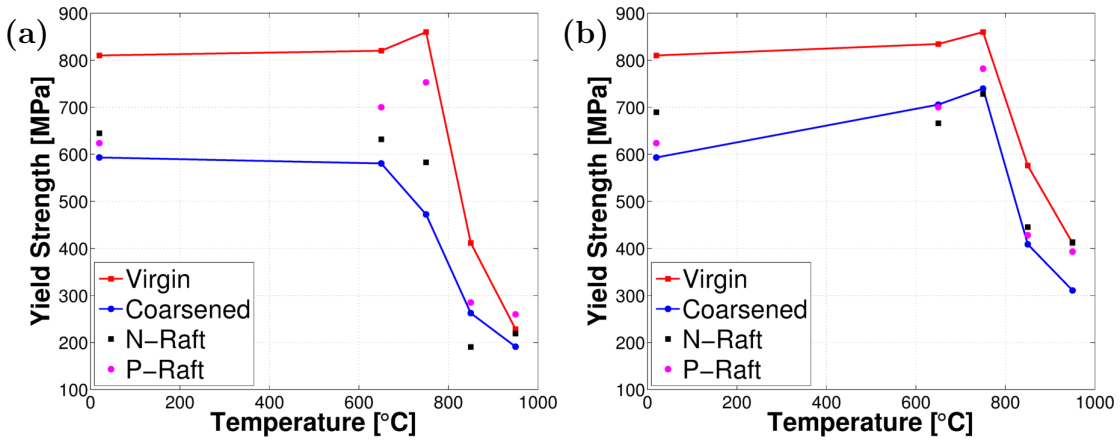

Figure 4.24: Tensile yield strength comparison in the L-orientation for the Virgin, isotropically coarsened, N-raft and, P-raft microstructures for $\dot{\epsilon} = 10^{-3}\frac{1}{s}$ (a) 0.02% yield strength (b) 0.2% yield strength.

In the case of the yield strength in the transverse orientation, an understanding

of the behavior is less clear as a result of the secondary orientations of the grains and definitive attribution can not be made based on the results as shown in Figure 4.25.

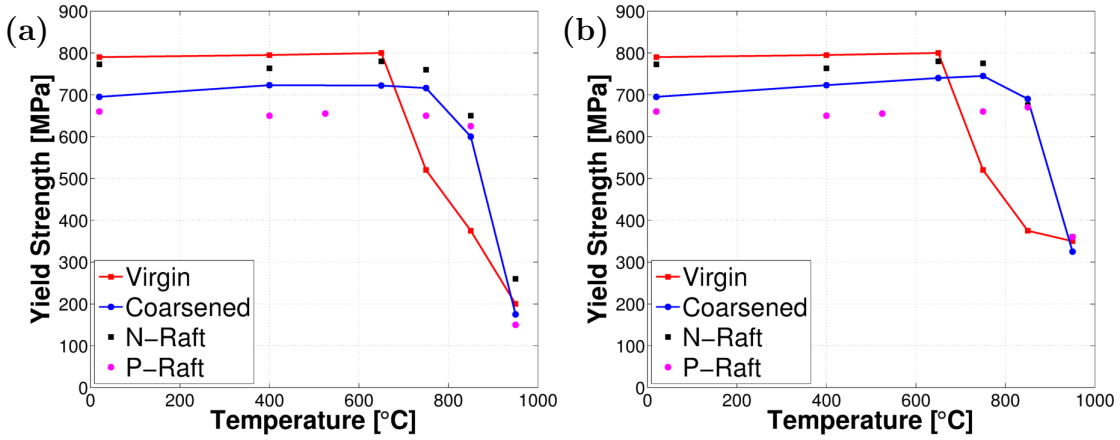

Figure 4.25: Tensile yield strength comparison in the T-orientation for the Virgin, isotropically coarsened, N-raft and, P-raft microstructures $\dot{\epsilon} = 10^{-3}\frac{1}{s}$ (a) 0.02% yield strength (b) 0.2% yield strength.

4.5.2 Room Temperature Cyclic Behavior

Under fully reversed room temperature (20°C) conditions, each of the microstructures was tested to examine their respective LCF resistance in the L-orientation. Shown in Figure 4.26 is the stress amplitude life curves for each of the microstructure responses. In the case of the virgin microstructure, the room temperature experiment was repeated two times to provide understanding of the potential scatter in the fatigue life distribution. Overall, the virgin microstructure exhibited a $+/-20\%$ variation from the mean life of 5250 cycles. In the case of the aged microstructures, only a single experiment was conducted for each. Overall the P-raft microstructure exhibited the greatest decline from the mean life of the virgin material with a 20% decline. While the N-Raft microstructure resulted in nearly identical life values as the virgin mean life and the stress-free coarsened microstructure a 25% increase in life over the virgin mean. However, these differences in the in the aged microstuctures can be considered to still fall within the experimental scatter of the virgin life, and as such the room temperature strain-life response can be considered to be microstructure independent.

Microstructural analysis further supported this as fatigue cracking was found to be associated with debonded carbides for each of the microstuctures.

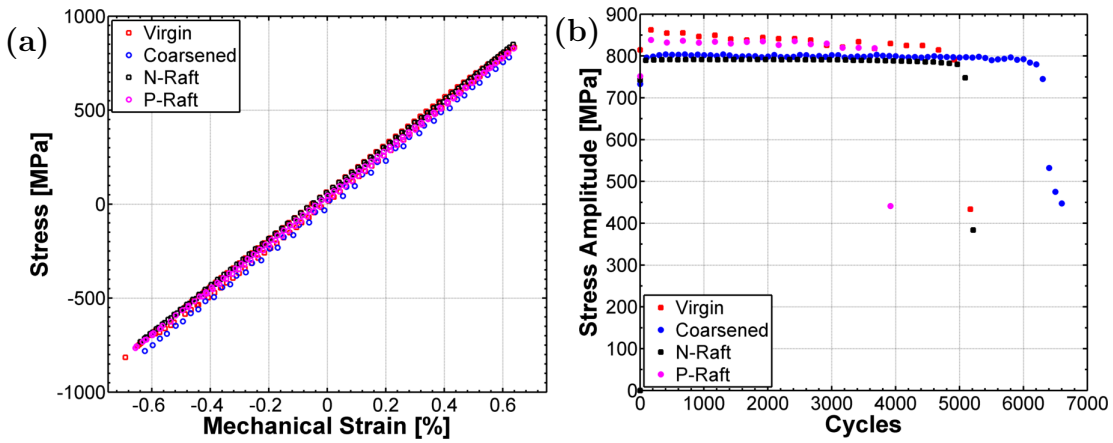

Figure 4.26: (a) Half-life (b) Stress amplitude curves for ambient fatigue tests with $\Delta\epsilon_{mech} = 1.3\%$ conducted on the virgin, isotropically coarsened, N-raft, and P-raft microstructures.

CHAPTER V

AS-HEAT TREATED TMF BEHAVIOR

No single set of TMF conditions can be considered truly representative of those in a IGTE. As a result, idealized TMF cycles are used; with the choice of the TMF conditions dependent on the information desired. To date there has yet to be presented a full consideration of the spectrum of TMF conditions and the corresponding effect on fatigue crack initiation in the low cycle regime on the as-heat treated microstructure. Considered in this work are the following TMF effects:

- Influence of temperature extremum on TMF life
- Effects of temperature-load phasing on TMF life
- Mean strain effects on TMF life
- Creep-fatigue interactions
- Effects of off-axis grain behavior

While plots of the primary experimental results are shown in the main body of the text, the details of all experimental results are tabulated in Appendix B. Further, for experimental conditions where the experimental scatter in the life was unknown, a scatter of $+/-20\%$ was assumed to provide a measure of the uncertainty when plotting the TMF lives. This uncertainty is based on the experimental scatter for test conditions where multiple experiments were conducted.

5.1 Influence of Temperature Extremum

The minimum temperature (T_{min}) experienced by material within gas turbine engines relates to the length of the engine's shutdown. Short shutdowns are associated with

minimum temperatures of 500°C and 100°C with long ones. Most often it is desirable to conduct TMF experiments in laboratories with a minimum cycle temperature as low as possible to replicate long-term shutdowns conditions; however, to accelerate testing by increasing the frequency of the cycle, a higher minimum temperature is often used. This has typically been justified assuming that TMF life is controlled by degradation processes occurring during the high temperature excursions in the cycle, while the yield strength for most Ni-base superalloys remains nearly constant below 500°C. The reductions in the T_{min} of the cycle have two possible impacts on the material. First being a reduction in the fatigue resistance, due to an increase in the inelastic strain range arising from increases in the elastic modulus with the decreasing temperature [7]. Second, the aging of the γ' microstructure has been reported to be observed at elevated temperatures [7]. However, in light of these observations, extension of these trends to T_{max} below 950°C when aging is insignificant is unclear.

TMF experiments were conducted under both IP, $R_\epsilon = 0$ and OP, $R_\epsilon = -\infty$ phasing conditions with a T_{min} of either 100°C or 500°C on specimens with an L-orientation. The T_{max} investigated for each phasing condition were 750, 850, and 950°C, with the corresponding mechanical strain amplitudes of 1.2, 1.1, and 1.0% respectively. The mechanical strain amplitudes were chosen to obtain TMF lives in the neighborhood of 1,000 cycles, which is long enough for TMF interactions to be significant, while short enough to achieve the result in a reasonable period of time. Through reducing not only the T_{min}, but also the T_{max}, the various damage mechanisms thought to be associated with this reduced T_{min} effect can be segregated. For T_{max} of 750°C, one can expect the failure mechanisms to be dominated by pure fatigue, when T_{max} is 850°C a mixture of creep-fatigue, and when T_{max} is 950°C, a combination of microstructure evolution, creep, and fatigue damage is occurring.

The resultant life values of the IP and OP TMF experiments conducted are presented in Figures 5.1 and 5.2, respectively. A reduction in the T_{min} was observed

to result on average in a 65% net reduction in life across all T_{max} conditions tested when the T_{min}=500°C experiments are used as baseline comparisons. The greatest comparative decrease in life was found to occur for the IP experiments with T_{max} of either 850°C or 950°C which correlated to a nearly 90% reduction in life. Of the experiments, the OP TMF experiment with T_{max} of 750°C exhibited the least decrease, with a 45% reduction in life. Overall the magnitude of the life knockdown effect observed here is similar in magnitude to that reported for CMSX-4 which was tested under OP TMF, $R_\epsilon = -\infty$ conditions with a T_{max} of 950°C for T_{min} values of 100 and 400°C [7]. As a note, the crack nucleation and ultimate failure for two experiments, OP 500-750 and 500-850°C occurred at a TC weld location. As a result, the failure life of the material under the true test conditions would likely be even higher, resulting in a greater difference.

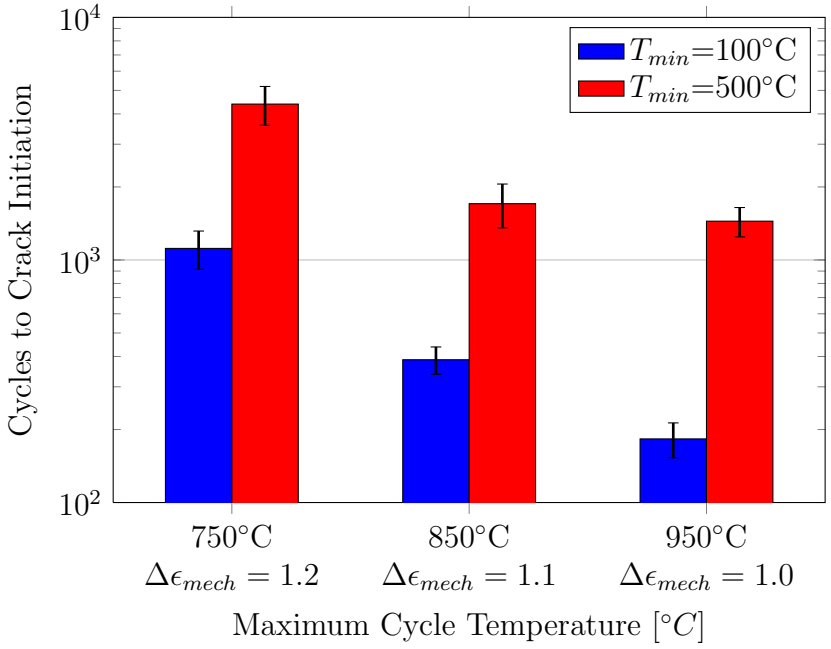

Figure 5.1: Influence of T_{min} on IP TMF life in the L-orientation.

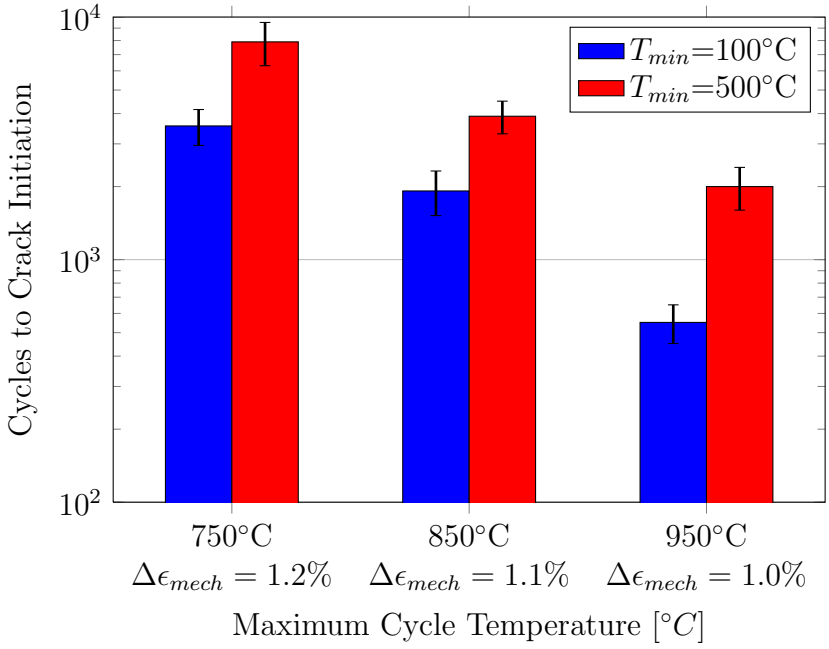

Figure 5.2: Influence of T_{min} on OP TMF life in the L-orientation.

The respective hysteresis responses at half-life were compared. All reduced T_{min} experiments exhibited increases in the inelastic strain range compared to the higher T_{min} responses under both IP and OP TMF loadings as shown in Figure 5.3a-f at half-life. In addition, the stress amplitude of the reduced T_{min} is greater. While the yield strength remains nearly constant in the 100-650°C temperature range (Figure 4.24), the elastic modulus increases nearly 20% when temperature decreases from 500 to 100°C as shown in Figure 4.23. For a given mechanical strain range, when the temperature is lower, the elastic strain range is reduced resulting in a greater inelastic strain range.

The reduced T_{min} experiments exhibit a 10-20% higher stress amplitude than T_{min} = 500°C as shown in Figure 5.4 from the onset of cycling. In most cases, the specimens were observed to have achieved stabilized hysteresis within the experiments first 10 cycles; however, the IP TMF 100-850°C experiment and the IP TMF experiments with a T_{max} of 950°C exhibited cyclic softening with the peak tensile stress occurring on the first cycle.

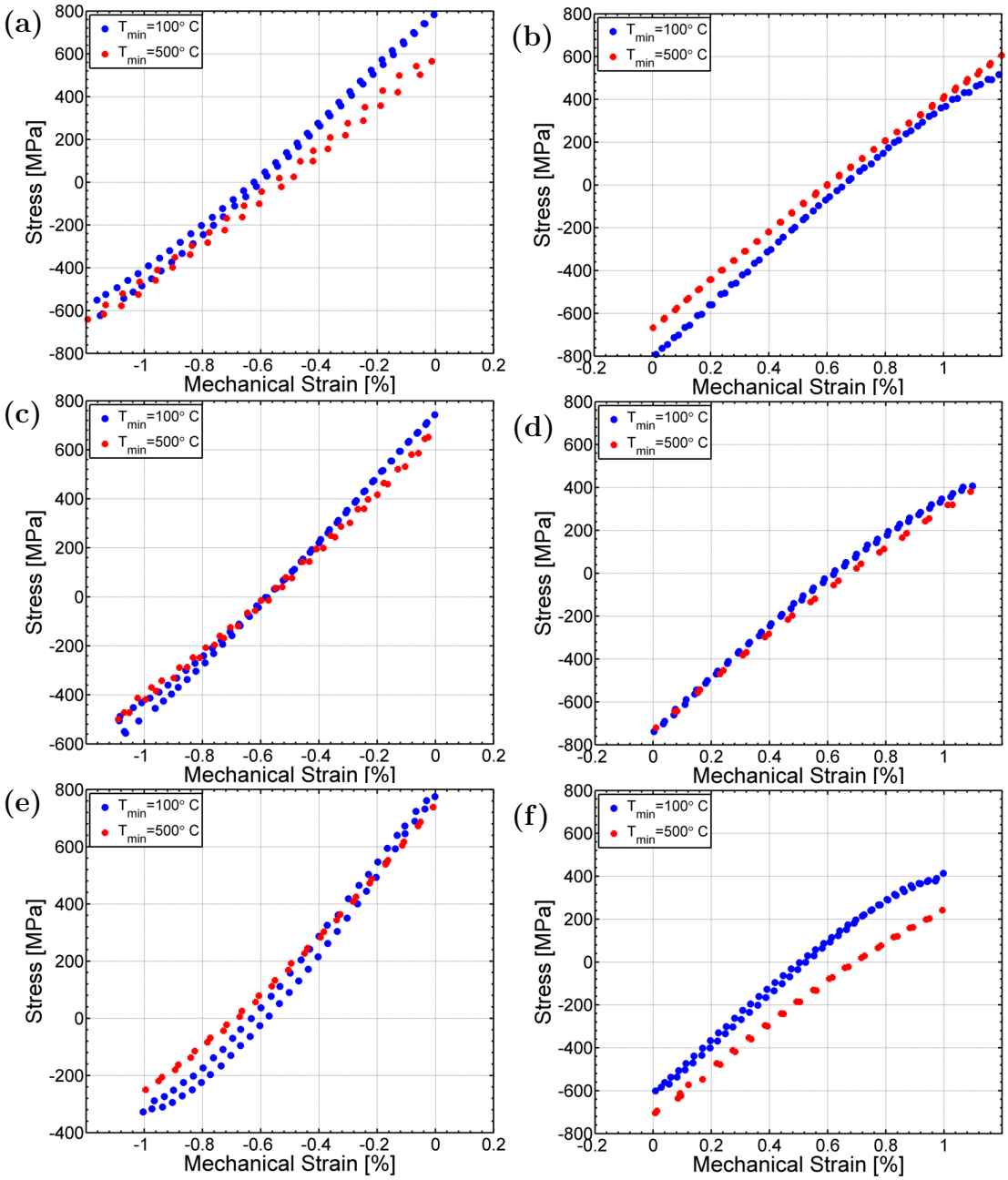

Figure 5.3: Hysteresis curves showing the influence of a 400°C reduction in the minimum cycle temperature at the respective half lives under (a) OP TMF T_{max}=750°C (b) IP TMF T_{max}=750°C (c) OP TMF T_{max}=850°C (d) IP TMF T_{max}=850°C (e) OP TMF T_{max}=950°C (f) IP TMF T_{max}=950°C.

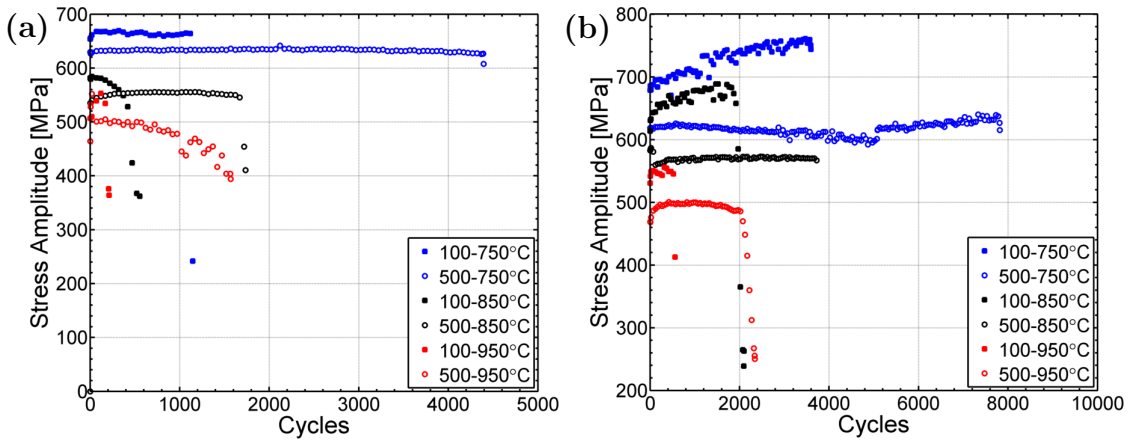

Figure 5.4: Stress amplitude curves for (a) IP TMF experiments with $R_\epsilon = 0$ (b) OP TMF experiments with $R_\epsilon = -\infty$.

In the case of IP TMF experiments with T_{max}=950°C, the cyclic softening can be attributed to extensive inelastic strains occurring in the γ channels perpendicular to the loading axis at peak temperatures as a result of the alignment of the peak temperature with the peak tensile strain that occurs in IP TMF [44]. In the case of OP TMF, the greatest inelastic deformation occurs in the γ channels parallel to the applied axial load [44]. In comparison, the cyclic softening observed in the 100-850°C IP experiments, is a combination of accumulation of plastic deformation in the γ channels perpendicular to the load and shearing of the γ' that occurs at temperatures below 750°C during the TMF cycle [16, 44].

OP TMF failure was dominated by preferential cracking along the oxidation spikes (Figure 5.5) when T_{max}=850°C and 950°C, but when T_{max}=750°C the mechanism of failure was pure fatigue, with the crack exhibiting macroscopic cube shear behavior. The mechanism can be determined through consideration of the activation energies for creep and oxidation of the alloy; which in the case of CM247LC-DS are 300 and 80 $\frac{KJ}{kmol}$ respectively [101, 118]. Further, in dropping the temperature from 950°C to 750°C, a 80% reduction in the rate of oxidation occurs [118]. As a result, the 750°C behavior was attributed to stress concentrations on fewer slip planes and γ' shearing, whereas above 800°C the deformation becomes more homogeneous with damage being

localized to the γ channels [68]. In contrast, fatigue cracks were observed to be emanating from carbide interfaces and the surrounding material in all IP TMF specimens as shown in Figure 5.6. In the coming sections, this IP fatigue failure mechanism will be discussed in greater detail. Ultimately, no discernible influence of minimum cycle temperature was observed on the failure mechanisms, with the temperature-strain phasing controlling which degradation mechanism operates.

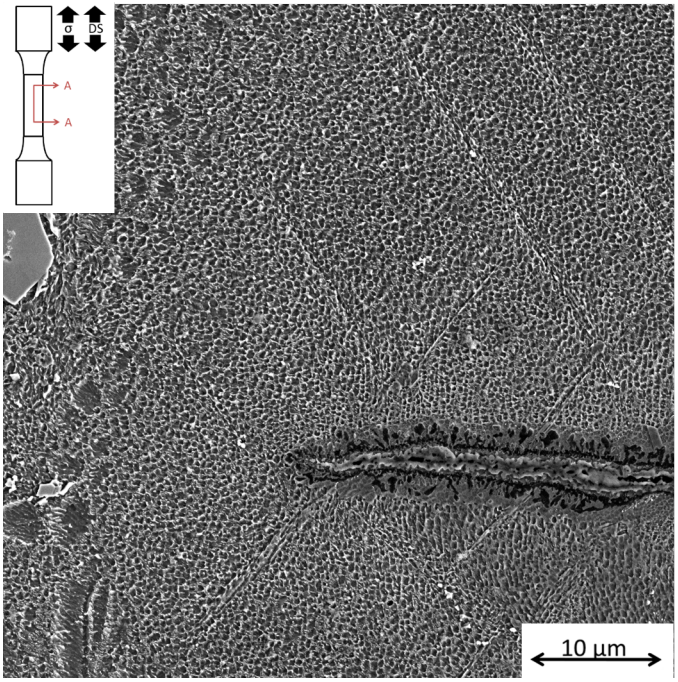

Figure 5.5: Fatigue crack propagating from an oxidation spike in material exposed to OP TMF $R_\epsilon = -\infty$ TMF (ΔT=100-950°C $\Delta\epsilon_{mech} = 1.0\%$).

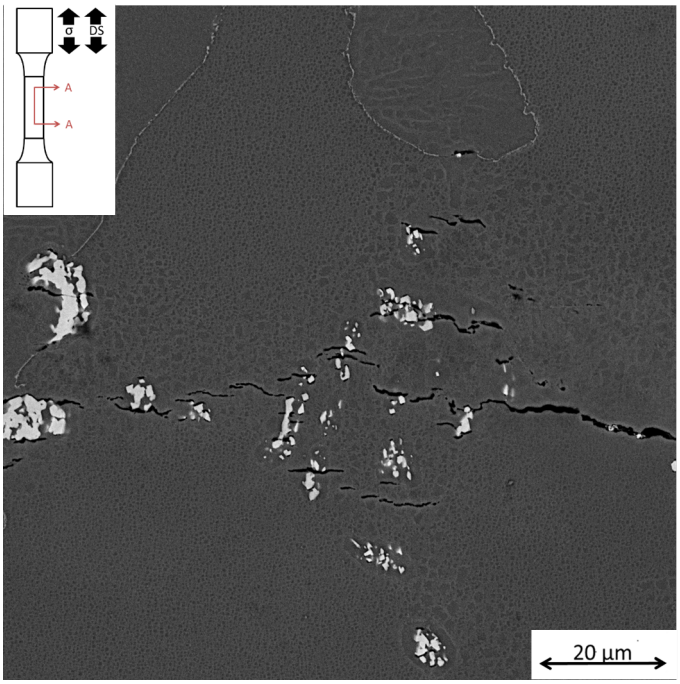

Figure 5.6: Fatigue cracks linking between debonded carbides in materail exposed to IP $R_\epsilon = 0$ TMF (ΔT=100-750°C $\Delta\epsilon_{mech} = 1.2\%$).

At the end of these experiments, the γ' precipitates were found to be in the early stages of directional coarsening for specimens tested with a T_{max} of 950°C as shown by the heavily cuboidal microstructure in Figure 5.7. No detectable microstructure evolution was observed in the experiments conducted at maximum temperatures of either 750°C or 850°C. These findings are consistent with the predictions of the analytical model for aging presented in Chapter 4 where directional coarsening was only observed at temperatures above 900°C. Further, the cumulative exposure time for the T_{max}=950°C specimens during the TMF experiment is too short to bring about a fully rafted structure, even though the thermodynamic driving force for directional coarsening is sufficient.

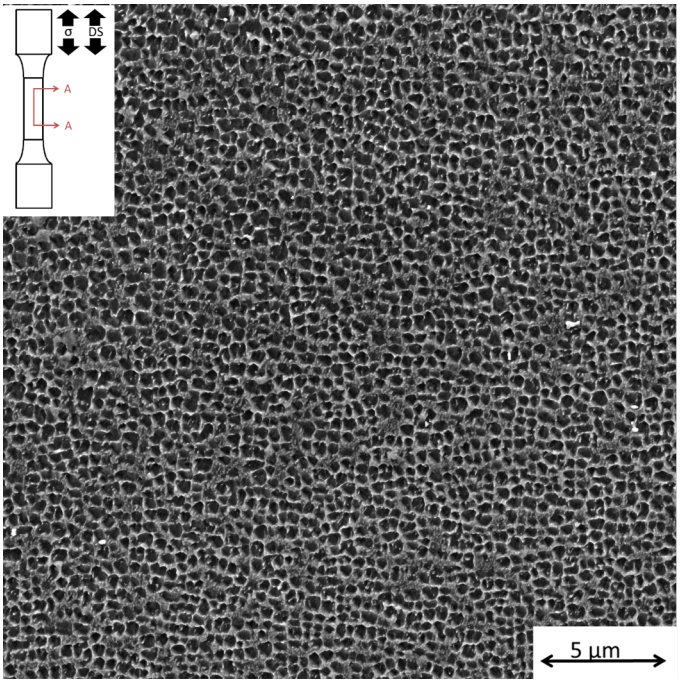

Figure 5.7: Resultant microstructure from failed material exposed to OP $R_\epsilon = -\infty$ TMF (ΔT=100-950°C $\Delta\epsilon_{mech} = 1.0\%$).

While coarsening of the γ' microstructure is known to induce a softening effect in Ni-base superalloys (Figure 4.24), microstructural analysis revealed this to be a non-factor in the TMF experiments conducted at T_{max} of 750°C and 850°C, and a secondary factor at 950°C [116]. As for the influence of environmental degradation on the life, continuous cracking and re-oxidizing of the specimen surface and subsurface γ' depletion at T_{max} of 850°C and 950°C can be considered primary contributing factors for OP TMF life; however, at T_{max} of 750°C the rate of oxidation is reduced 80% due to the oxidation kinetics having an exponential dependence on temperature [118]. In the case of the IP experiments conducted at 850°C and 950°C, accumulation of creep damage can be considered a contributing factor as evidenced by the cyclic softening in the stress amplitude curves. At 750°C, peak tensile stresses greater than those observed in the IP T_{max}=750°C cycles would be required for the material to see significant creep damage accumulation based on the creep-rupture behavior of this DS alloy [101]. With three of four potential contributing factors for the reduction in

life discounted for specimens tested at 750°C under both IP and OP conditions, the observed reduction in life when the minimum cycle temperature is reduced can be fully explained as a result of the greater inelastic strain that occurs from an increase in the elastic modulus in the sub-500°C temperature regime.

5.2 Influence of Temperature-Load Phasing

Amongst TMF loadings, OP TMF loadings generally become the life limiting cycle type [68,90,119]. This is attributed to the material degradation that occurs from the the continuous cracking of oxide layers and re-oxidation in the areas surrounding a growing fatigue crack [84]. The characteristics of an O-type crossover being that IP loading conditions are life limiting for large strain amplitudes and OP life limiting for small strain amplitudes [120]. In the case of CM247LC-DS undergoing TMF in the temperature ranges of both 100-950°C and 500-950°C for IP $R_\epsilon = 0$ and OP $R_\epsilon = -\infty$ the IP behavior is life limiting at high $\Delta\epsilon_{mech}$, while at low $\Delta\epsilon_{mech}$ OP TMF become life limiting. This is shown in Figure 5.8. The experimental findings indicate that with changes in the TMF cycle temperature range, a shift in the IP-OP mechanical strain crossover occurs. For the 500-950°C temperature range, the IP-OP curves cross at a $\Delta\epsilon_{mech} \approx 0.9\%$, while TMF with a $\Delta T = 100 - 950$°C resulted in a crossover occurring at a $\Delta\epsilon_{mech} \approx 0.7\%$.

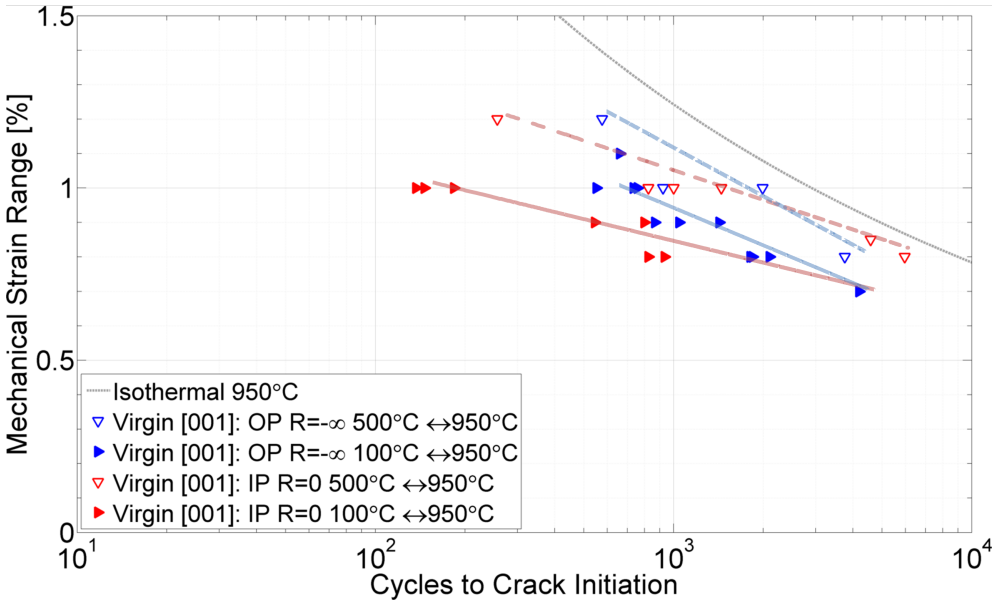

Figure 5.8: IP-OP TMF strain-life curves for material in the L-orientation depicting the influence of T_{min} on the IP-OP mechanical strain crossover.

Similar IP-OP crossovers have also been reported for the Ni-base superalloys IN-718-LC, Mar-M247LC-DS, and GTD-111 undergoing TMF with a T_{max} in the 871-971°C range [86, 119, 121, 122]. In addition, the results presented in Figures 5.1 and 5.2 indicate that IP-OP crossovers may occur for TMF cycles with T_{max} of either 750°C and 850°C due to the fact that the OP TMF experiments exhibited greater lives than the corresponding IP TMF experiments. However, due to the extended cyclic life of experiments conducted with T_{max} of either 750°C or 850°C, determining the potential crossover points would have been impractical.

Specimens exposed to IP TMF conditions above the cross-over point revealed that a large majority of the $M_{23}C_6$ carbides within the microstructure had fatigue cracks either emanating from their interfaces with the $\gamma - \gamma'$ matrix or in the matrix material directly surrounding them as shown in Figure 5.9. Due to the three-dimensional nature of the carbides, the cracks in the matrix could be the result of below carbide debonding [26]. In addition, the minority of carbides with chord lengths greater than 20 μm were themselves observed to have cracked; most likely on the initial cycle [123,

124]. Similar microstructural observations have been reported for IP TMF of other Ni-base superalloys where the T_{max} values used were in the 870-970°C range [86,119,121, 122]. However, these occurrences were attributed to creep related mechanisms [86,119, 121,122]. For IP TMF, 500-950°C experiments conducted below the mechanical strain crossover point, fatigue cracks were still observed to be emanating from debonded carbides and the surrounding regions.

The preferred fatigue crack growth and propagation mechanisms were observed to be the linking-up of cracks with neighboring carbides as shown in Figure 5.10. While creep interactions between the carbides and surrounding matrix can be assumed to most certainty occur for TMF tests conducted with high mechanical strain amplitudes and $T_{max}s$ of either 750°C and 850°C, the presence of debonded carbides in specimens tested under IP TMF conditions with a T_{max}=750°C and low mechanical strain amplitude (relatively speaking) is indicative that this is a creep modulated mechanism for TMF cycles with a T_{max} above 850°C. Under OP TMF conditions carbide decohesion is not observed. However, the carbides can still be observed as a stress concentrator as a result of slip bands emanating from the carbides as shown in Figure 5.11.

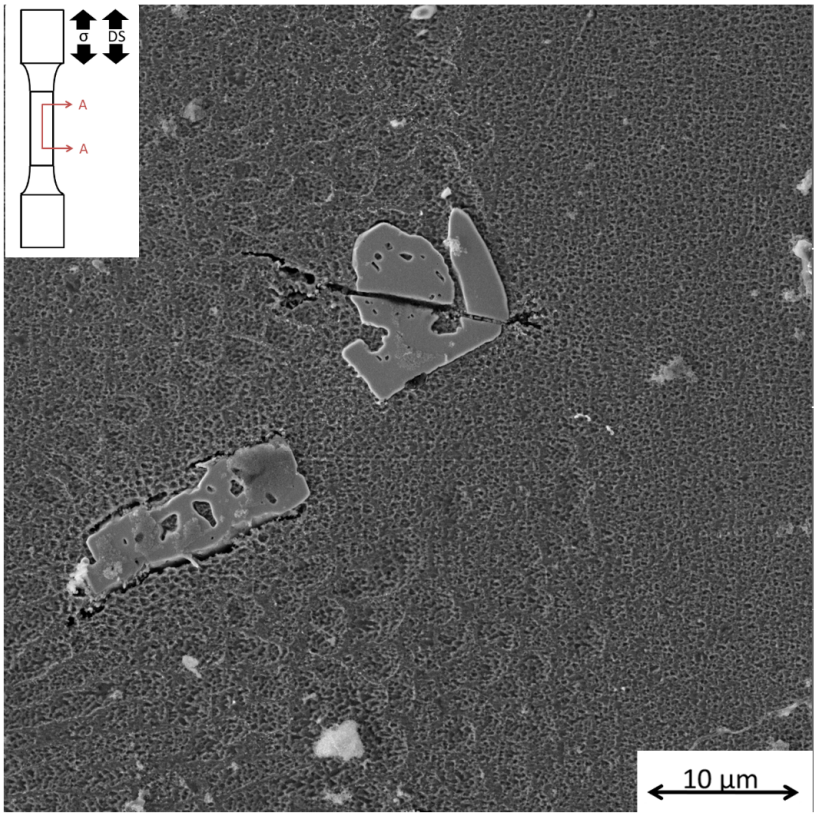

Figure 5.9: Cracks emanating from a debonded MC carbide under IP $R_\epsilon = 0$ TMF loading (ΔT=100-950°C $\Delta\epsilon_{mech} = 0.8\%$.)

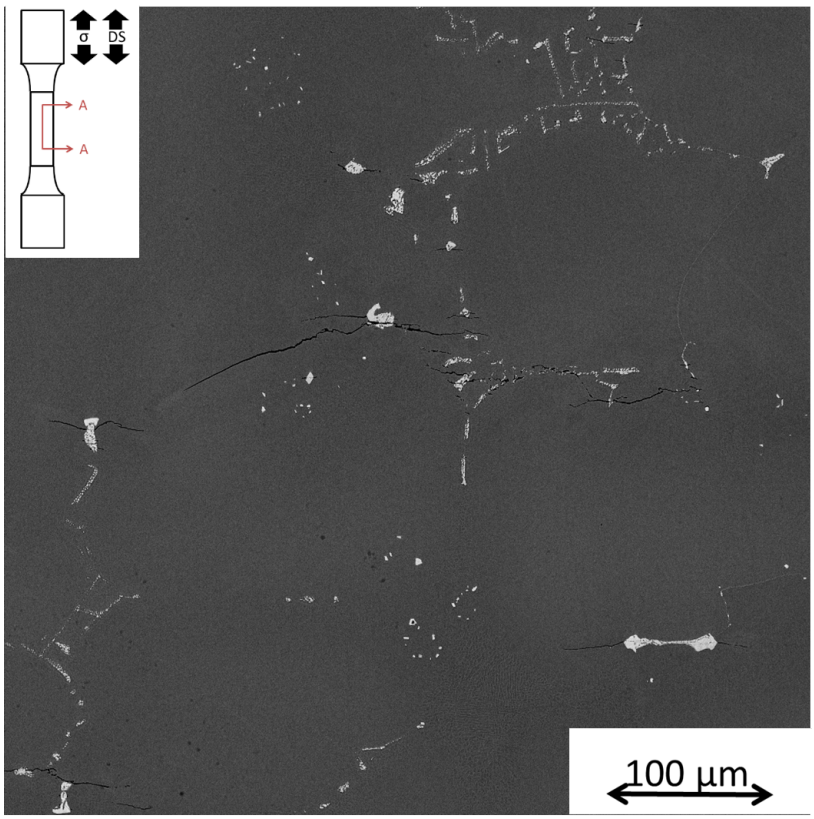

Figure 5.10: The linking of fatigue cracks originating from carbides in material exposed to IP $R_\epsilon = 0$ TMF (ΔT=500-750°C $\Delta\epsilon_{mech} = 1.2\%$). The carbides appear as white.

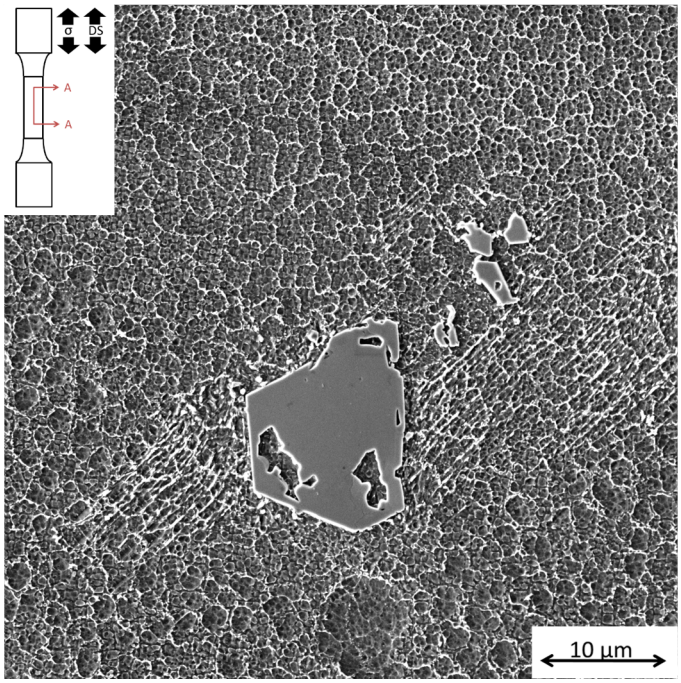

Figure 5.11: Slip band impingement on a $M_{23}C_6$ carbide occurring as a result of OP $R_\epsilon = -\infty$ TMF exposure within a interdendritic region (ΔT=100-950°C $\Delta\epsilon_{mech} = 0.8\%$).

For Mar-M200 undergoing isothermal LCF in the 20-800°C temperature range, the primary fatigue crack propagation mechanism was determined to be the linking of cracks emanating from debonded carbides [124, 125]. Above, 850°C, was reported the fatigue crack propagation mechanism changed to that of cracks initiating at casting porosity in Mar-M200 [124,125]. However, in the case of CM247LC-DS there is no significant casting porosity. Additionally, quantitative fractography measurements of failed tensile surfaces tested in the 20-880°C range revealed the carbide area fraction was found to average 10%, while the average volume fraction of carbides within the bulk was determined to be less than 2% [126]. Further, the expected thermal strain mismatch between the bulk superalloy and the MC/$M_{23}C_6$ carbides are ≈1.0% resulting in compressive strains developing in the material surrounding the carbides at room temperature [127–129].

Overall, the IP-OP mechanical strain-life crossover point and the associated temperature dependence can be linked with the microscopic TMF conditions in the material surrounding the carbides and the associated interfaces. When accounting for the strains induced by the thermal strain mismatch, the matrix material in regions in the immediate vicinity of the carbides experiences a local mechanical strain amplitude that is a composite value of the thermal misfit and the applied mechanical strain amplitude for a given TMF cycle that ultimately results in extensive fatigue damage accumulation in these localized regions. Ultimately, below the IP-OP crossover point, fatigue damage accumulation in regions near the debonded carbides under IP TMF continues to occur, however the damage accumulation is at a reduced rate compared to the OP TMF experiments leading to restoration of OP TMF being the life limiting cycle [86].

5.3 Influence of Mean Strain

While the loading conditions in service components are typically associated with OP $R_\epsilon = -\infty$ TMF and IP $R_\epsilon = 0$ TMF loadings, variations in mean strains do occur within service components. To examine the influence of mean strain on strain-life behavior in the L-orientation, OP $R_\epsilon = -\infty$ and $R_\epsilon = -1$ TMF experiments in the 500-950°C temperature range were conducted. Similarly, IP experiments were conducted for both $R_\epsilon = 0$ and $R_\epsilon = -1$ in the 500-950°C range. The strain-life curves for each set of mean strain conditions is shown in Figure 5.12 with the isothermal LCF behavior at 950°C under fully-reversed conditions as a reference to the upper strain-life limit.

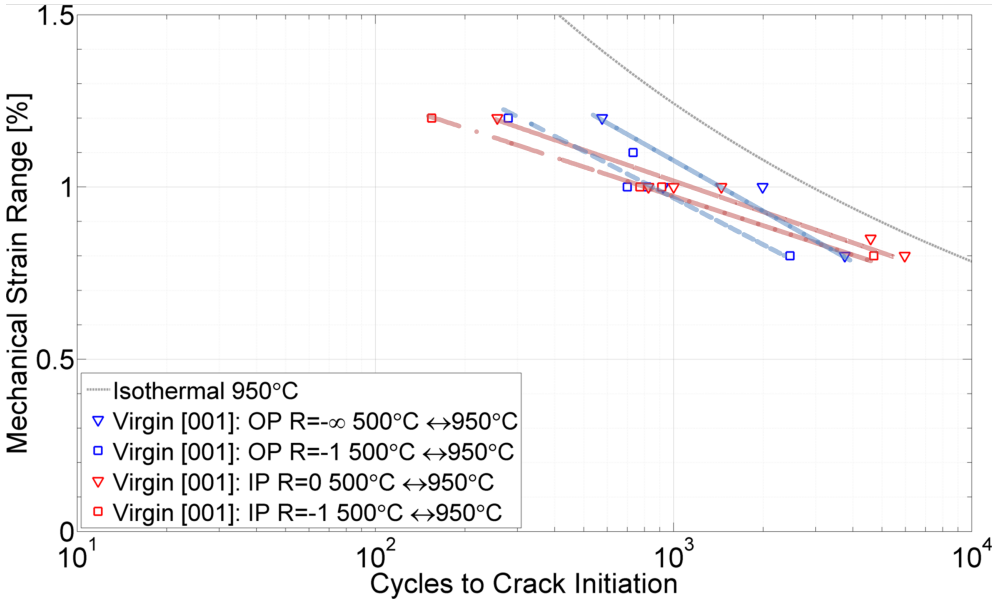

Figure 5.12: Life curves for TMF experiments for material in the L-orientation conducted in the 500-950°C temperature range under IP $R_\epsilon = -1$ and $R_\epsilon = 0$ loading conditions and OP $R_\epsilon = -1$ and $R_\epsilon = -\infty$ conditions in comparison to the strain-life at 950°C under fully-reversed loading conditions.

Specimens tested under both IP and OP $R_\epsilon = -1$ TMF generally exhibited shorter fatigue lives than the TMF experiments with a mean strain. However, the results are well within the experimental scatter of the material and the allowable variations for grain misorientation. Through repetition of the TMF experiments, a $+\backslash -20\%$ range in the life from the mean value was found.

Shown in Figures 5.13 and 5.14 are comparative sets of initial cycle and half-life stress-train curves with the corresponding mean stress evolution curves for both IP and OP TMF. Aside from the shift in strain associated with the difference in strain ratios, the half-life hysteresis behavior under both IP and OP conditions with a mean strain result in statistically identical peak stresses as the corresponding fully-reversed experiments at half-life. In addition the accumulated inelastic strains were also equivalent between the cycles. From the evolution of the mean stress is observed those IP and OP experiments conducted with a mean strain exhibited nearly symmetric loading on the initial cycle, with the material ultimately reaching stabilized hysteresis at

approximately 15% life, whereas the fully-reversed experiments stabilized within 10% of the life value. Further, both IP and OP experiments with $R_\epsilon = -1$ experienced higher magnitude stresses on the cold portion of their respective TMF cycles early in life driving the rate of stress stabilization.

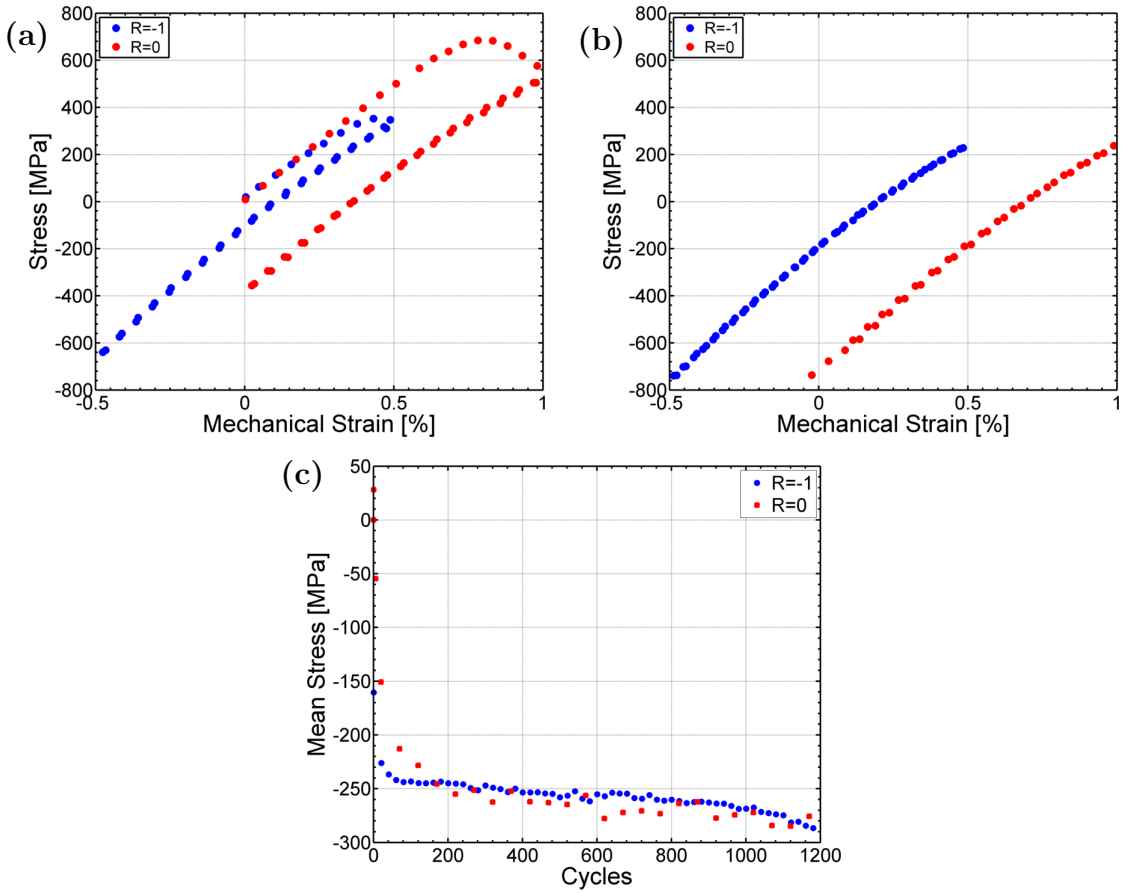

Figure 5.13: IP TMF results with ΔT=500-950°C comparing the effect of mean strain on (a) First cycle response (b) Half-life hysteresis response (c) Mean stress evolution.

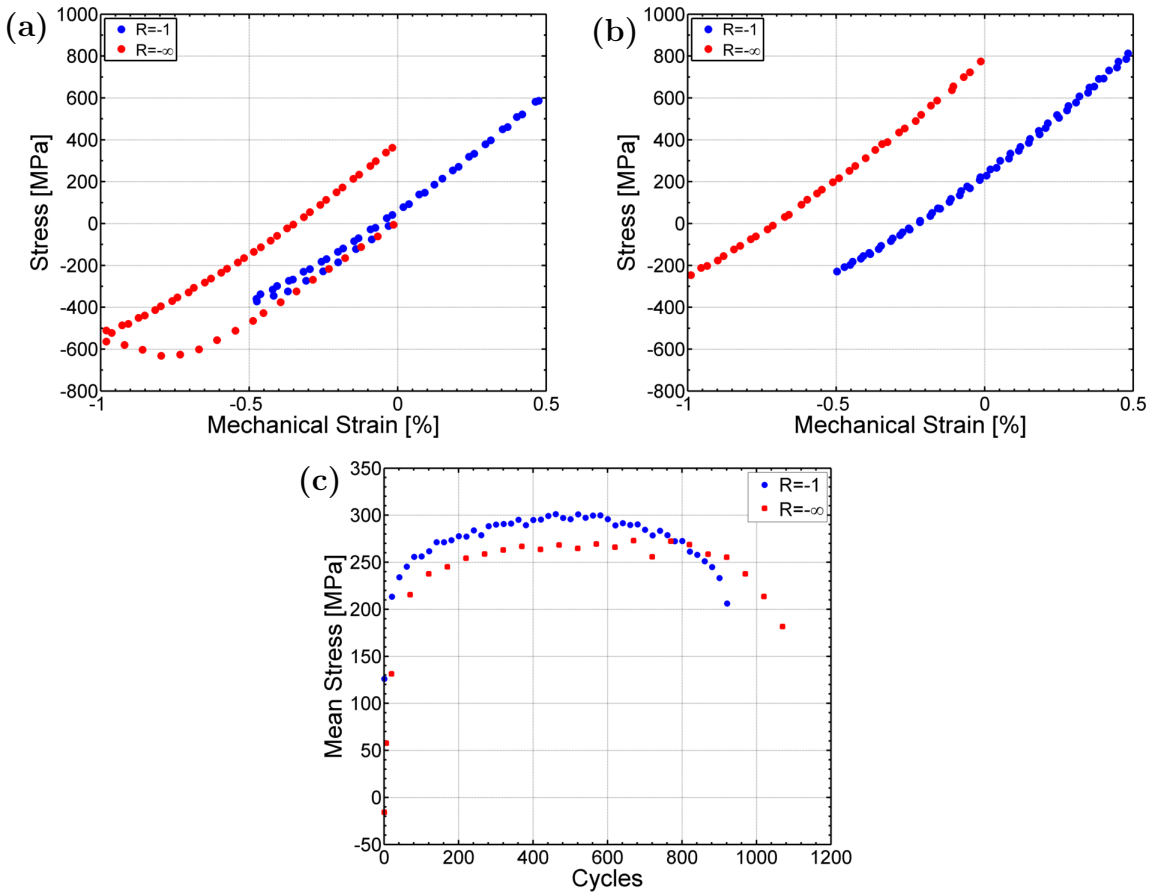

Figure 5.14: OP TMF results with ΔT=500-950°C comparing the effect of mean strain on (a) First cycle response (b) Half-life hysteresis response (c) Mean stress evolution.

While differences exist in the stress evolution, knowledge of the known statistical scatter in the strain-life results and the similarities of the resultant strain-life and stress response, the TMF response is essentially independent of mean strain. As a result, the mechanical strain amplitude controls the strain-life under TMF conditions. These findings are consistent with the behavior of other Ni-base superalloys under various mean strain conditions [25].

5.4 Creep-Fatigue Interaction

From this point forward, CC and CF will be used to distinguish between continuous cycled and creep-fatigue TMF cycle types. In all cases, CF TMF cycles included a

20 minute strain hold at the peak cycle temperature. The life comparisons between CC TMF and CF TMF experiments are shown in Figure 5.15. On average, the inclusion of a dwell period resulted in a 2x or greater reduction in TMF life, with the greatest life reductions occurring for IP TMF conditions. This IP life reduction can be attributed to the rapid debonding of the carbides and fatigue crack nucleation in the surrounding matrix material through the accumulation of voids. In the case of OP TMF, the increase in cyclic inelastic strain coupled with the accelerated environmental damage can be considered the primary reason for the life reduction.

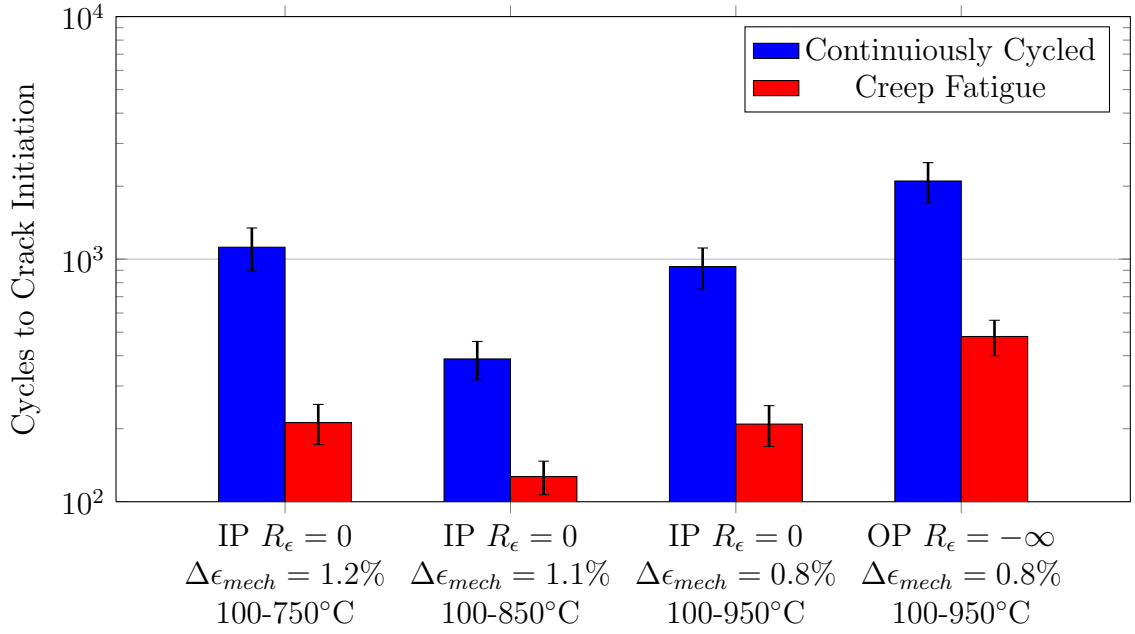

Figure 5.15: Comparison of the CF effect on the TMF life behavior in the L-orientation in relation to CC TMF conditions for both IP and OP loadings.

Shown in Figures 5.16-5.19 are the half-life hysteresis and mean stress evolution curves comparing the CC and CF responses for the life results in Figure 5.15. The dwell periods were generally found to result in an increase in the amount of accumulated inelastic strain, with nearly complete stress relaxation occurring for CF TMF cycles with T_{max} of 850°C and 950°C. At 750°C, minimal stress relaxation is observed to occur as a result of the limited creep deformation. This is consistent with trends

observed for DS Ni-base superalloys under isothermal CF conditions [25].

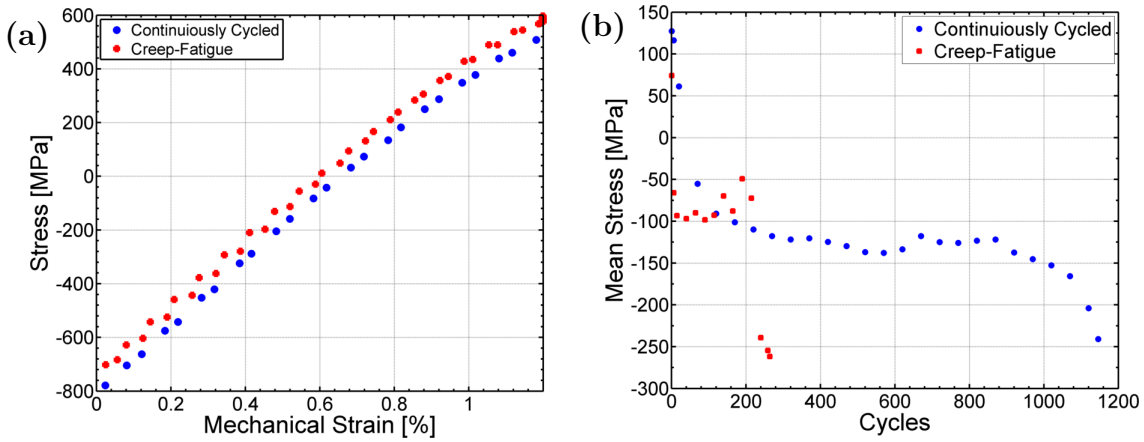

Figure 5.16: IP $R_\epsilon = 0$ TMF results for ΔT=100-750°C comparing CC to CF in the L-orientation on the (a) Half-life hysteresis response (b) Mean stress evolution.

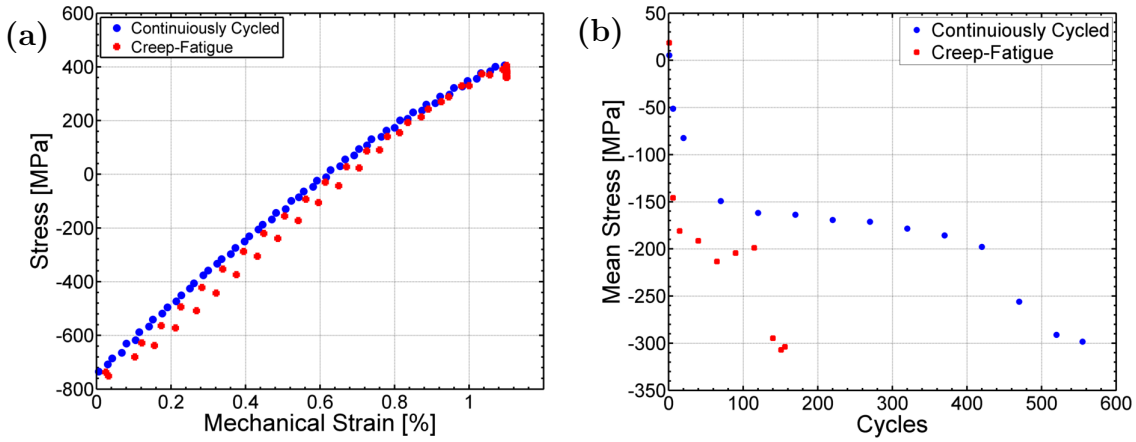

Figure 5.17: IP $R_\epsilon = 0$ TMF results for ΔT=100-850°C comparing CC to CF in the L-orientation on the (a) Half-life hysteresis response (b) Mean stress evolution.

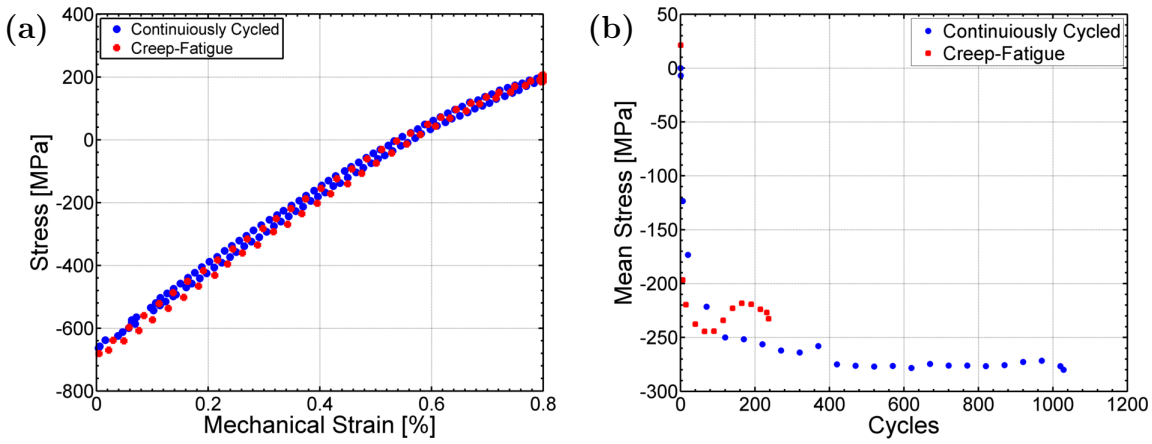

Figure 5.18: IP $R_\epsilon = 0$ TMF results for ΔT=100-950°C comparing CC to CF in the L-orientation on the (a) Half-life hysteresis response (b) Mean stress evolution.

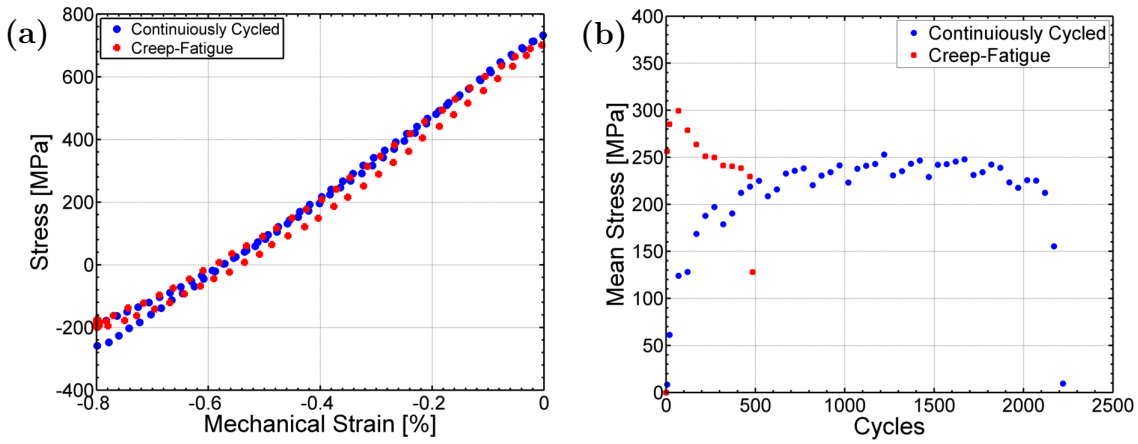

Figure 5.19: OP $R_\epsilon = -\infty$ TMF results for ΔT=100-950°C comparing CC to CF in the L-orientation on the (a) Half-life hysteresis response (b) Mean stress evolution.

For experiments conducted in the L-orientation under IP TMF conditions, the mean stress initially decreases before stabilizing at a value 20% above the peak mean stress. Whereas, in the OP CF case, the mean stress initially decrease 20% before increasing again, being indicative that changes in the internal stresses of the $\gamma - \gamma'$ microstructure are occurring. While the temporal length of the OP CF TMF experiment is enough to bring about directional coarsening as shown in Figure 5.20, the microstructure in the IP CF TMF experiments were prevented from directional

coarsening by the rapid propagation of fatigue cracks from debonded carbides. The temporal findings are consistent with the aging kinetics presented in Chapter 4 shown by characterizing the microstructure using two-point correlation statistics.

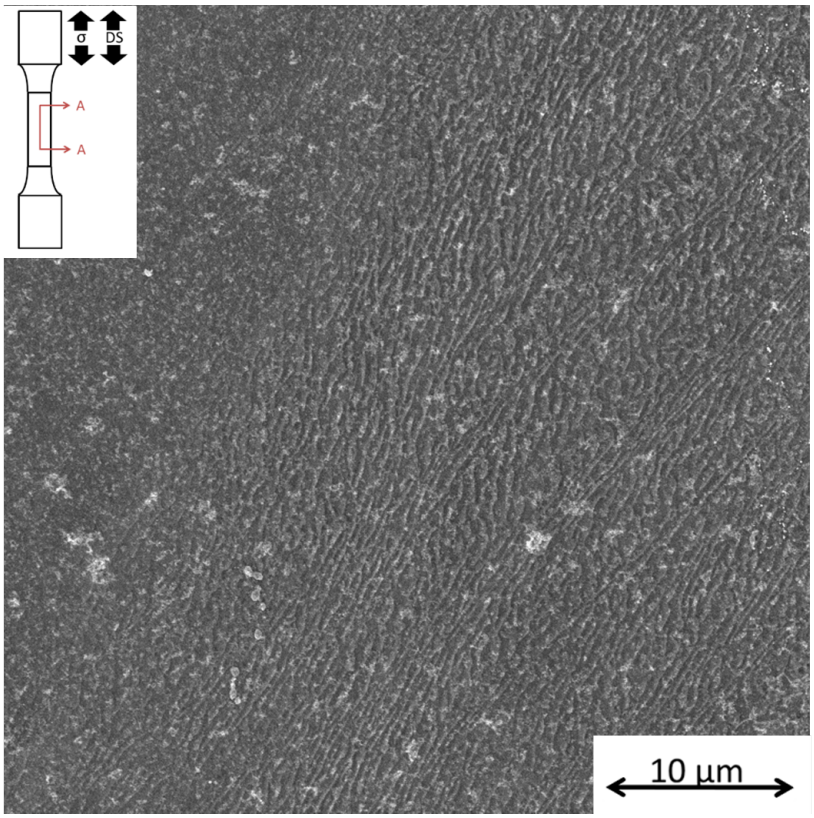

Figure 5.20: Resulting microstructure obtained after exposure to OP $R_\epsilon = -\infty$ CF TMF with ($\Delta T = 100 - 950°C$ $\Delta\epsilon_{mech} = 0.8\%$).

5.5 Orientation Effects

In the transverse orientation are shared many of the life trends observed for TMF loadings in the L-orientation, however the transverse life is reduced from the L-orientation as a result of the differences in the elastic moduli. For this study, TMF experiments in the T-orientation were conducted to analyze the T_{min} influence, IP-OP TMF life behavior, and the effects of CF interactions on the TMF life. Complicating the interpretation of the results is the variability of the secondary grain orientations and their net effect on the elastic properties. For the specimens tested in this study, all

had elastic moduli within +/- 10% of 170 GPa at room temperature.

For the experiments conducted in the T-orientation, the OP $R_\epsilon = -\infty$ TMF life behavior for the 100-950°C range was consistently found to exhibit a greater life than the corresponding IP $R_\epsilon = 0$ TMF experiments as shown in Figure 5.21. As to whether or not the T-orientation exhibits a O-type crossover similar to the L-orientation is unclear. If a crossover does occur, the crossover would likely occur below $\Delta\epsilon_{mech} \approx 0.3\%$ based on the life trend curves. Similar to the L-orientation, CF fatigue conditions in the T-orientation result in a nearly 2x reduction in the fatigue life under both IP and OP TMF conditions as shown in Figure 5.22. Comparisons of the half-life behaviors between CC and CF reveal little difference in the mechanical response as shown in Figure 5.23. In the case of the failed gage sections exposed to OP TMF can be seen significant differences between the material exposed to CC and CF conditions as shown in Figure 5.24.

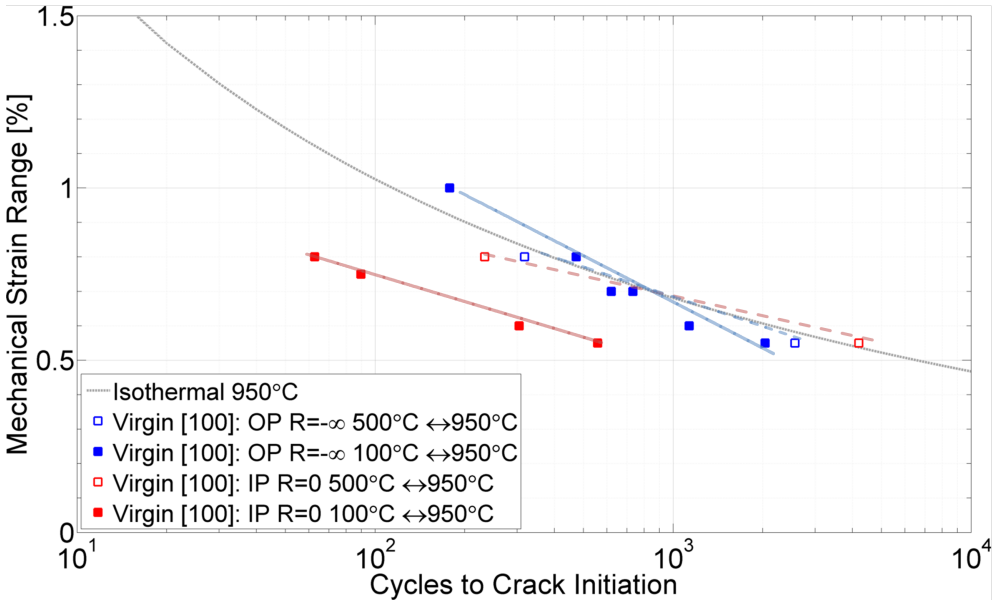

Figure 5.21: TMF life in the T-orientation for IP $R_\epsilon = 0$ and OP $R_\epsilon = -\infty$ TMF loadings.

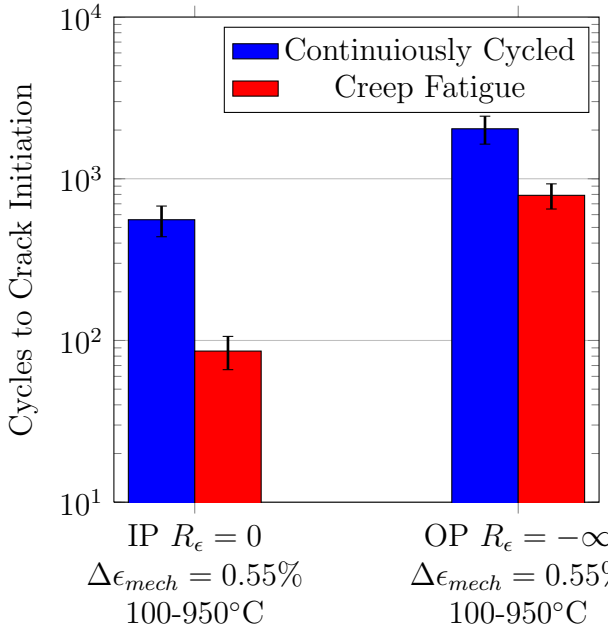

Figure 5.22: Comparison of the CF effect on the TMF stain-life behavior in the T-orientation in relation to CC TMF conditions for both IP and OP 100-950°C loadings.

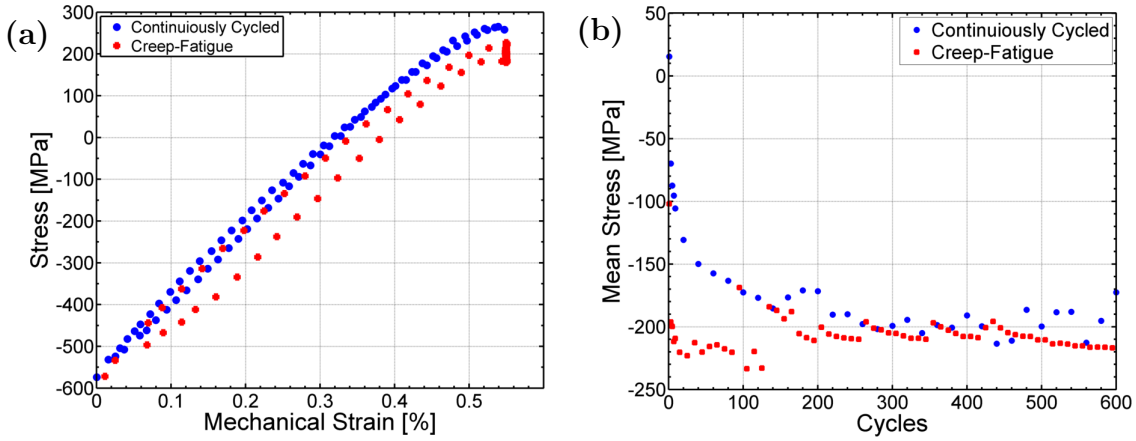

Figure 5.23: IP TMF results for ΔT=100-950°C comparing CC to CF in the T-orientation on the (a) Half-life hysteresis response (b) Mean stress evolution.

Microscopy of the failed specimens indicates that under IP TMF conditions, fatigue crack propagation is dominated by intergranular cracking and cracks eminating from grain boundary carbides. This can be seen in the macroscopic micrograph in Figure 5.25 and the microscopic micrograph in Figure 5.26. The implications of the

grain boundaries become significant in deciding the mode of fatigue crack growth and the materials susceptibility to environmental damage under TMF conditions. This behavior is similar to that reported for the DS Ni-base superalloy Mar-M247 [86,121]. Further, aging of the $\gamma - \gamma'$ microstructure in the T-oriented was not observed as a result of exposure to CF conditions as in the L-oriented, this can be attributed to the sensitivity of the evolution kinetics to crystallographic orientation [130].

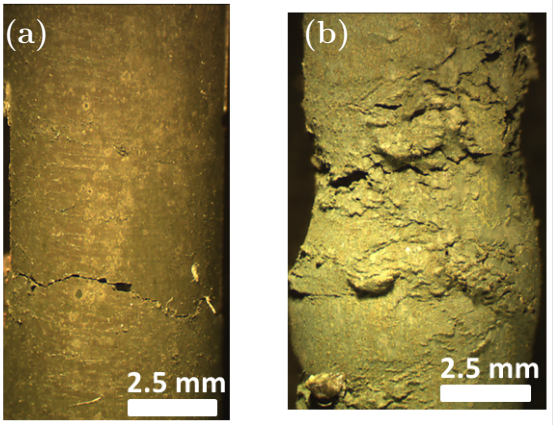

Figure 5.24: Comparison of the failed gage surfaces exposed to OP TMF, ΔT =100-950°C and $\Delta\epsilon_{mech} = 0.55\%$ in the T-orientation (a) under CC conditions (b) under CF conditions.

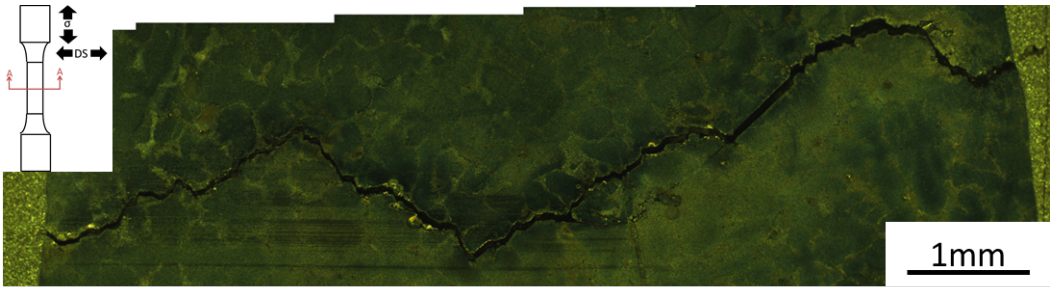

Figure 5.25: Transgranular cracking occurring under IP $R_\epsilon = 0$ TMF conditions (ΔT =100-950°C $\Delta\epsilon_{mech} = 0.55\%$).

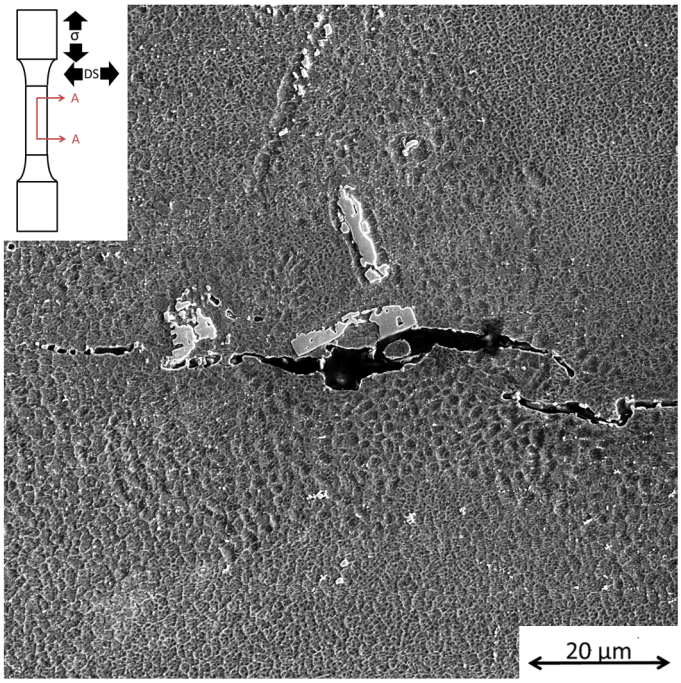

Figure 5.26: Fatigue crack emanating from a carbide along a grain boundary in material tested under IP $R_\epsilon = 0$ CC TMF conditions (ΔT =100-950°C $\Delta\epsilon_{mech} = 0.55\%$).

CHAPTER VI

INFLUENCE OF AGED STATES ON TMF

Unclear is whether aged microstructures are beneficial or detrimental to the fatigue life of Ni-base superalloys. Specifically, if a aged microstructure is beneficial, what are the fatigue conditions? To answer these questions, this chapter presents experimental results conducted for three distinct aged micrsotructure states observed in service components, isotropic coarsened, N-raft, and P-raft microstructures. Again presented within the main body of the text are the life plots of the primary results, while the complete experimental results are tabulated in Appendix B. As before, the error bars provide a +/- 20 % measure of the potential scatter in the life results based on repeated experiments in the virgin microstructure.

6.1 Isotropically Coarsened

To explore the influence of isotropic coarsening conditions, the most relevant TMF conditions in the context of a service component are IP TMF with $R_\epsilon = 0$. For all isotropically coarsened TMF experiments, a T_{max} of 750°C was used. A peak temperature of 750°C being representative of material near internal cooling passages within the service component where fatigue cracking is a prominent issue [101]. While material near the surfaces of the internal cooling cavities can reach temperatures well in excess of 750°C, 750-800°C is near the upper limit under which the application of stress and temperature are expected to result in a non-rafted coarsened microstructure [16, 63]. Above 850°C, the expectations are for the γ' cuboids to form a rafted microstructure.

The TMF life results in the L-orientation are shown in Figure 6.1. In the L-orientation, the coarsened microstructure under 500-750°C CC TMF conditions resulted in a 85% life reduction, while the TMF cycle with the 100-750°C temperature range exhibited a 65% life reduction when compared to the virgin material response. Similar decreases in life have been reported for Rene 80 in the overaged state tested under isothermal LCF conditions [131]. In the case of the influence of CF on the coarsened microstructure, no discernible difference between the virgin and coarsened microstructure was observed. Further, comparison within the coarsened experiments, reveals the trends of reduced life accompanying both the reduction in the T_{min} and the inclusion of a tensile strain hold similar to those observed for the virgin microstructure in Chapter 5.

For the TMF conditions tested, no statistically meaningful difference in the measurable inelastic strains was detected for the coarsened and virgin microstructures undergoing CC and CF TMF as shown in the representative half-life curves in Figures 6.2a and 6.3a. While the inelastic strains were similar, the coarsened microstructure exhibited a tensile mean stress in each of the CC TMF experiments, while the corresponding virgin experiments consistently experienced compressive mean stresses as shown in Figure 6.2b. This trend was observed to be repeatable for specimens taken from different slabs. However, in the case of the CF cycles, the mean stress occurring within the virgin material is observed to evolve towards and reach the stabilized mean stress of the coarsened microstructure (Figure 6.3b).

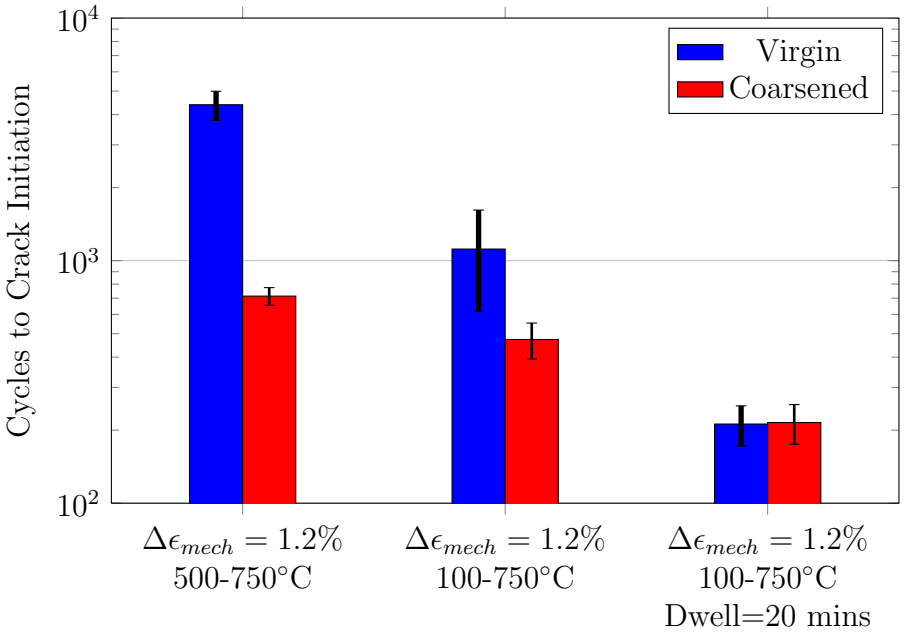

Figure 6.1: Life comparison between the isotropically coarsened and virgin microstructures in the L-orientation under IP $R_\epsilon = 0$ TMF loading conditions.

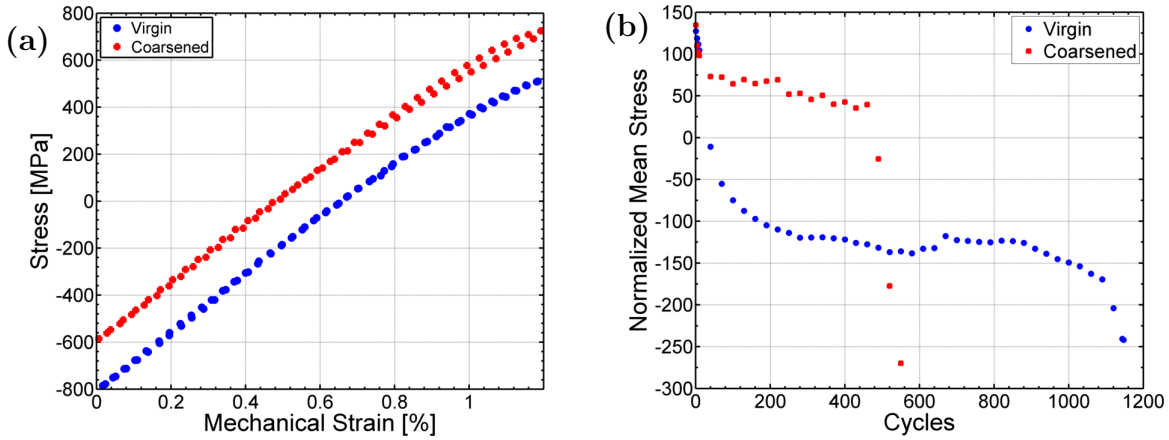

Figure 6.2: IP $R_\epsilon = 0$ TMF results for ΔT=100-750°C comparing the isotropically coarsened microstructure to the virgin under CC conditions in the L-orientation on the (a) Half-life hysteresis response (b) Mean stress evolution.

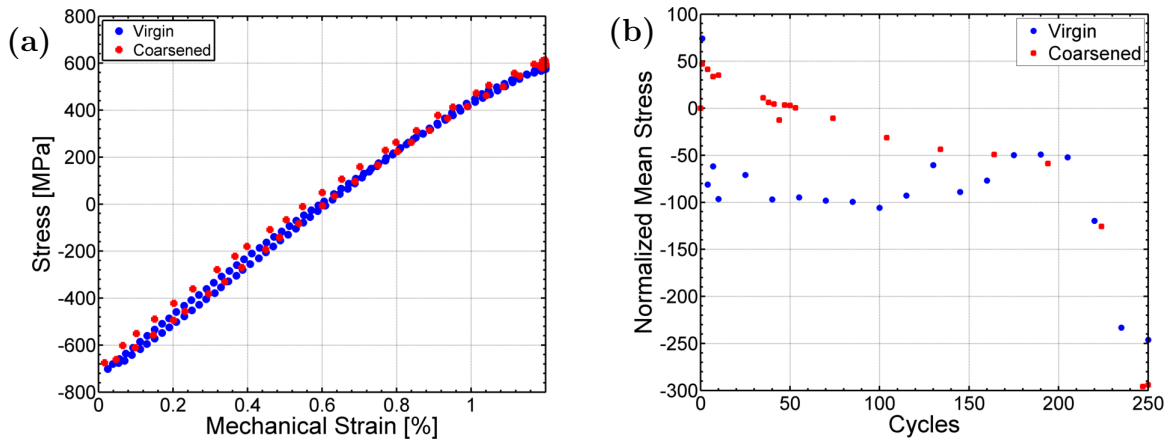

Figure 6.3: IP $R_\epsilon = 0$ TMF results for ΔT=100-750°C comparing the isotropically coarsened microstructure to the virgin under CF conditions in the L-orientation on the (a) Half-life hysteresis response (b) Mean stress evolution.

For both the coarsened and virgin microstructures, the mode of crack growth was observed to be of macroscopic cube shear Figure 6.4. This can be considered typical of Ni-base superalloys fatigued in the intermediate temperature regime [19]. In addition, the failed coarsened microstructure revealed significant carbide debonding similar to that in the virgin material that ultimately leads to a rapid propagation of fatigue cracks throughout the microstructure as shown in Figure 6.5.

In the CC case, the higher mean stress in the coarsened microstructure can be associated with the relaxation of the internal $\gamma - \gamma'$ misfit stresses and the resulting life reductions on the decrease in shear resistance of the overaged γ' microstructure [132, 133]. In the case of the CF cycle, the ultimate stabilization of both the coarsened and virgin microstructures at the near identical mean stress values indicates that the inelastic strain accumulated by inclusion of the tensile dwell drives both microstructures to the same internal stress state, i.e. relaxation of the misfit stress.

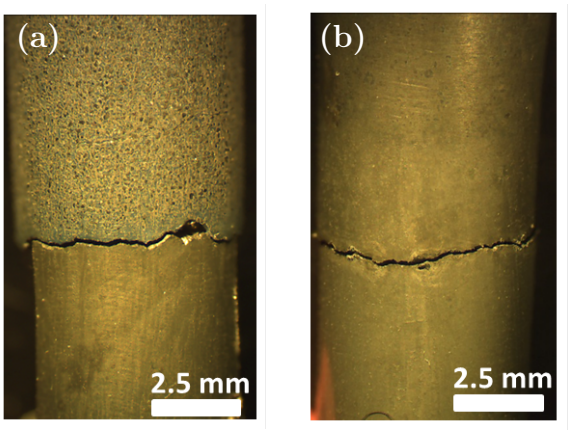

Figure 6.4: Comparison of failed gage surfaces exposed to IP $R_\epsilon = 0$ CC TMF conditions with $\Delta T = 100 - 750°C$ and $\Delta\epsilon_{mech} = 1.2\%$ for the (a) Virgin microstructure and (b) Coarsened microstructure. Note: after failure of the virgin specimen, the upper half of the gauge section continued to be heated by the induction coil resulting in alterations to the failure surface texture.

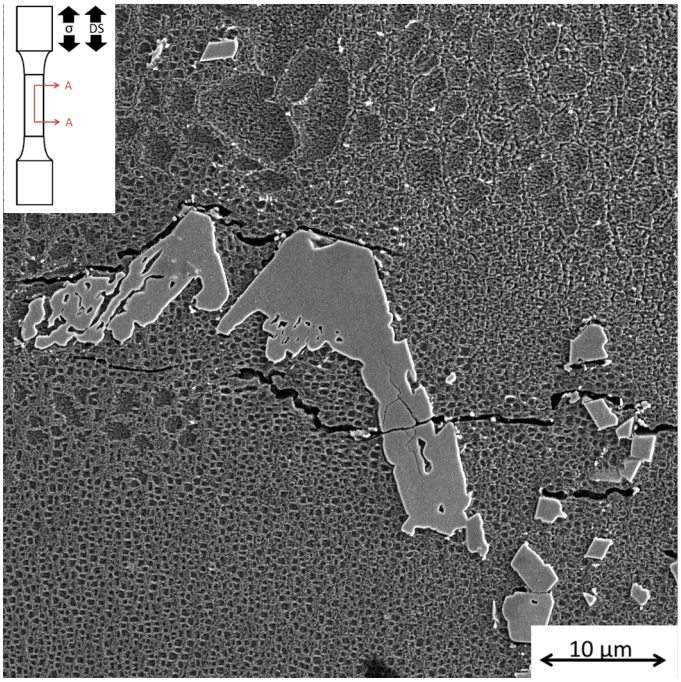

Figure 6.5: Debonded/cracked carbide within a stress-free coarsened microstructure at a dendritic-interdendritic boundary after exposure to IP $R_\epsilon = 0$ CC TMF ($\Delta T = 500 - 750°C$ $\Delta\epsilon_{mech} = 1.2\%$).

6.2 N-raft

In service components, N-rafts occur only under IP conditions for the case of a negative lattice mismatch alloy [16]. And similar to the coarsened microstructure, the N-rafts form in regions surrounding cooling passages. Above temperatures of 900°C and moderate stresses, N-rafts are expected to rapidly develop as observed in the microstructure evolution kinetics observed in Chapter 4. Long term exposure $(10,000hrs)$ at temperatures as low as 850°C and high stresses are capable of bringing about a rafted state [48, 72]. For the TMF test conditions, T_{max} of both 850°C and 950°C were considered with $R_\epsilon = 0$.

Shown in Figure 6.6 and 6.7 are the life results of the N-raft microstructure in relation to the virgin material for both T_{max} of 850°C and 950°C in the L-orientation. When increasing the mechanical strain amplitude from 0.8 to 1.0% under 100-950°C IP TMF conditions, the TMF life was observed to become microstructure insensitive as shown in Figure 6.7. With a decreasing mechanical strain amplitude the strain-life values were observed to become microstructure sensitive, with the N-raft microstructure exhibiting a 50% reduction in the strain-life over the virgin microstructure under CC conditions at T_{max} of 850 and 950°C. These life reductions are consistent with reported results for other Ni-base superalloys given tensile pre-creep treatments [7, 25, 89, 90, 134]. However, CF TMF of the N-raft microstructure in the L-orientation for T_{max} of both 850 and 950°C, no discernible difference in TMF life was observed. Further, under CC TMF conditions in the T-orientation as shown in Figure 6.8, no distinguishable effects of aging were found on the TMF behavior for the conditions tested.

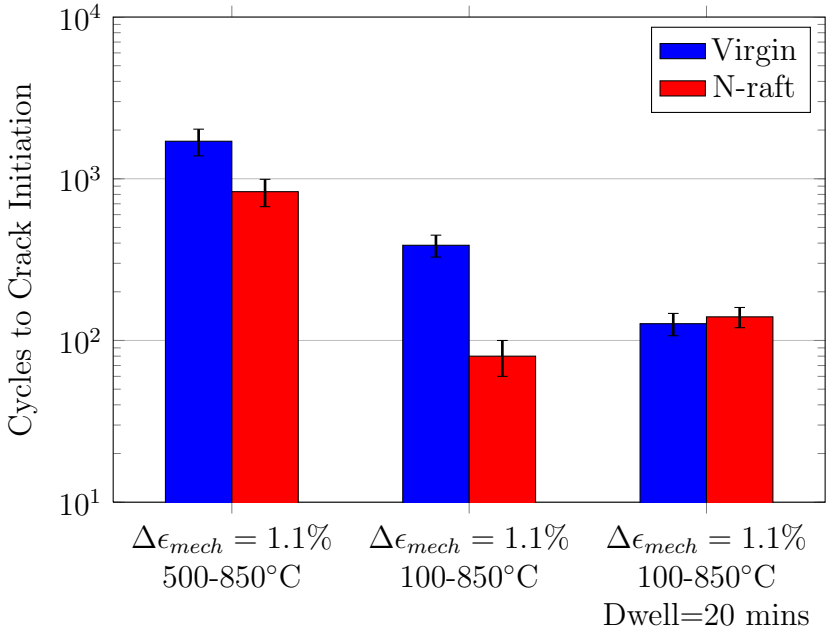

Figure 6.6: Life comparison between the N-raft and virgin microstructures in the L-orientation under IP TMF loading conditions for T_{max}=850°C.

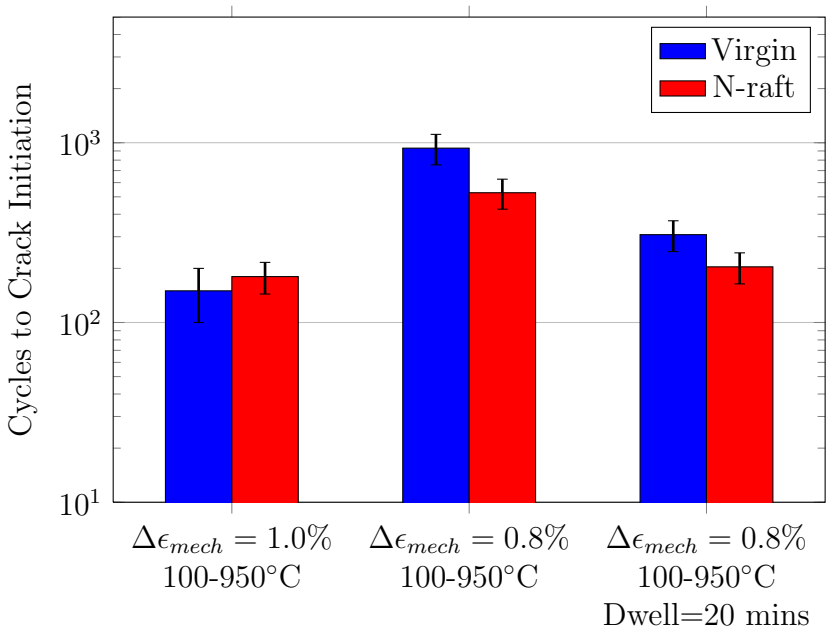

Figure 6.7: Life comparison between the N-raft and virgin microstructures in the L-orientation under IP TMF loading conditions for T_{max}=950°C.

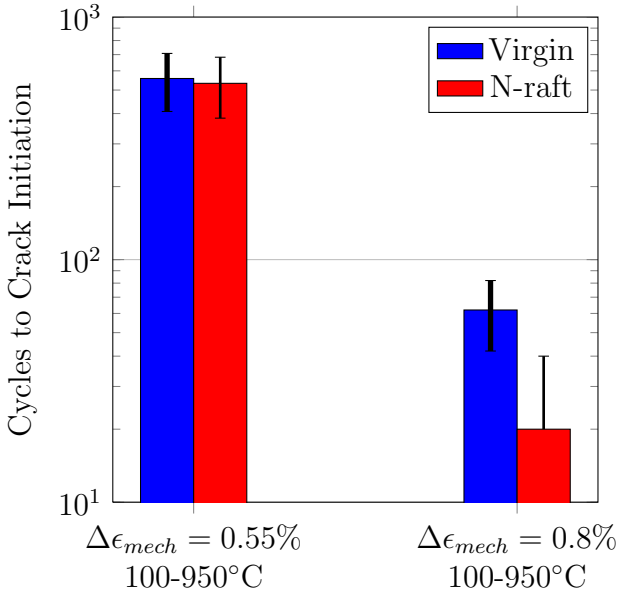

Figure 6.8: Life comparison between the N-raft and virgin microstructures in the T-orientation under IP TMF loading conditions.

.

With decreasing strain amplitudes, the N-raft microstructure exhibited similar behavior as that observed with the stress-free coarsened microstructure, in that the mean stresses of the CC TMF experiments did not relax to the extent exhibited by the virgin microstructure shown in Figure 6.9. The reduced relaxation of mean stress at T_{max} of 850°C and 950°C resulted in a 20% on average larger mean tensile stress. This can in-part be attributed to the decrease in the mean-free dislocation path between the γ' precipitates within the dendritic core. Similar experimental findings have been made on CMSX-4 and CMSX-6 single crystals given a pre-creep treatment [111].

In the case of CC TMF of the N-raft microstructure in the T-orientation, small variations ($\leq 5\%$) in both the mean stress and induced inelastic strains were observed as shown in Figure 6.10. However, these can most likely be attributed to the random secondary orientation of the grains.

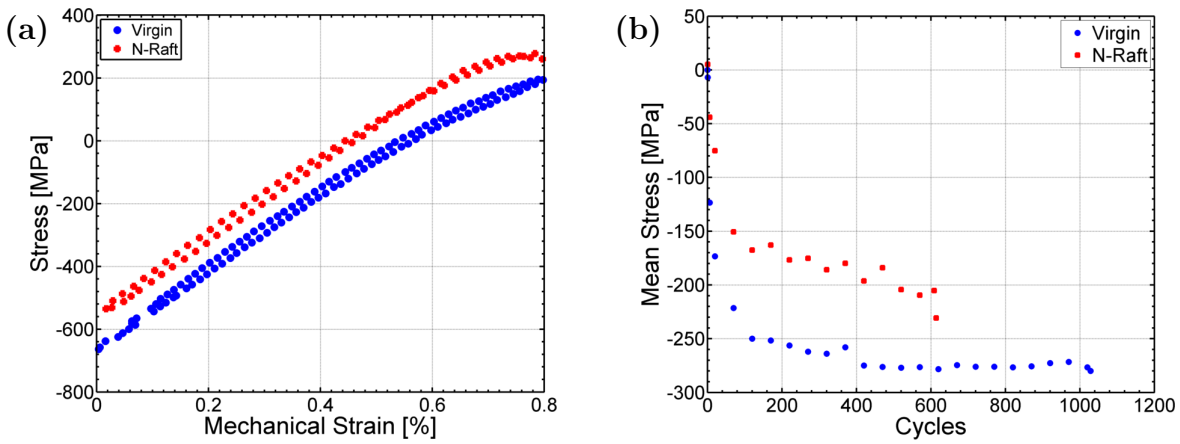

Figure 6.9: IP $R_\epsilon = 0$ TMF results for ΔT=100-950°C comparing the N-raft microstructure to the virgin under CC conditions in the L-orientation on the (a) Half-life hysteresis response (b) Mean stress evolution.

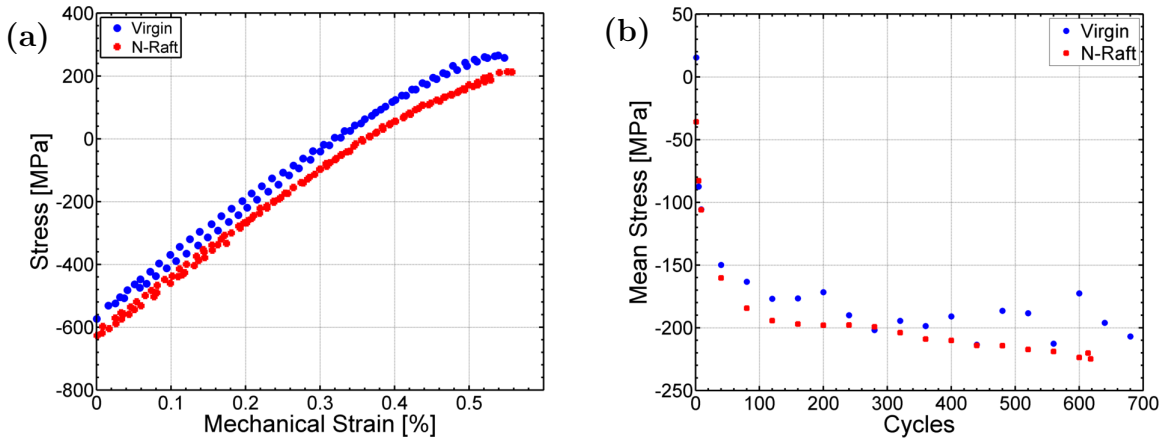

Figure 6.10: IP $R_\epsilon = 0$ TMF results for ΔT=100-950°C comparing the N-raft microstructure to the virgin under CC conditions in the T-orientation on the (a) Half-life hysteresis response (b) Mean stress evolution.

For the cases where the N-raft microstructure is tested under CF conditions, the mean stresses in the virgin material are observed to converge towards the stabilized mean stress of the N-raft microstructure as shown in Figure 6.11. For CF at a T_{max} of 950°C, the N-raft achieved stabilized hysteresis after 5% life, while the virgin microstructure stabilizes within 25% of the respective life value.

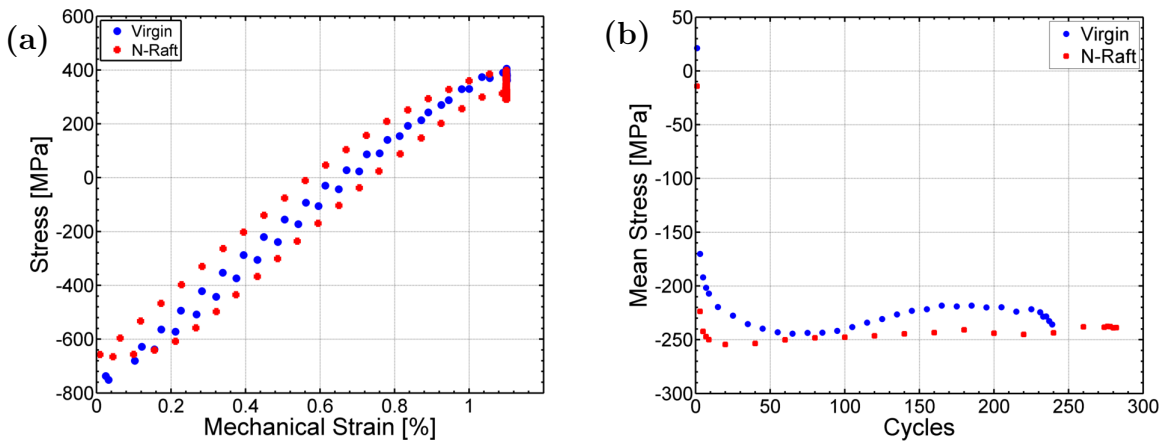

Figure 6.11: IP TMF results for ΔT=100-950°C comparing the N-raft microstructure to the virgin under CF conditions in the L-orientation on the (a) Half-life hysteresis response (b) Mean stress evolution.

A comparison of the macroscopic fatigue cracks for the virgin and N-raft microstructure are compared in Figure 6.12a. Fatigue cracks in the N-rafted specimens with a L-orientation behaved in a manner consistent with a macroscopic cube shear crack propagation mechanism even with a T_{max}=950°C, whereas the virgin microstructure allows for large scale fatigue crack propagation along the {111} planes. The N-raft microstructures indicates a crack propagation mechanism dependent on two factors: The primary component being the initiation of fatigue cracks emanating from debonded carbides as in the virgin material under IP TMF conditions as shown in Figure 6.13, followed by rapid fatigue crack propagation along the high dislocation density γ channels perpendicular to the applied load. A schematic that illustrates this mechanism is depcited in Figure 6.14. Similar findings have been reported for the GTD-111 and CMSX-4 amongst other Ni-base superalloys [48, 89, 134].

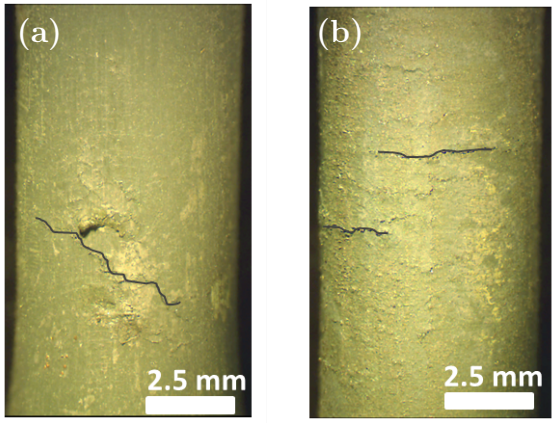

Figure 6.12: Comparison of the failed gage surfaces under IP $R_\epsilon = 0$ CC, ΔT =100-950°C, $\Delta\epsilon_{mech} = 0.8\%$ TMF conditions of (a) the virgin microstructure and (b) the N-raft microstructure. Note: The observable surface cracks were enhanced to distinguish from surface undulations in the oxide layer.

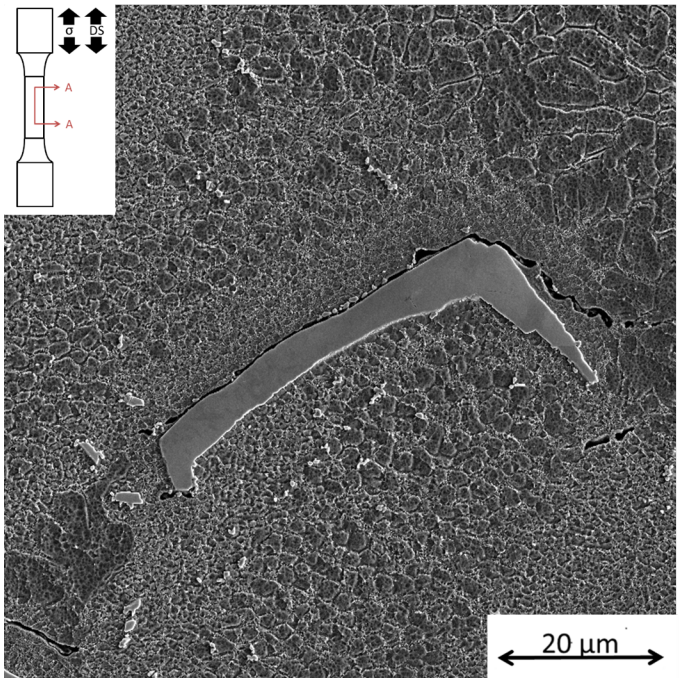

Figure 6.13: Debonded carbide in the N-raft microstructure with fatigue cracks emanating from the interface between the matrix and carbide. Test conditions for the specific case shown are IP CC TMF (ΔT =100-850° C $\Delta\epsilon_{mech} = 1.1\%$).

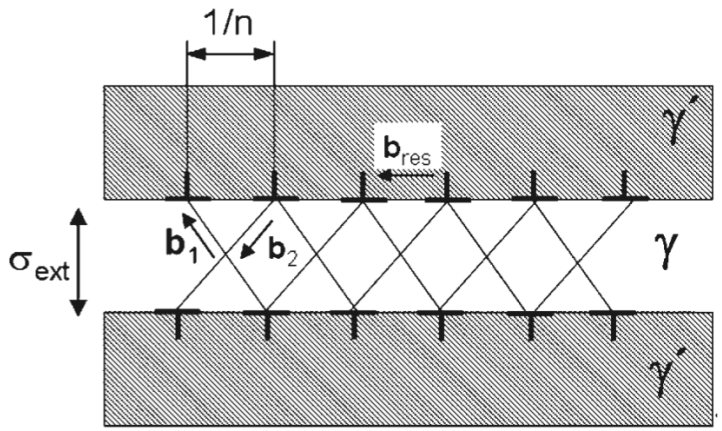

Figure 6.14: Glide of dislocations with Burgers vectors b_1 and b_2 between N-raft γ', where n is the lattice spacing and b_{res} is the resultant Burgers vector of b_1 and b_2 [135, 136].

Microstructural analysis revealed that the N-rafted material failed by a similar fatigue crack propagation mechanism as the virgin in the T-orientation. That is fatigue crack propagated via debonded carbides and the grain boundaries as shown in Figure 6.15.

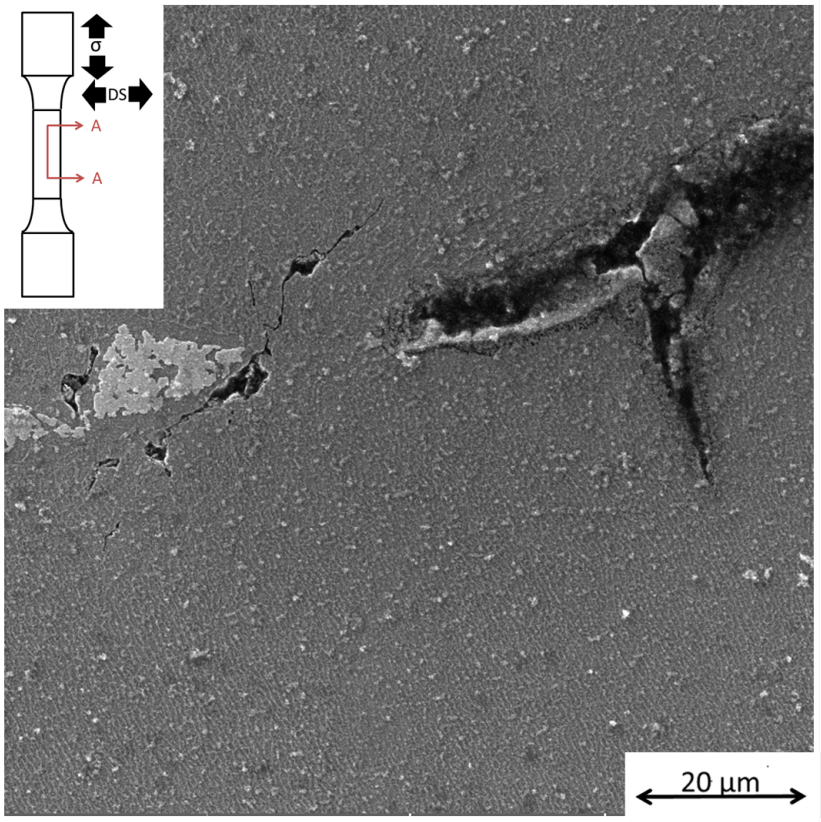

Figure 6.15: Propagation of fatigue crack in the N-raft microstructure in the T-orientation under IP $R_\epsilon = 0$ TMF ($\Delta T = 100 - 950$°C $\Delta\epsilon_{mech} = 0.55\%$).

6.3 P-raft

Within service components P-raft microstructures form in regions near the exterior surface which is exposed to the high temperature gases and as a result of constrains associated with the cooler material on the airfoil interior, OP, $R_\epsilon = -\infty$ TMF conditions arise. Based on the combination of thermal analysis and component analysis, the typical conditions where the P-raft microstructure is generated coincide with a maximum surface temperature of 950°C. As a result, all P-raft TMF experiments were conducted with a T_{max}=950°C under OP TMF loadings.

The influence of the P-raft microstructure in the L-orientation on OP TMF is shown in Figure 6.16. The P-raft microstructure in CC TMF conditions exhibited a 50% or greater reduction in life when compared to the virgin material for T_{min} of

both 100 and 500°C. However, with the introduction of a 20 minute compressive strain hold, the strain-life of the P-raft microstructure was found to increase 100% over that of the virgin microstructure. Further, the P-raft microstructure is less sensitive to CF conditions than the virgin microstructure, as the P-raft microstructure only experiences a 10% life reduction over the P-raft CC case with a T_{min}=100°C. This represents a significant improvement over that of the comparative virgin microstructure results in which case CF conditions resulted in a 80% life reduction.

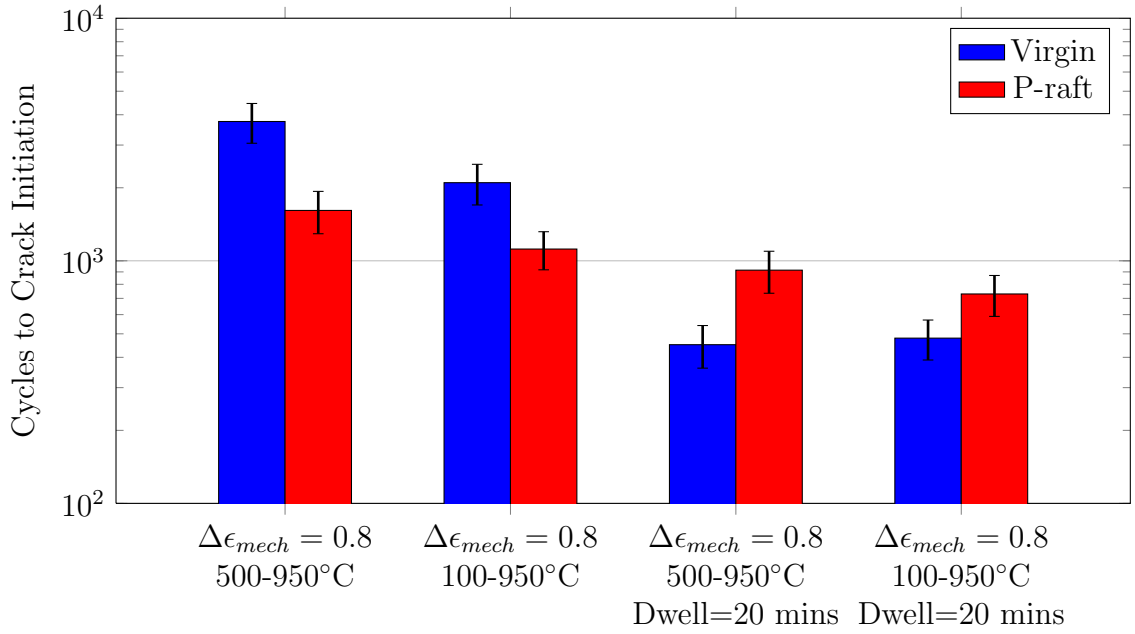

Figure 6.16: TMF life comparison between the P-raft and virgin microstructures in the L-orientation under OP TMF loading conditions.

For both CC and CF TMF, the positions of the hysteresis curves at half-life for specimens in the L-orientation stabilized at nearly identical positions in stress-strain space, as shown in Figure 6.17 and 6.18. In the case of the mean stress of the virgin microstructure under CF conditions, the mean stress initially increases before relaxing at a stabilized value by mid-life as shown in Figure 6.18. Coincidently, the stabilized value of the virgin mean stress is that of the P-raft microstructure. In the case of the P-raft microstructure the mean stress value was achieved within 2% of

life. Ultimately, the time over which the mean stress of the virgin CF experiments spends evolving corresponds to 70 hours of compressive creep exposure which from a kinetics view (Chapter 4) is sufficient to bring about a P-raft microstructure within the virgin material comparative to that of the artificially manufactured one as was shown in Figure 5.20.

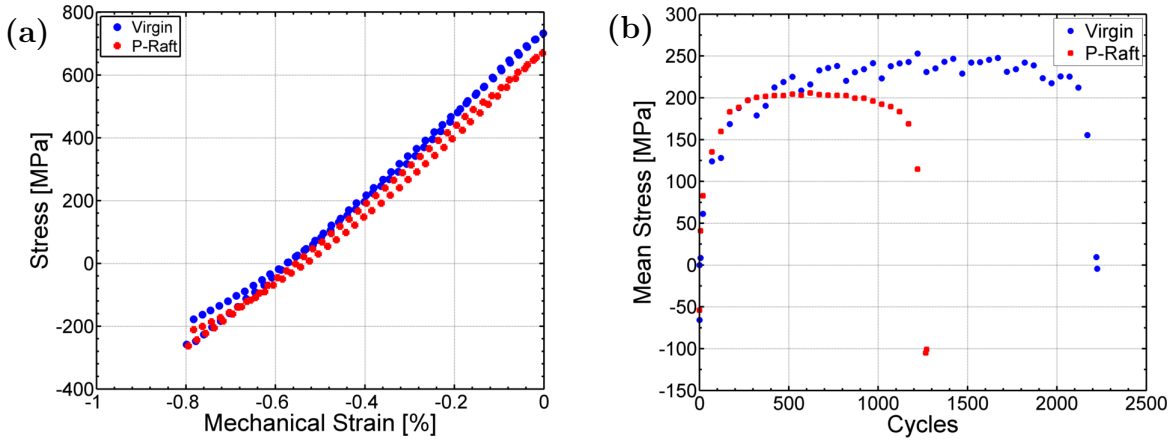

Figure 6.17: OP TMF results for ΔT=100-950°C comparing the P-raft microstructure to the virgin under CC conditions in the L-orientation on the (a) Half-life hysteresis response (b) Mean stress evolution.

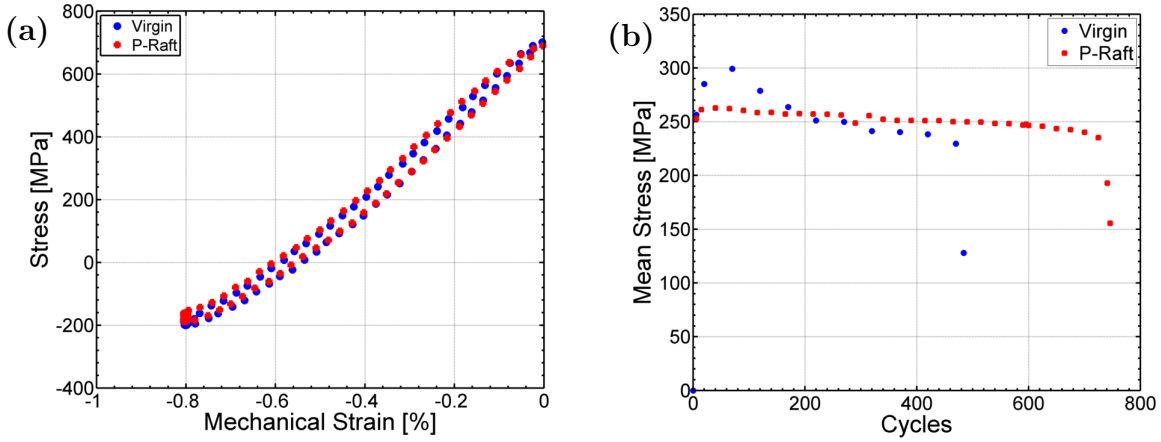

Figure 6.18: OP TMF results for ΔT=100-950°C comparing the P-raft microstructure to the virgin under CF conditions in the L-orientation on the (a) Half-life hysteresis response (b) Mean stress evolution.

Additionally, shown in Figure 6.19 are the P-raft strain-life results of the material

in the transverse orientation. In the T-orientation the CC P-raft life behavior was found to follow a similar trend as the L-orientation in a 80% life reduction for a T_{min} of 100°C and 500°C. Shown in Figure 6.20 is the half-life hysteresis behavior under CC TMF conditions. Under CF TMF conditions no distinguishable difference between the virgin and P-raft microstructures was apparent from the TMF life values. At this time, a complete set of conclusions on the effects of the P-raft microstructure in the T-orientation can not be made due to the lack of repeated experiments under identical conditions to separate the effects of the random secondary grain orientation from those of the P-raft microstructure.

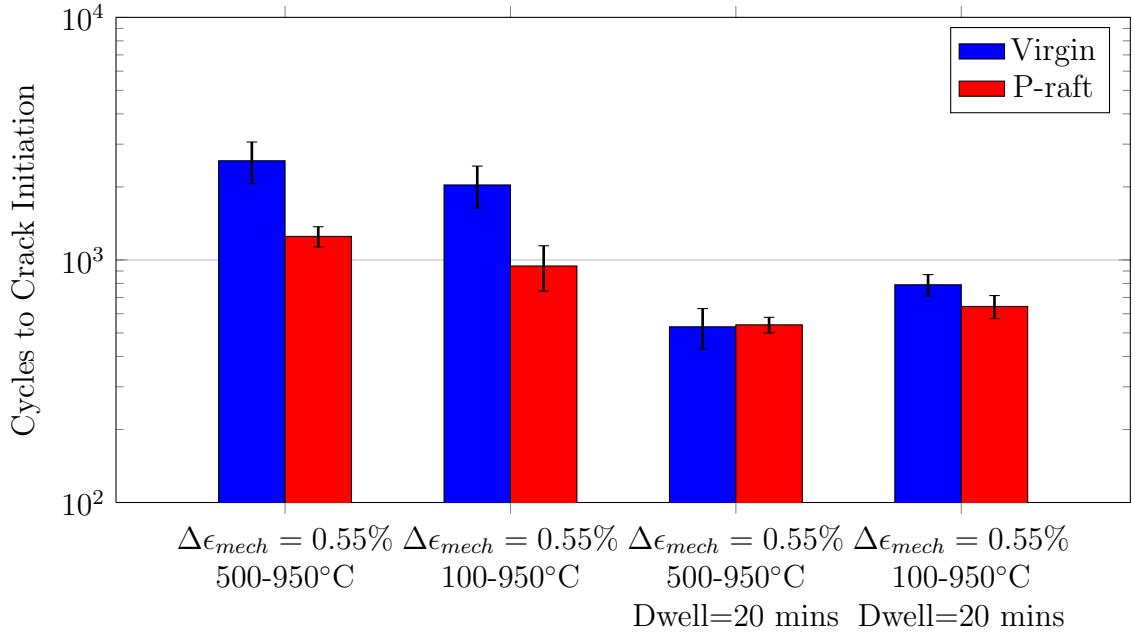

Figure 6.19: TMF life comparison between the P-raft and virgin microstructures in the T-orientation under OP TMF loading conditions.

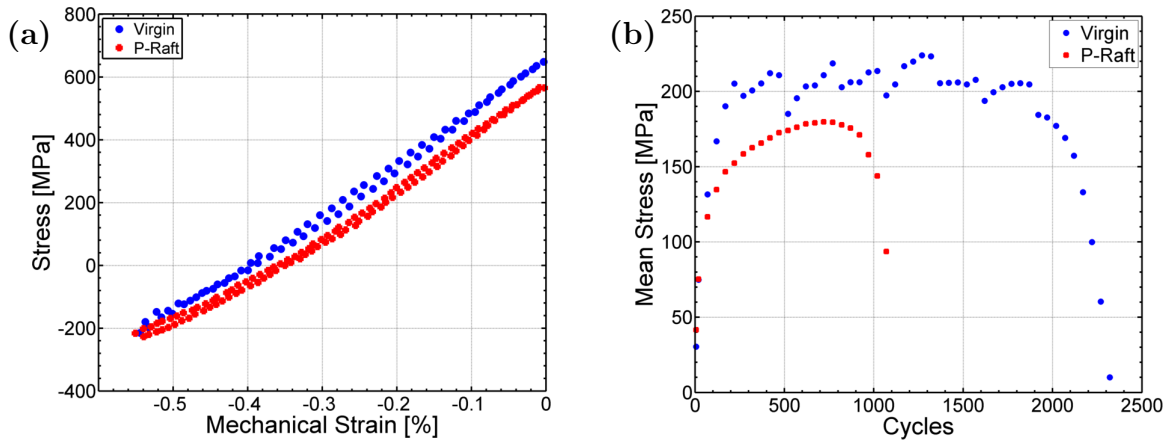

Figure 6.20: OP TMF results for ΔT=100-950°C comparing the N-raft microstructure to the virgin under CC conditions in the T-orientation on the (a) Half-life hysteresis response (b) Mean stress evolution.

The surfaces of the failed gage sections indicate, that failure in the P-raft microstructure is associated with limited damage within the microstructure in both the CC and CF cases as shown in Figure 6.21. In contrast, the surfaces of the virgin material in both the CC and CF cases can be observed to have sustained significant amounts of damage. Microscopic observation of cracks in the failed P-raft microstructures confirmed the observations from the gage surface, that primary failure of the material is associated with a single fatal fatigue crack originating from an oxidation spike along the interdendritic-dendritic boundary similar to the one shown in Figure 6.22. Further, once propagating along the interdendritic-dendritic boundary is no longer favorable, the fatigue crack is observed to change direction and propagate in a near vertical manner along the P-raft-γ channel interface within the dendritic matrix as shown in Figure 6.23.

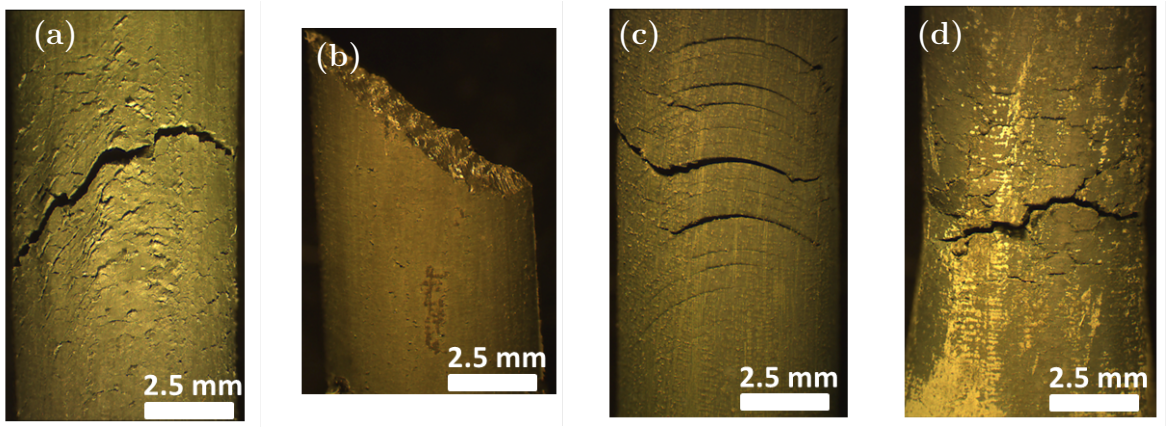

Figure 6.21: Failed gage section surfaces under OP TMF, ΔT =100-950°C, $\Delta\epsilon_{mech} = 0.8\%$ for (a) Virgin microstructure CC TMF (b) P-raft microstructure CC TMF (c) Virgin microstructure CF TMF (d) P-raft microstructure CF TMF.

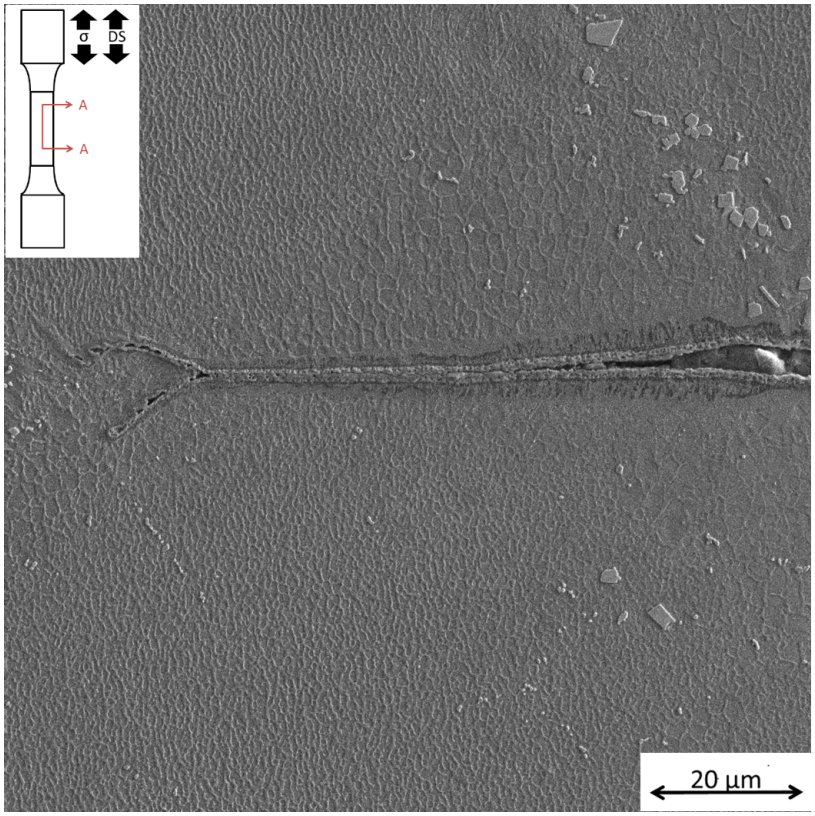

Figure 6.22: Crack propagation through an oxidation spike penetrating into a interdendritic region within the P-raft microstructure exposed to OP $R_\epsilon = -\infty$ TMF conditions (ΔT =100-950°C $\Delta\epsilon = 0.8\%$).

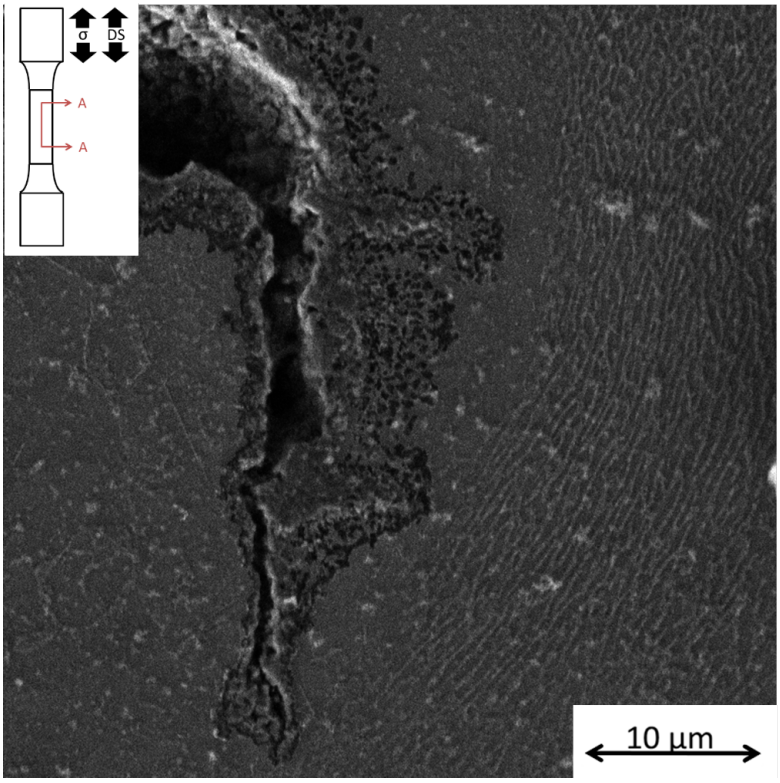

Figure 6.23: Vertical fatigue crack growth occurring within the P-raft microstructure exposed to OP $R_\epsilon = -\infty$ TMF conditions (ΔT =100-950°C $\Delta\epsilon = 0.8\%$).

CHAPTER VII

MICROSTRUCTURE SENSITIVE CONSTITUTIVE MODELING

The complexity of conditions that hot section service components are exposed to can not be captured directly laboratory experiments. As a result, constitutive models bridge the gap and provide component designers with estimates of service conditions. While most crystal viscoplasticity (CVP) models implicitly capture microstructure dependence through the material parameters, the microstructure morphology is typically assumed to remain constant. Attempts have been made at capturing microstructure evolution, but the softening effects the aged microstructure states have on Ni-base superalloys are not accounted for through the evolution of the model's material parameters. This Chapter presents the necessary adaptations and methodologies through which the effects of microstructure aging on the constitutive response can be captured within a temperature-dependent CVP model framework.

7.1 Crystal Viscoplasticity Model Description

The CVP model framework is developed around the assumption that the deformation gradients associated with elasticity, inelastic deformation, and thermal expansion can be decomposed through the tensor multiplicative rule [137–139],

$$\mathbf{F} = \mathbf{F}_{el} \cdot \mathbf{F}_{pl} \cdot \mathbf{F}_{\theta} \tag{7.1}$$

as depicted in Figure 7.1. The deformation gradient associated with thermal expansion is directly related to the coefficient of thermal expansion of the material through

the relation [139],

$$\mathbf{F}_{\theta}^{n+1} = \frac{1}{2}\left(exp\left(2\int_{T_o}^{T}\beta(x)dx\right)\right)\mathbf{F}_{\theta}^{n} \tag{7.2}$$

where, $\beta(T)$ is the coefficient of thermal expansion (CTE) of the material as a function of temperature, and $\mathbf{F}_{\theta}^{n}$ and $\mathbf{F}_{\theta}^{n+1}$ are the thermal strain deformation gradients and the beginning and end of a finite time step respectively.

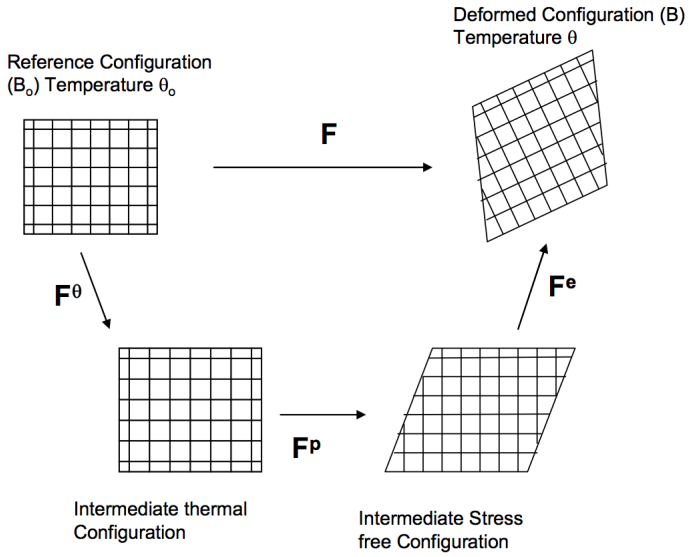

Figure 7.1: Multiplicative decomposition of the deformation gradient into elastic, plastic, and thermal components [137, 139, 140].

Within the CVP framework, all plastic deformation is assumed accountable through the inelastic shear on the individual slip planes within a crystal, which arises from the movement of dislocations on the slip systems. As a result, to uniquely define the plastic deformation, special relations must be introduced. To relate the plastic component of the deformation gradient with that of the cumulative inelastic shear strain rate, the following relation which arises from continuum mechanics arguments is used [141],

$$\boldsymbol{L}_p = \dot{\boldsymbol{F}}_p\boldsymbol{F}_p^{-1} = \sum_{\alpha=1}^{N_{slip}}\dot{\gamma}^{\alpha}\left(\boldsymbol{s}_o^{\alpha}\otimes\boldsymbol{m}_o^{\alpha}\right) \tag{7.3}$$

where $\boldsymbol{L}_p$ is the material time derivative of $\boldsymbol{F}_p$, and $\boldsymbol{F}_p^{-1}$ is the inverse of $\boldsymbol{F}_p$ and $\boldsymbol{s}_o^\alpha$ is a unit vector in the slip direction, $\boldsymbol{m}_o^\alpha$ is a unit vector in the direction normal to the slip plane, α is a slip system, and $\dot{\gamma}^\alpha$ is the inelastic shear strain rate on slip system α and N_{slip} is the number of slip systems. In the case of Ni-base superalloys, a homogenized face centered cubic structure of twelve octahedral $\{111\}\langle 110\rangle$, and six cubic $\{100\}\langle 110\rangle$ slip systems is assumed, with cubic slip systems only activated above 750°C [142].

The rate of inelastic shear strain on each slip system is calculated by [143],

$$\dot{\gamma}^\alpha = \dot{\gamma}_o \Theta(T) \left\langle \frac{\tau_v^\alpha}{D^\alpha} \right\rangle^{n_1} exp\left\{ B_o \left\langle \frac{\tau_v^\alpha}{D^\alpha} \right\rangle^{n_2} \right\} sgn\left(\tau^\alpha - \chi^\alpha\right) \tag{7.4}$$

which is a power law multiplying an exponential term. The rationale for the two terms is that the power law term captures the creep regime while the exponential captures the rate insensitive regime of the deformation [144]. The inelastic shear strain only becomes active when the viscous overstress,

$$\tau_v^\alpha = |\tau^\alpha - \chi^\alpha| - \kappa^\alpha \frac{\mu}{\mu_o} \tag{7.5}$$

is positive, otherwise the Macaulay brackets, $\langle\ \rangle$ keeps the flow rule turned off. In the above, χ^α is the back stress and κ^α is the threshold stress on the α slip system. The drag stress, D^α, is a measure of the flow potential of the material and effectively accounts for the component of flow resistance than can be overcome by thermal fluctuation. The reference inelastic shear strain rate, $\dot{\gamma}_o$ is related to the maximum strain rate associated with the limit on dislocation velocity. The rate insensitive regime is set by B_o and n_2 collectively, while the rate sensitive or creep regime is determined by n_1. The temperature-dependent diffusivity Arrhenius like function, $\Theta(T)$ is is defined later.

The drag stress, D^α, is assumed to scale with the shear modulus μ,

$$D^\alpha = D_o \frac{\mu}{\mu_o} \tag{7.6}$$

where μ_o is the shear modulus at 0°K. The back stress evolution equation is a Frederick-Armstrong relation with modifications to account for temperature changes [143],

$$\dot{\chi}^\alpha = h_\chi |\dot{\gamma^\alpha}| - h_{\chi d} |\dot{\gamma}^\alpha| \chi^\alpha + \left(\frac{1}{R_\chi} \frac{\partial R_\chi}{\partial T} + \frac{1}{h_\chi} \frac{\partial h_{\chi d}}{\partial T} \right) \chi^\alpha \dot{T} - h_{\chi s} \Theta_{\chi s} |\chi^\alpha|^{r_{\chi s}} \chi^\alpha \tag{7.7}$$

The back stress is associated with the evolution of the dislocation structure within the material and has a temperature rate term to allow for consistency in temperature-dependent loadings [145]. The first term, represents hardening due to dislocations piling up on obstacles while the second captures the dynamic recovery, which is the reduction in dislocation density due to annihilation of dislocations of opposite sign. As a note, $R_\chi = \frac{h_\chi}{h_{\chi d}}$ represents the saturated value of the back stress. The third term, accounts for the evolution of the back stress due to changes in temperature and the last term accounts for the static thermal recovery of the back stress during creep like loadings, which is important for long-term dwells.

The threshold stress is composed of rate-independent and rate-dependent components,

$$\kappa^\alpha = \kappa_c^\alpha + \kappa_e^\alpha \tag{7.8}$$

The rate-independent portion of the threshold stress is given by [146],

$$\kappa_c^\alpha = \kappa_o(T) + h_{pe} \tau_{pe}^\alpha + h_{se} \tau_{se}^\alpha + h_{cb} |\tau_{cb}^\alpha| \tag{7.9}$$

where κ_o captures the temperature-dependent resistance to dislocation movement. The last three terms of Equation 7.9 capture the non−Schmid effects that result

in an increased resistance of dislocation movement through the γ' precipitates prior to dislocation looping, with the strongest effects occurring in the neighborhood of 750°C [147]. Additionally, the functional form of Equation 7.9 captures the anomalous increase in yield strength as temperature is increased [146, 148, 149]. The κ_e^α term in Equation 7.8 evolves according to a competition between dislocation storage, h_κ, rearrangement, $h_{\kappa d}$, and annihilation mechanisms, $h_{\kappa s}$,

$$\dot{k}_e^\alpha = h_k \Sigma q^{\alpha\beta} |\dot{\gamma}^\beta| - h_{kd} k_e^\alpha \Sigma |\dot{\gamma}^\beta| - h_{ks} \Theta k_e^\alpha \tag{7.10}$$

Lastly the diffusivity parameter in Equation 7.4 and 7.10 is defined,

$$\Theta(T) = \begin{cases} exp\left(-\frac{Q_o}{RT}\right) .....T \geq \frac{T_m}{2} \\ exp\left(-\frac{2Q_o}{RT_m}\left[ln\left(\frac{T_m}{2T}+1\right]\right)\right) .....T \leq \frac{T_m}{2} \end{cases} \tag{7.11}$$

where Q_o is the activation energy for thermally activated dislocation bypass of obstacles and linked to the self diffusion of nickel in the alloy, R is the universal gas constant, and T_m is the absolute melting temperature of the alloy.

7.2 Microstructure Sensitive Adaptations

7.2.1 Microstructure Sensitive Material Parameters

In capturing the influence of aging on the mechanical response of a Ni-base superalloy, parameters in the CVP model require extension to microstructure-sensitivity. Specifically, in calibrating the CVP model for the aged microstructure, the material parameters κ_o in the threshold stress (Equation 7.9) and R_χ and h_χ in the backstress evolution (Equation 7.7)were found to be most sensitive to the aged microstructure states and were the material parameters used to capture the effects of aging on the constitutive response in this work. In full generality, the definition of a microstructure-sensitive parameter at a given material point requires knowledge of the temperature,

volume fraction of each phase, the compositions of each of the phases and a geometric measure of the morphology of each of the phases. In mathematical terms the generic microstructure-sensitive material parameter in the CVP model can be given by,

$$A = A(T, V_f(T), M_i(T, c_i^{\beta})) \tag{7.12}$$

where $V_f(T)$ is the temperature dependent volume fraction of phase i, M the geometric measure of the morphology of phase i, and c_i^{β} the composition of elemental species β in phase i at a given material point. While providing the necessary information to fully describe the material parameters is feasible for binary and ternary systems, the requirements for industrial alloys is highly complex and simplifying assumptions must to be made.

In implementing microstructure-sensitivity in the CVP model for Ni-base superalloys with the objective of describing the influence of directional coarsening, the following assumptions are made about the microstructure:

1) The $\gamma - \gamma'$ volume fraction remains constant throughout thermomechanical exposure of the models calibration range. This being reasonable with only a 10% error over the 20-1050°C temperature range [150].

2) Only the γ and γ' control the mechanical behavior of the material. In modern Ni-base superalloys, $\approx 98\%$ of the alloy's volume fraction is either γ or γ'.

3) The chemical composition of each of the phases is assumed uniform throughout, such that the dendritic and interdendritic regions are chemically identical.

4) The morphology of the $\gamma - \gamma'$ microstructure is representable by an idealized cuboidal morphology.

As a result of these assumptions, the generic microstructure-sensitive material parameter is reduced to $A = A(T, M(T))$. In developing a mathematical definition

for M, a representative geometric microstructure morphology is adopted. In the case of modern cast Ni-base superalloys, the $\gamma - \gamma'$ microstructure can be idealized by the cuboidal unit cell as shown in Figure 4.12. The secondary γ', located in the γ channels between the primary γ', in cast Ni-base superalloys are often short lived once the microstructure begins to undergo thermomechanical exposure [19] and are ignored in this construction.

From this idealized microstructure, the geometric measures can be associated with the lengths of the γ' cuboid sides and the widths of the γ channels separating γ' cuboids from one another. In the initial as heat treated configuration, the widths of all γ channels are assumed equivalent, i.e. $w^o_{[001]} = w^o_{[100]} = w^o_{[010]}$. Further, the γ' precipitates are assumed to be initially perfect cubes, with an initial cube length of L_o.

As has been discussed in Chapter 4, the periodicity and changes in both the γ channels and γ' precipitate size are linked to one another through the evolution kinetics of the microstructure. While there are six direct measures that characterize the $\gamma - \gamma'$ microstructure, three being the side lengths of the γ' precipitate cuboids, and the other three being the width of the γ channels in each of the crystallographic directions, only two measures from each of the phases is required to uniquely define the microstructure state. This is based on the kinetic linkages of between all the microstructural dimensions. Further, because of the geometric relationships the dimensions share in the periodic cell, only two dimensions are required for uniquely determining the value of a microstructure-sensitive parameter.

In this work, the measure of the γ channel widths in the [001] and [100] orientations or $h_{[001]}$ and $h_{[100]}$ are used. The directions following the definitions as shown in Figure 4.12. The evolution of aging is characterized by the dimensionless γ channel widths,

$$\eta = \frac{h_{[001]} - h^o_{[001]}}{h^o_{[001]}} \tag{7.13}$$

and

$$\zeta = \frac{h_{[100]} - h^o_{[100]}}{h^o_{[100]}} \tag{7.14}$$

where, $h^o_{[001]}$ and $h^o_{[100]}$ are the initial widths of the γ channels in the [001] and [100] crystallographic reference frame. And $h_{[001]}$ and $h_{[100]}$ are the widths of the γ channels in the [001] and [100] crystallographic directions at some time t after thermomechanical exposure. In the case of N-rafts, the expectation is that the γ channel increases in width in the [001] direction and contract in the [100] direction, hence $\eta > \zeta$. Likewise, for P-rafts the γ channel to increase in width in the [001] direction, $\zeta > \eta$ as shown in Figure 4.12. For stress-free coarsening $\eta = \zeta > 1$. Arising from the above definitions, the generic microstructure function M can now be replaced by η and ζ to define the generic material parameter as

$$A = A(T, \zeta, \eta) \tag{7.15}$$

where the variables follow the definitions given previously.

To define the virgin material parameters in the CVP model, temperature dependent polynomials were used. This was initially done by Shenoy et al. [142] to ensure the uniqueness and smoothness of the material parameter values and their associated derivatives. In expanding the mathematical functions that describe the material parameters to three variables, T, η, and ζ, polynomials will be used. Polynomials still offer the greatest flexibility and ease for implementation. In further describing the generic material parameter, a multiplicative polynomial decomposition given by,

$$A(T, \eta, \zeta) = A_T(T) A_\eta(T, \eta) A_\zeta(T, \zeta) \tag{7.16}$$

is proposed. The temperature dependent functions A_T, A_η, and A_ζ are polynomial functions of a single variable. The benefit of the multiplicative form is ease by which differentiation via the chain rule can be carried out.

In the specific cases of R_χ and h_χ the temperature-dependent derivatives are required for the back stress evolution equation. Using R_χ as an example, Equation 7.16 becomes,

$$R_\chi(T,\eta,\zeta) = R_T(T)R_\eta(T,\eta)R_\zeta(T,\zeta) \tag{7.17}$$

Applying the chain rule, the temperature-dependent derivative of R_χ is given by,

$$\frac{\partial R_\chi}{\partial T} = \frac{\partial R_T}{\partial T}R_\eta R_\zeta + \frac{\partial R_\eta}{\partial T}R_T R_\zeta + \frac{\partial R_\zeta}{\partial T}R_T R_\eta \tag{7.18}$$

Assuming that the functions R_η and R_ζ are continuously decreasing functions of the form,

$$R_\eta = 1 - c_\eta(T)\eta \tag{7.19}$$

and

$$R_\zeta = 1 - c_\zeta(T)\zeta \tag{7.20}$$

which accounts for the softening of the material during aging [107], where $c_\eta(T)$ is the temperature dependent polynomial associated with, the partial derivatives $\frac{\partial R_\eta}{\partial T}$ and $\frac{\partial R_\zeta}{\partial T}$ can further be expressed as,

$$\frac{\partial R_\eta}{\partial T} = -\frac{\partial c_\eta(T)}{\partial T}\eta \tag{7.21}$$

and

$$\frac{\partial R_\zeta}{\partial T} = -\frac{\partial c_\zeta(T)}{\partial T}\zeta \tag{7.22}$$

After substitution of the derivatives, Equation 7.18 becomes,

$$\frac{\partial R_\chi}{\partial T} = \frac{\partial R_T}{\partial T}R_\eta R_\zeta - \frac{\partial c_\zeta(T)}{\partial T}\zeta R_T R_\eta - \frac{\partial c_\eta(T)}{\partial T}\eta R_T R_\zeta \tag{7.23}$$

7.2.2 Backstress Evolution Equation Modifications

The CVP model as implemented by Shenoy et al. [142], was developed with the intent of capturing the as-heat treated constitutive response. In the as-heat treated state, the internal misfit stresses within the $\gamma - \gamma'$ microstructure are initially equivalent throughout [111]. However, with the occurrence of aging in the $\gamma - \gamma'$ microstructure, select components of the internal misfit stresses begin to relax, while others increase. In terms of the cyclic constitutive response, aging results in a reduction in the stress at which the material begins to yield. This can most likely be attributed with the manner in which dislocations selectively conglomerate on the $\gamma - \gamma'$ interfaces in the aged state [111]. Through modification of the back stress this aging effect can be captured,

$$\dot{\chi}^{\alpha} = h_{\chi}|\dot{\gamma^{\alpha}}| - h_{\chi d}|\dot{\gamma}^{\alpha}|\chi^{\alpha} + \left(\frac{1}{R_{\chi}}\frac{\partial R_{\chi}}{\partial T} + \frac{1}{h_{\chi}}\frac{\partial h_{\chi d}}{\partial T}\right)\chi^{\alpha}\dot{T} - h_{\chi s}\Theta_{\chi s}|\chi^{\alpha}|^{r_{\chi s}}\chi^{\alpha} + h_{ms}sgn(\chi^{\alpha})|\chi^{\alpha}|^{a} \quad (7.24)$$

The back stress evolution equation differs from that of the one in Equation 7.7 through the addition of the term $h_{ms}sgn(\chi^{\alpha})|\dot{\gamma}^{\alpha}||\chi^{\alpha}|^{a}$. This term can be considered similar to ones used to capture internal stress effects associated with dislocation pileups, bowed segments, and curved subgrain boundaries in braze alloys [151]. While this parameters is capable of capturing the effect of the internal misfit stresses under isothermal conditions, the temperature and rate dependence cause the parameter to become numerically unstable. As a result, the parameter was not used further in this work.

7.3 Crystal Viscoplasticity Model Implementation

The CVP model utilized in this work is an adapted version of the CVP model implemented as an ABAQUS User MATerial (UMAT) subroutine in the Fortran programming language by McGinty [152] and modified by Shenoy [142, 153] for the DS Ni-base superalloy GTD-111. The continuum equations used in the implementation are described by hyperelastic formulation was used, valid for small strains, i.e less than 5%.

Implicit Newton-Raphson solvers are more difficult to implement than explicit, however the implicit solutions are generally more accurate and stable [154]. A downside in solving crystal plasticity equations with the implicit method is that the solution may be slow to converge. To overcome this, a line search algorithm that subincrements the time step is used. This is discussed elsewhere [152, 155]. This method is more robust than the explicit method since it, in theory, can take very large steps in time and strain and still converge to an accurate solution. The accuracy of the method however increases the computational demands over the other methods.

Generally speaking, there are five different starting points for the implicit method, which uses a predictor-corrector scheme where a prediction of the stress required to obtain a particular strain is generated [156]. These are shown in Figure 7.2 which also shows the order of updating the prediction. The symbol $\mathbf{S}$ in this case represents the second Piola-Kirchoff stress. The Piola-Kirchoff stress can be found from the Cauchy stress, $\boldsymbol{\sigma}$ by,

$$\mathbf{S} = \mathbf{J} \cdot \mathbf{F}^{-1} \cdot \boldsymbol{\sigma} \cdot \mathbf{F}^{-T} \tag{7.25}$$

where $\mathbf{J}$ is the Jacobian, $\mathbf{F}^{-1}$ is the inverse of $\mathbf{F}$, and $\mathbf{F}^{-T}$ is the transpose of $\mathbf{F}^{-1}$. The most common starting points are $\mathbf{F}_e$, $\mathbf{F}_p$, $\mathbf{S}$, or $\dot{\gamma}^{\alpha}$, and should result in identical solutions. However in choosing a starting point one must consider that the Jacobian matrix will need to be inverted when using the Newton-Raphson method, and that

the equations may be more or less difficult to evaluate. However starting with $\dot{\gamma}^{\alpha}$ produces much better stability since there are small variations in stress associated with variations in $\dot{\gamma}^{\alpha}$ as it gets larger. The inverse is true for the other three, which results in less stability [156].

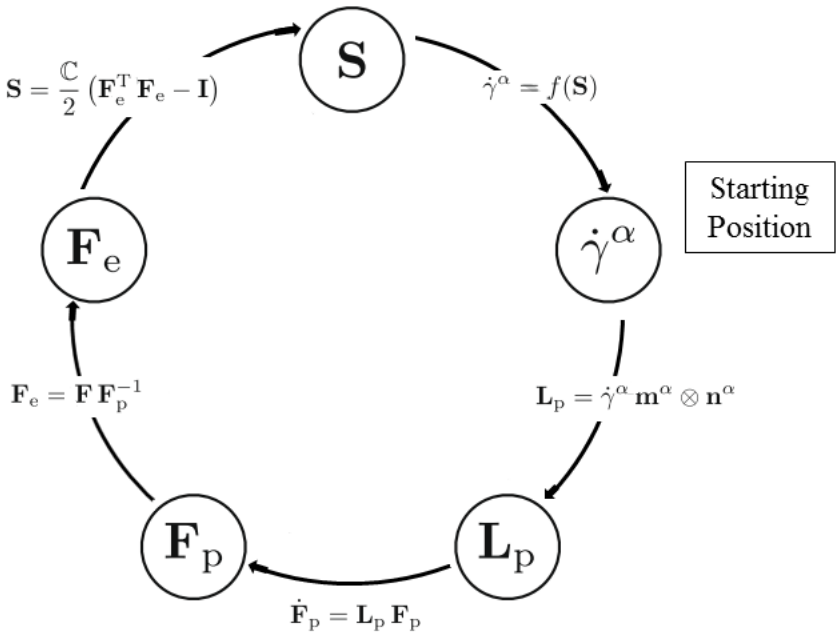

Figure 7.2: CVP model implementation adapted from [156].

7.3.1 Intergranular Interactions

In capturing the interactions between multiple grains within a polycrystal, the grains can be modeled explicitly with finite elements or implicitly at each integration point through averaging techniques such as the Sachs or Taylor averaging methods [157,158]. The Taylor constraint assumes that the deformation gradient experienced by each grain is the same as depicted in Figure 7.3. Within the CVP model framework the Taylor approach captures the aggregate Cauchy stress through averaging,

$$\bar{\boldsymbol{\sigma}} = \sum_{k=1}^{N} v^{(k)} \boldsymbol{\sigma}^{(k)} \tag{7.26}$$

where, $\boldsymbol{\sigma}^{(k)}$ denotes the Cauchy stress acting on each grain and $v^{(k)}$ is the volume fraction of each grain [159]. When all the grains have equal volume, the averaged stress, $\bar{\sigma}$, is given as

$$\bar{\boldsymbol{\sigma}} = \frac{1}{N}\sum_{k=1}^{N}\boldsymbol{\sigma}^{(k)} \tag{7.27}$$

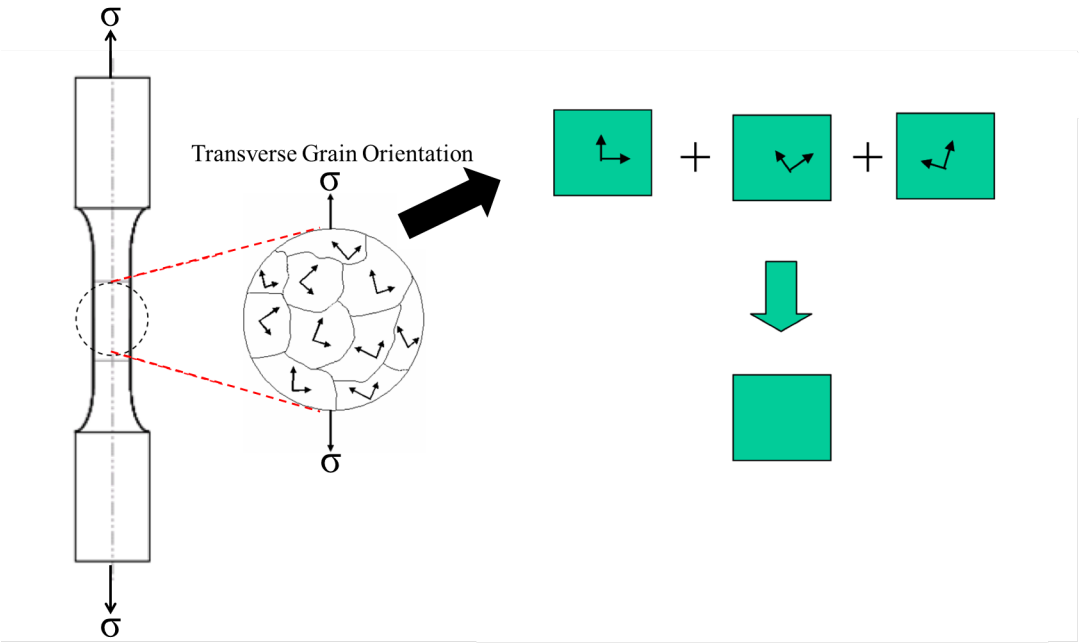

Figure 7.3: Taylor averaging method used within the CVP model to predict off-axis responses of DS materials and polycrystals.

Under cyclic loading, lattice rotation may be insignificant, but in the presence of creep or cyclic ratcheting, lattice rotation may build up at sites of stress concentration such as grain boundaries. For the purposes of material parameter calibration, the effect of creep and strain ratcheting are minimal in the calibration experiment. The cubic material parameters are assumed active under transverse loading conditions and are calibrated through utilizing the Taylor averaging option with a single element. As will be discussed later, this approach is convenient for obtaining a first order approximation of smooth bar results in that a single element can be used. The use of the Taylor averaging shown must be used judiciously as the Taylor method is known

to over predict the degree of texture [160, 161]. However, the Taylor method is still simpler than explicitly modeling each grain individually.

7.4 Material Parameter Determination

7.4.1 CVP Model Calibration Experiments

For the accurate calibration of a temperature dependent and microstructure-sensitive CVP model, there exists a minimum amount of data. Table 7.1 summarizes the experimental data requirements for an accurate, complete, microstructure-sensitive, temperature-dependent calibration of the CVP model, for the simulation of a stable cyclic hysteresis. Of the requirements, the experimental results used for determining the elastic constants and the CTE, β can be considered microstructure independent, as these are primarily controlled by the chemistry of the Ni-base superalloy. To simulate a generic microstructure state, a set of experimental data from each of the distinct microstructure morphologies, as-heat treated, stress-free coarsened, N-raft, and P-raft is required.

Table 7.1: Experimental data requirements for complete calibration of the CVP model.

Requirement	Reason
Elastic modulus in three directions	Calibration of the stiffness constants, C_{11}, C_{12}, C_{44}
Thermal strain vs. temperature	Calibration of the CTE
Minimum four distinct microstructure morphologies	Calibration of microstructure-sensitive parameters
Multiple material directions per microstructure	Calibration of octahedral and cubic slip parameters
Large plastic strain range in cyclic response	Calibration of internal state variable evolution
Stabilized hysteresis	Evolution of internal state variables
Minimum of six temperatures per microstructure	Temperature-dependent polynomial creation
Minimum of three strain rates at each temperature	Calibration of the strain rate dependent parameters

The need for experimental data from multiple crystallographic directions allows for the calibration of both the octahedral and cubic material parameters. In addition off-axis experimental data allows for determining the asymmetry of the elastic constants. Through selectively choosing the material tested material orientations, the activation of desired slip systems for easier calibration results. Suggested testing directions for

SX and DS Ni-base superalloys are presented in Tables 7.2-7.3, respectively.

Table 7.2: Active slip systems in SX Ni-base superalloy based on crystallographic orientation.

Direction	Reason
[0 0 1]	8 octahedral slip systems active
[0 1 1]	4 octahedral slip systems active, 4 cubic slip systems mildly active
[1 1 1]	6 octahedral and 3 cubic slip systems active
[1 2 3]	Single slip system active

Table 7.3: Active slip systems in DS Ni-base superalloy based on crystallographic orientation.

Direction	Reason
L	Only octahedral slip systems active
T	Both octahedral and cubic slip systems active
45	Both octahedral and cubic slip systems active

Concerning the cyclic behavior, capturing a significant amount of plasticity in addition to the stabilized hysteresis at a given isothermal temperature is crucial for the calibration of the CVP model. A significant amount of plasticity is required to properly capture the saturated state of the material. Typically low cycle fatigue tests used in the fatigue life prediction of Ni-base superalloys contain inelastic strain ranges less than 0.2%; such small plastic strain ranges contain insufficient information on the evolution of the internal state variables. To ensure capture of the material's saturated state, a minimum inelastic strain range of 0.4% was used.

Ni-base superalloys are rate dependent at 750°C and above, and therefore multiple strain rates are required in the calibration dataset. At these temperatures a minimum of three strain rates spanning three orders of magnitude are required to accurately predict the strain rate dependence of a Ni-base superalloy. While below 750°C, Ni-base superalloys are strain rate insensitive and only a single strain rate is required to determine the deformation response.

Table 7.4: CVP model isothermal calibration experiments.

Material Oirentation	Hold Time [min]	Strain Range [%]	Temperature [°C]
L	—	2.0	20
L	—	2.4	650
L	90	2.4	750
L	90	2.0	850
L	90	2.0	950
L	90	2.0	1050
T	90	1.6	750
T	90	1.4	950

To obtain the necessary temperature information while minimizing the number of calibration experiments at an isothermal temperature, a test profile was developed as shown in Figure 7.4. Within the efficient calibration experiment are blocks of five cycles at strain rates 10^{-2} and $10^{-3}\frac{1}{s}$ respectively, followed by a single compressive strain hold closing with a creep-fatigue interaction cycle at a strain rate of $10^{-4}\frac{1}{s}$. Within the strain rate sensitive temperature regime (T $\geq$ 750°C), most Ni-base superalloys become cyclically stable within a short period, as such five cycles are deemed sufficient to capture the stable response at a given strain rate [162]. For temperatures below 750°C where Ni-base superalloys are rate independent, conducting the experiment at a constant strain rate ($10^{-2}\frac{1}{s}$) until a stabilized hysteresis is obtained is acceptable. With the given strain ranges, this typically occurs within the first few hundred cycles. Overall, each isothermal calibration experiment requires approximately six hours of machine time, making the experiments highly efficient from a test system usage.

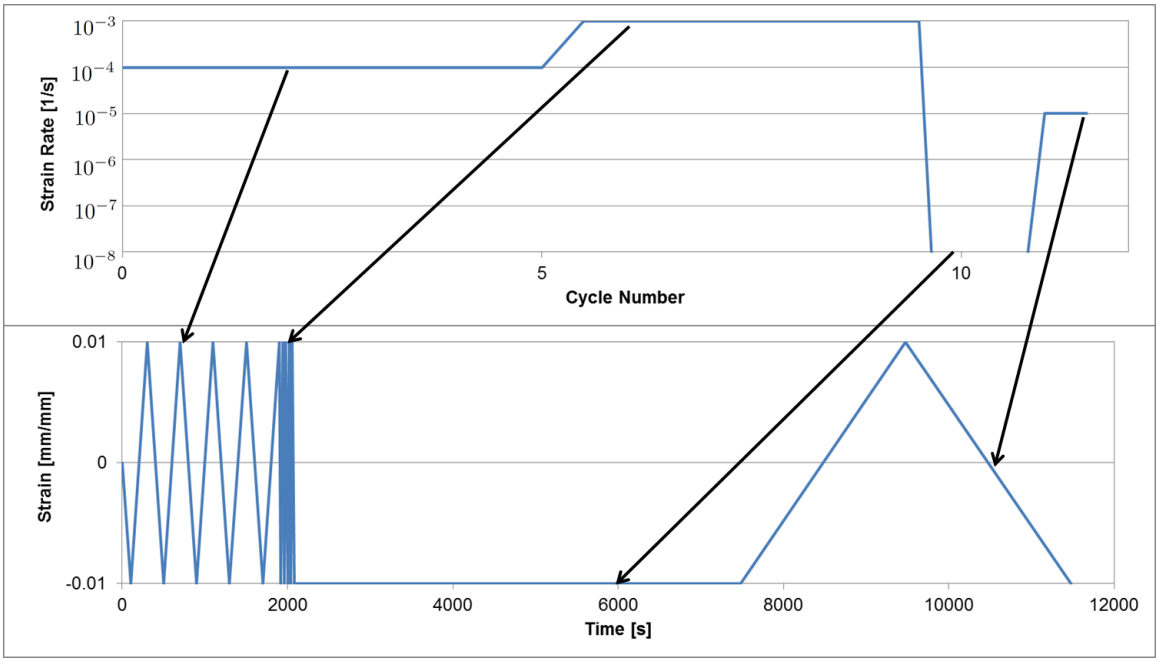

Figure 7.4: Strain history for efficient calibration experiment in the strain rate sensitive regime.

7.4.2 Single Element RVE

For smooth bar specimens like the one shown in Figure 3.2, a single element model is sufficient to model the macroscopic anisotropic response. The simulations are performed in displacement control, which effectively simulates uniaxial mechanical strain-controlled experiments. A single quadratic C3D8 brick element is utilized under the assumption that four-fold symmetry is applicable within the gage section. The boundary conditions applied to this single element are such that four-fold symmetry is assumed to exist within the gauge section as shown in Figure 7.5 where the arrows indicate the degree of freedom(s) that exist at each node. To simulate loading of the material, the top surface is displaced. When simulating the off-axis response of the material, a single element is still used in conjunction with the Taylor averaging approach. To adequately capture the multigrain response with the Taylor averaging technique, six grains were used for the T-orientation with the angles listed in Table 7.5. The angles are described using the Roe convention as shown in Figure 7.6. With

the Roe convention, the first rotation (ϕ_1) is about the global Z-axis, the second rotation (ψ) is about the new local Y-axis, and the final rotation (ϕ_2) is about the new local Z axis.

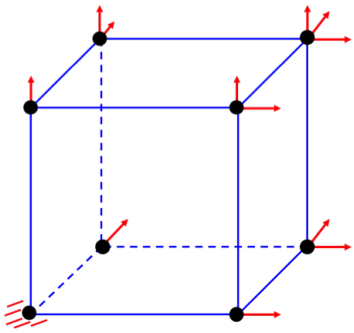

Figure 7.5: Single element RVE used in predicting smooth bar mechanical response depicting the boundary conditions. The arrows indicate a degree of freedom at each node.

Table 7.5: Euler angles used in the Taylor approximation for the T-orientation.

ϕ_1	φ	ϕ_2
90	0	0
90	15	0
90	30	0
90	45	0
90	60	0
90	75	0

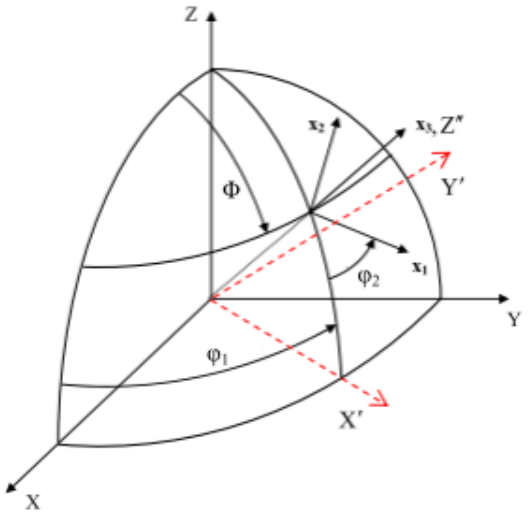

Figure 7.6: Euler angle Roe convention used in the CVP model.

7.4.3 Parameterization

As a result of the interdependencies amongst the material parameters, an efficient calibration of the material parameters requires a order of parameterization that at times by passes the material parameters appearance in the evolution equations (Equations 7.4-7.10). Shown in Figure 7.7 are three tiers of parameters; microstructure-sensitive, temperature-independent, and isothermal parameters with the hierarchy occurring in that order. This optimal parameter path is developed based on the influence each parameter has on one another, in conjunction with the net effect on the simulated material response.

As an overview to the calibration process that is discussed in detail in the following sections, the isothermal parameters for each microstructure at each temperature are determined though an iterative process with the temperature-independent parameters. Once a satisfactory set of parameters is obtained at each of the isothermal temperatures, the final phase is determining the coefficents of the microstructure-sensitive polynomials.

Distinguished in parameter determination process are the material parameters

that are temperature-dependent (left side of Figure 7.7) and those that require a range of temperatures to properly calibrate (right side of Figure 7.7) per each microstructure. Beginning the iterative process, not all material parameters can be given a initial null value due to the formulation of the CVP model equations. Given in Table 7.6 are the starting values of the material parameters used in the calibration of the CVP model in this work.

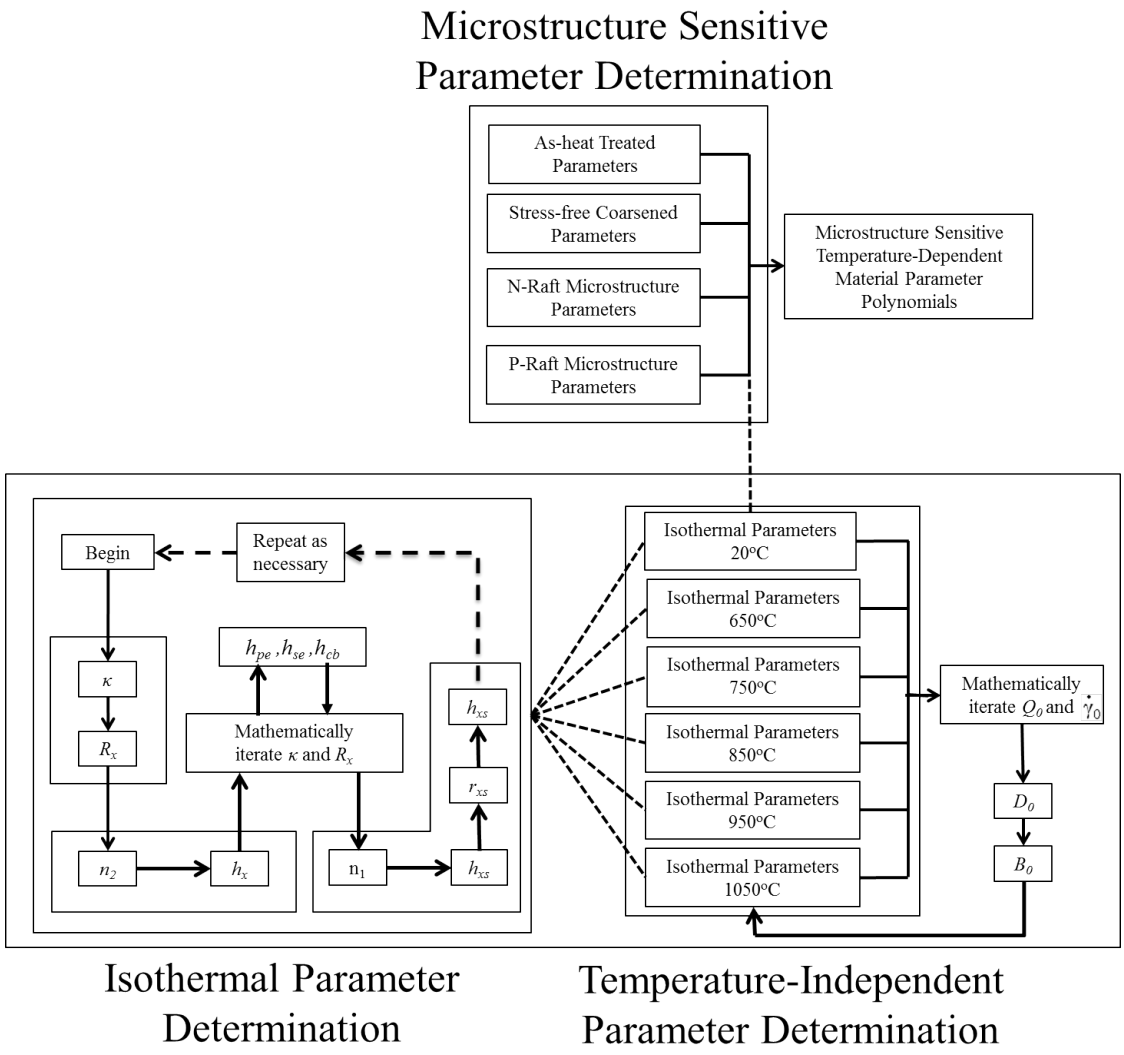

Figure 7.7: Iterative procedure used for the calibration of material parameters in the CVP model.

Table 7.6: Initial material parameters used in CVP model calibration.

h_χ [MPa]	D_o [MPa]	Q_o $[\frac{J}{molK}]$	$\dot{\gamma}_o$ $[\frac{1}{s}]$	B_o —	n_2 —
1x10^9	100	400	1x10^{13}	0.05	5

7.4.3.1 Isothermal Parameter Determination

Elastic Constants In calibrating these parameters one must be aware, that although Young's modulus and Poisson's ratio often measured in uniaxial experiments, the CVP theory is framed in terms of the stiffness constants C_{11}, C_{12}, and C_{44}, as such relations between them are required and are dependent on the ordering of the material. For the generic cubic material system, the stiffness matrix is given by,

$$\mathbf{C} = \begin{pmatrix} C_{11} & C_{12} & C_{12} & 0 & 0 & 0 \\ C_{12} & C_{11} & C_{12} & 0 & 0 & 0 \\ C_{12} & C_{12} & C_{11} & 0 & 0 & 0 \\ 0 & 0 & 0 & C_{44} & 0 & 0 \\ 0 & 0 & 0 & 0 & C_{44} & 0 \\ 0 & 0 & 0 & 0 & 0 & C_{44} \end{pmatrix} \tag{7.28}$$

with the conditions on the stiffness constants being $C_{44} > 0$, $C_{11} > |C_{12}|$, and $C_{11} + 2C_{12} > 0$ [163]. The constants C_{11}, C_{12}, and C_{44} should all be determined through experimentation, and checked to ensure they exhibit the trends consistent with Ni and other Ni-base superalloys. Generally, the values of the elastic constants vary minimally from one Ni-base superalloy to another [164, 165].

Coefficient of Thermal Expansion Concerning the CTE, β, the material's thermal strain is related to the CTE according to the secant definition,

$$\epsilon_{th} = \beta(T - T_o) \tag{7.29}$$

where both the thermal strain and the CTE are functions of temperature. With most Ni-base superalloys, a second order polynomial ($\epsilon^{th} = M_0 + M_1 X + M_2 X^2$) is sufficent to fit the thermal strain, such that,

$$\frac{d\epsilon^{th}}{dT} = \beta + 2\frac{d\beta}{dT}(T - T_o) \tag{7.30}$$

where, M_1 and M_2 are the coefficients of the second order polynomial. Upon solving the above differential equation and evaluating with Equation 7.29, the CTE can be defined as,

$$\beta = M_1 + M_2(T - T_o) \tag{7.31}$$

Yield Phenomena The first parameter that requires determination is that of the threshold stress, κ_o at the given isothermal temperature. Given that the value of the yield stress, σ_o is known from the initial cycle of the calibration experiment, an initial approximation for κ_o can be determined knowing that inelastic deformation does not become significant until the quantity $\frac{\tau_v^\alpha}{D^\alpha}$ in Equation 7.4 is equivalent to 1. Substituting, Equation 7.5 and 7.6 into this equality, the following is obtained,

$$\kappa_o = \frac{\mu_o}{\mu}\left(\frac{\sigma_o}{M} - D_o\frac{\mu}{\mu_o}\right) \tag{7.32}$$

where, M is the Taylor factor. In the case of a DS Ni-base superalloy, if one assumes the material is entirely FCC, the Taylor factor, M=1.73 [166].

For R_χ, an estimate can be developed considering the saturated value of the back

stress ($\dot{\chi}^{\alpha} = 0$), where Equation 7.7 can be rearranged to yield χ^{α}=R_{χ}. Through substitution of the prior result into Equation 7.5 and subsequent substitution of the resultant into the equality $\frac{\tau_v^{\alpha}}{D^{\alpha}}$=1, an approximation for R_{χ} based on the current value of κ_o can be obtained,

$$R_{\chi}^{i} = \frac{\sigma_{sat}}{M} - \left(D^{\alpha} + \kappa_o^{i} \frac{\mu}{\mu_o} \right) \tag{7.33}$$

where σ_{sat} is the maximum stress of the cycle, and κ_o^i is the current approximate of the threshold stress being used in the calibration at a given temperature.

Due to the interdependencies of κ_o and R_{χ} iterative adjustments to each of the material parameters is required to generate a hysteresis curve with the desired yield point and saturation level. At this step in the calibration, the saturated values for the tensile/compressive stress may not exhibit the desired tension/compression asymmetry. Accounting of this phenomena is done through the non-Schmid parameters for later in the calibration process, as these parameters have a minimal influence on the other parameters.

Hardening Phenomena Next in the efficient path is determining the hardening parameters. Considering that for high strain rates ($\approx 10^{-3} \frac{1}{s}$) the creep portion of the flow equation (Eqaution 7.4) has minimal influence on the result, Equation 7.5 can be substituted into the flow equation and rearranged to result a function for estimating n_2,

$$n_2 = \frac{ln\left(\frac{ln(\dot{\gamma}^{\alpha}) - ln(\gamma_o \Theta)}{B_o} \right)}{ln\left(\frac{\frac{\sigma_{sat}}{M} - R_{\chi} - \kappa_o \frac{\mu}{\mu_o}}{D^{\alpha}} \right)} \tag{7.34}$$

Similarly, n_2 can be estimated through the plotting of the saturation stress obtained from experiments in the fatigue regime versus the strain rate on a log-log plot and fitting a trend line through the data, where the exponent of the trend line gives an approximate value for n_2 as shown in Figure 7.8.

Next to be determined is the rate of hardening parameter, h_{χ}. The value of h_{χ} is

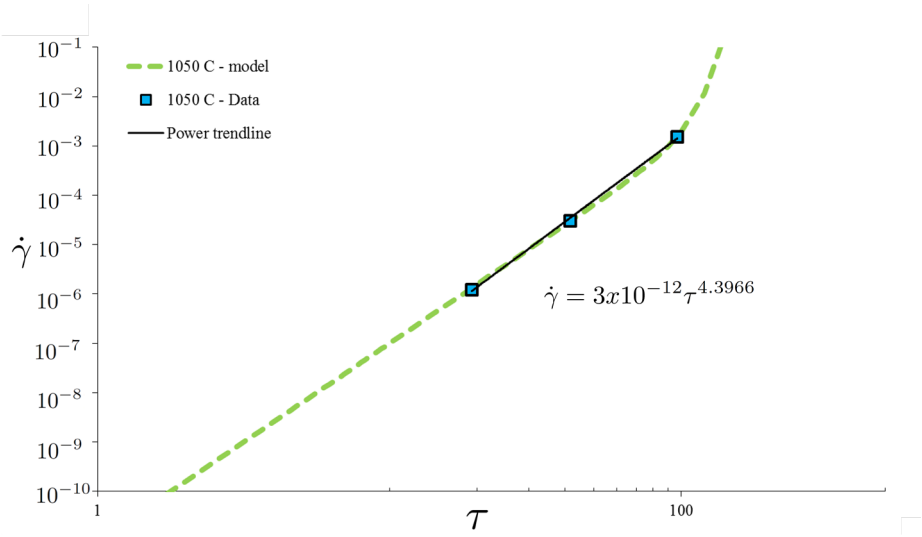

Figure 7.8: Determination of the hardening exponent, n_2 through fitting of a power law trend line to experimental data.

determined through a slow reduction from the highly saturated quantity (1x10^{9}MPa) used during the initial calibration of R_χ until the hardening behavior of the hysteresis loop is approximately correct. Once a good approximation for h_χ is known, a check for the accuracy of R_χ and κ_o should be conducted, with additional iterations of the two parameters as needed to ensure overall good fits to the experimental data.

Non-Schmid Factors The non-Schmid terms account for tension/compression asymmetries that some Ni-base superalloys have been known to exhibit at temperatures below the anomalous point. In the case of CM247LC-DS, these parameters were only required at 750°C. The net effect of the non-Schmid parameters is that h_{cb} increases the size of the yield surface, h_{pe} and h_{se} shift the yield surface in stress space.

Creep Within the CVP model, the long-term rate dependence of the material is influenced through three different locations: the exponent of the power-law term in the flow equation (Equation 7.4), the parameters $h_{\chi s}$, $r_{\chi s}$ in the thermal static recovery

term in the back stress (Equation 7.7), and $h_{\kappa s}$ in the static thermal recovery term in the threshold stress evolution (Equation 7.10). To calculate these terms, stress relaxation data from the calibration experiments is used. For CM247LC-DS, n_1 was found to be related to n_2 through the relationship $n_1 = n_2 - 1$.

7.4.3.2 Temperature-Independent Parameter Determination

The last of the material parameters to be determined in the iterative process are the temperature independent parameters $\dot{\gamma}_o$, D_o, B_o and, Q_o. Of these four parameters, the reference inelastic shear strain rate, $\dot{\gamma}_o$ and the activation energy for self diffusion of Ni in the matrix, Q_o, are highly coupled at low and intermediate temperatures such that a change in one, requires compensation in the other to assure that the constitutive model remains within the domain of stability as far as the material parameters are concerned. To assure this balance, a set of coupled temperature-dependent iterative functions is derived,

$$\dot{\gamma}_o^{i+1} = \dot{\gamma}_o^i exp\left(\frac{Q_o^{i+1} - Q_o^i}{\psi^i}\right) \tag{7.35}$$

$$\psi^i(T) = \dot{\gamma}_o^i \Theta(T) = \begin{cases} \dot{\gamma}_o^i exp\left(-\frac{Q_o^i}{RT}\right) .....T \geq \frac{T_m}{2} \\ \dot{\gamma}_o^i exp\left(-\frac{2Q_o^i}{RT_m}\left[ln\left(\frac{T_m}{2T}+1\right]\right)\right) .....T \leq \frac{T_m}{2} \end{cases} \tag{7.36}$$

where i+1 is the new estimate and i the previous one of the material parameters.

For the initial value of $\dot{\gamma}_o$, i.e. $\dot{\gamma}_o^1$, the parameter was calibrated to the experimental data from 1050°C while leaving Q_o unchanged. To determine $\dot{\gamma}_o^1$, the rate equation was plotted on a log-log plot of the viscous shear stress versus the inelastic shear strain rate and iteratively adjusted until the simulated data corresponded to the experimental data as shown in Figure 7.9.

For the initial approximation of Q_o, the value of a Ni-base superalloy that is a close derivative of the one of interest is an appropriate starting point and often available

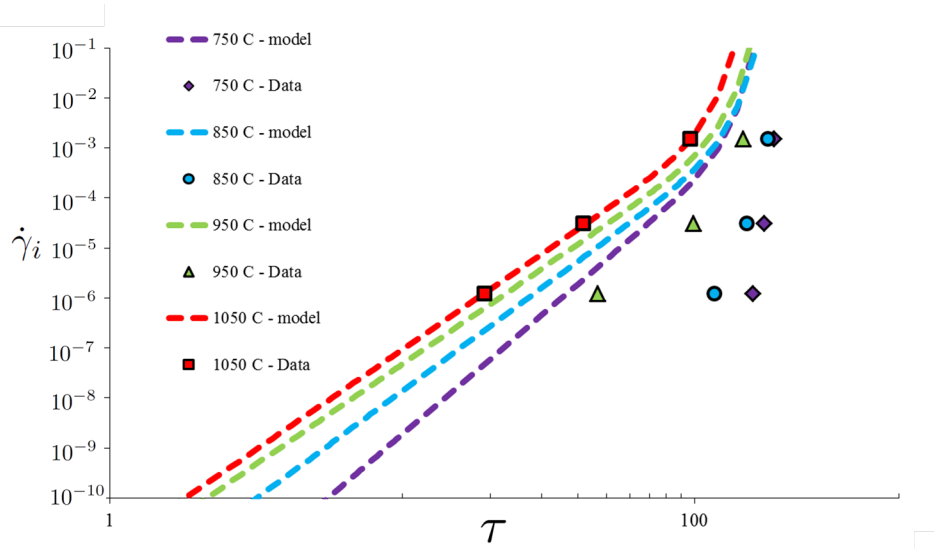

Figure 7.9: Calibration of $\dot{\gamma}_o^i$ to experiential data at 1050°C.

in the literature [73, 167]. In proceeding through the iterative process of Equations 7.35-7.36, the values of Q_o and $\dot{\gamma}_o$ were modified until the isothermal lines at each temperature capture the strain rate dependence as shown in Figure 7.10. B_o was determined such that the rate insensitive regime of the rate equation matches the behavior of the data as well as possible for the lower temperatures as shown in Figure 7.10. Higher temperatures ($> 900°C$) can be used; however, in many instances, Ni-base superalloys may not be observed entering the rate insensitive regime. The drag stress D_o was determined through fitting the rate equation to the experimental data in the rate insensitive regime of the flow equation at higher temperatures ($> 900°C$).

7.4.3.3 Microstructure Sensitive Temperature Dependent Interpolation Function Creation

Once all isothermal and temperature independent material parameters for each microstructure were determined, the microstructure-sensitive temperature-dependent interpolation functions of the form discussed previously,

$$A = A_T(T)\left(1 - c_\eta(T)\eta\right)\left(1 - c_\zeta(T)\zeta\right) \tag{7.37}$$

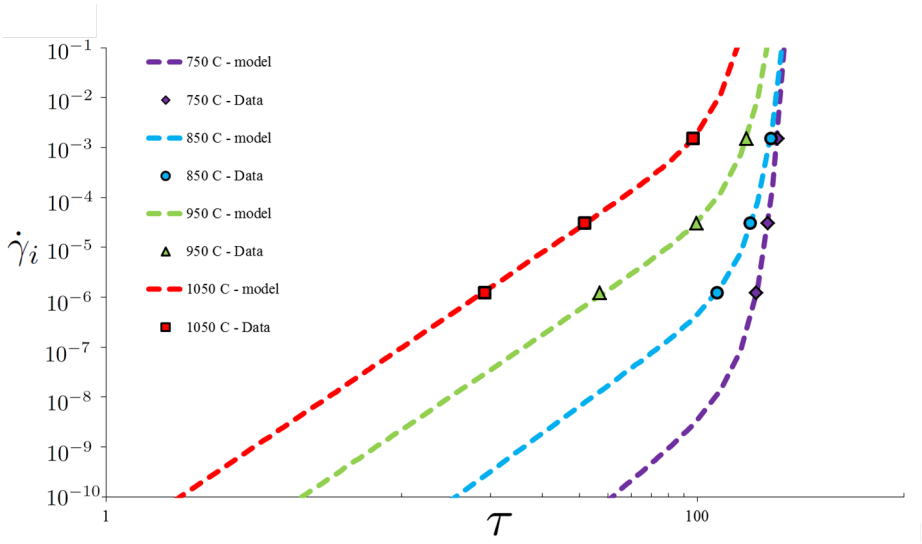

Figure 7.10: Calibration of Q_o, D_o, and B_o after iteration.

were fit. To reiterate an earlier statement, the effects of aging on the constitutive response were found to be adequately captured through the parameters R_χ, h_χ, and κ_o. As a result, the virgin material parameters were satisfactory for capturing the aged response. As will be discussed later, a exception to the polynomial rule is $h_{\chi s}$. In determining the coefficients of the interpolating polynomials in Equation 7.37, first determined was the temperature dependent virgin material polynomial, A_T properties followed by c_η and c_ζ.

With exception to h_χ, a single polynomial was capable of capturing the temperature-dependence of the material parameters. Because of anomalous yield behavior exhibited by Ni-base superalloys, a rapid increase followed by a decrease in the value of h_χ prohibits a single interpolating polynomial from adequately capture the trend. As a result two polynomials must were spliced together while maintaining both C^0 and C^1 continuity at the transition point between them. First order continuity is required because of the derivative of h_χ being used in the back stress evolution equation in addition to the primary function. The splicing of the polynomials was achieved through first fitting a higher order interpolating polynomial (4th order or higher) to the high

temperature regime (650-1050°C). Obtaining an adequately behaved polynomial in the high temperature regime required a polynomial of order greater than available isothermal data points. As a result, data points for fitting the polynomial at intermediate temperatures were introduced. The added data points were obtained through linear interpolation of the calibrated isothermal values.

To determine the low temperature polynomial, a constrained equations approach was used to impose the necessary continuity conditions and solve for the polynomial's coefficients. Following this approach, four conditions were prescribed to obtain a third order polynomial. The conditions used were the equivalence of h_χ (C^0) and corresponding derivate (C^1) at the splice point, the value of h_χ at 20°C, and $\frac{dh_\chi}{dx}|_{T=20°C}= 0$. The constrained set of equations is given by,

$$\begin{bmatrix} h_\chi|_{T=T_1} \\ h_\chi|_{T=T_2} \\ \frac{dh_\chi}{dx}|_{T=T_1} \\ \frac{dh_\chi}{dx}|_{T=T_2} \end{bmatrix} = \begin{bmatrix} T_1^3 & T_1^2 & T_1 & 1 \\ T_2^3 & T_2^2 & T_2 & 1 \\ 3T_1^2 & 2T_1 & 1 & 0 \\ 3T_1^2 & 2T_2 & 1 & 0 \end{bmatrix} \begin{bmatrix} a_3 \\ a_2 \\ a_1 \\ a_0 \end{bmatrix} \tag{7.38}$$

where T_1 is the minimum temperature (20°C), while T_2 is the temperature at the splice point. In the case of the calibration performed, the splice point was set to 617°C and a 6th order polynomial used to represent the higher temperature regime polynomial as depicted in Figure 7.11.

For nearly all the temperature-dependent material parameters, polynomials or groups thereof are well suited, the lone exceptions being the creep parameter in the back stress h_{xs} which is fit to exponentials; $h_{xs} = e^{\left(\sum_{i=1}^{n} a_i T^i\right)}$. This functional form is better suited because creep is an activation process that typically exhibits a exponential dependence on temperature. Once the interpolation functions were generated for all the material parameters, a check of the accuracy of the functions

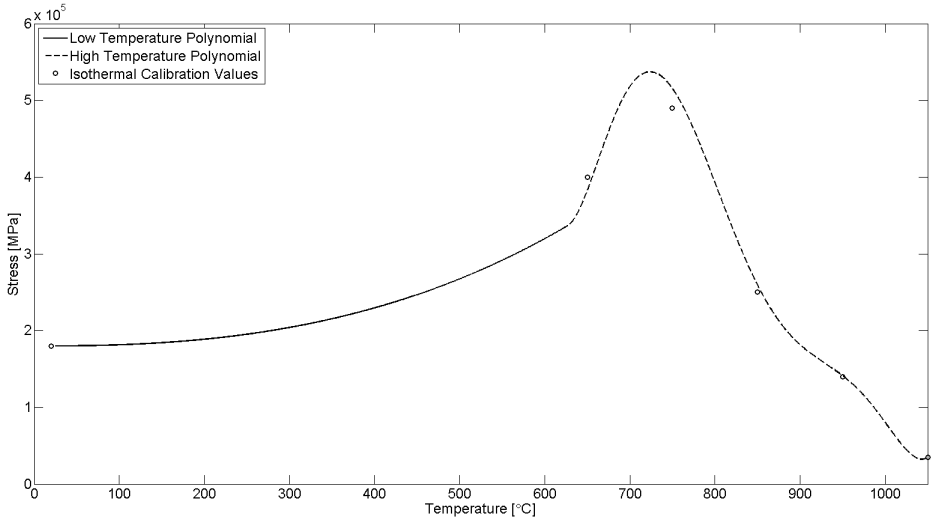

Figure 7.11: Comparison of the spliced polynomials to the values of h_χ determined through isothermal fitting, where C^0 and C^1 continuity is maintained at the transition from the solid to the dotted line.

was done and compared to the isothermal experimental data for each microstructure.

7.4.4 Material Parameters

Following the calibration approach presented above, the resulting material parameters are presented in Tables 7.7-7.11. In addition, the resultant isothermal calibration fits are provided in Figures 7.12-7.18. Generally, good arrangement is obtained between each of the experimental isothermal data sets and the CVP model for each microstructure. The greatest deviations occur between the CVP model and the calibration data sets at 750°C for all microstructures and 850°C for each of the aged microstructures. In the case of the aged microstructures, the primary difference between the as-heat treated constitutive behavior and the aged behavior is that the aged microstructures begin yielding on the reversal while in macroscopic compression. This being the result of relaxation of internal stresses in the $\gamma - \gamma'$ microstructure.

Table 7.7: General microstructure insensitive material parameters.

(a) General Temperature-dependent Material Constants

Temperature [C]	C_{11} [MPa]	C_{12} [MPa]	C_{44} [MPa]	n_1	n_2	μ [MPa]
20	341000	250000	127000	7	6	127000
650	219000	144000	104000	7	6	104000
750	199000	128000	99000	7	6	99000
850	178000	112000	93000	6	5	93000
950	157000	97000	87500	6	5	87500
1050	135000	81500	81000	6	5	81000

Review of Effect of Post-solutionizing Cooling Rate on Low Cycle Fatigue Behavior of Nickel base Superalloy By Mehta, Mitra, and Chawla

(b) General Temperature-independent Material Constants

D_o [MPa]	Q_o $[\frac{J}{molK}]$	$\dot{\gamma}_o$ $[\frac{1}{s}]$	B_o
100	400	1x10^{13}	0.05

Table 7.8: CVP material parameters for DS Ni-base superalloy in as-heat treated state.

(a) Octahedral Slip System Constants, Initial Conditions: $\chi^\alpha(0) = 0$, $\kappa_e^\alpha(0) = 0$

Temperature [C]	h_χ [MPa]	R_χ [MPa]	κ_o [MPa]	$h_{\chi s}$	$r_{\chi s}$	h_{pe}	h_{cb}	h_{se}
20	160000	75	30	0.0	0.0	0.0	0.0	0.0
650	450000	110	55	0.0	0.0	0.0	0.0	0.0
750	500000	120	85	2.8x10^8	2	0.15	-0.25	0.03
850	440000	115	40	4.3x10^{10}	2	0.0	0.0	0.0
950	160000	100	30	1.8x10^{12}	2	0.0	0.0	0.0
1050	45000	50	10	2.2x10^{13}	2	0.0	0.0	0.0

(b) Cubic Slip System Constants, Initial Conditions: $\chi^\alpha(0) = 0$, $\kappa_e^\alpha(0) = 0$

Temperature [C]	h_χ [MPa]	R_χ [MPa]	κ_o [MPa]	$h_{\chi s}$	$r_{\chi s}$
750	310000	110	150	2.8x10^8	2
950	10000	80	15	1.8x10^{12}	2

Table 7.9: CVP material parameters for DS Ni-base superalloy in isotropically coarsened state.

(a) Octahedral Slip System Constants, Initial Conditions: $\chi^\alpha(0) = 0$, $\kappa_e^\alpha(0) = 0$

Temperature [C]	h_χ [MPa]	R_χ [MPa]	κ_o [MPa]
20	160000	75	30
650	450000	110	55
750	250000	110	75
850	150000	80	15
950	110000	80	10
1050	45000	50	5

(b) Cubic Slip System Constants, Initial Conditions: $\chi^\alpha(0) = 0$, $\kappa_e^\alpha(0) = 0$

Temperature [C]	h_χ [MPa]	R_χ [MPa]	κ_o [MPa]
750	25000	90	90
950	6500	40	5

Table 7.10: CVP material parameters for DS Ni-base superalloy in N-Raft state.

(a) Octahedral Slip System Constants, Initial Conditions: $\chi^\alpha(0) = 0$, $\kappa_e^\alpha(0) = 0$

Temperature [C]	h_χ [MPa]	R_χ [MPa]	κ_o [MPa]
20	100000	45	20
650	450000	110	55
750	250000	120	75
850	90000	80	40
950	75000	75	30
1050	45000	50	10

(b) Cubic Slip System Constants, Initial Conditions: $\chi^\alpha(0) = 0$, $\kappa_e^\alpha(0) = 0$

Temperature [C]	h_χ [MPa]	R_χ [MPa]	κ_o [MPa]
750	310000	110	150
950	10000	80	15

Table 7.11: CVP material parameters for DS Ni-base superalloy in P-Raft state.

(a) Octahedral Slip System Constants, Initial Conditions: $\chi^\alpha(0) = 0$, $\kappa_e^\alpha(0) = 0$

Temperature [C]	h_χ [MPa]	R_χ [MPa]	κ_o [MPa]
20	160000	75	30
650	450000	110	55
750	410000	120	85
850	350000	110	40
950	130000	70	20
1050	45000	50	10

(b) Cubic Slip System Constants, Initial Conditions: $\chi^\alpha(0) = 0$, $\kappa_e^\alpha(0) = 0$

Temperature [C]	h_χ [MPa]	R_χ [MPa]	κ_o [MPa]
750	310000	110	150
950	90000	70	5

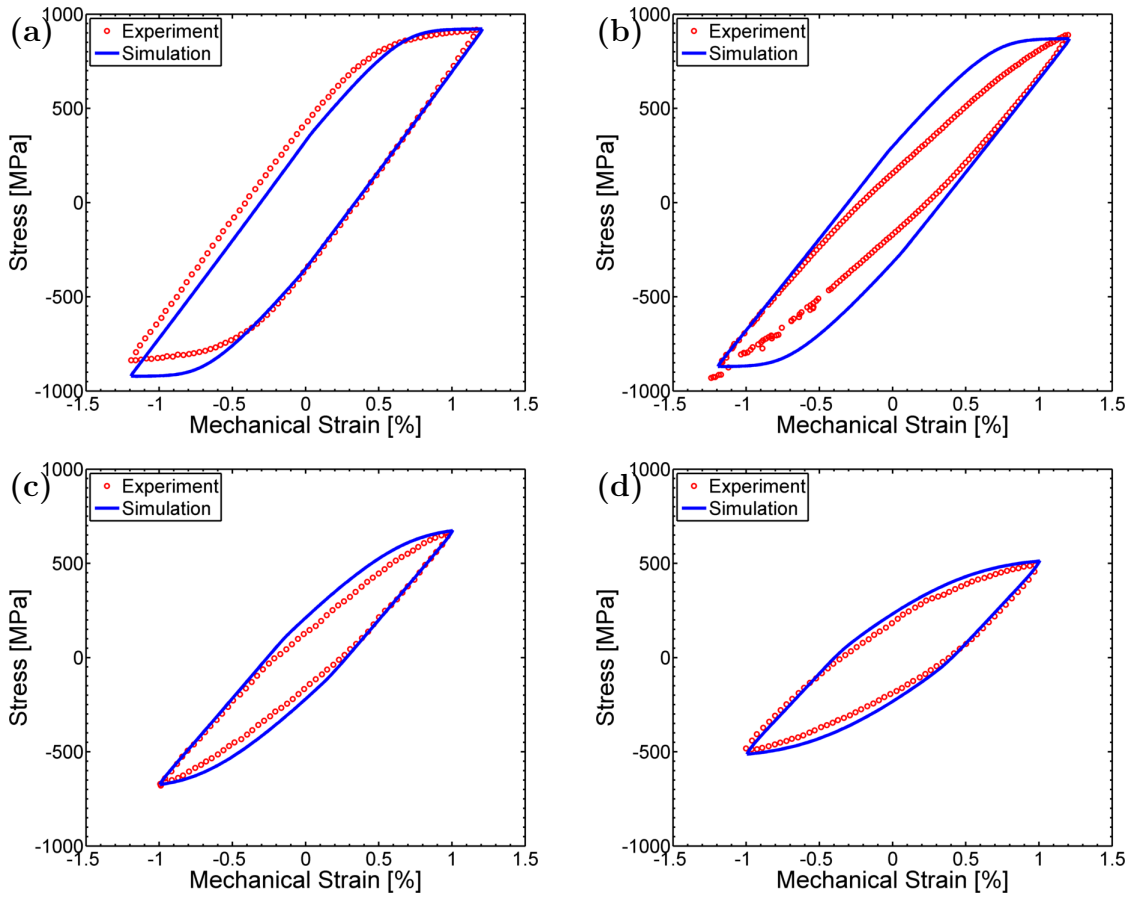

Figure 7.12: Comparison of the experimental isothermal hysteresis response of the virgin microstructure in the L-orientation to the CVP calibration results at (a) 650°C (b) 750°C (c) 850°C (d) 950°C.

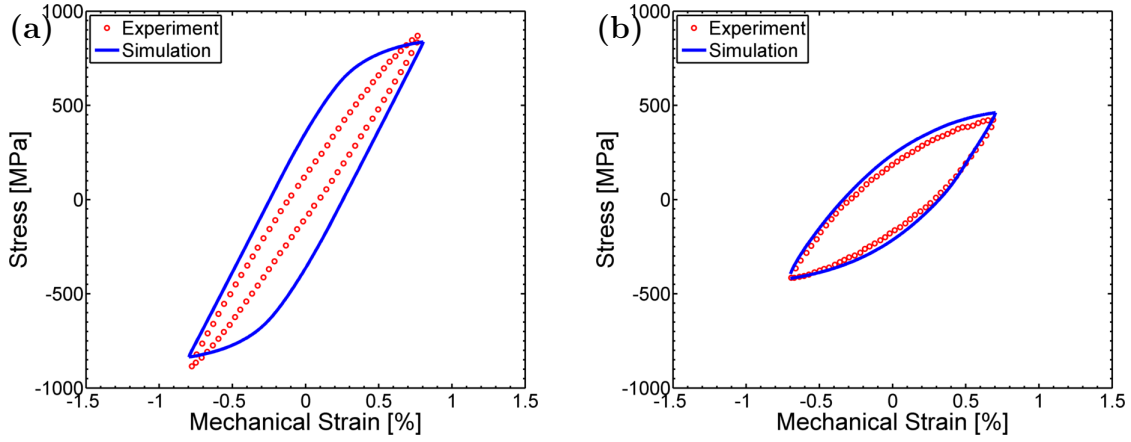

Figure 7.13: Comparison of the experimental isothermal hysteresis response of the virgin microstructure in the T-orientation to the CVP calibration results at (a) 750°C (b) 950°C.

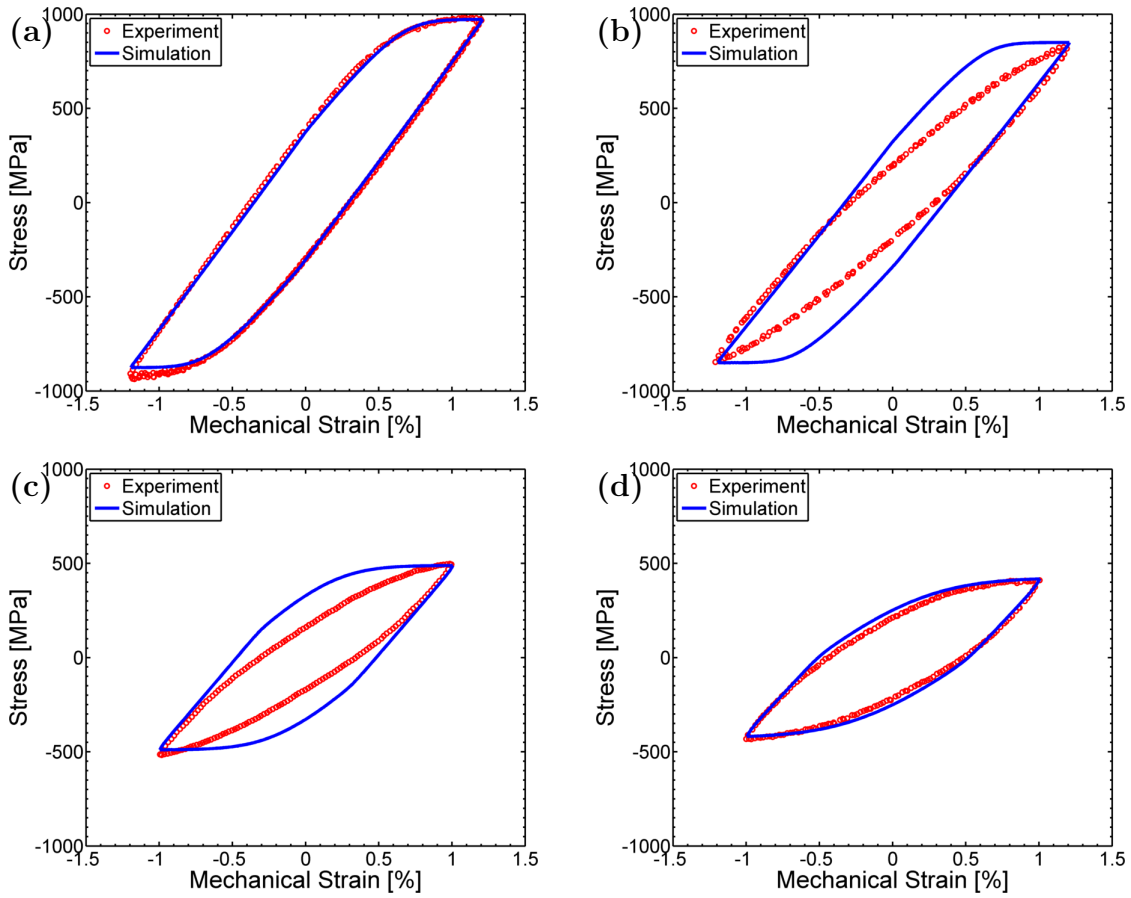

Figure 7.14: Comparison of the experimental isothermal hysteresis response of the isotropically coarsened microstructure in the L-orientation to the CVP calibration results at (a) 650°C (b) 750°C (c) 850°C (d) 950°C.

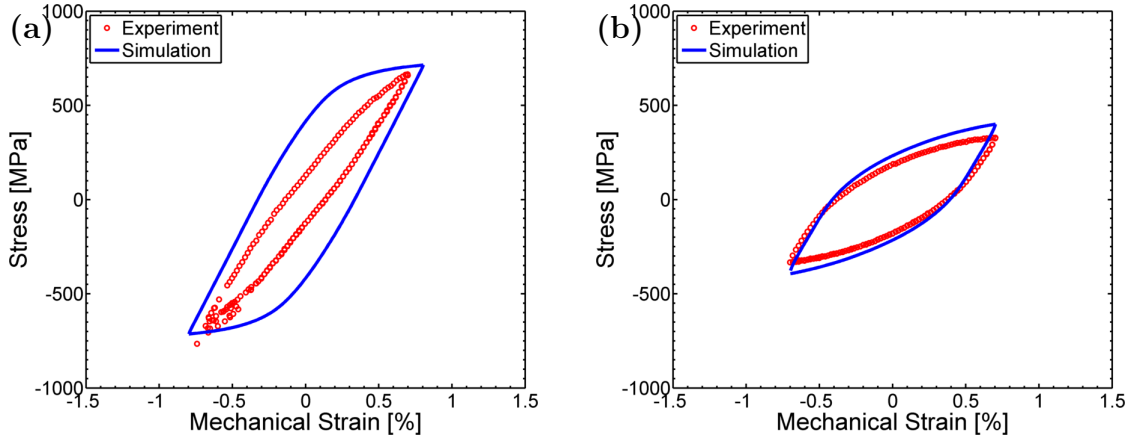

Figure 7.15: Comparison of the experimental isothermal hysteresis response of the isotropically coarsened microstructure in the T-orientation to the CVP calibration results at (a) 750°C (b) 950°C.

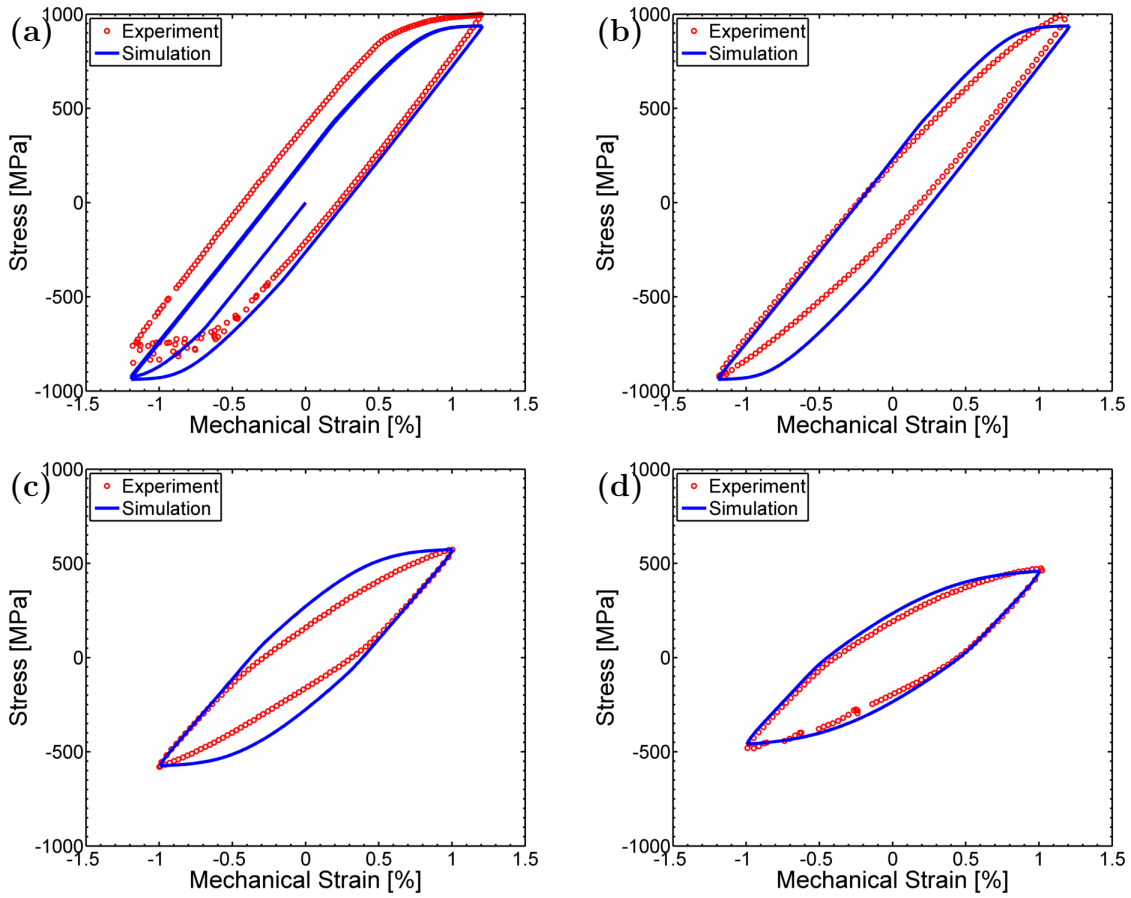

Figure 7.16: Comparison of the experimental isothermal hysteresis response of the N-raft microstructure in the L-orientation to the CVP calibration results at (a) 650°C (b) 750°C (c) 850°C (d) 950°C.

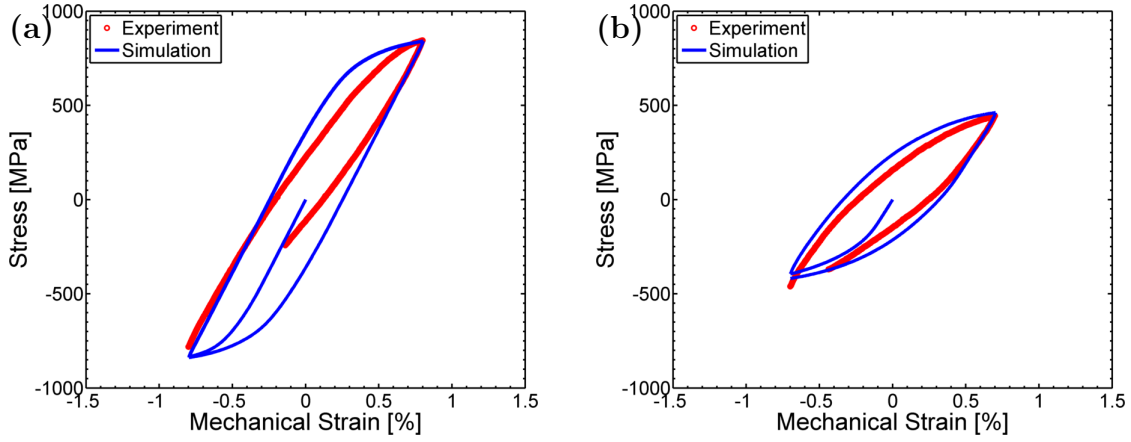

Figure 7.17: Comparison of the experimental isothermal hysteresis response of the N-raft microstructure in the T-orientation to the CVP calibration results at (a) 750°C (b) 950°C. Note: 750°C calibration experiment fractured on initial cycle.

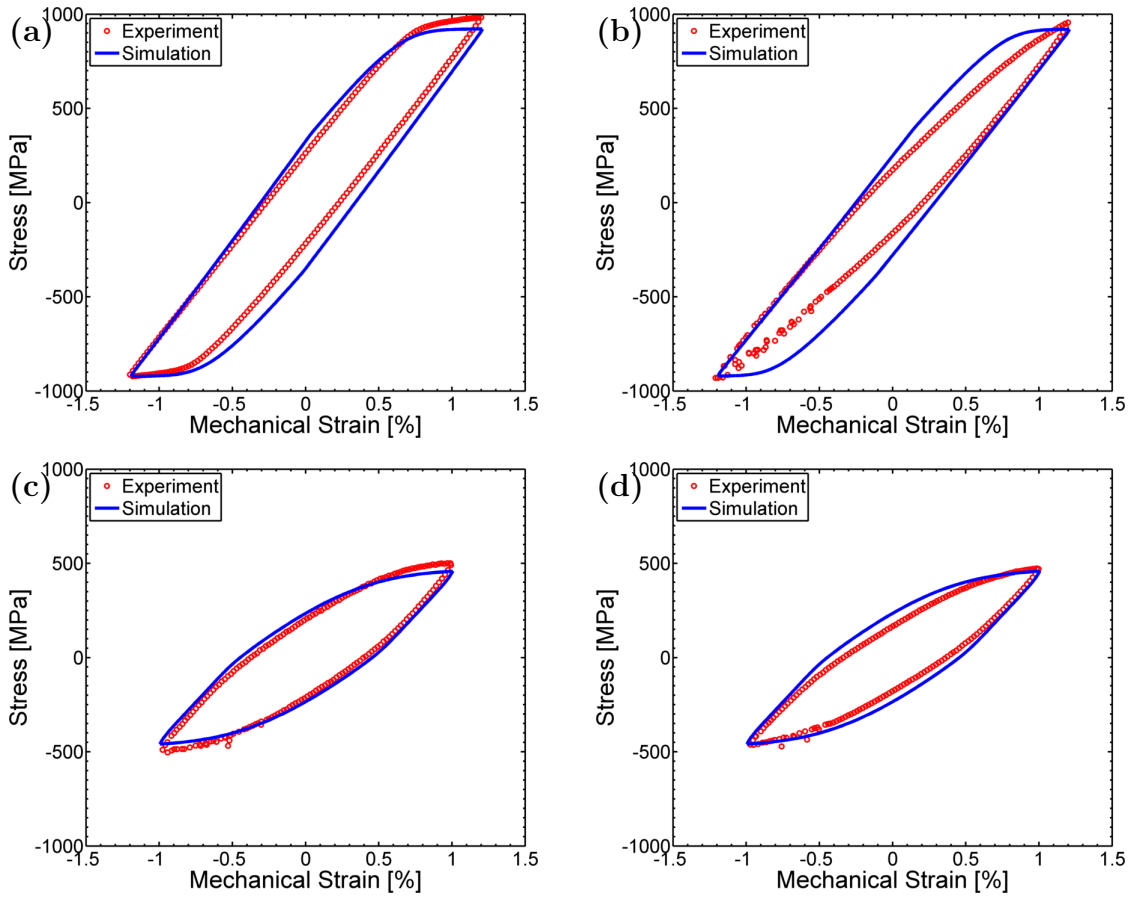

Figure 7.18: Comparison of the experimental isothermal hysteresis response of the P-raft microstructure in the L-orientation to the CVP calibration results at (a) 650°C (b) 750°C (c) 850°C (d) 950°C

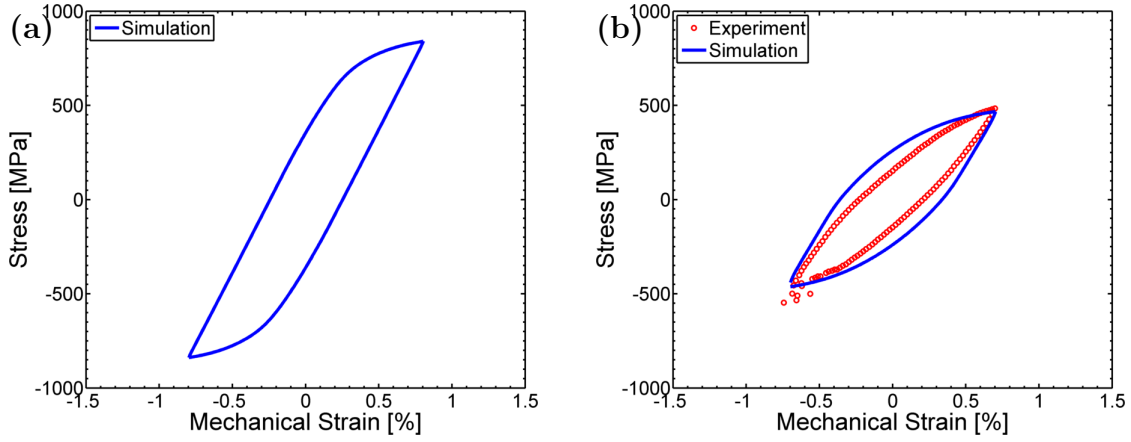

Figure 7.19: Comparison of the experimental isothermal hysteresis response of the P-raft microstructure in the T-orientation to the CVP calibration results at (a) 750°C (b) 950°C. Note: 750°C calibration experiments fractured on initial loading.

7.5 CVP Model Validation

The model was validated by showing its ability to correctly predict the responses of several TMF loading histories that had been conducted in the laboratory. TMF experiments were conducted on the virgin, isotropically coarsened, N-raft, and P-raft microstructures as discussed in Chapter 5 and 6. Shown in Figures 7.20-7.25 are the simulated responses in comparison to the experimentally determined ones. In the virgin state, the CVP model is able to capture the peak stresses and inelastic strain under CC TMF conditions accurately. In simulating CF TMF conditions, the CVP model captures the relaxation behavior and inelastic strain of the cycle; however, the CVP model does not fully account for the reversed yielding that is experimentally observed to occur during cold portion of the TMF cycle. Similarly, in the aged states, the CVP model is unable to fully account for the reverse yielding that occurs under both CC and CF TMF loadings as shown in Figures **??**-7.25. However, the CVP model is able to predict the peak stresses to within 50 MPa of the experimental response of valid TMF tests, which is within the realm of experimental statistical similarity for the alloy. Overall, the lack of predictability of the reverse yielding effects by the CVP model in the aged states, and under CF conditions in the as-heat treated can be attributed to the lack of inclusion of the back stress modifier term as discussed in the recommendations sections.

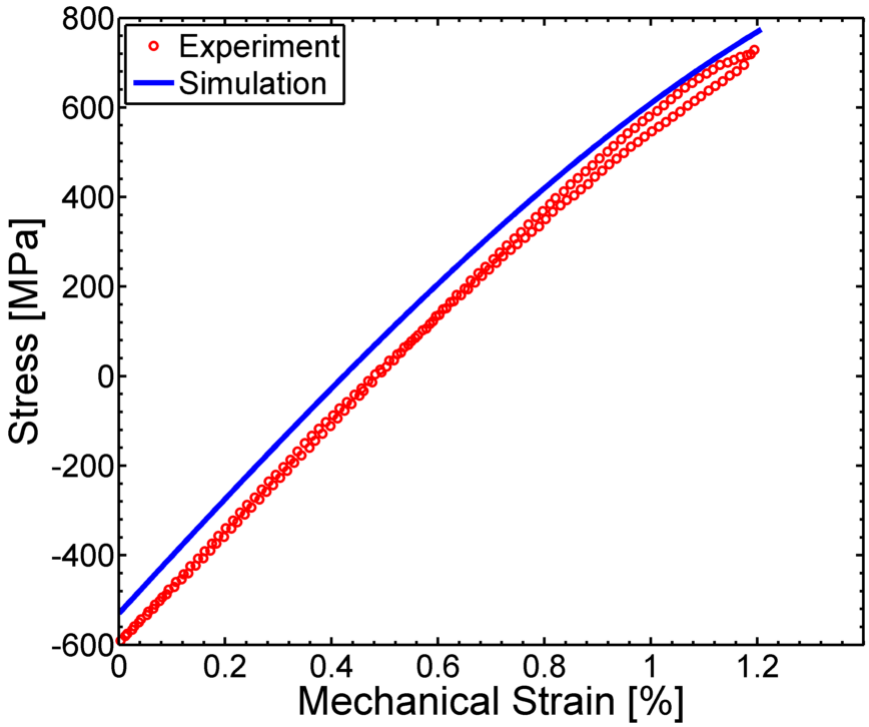

Figure 7.20: CVP model prediction for half-life hysteresis behavior of isotropically coarsened microstructure under IP $R_\epsilon = 0$ TMF, 100-750°C loading conditions.

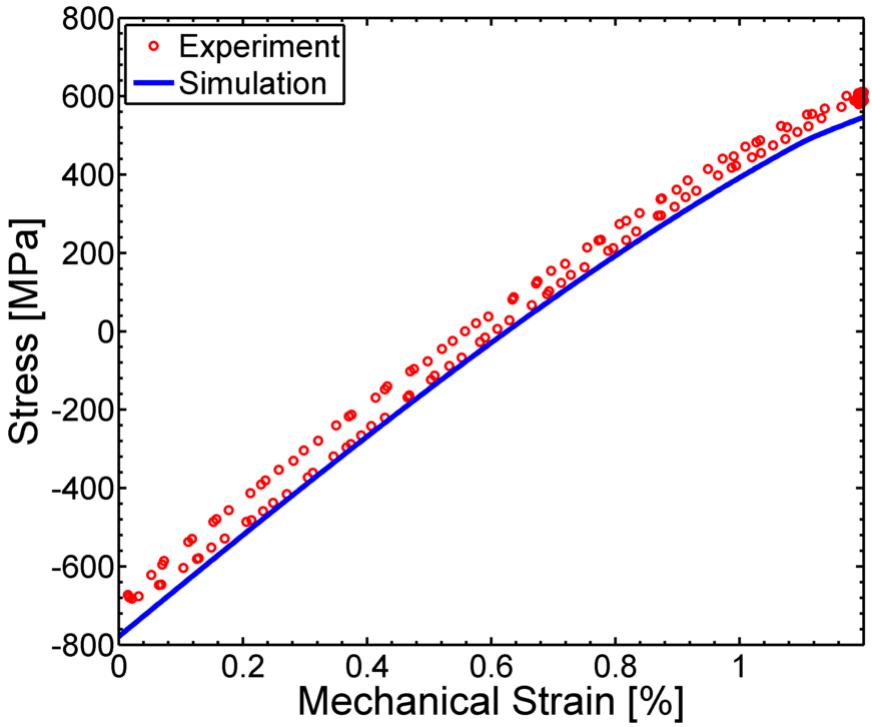

Figure 7.21: CVP model prediction for half-life hysteresis behavior of isotropically coarsened microstructure under IP $R_\epsilon = 0$ TMF, 100-750°C loading conditions with 20 minute tensile dwell.

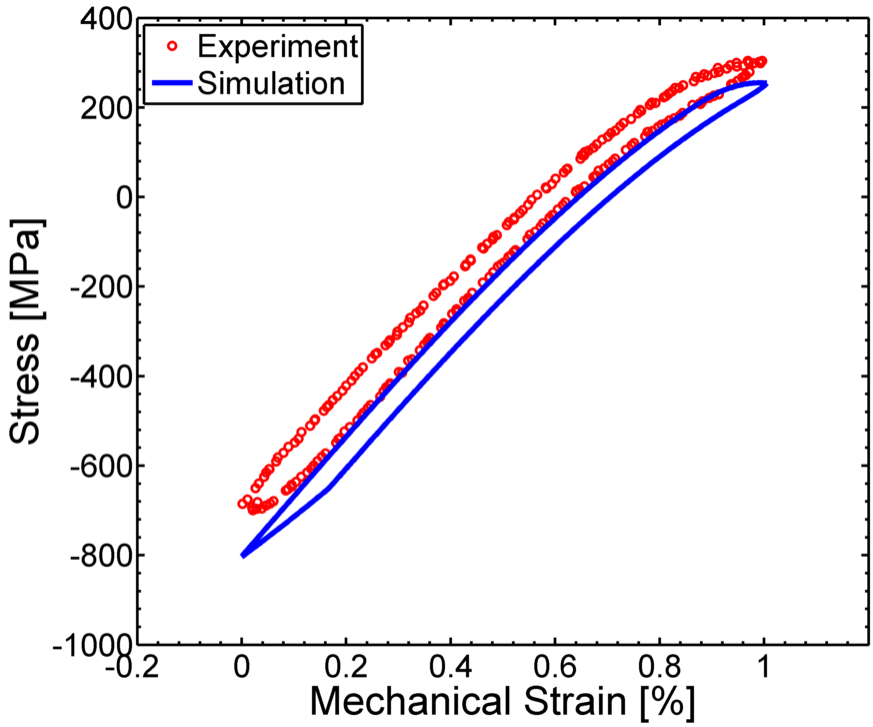

Figure 7.22: CVP model prediction for half-life hysteresis behavior of N-raft microstructure under IP $R_\epsilon = 0$ TMF, 100-950°C loading conditions.

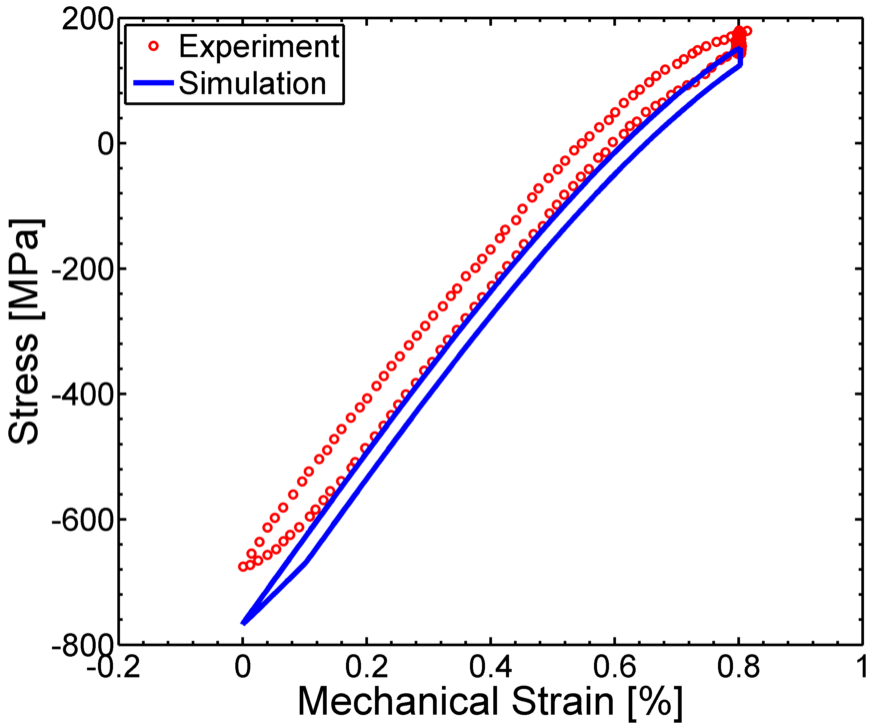

Figure 7.23: CVP model prediction for half-life hysteresis behavior of N-raft microstructure under IP $R_\epsilon = 0$ TMF, 100-950°C loading conditions with 20 minute tensile dwell.

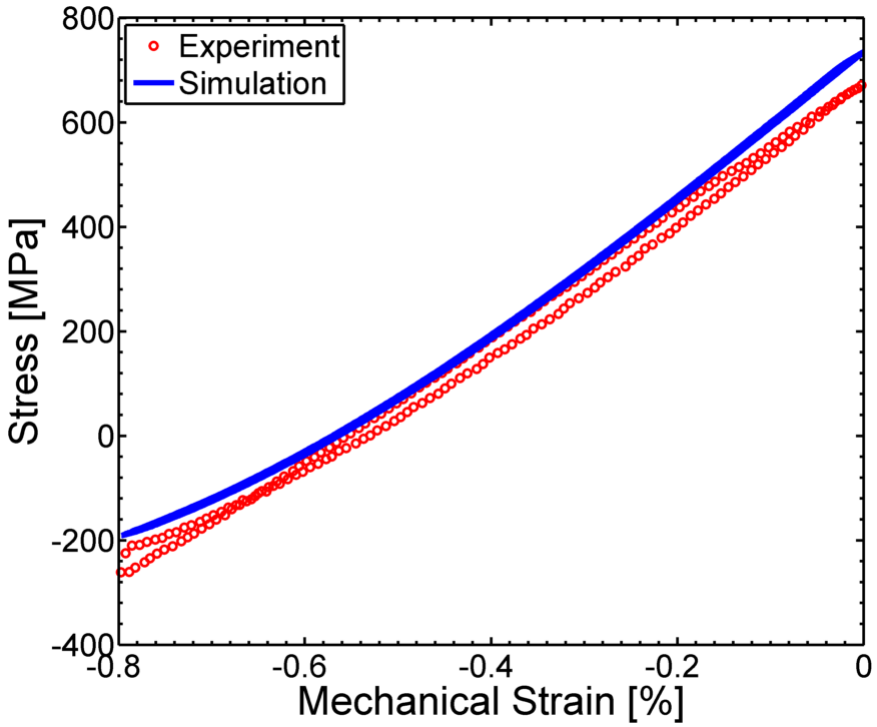

Figure 7.24: CVP model prediction for half-life hysteresis behavior of P-raft microstructure under OP $R_\epsilon = -\infty$ TMF, 100-950°C loading conditions.

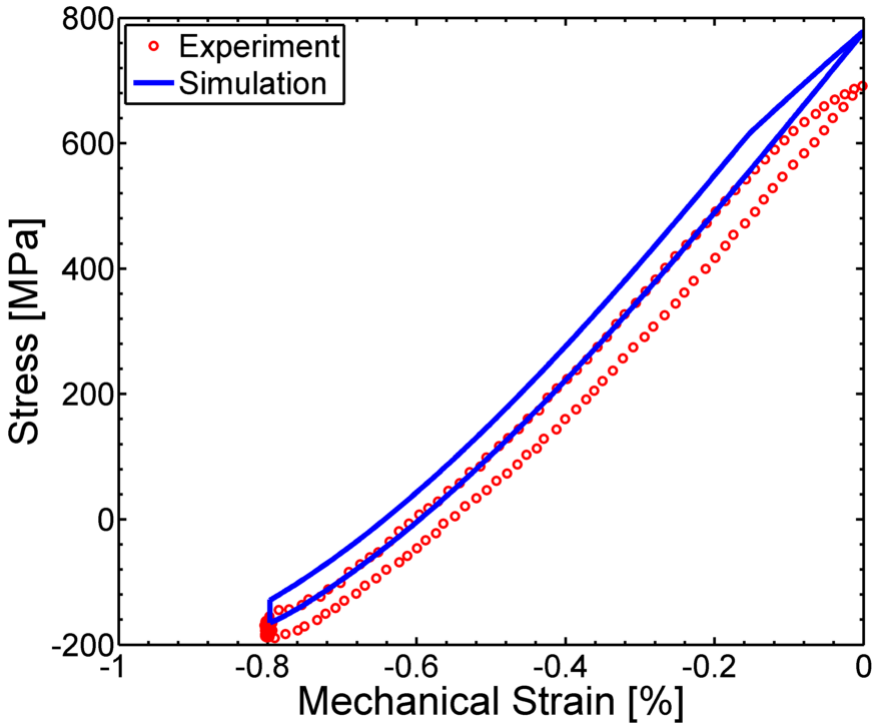

Figure 7.25: CVP model prediction for half-life hysteresis behavior of P-raft microstructure under OP $R_\epsilon = -\infty$ TMF, 100-950°C loading conditions with 20 minute compressive dwell.

CHAPTER VIII

CONCLUSIONS

The results of this research are as follows:

1. **Characterize the kinetics of aging in a Ni-base superalloy**

    - The microstructure of an IGTE second stage airfoil removed from service after 32,000 hours of exposure was metallographically examined. Observed were isotropically coarsened and N-raft like microstructures in material near the internal cooling passages, and P-raft like microstructures in both the platform and outer surface of the airfoil root exposed to the hot combustions gases. In each case, the γ' precipitates were found to be nearly four times the width of the initial γ' in the as-heat treated state in their shortest dimension. The width of the γ' being indicative that the microstructures were in the late stages of coarsening.
    - As-heat treated microstructure was artificially aged to produce the three microstructure states observed in the service component; isotropically coarsened, N-raft, and P-raft. Isotropic coarsening was observed to occur over the entire temperature range considered (850-1000°C). Similarly, directional coarsening was observed under loads at 900°C and 950°C. However, directional coarsening was observed to be in the extreme early stages for exposure to 850°C. Further, the aging characteristics of the microstructure were captured through an analytical model.
    - Experimentally, the elastic modulus was determined to be microstructure independent within statistical reason, while aging was found to

have an effect on the yield strength. Overall, aging of the microstructure resulted in a softening effect with regards to the 0.02% yield strength, while the 0.2% yield strength of the aged microstructure exhibited similar values to the as-heat treated microstructure in the 20-750°C temperature range.

2. **Determine the effects of TMF loading conditions on the crack initiation in a DS Ni-base superalloy in the as-heat-treated state.**

    - Experiments were conducted under both IP and OP TMF conditions with T_{min} of 100°C and 500°C, while the T_{max} was varied between 750°C and 950°C. Overall, experiments with the T_{min}=100°C were observed to have a 50-80% reduced TMF life over the TMF life of material exposed to identical mechanical strain amplitudes at the T_{min}=500°C. Ultimately, due to the lack of observed microstructure evolution and creep interactions, especially with T_{max}=750°C, the reduction in TMF life was related to the increase in the elastic properties with decreasing temperature from 500°C to 100°C resulting in an increase in the plastic strain amplitude.

    - Above a threshold mechanical strain amplitude, IP TMF loadings were life limiting, while below OP TMF loading were. Ultimately this occurrence was found to be associated with the fatigue crack propagation from debonded carbides under IP TMF conditions within the interdendritic regions and along the grain boundaries in the L-orientation. Additionally, the transition between IP and OP TMF dominance was determined to vary with both T_{min} and orientation.

    - TMF life was found to be independent of mean strain. This was determined through conducting TMF experiments under IP $R_\epsilon = -1$ and

$R_\epsilon = 0$ as well as OP $R_\epsilon = -1$ and $R_\epsilon = -\infty$. While the starting stresses and strain were different, the half-life, cyclic deformation response, and cycles to crack initiation were found to be within typical variations for TMF experiments conducted with the same temperature-load phasing and mean strains.

- Creep-fatigue (CF) interactions were found to result in a drastic life reduction over material exposed to identical conditions under continuously cycled (CC) CC conditions. Under low mechanical strain amplitude conditions, microstructures exposed to OP CF TMF conditions were observed to have undergone directionally coarsening, whereas those exposed to IP CF TMF conditions were not directionally coarsened. Sufficient exposure time was not available in the IP CF TMF experiments to allow for directional coarsening to occur.
- Experiments conducted in the transverse orientation were found to exhibit the same TMF life traits as the longitudinal orientation, except the primary fatigue crack propagation mechanism was observed to be transgranular cracking and the life was reduced in comparison to the L-orientation.

3. **Determine the effect of thermally induced microstructure changes on the cyclic deformation response of a Ni-base superalloy.**

    - Material in a isotropically coarsened state was found to exhibit a 2x reduction in life under both CC and CF TMF conditions. Ultimately, this was determined to be associated with the increase in the size of the γ' size resulting in a reduction in the threshold stress to by-pass the γ' precipitates at temperatures below 750°C when compared to the as-heat treated microstructure.

- Similar to the isotropically coarsened microstructure, the N-raft microstructure was also observed to result in a 2x reduction in TMF life when compared to the as-heat treated TMF behavior. As a result of the preferential alignment of the γ' rafts normal to the axis of the applied load, the γ channels provided a preferred avenue for fatigue crack propagation.
- Unlike the other aged microstructure states, P-rafts were observed to be beneficial towards enhancing the TMF life under creep fatigue conditions. When compared to the as-heat treated material a 2x increase was observed. However, a 2x decrease under CC conditions was also found. Explaining these findings was the fact that the P-raft microstructure hindered the movement of dislocations at temperatures above 850°C and as a result was able to enhance the lives of material exposed to CF TMF.

4. **Establish a crystal viscoplastic model that captures the influences of aging on the cyclic behavior of a Ni-base superalloy.**

    - Microstructure sensitivity was successfully introduced into the CVP model framework through coupling the influence of the γ' evolution and material parameter evolution. Within the CVP model framework the state of the microstructure was determined through considering the evolution of the γ channel width.
    - Acceptable predictions of TMF responses in the aged state were determined by the CVP model, with the only aspect of the behavior not being fully captured being the reverse yielding that the aged microstructures exhibit when undergoing TMF.

CHAPTER IX

RECOMMENDATIONS

There are several additional research opportunities that could add value and broaden the findings presented in this study. Listed below are several potential research areas that could add to the knowledge-base of thermomechanical fatigue crack formation in Ni-base superalloys in the presence of aged microstructures.

Assess Statistical Life Distribution in the Transverse and Off-Axis Orientation In the L-orientation, the well ordered dendritic structure provided for a low amount of experimental scatter in the TMF life results. However, for TMF experiments conducted in the T-orientation, the presence of random grain orientations, grain boundaries, and grain boundary carbides introduced additional scatter in the TMF life results. As a result, identification of specific trends and effects of TMF loadings conditions could not be made. In future work, enhanced testing for determining the statistical life distribution coupled with modeling the behavior with statistical volume elements in the transverse and off-axis orientations is proposed.

Advanced Artificial Aging Within this work the $\gamma - \gamma'$ microstructure was successfully artificially aged to generate three unique microstructural states. While the unique artificial states were similar of those found within a service component at the end of its service life, the actual service component microstructures exhibited a degree of isotropic coarsening 10x that of the artificial aged microstructures. In future work, it is proposed that alternative aging methods be developed to accelerate the coarsening within reasonable laboratory time periods.

TEM Microstructural Analysis In this work only optical and scanning electron microscopy were utilized to examine the microstructure and provide interpretation of fatigue mechanisms. Through examining the microstructures with transmission electron microscopy an understanding of the dislocation movement and interaction with each of the unique microstructural states under TMF conditions can be determined. This analysis would then provide definitive information determining the controlling aspects for fatigue crack initiation and propagation through each of the aged microstructures.

CVP Model Iterative Solver Proposed were modifications to the back stress in the CVP to capture the effects of aging on the hardening behavior of the material. The modification to the back stress was found to be unstable when iteratively solving for a converging solution. In future work, it would be beneficial if the CVP model would be reformulated with a new numerical solver that provides for enhanced numerical stability and ability to capture to effects of microstructure aging on the hardening behavior.

Phase Field Microstructure Model To capture microstructure evolution within the CVP model, an analytical model was used. While this model was able to capture the desired microstructure evolution, the model was limited in scope. To further enhance the capability of the CVP model, the incorporation of a phase field model similar to the ones developed by Gaubert et al. [168] and Zhou et al. [169] would be capable of capturing the evolution of the microstructure and interaction amongst neighboring precipitates would prove beneficial. Through such a phase field model could also be captured the length effects of the γ' rafts.

Composition Dependent CVP Model To further enhance the CVP model beyond microstructure dependence, the CVP model can be made composition dependent

through coupling material data packages such as Thermo-Calc and DICTRA to the CVP model. The added benefit of a compositional dependent CVP model would be the ability to simulate the effects of diffusional processes that occur in service components on the mechanical response of the material similar to the work of Bench et al. [170] and as a tool through which the optimal alloy chemical composition could be determined in relation to mechanical performance.

Reduced Order Constitutive Modeling To build upon previous work of Neal and Neu [171], the addition of microstructure sensitivity to a reduced order modeling framework would prove beneficial for service component design. Following the approach of Neal and Neu, the microstructure sensitive CVP model could be used to generate a training data set for each unique microstructure as a function of temperature, strain rate, and loading orientation. Coupled with an artificial neural network, sets of microstructure sensitive Ramberg-Osgood parameters could then be determined for use in a reduced order constitutive model. Overall, this reduced order constitutive model would prove beneficial as a first order estimate for determining the material's behavior after extended service life for enhancing component design life.

APPENDIX A

COMPRESSION CREEP FRAME MECHANICAL DRAWINGS

BILL OF MANUFACTURED COMPONENTS

ITEM NO.	PART NUMBER	COMMENT	QTY.
1	SIDE BRACKET	WATER-JET	4
2	STAINLESS SUPPORT #1	MACHINE	1
3	STAINLESS SUPPORT#2	MACHINE	2
4	HYDRAULIC SUBASSEMBLY		
4.1	HYDRAULIC SUPPORT BRACKET	WATER-JET	2
4.2	HYDRAULIC BASE	MACHINE	1
4.3	BALL JOINT	MACHINE	1
4.4	STAINLESS SUPPORT#5	MACHINE	1
4.5	INDICATOR MOUNT	MACHINE	1
4.6	TOP HYDRAULIC BRACKET	MACHINE	1
4.8	INDICATOR BRACKET	MACHINE	1
5	LOCATOR PLATE	WATER-JET	1
6	SPECIMEN LOCATOR	WATER-JET/MACHINE	2
7	STEEL BASE PLATE	MACHINE	1

MATERIAL INFORMATION

MATERIAL

SPECIFICATIONS

FINISH / COND

SPECIAL NOTES

DIM / TOLERANCE INFORMATION

UNLESS OTHERWISE SPECIFIED

UNITS -UNITS ARE INCHES
-ALTERNATE UNITS ARE MILLIMETERS IN [BRACKETS]
-REF DIMS IN (PARENTHESES)

TOLERANCES

DECIMAL:	ANGULAR:
X ± .03	X°±1°
XX ± .01	X°± 5°
XXX ± .005	

DRAWING / SHEET INFORMATION

Georgia Institute of Technology

DO NOT SCALE DRAWING

DRAWN M. KIRKA

DATE 24 JUNE 2013

DWG NAME COMPRESSION FRAME BILL OF MANUFACTURED COMPONENTS

NAME COMPRESSION FRAME BILL OF MANUFACTURED COMPONENTS

CHECKED

DATE

CFG NAME

APPROVED

PART NO

DATE

REVISION PROTOTYPE

SHEET SHEET 1 OF 3

SIZE B

SHEET SCALE 1:1

THIRD ANGLE PROJECTION

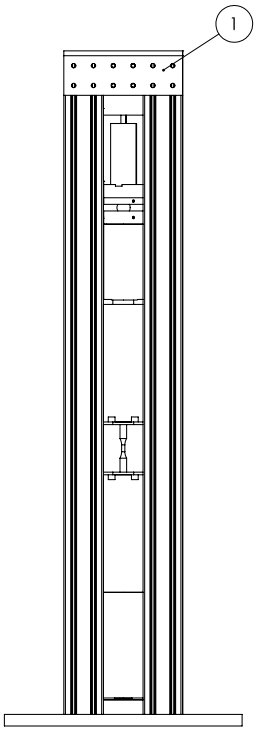

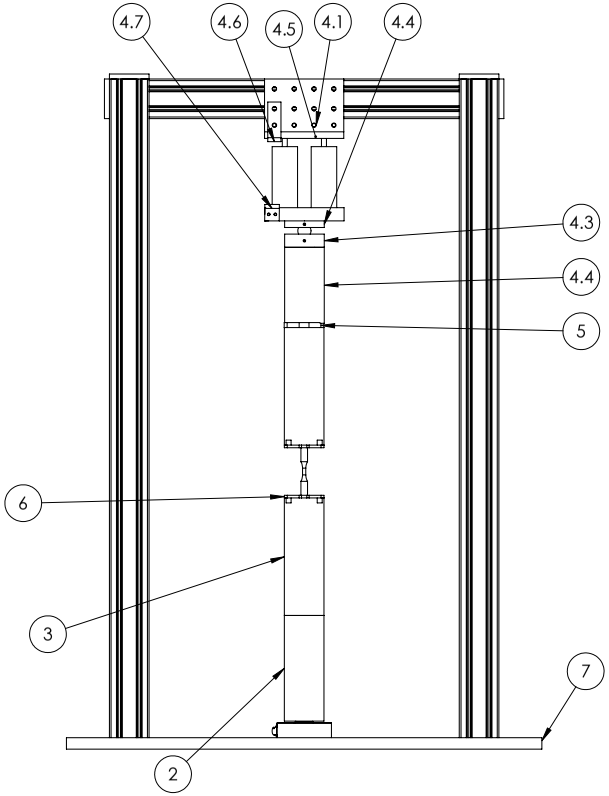

MATERIAL INFORMATION
MATERIAL
SPECIFICATIONS
FINISH / COND
SPECIAL NOTES

DIM / TOLERANCE INFORMATION	
UNLESS OTHERWISE SPECIFIED	UNITS: -UNITS ARE INCHES -ALTERNATE UNITS ARE MILLIMETERS IN [BRACKETS] -REF DIMS IN (PARENTHESES)
	TOLERANCES DECIMAL: X ± .03, XX ± .01, XXX ± .005 ANGULAR: X° ± 1°, X° ± 5°

DRAWING / SHEET INFORMATION			
Georgia Institute of Technology		DO NOT SCALE DRAWING	
		DRAWN: M. KIRKA	
		DATE: 21 JUNE 2013	
DWG NAME		CHECKED	
NAME: COMPRESSION CREEP FRAME		DATE	
CFG NAME		APPROVED	
PART NO		DATE	
REVISION: PROTOTYPE	SHEET: SHEET 2 OF 3	SIZE: B	SHEET SCALE: 1:8
THIRD ANGLE PROJECTION			

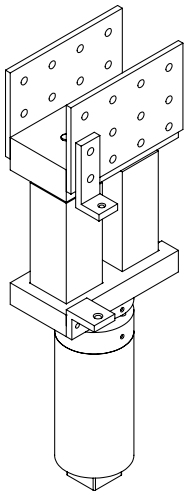

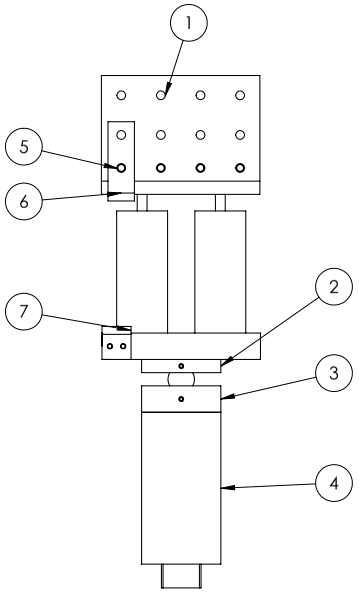

MATERIAL INFORMATION	
MATERIAL	
SPECIFICATIONS	
FINISH / COND	
SPECIAL NOTES	

DIM / TOLERANCE INFORMATION	
UNLESS OTHERWISE SPECIFIED	UNITS: -UNITS ARE INCHES -ALTERNATE UNITS ARE MILLIMETERS IN [BRACKETS] -REF DIMS IN (PARENTHESES)
	TOLERANCES DECIMAL: X ± .03, XX ± .01, XXX ± .005 ANGULAR: X° ±1°, X° ± 5°

DRAWING / SHEET INFORMATION			
Georgia Institute of Technology		DO NOT SCALE DRAWING	
		DRAWN	M. KIRKA
		DATE	24 JUNE 2013
DWG NAME	HYDRAULIC SUBASSEMBLY	CHECKED	
NAME	HYDRAULIC SUBASSEMBLY	DATE	
CFG NAME		APPROVED	
PART NO		DATE	
REVISION	PROTOTYPE	SHEET	SHEET 3 OF 3
SIZE	B	SHEET SCALE	1:4
THIRD ANGLE PROJECTION			

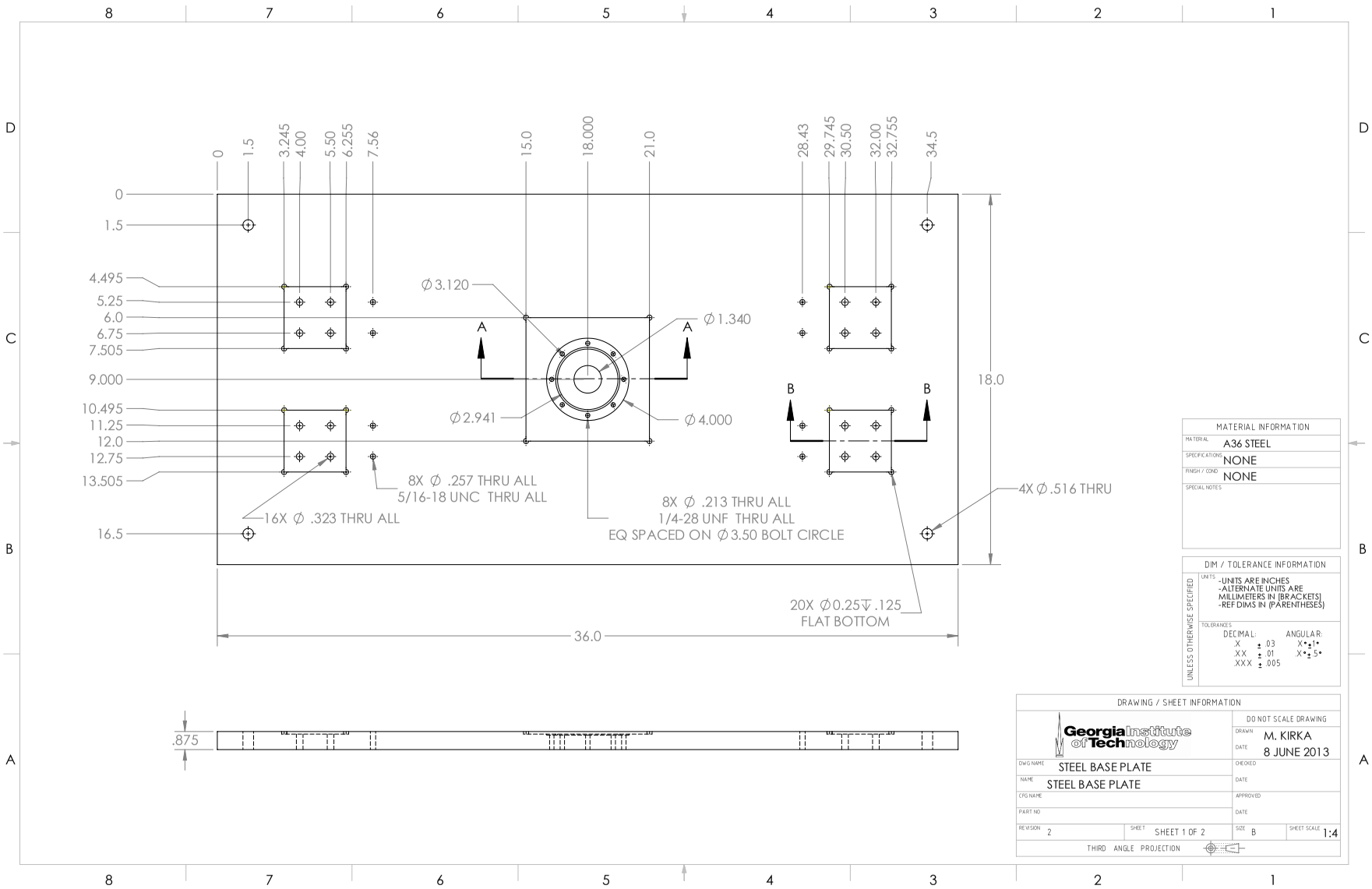

MATERIAL INFORMATION	
MATERIAL	A36 STEEL
SPECIFICATIONS	NONE
FINISH / COND	NONE
SPECIAL NOTES	

DIM / TOLERANCE INFORMATION		
UNLESS OTHERWISE SPECIFIED	UNITS	-UNITS ARE INCHES -ALTERNATE UNITS ARE MILLIMETERS IN [BRACKETS] -REF DIMS IN (PARENTHESES)
	TOLERANCES	DECIMAL: X ± .03, XX ± .01, XXX ± .005 ANGULAR: X° ± 1°, X° ± 5°

DRAWING / SHEET INFORMATION		
Georgia Institute of Technology		DO NOT SCALE DRAWING
	DRAWN	M. KIRKA
	DATE	8 JUNE 2013
DWG NAME	STEEL BASE PLATE	CHECKED
NAME	STEEL BASE PLATE	DATE
CFG NAME		APPROVED
PART NO		DATE
REVISION 2	SHEET SHEET 1 OF 2	SIZE B / SHEET SCALE 1:4
THIRD ANGLE PROJECTION		

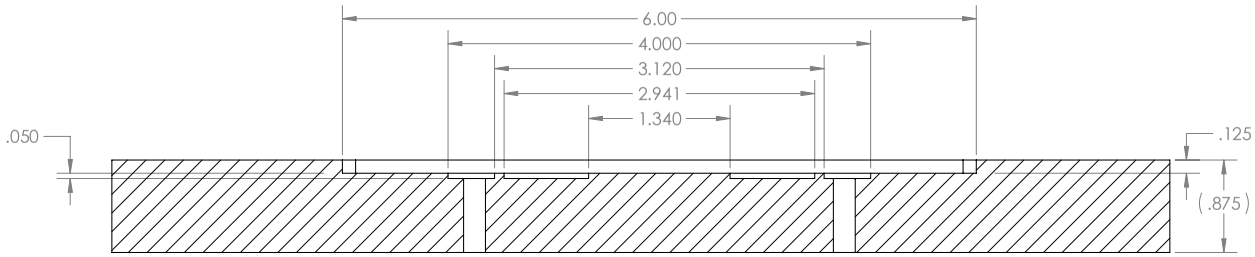

SECTION A-A

SCALE 1 : 1

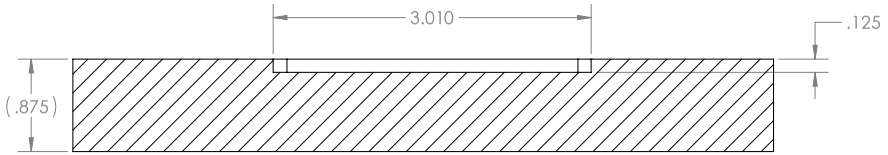

SECTION B-B

SCALE 1 : 1

MATERIAL INFORMATION	
MATERIAL	A36 STEEL
SPECIFICATIONS	NONE
FINISH / COND	NONE
SPECIAL NOTES	

DIM / TOLERANCE INFORMATION	
UNLESS OTHERWISE SPECIFIED	UNITS: -UNITS ARE INCHES -ALTERNATE UNITS ARE MILLIMETERS IN [BRACKETS] -REF DIMS IN (PARENTHESES)
TOLERANCES	DECIMAL: X ± .03, XX ± .01, XXX ± .005 ANGULAR: X° ± 1°, .X° ± 5°

DRAWING / SHEET INFORMATION			
Georgia Institute of Technology		DO NOT SCALE DRAWING	
		DRAWN	M. KIRKA
		DATE	8 JUNE 2013
DWG NAME	STEEL BASE PLATE	CHECKED	
NAME	STEEL BASE PLATE	DATE	
CFG NAME		APPROVED	
PART NO		DATE	
REVISION	2	SHEET	SHEET 2 OF 2
SIZE	B	SHEET SCALE	1:1
THIRD ANGLE PROJECTION			

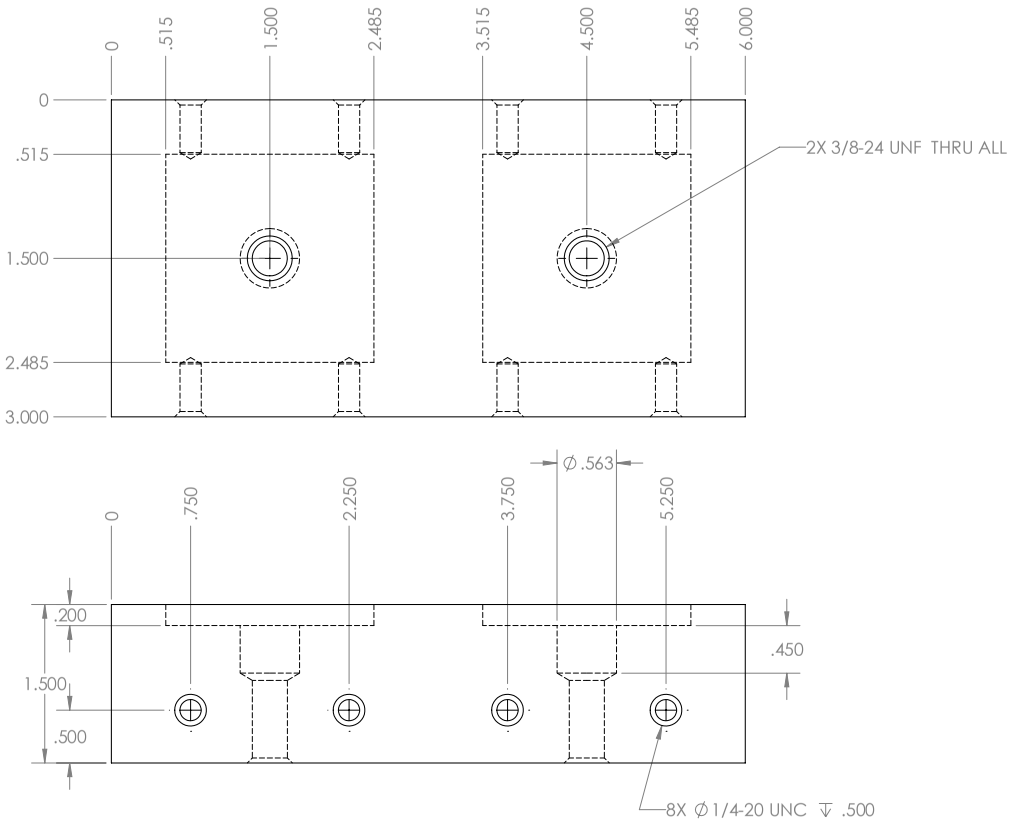

MATERIAL INFORMATION	
MATERIAL	4140 STEEL
SPECIFICATIONS	NONE
FINISH / COND	NONE
SPECIAL NOTES	

DIM / TOLERANCE INFORMATION	
UNLESS OTHERWISE SPECIFIED	UNITS: -UNITS ARE INCHES -ALTERNATE UNITS ARE MILLIMETERS IN [BRACKETS] -REF DIMS IN (PARENTHESES)
TOLERANCES	DECIMAL: X ± .03, XX ± .01, XXX ± .005 ANGULAR: X° ±1°, .X° ± 5°

DRAWING / SHEET INFORMATION			
Georgia Institute of Technology		DO NOT SCALE DRAWING	
		DRAWN	M. KIRKA
DWG NAME	TOP HYDRALIC BRACKET	DATE	17 APRIL 2013
NAME	TOP HYDRALIC BRACKET	CHECKED	
CFG NAME		DATE	
PART NO		APPROVED	
REVISION	PROTOTYPE	DATE	
SHEET	SHEET 1 OF 1	SIZE	B
SHEET SCALE	1:1		
THIRD ANGLE PROJECTION			

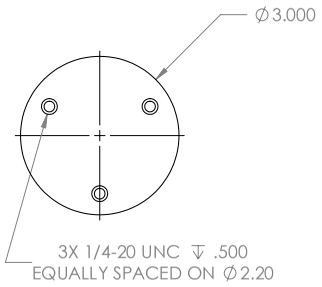

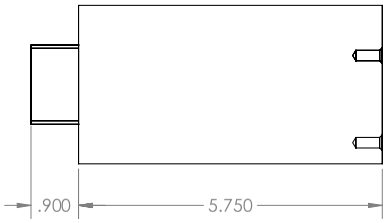

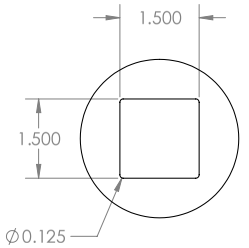

MATERIAL INFORMATION	
MATERIAL	4140 STEEL
SPECIFICATIONS	NONE
FINISH / COND	NONE
SPECIAL NOTES	

DIM / TOLERANCE INFORMATION	
UNLESS OTHERWISE SPECIFIED	UNITS: -UNITS ARE INCHES -ALTERNATE UNITS ARE MILLIMETERS IN [BRACKETS] -REF DIMS IN (PARENTHESES)
	TOLERANCES: DECIMAL: X ± .03, XX ± .01, XXX ± .005; ANGULAR: X°±1°, .X°±.5°

DRAWING / SHEET INFORMATION			
Georgia Institute of Technology		DO NOT SCALE DRAWING	
		DRAWN	M. KIRKA
		DATE	17 APRIL 2013
DWG NAME	STEEL SUPPORT #5	CHECKED	
NAME	STEEL SUPPORT #5	DATE	
CFG NAME		APPROVED	
PART NO		DATE	
REVISION	PROTOTYPE	SHEET	SHEET 1 OF 1
SIZE	B	SHEET SCALE	1:2
THIRD ANGLE PROJECTION			

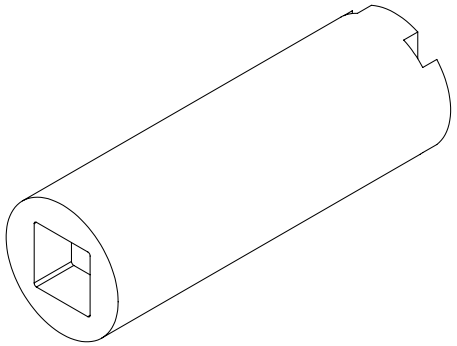

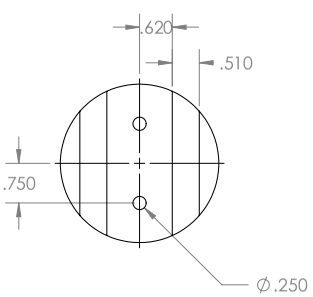

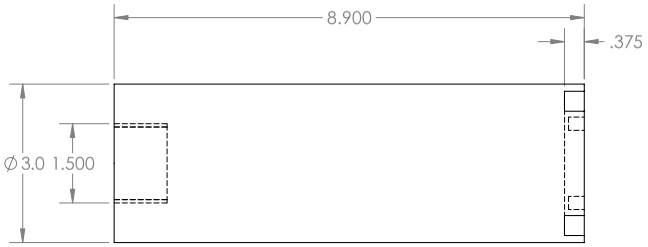

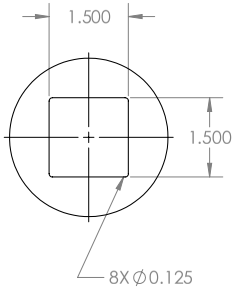

MATERIAL INFORMATION	
MATERIAL	316 STAINLESS STEEL
SPECIFICATIONS	NONE
FINISH / COND	NONE
SPECIAL NOTES	

DIM / TOLERANCE INFORMATION	
UNLESS OTHERWISE SPECIFIED	UNITS: -UNITS ARE INCHES -ALTERNATE UNITS ARE MILLIMETERS IN [BRACKETS] -REF DIMS IN (PARENTHESES)
TOLERANCES	DECIMAL: X ± .03, XX ± .01, XXX ± .005 ANGULAR: X° ± 1°, X.X° ± 5°

DRAWING / SHEET INFORMATION			
Georgia Institute of Technology		DO NOT SCALE DRAWING	
		DRAWN	M. KIRKA
		DATE	3 MAR 2013
DWG NAME	STAINLESS SUPPORT #2	CHECKED	
NAME	STAINLESS SUPPORT #2	DATE	
CFG NAME		APPROVED	
PART NO		DATE	
REVISION	PROTOTYPE	SHEET	SHEET 1 OF 1
SIZE	B	SHEET SCALE	1:1
THIRD ANGLE PROJECTION			

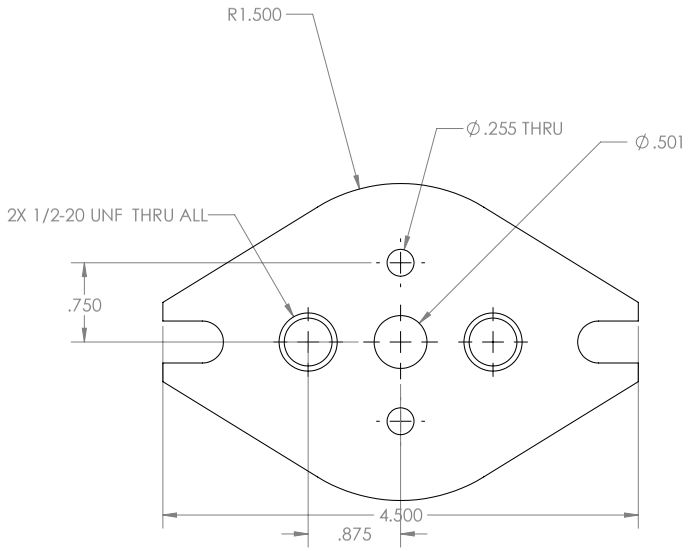

MATERIAL INFORMATION	
MATERIAL	4140 STEEL
SPECIFICATIONS	NONE
FINISH / COND	NONE
SPECIAL NOTES	

DIM / TOLERANCE INFORMATION	
UNLESS OTHERWISE SPECIFIED	UNITS: -UNITS ARE INCHES -ALTERNATE UNITS ARE MILLIMETERS IN [BRACKETS] -REF DIMS IN (PARENTHESES)
	TOLERANCES: DECIMAL: X ± .03, XX ± .01, XXX ± .005; ANGULAR: X° ±1°, .X° ± 5°

DRAWING / SHEET INFORMATION			
Georgia Institute of Technology		DO NOT SCALE DRAWING	
		DRAWN	M. KIRKA
		DATE	6 JUNE 2013
DWG NAME	SPECIMEN LOCATOR	CHECKED	
NAME	SPECIMEN LOCATOR	DATE	
CFG NAME		APPROVED	
PART NO		DATE	
REVISION	PROTOTYPE	SHEET	SHEET 1 OF 1
SIZE	B	SHEET SCALE	1:1
THIRD ANGLE PROJECTION			

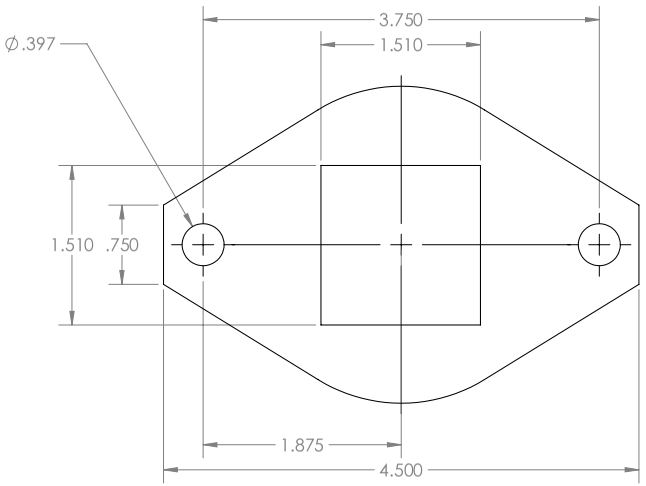

MATERIAL INFORMATION	
MATERIAL	4140 STEEL
SPECIFICATIONS	NONE
FINISH / COND	NONE
SPECIAL NOTES	

DIM / TOLERANCE INFORMATION	
UNLESS OTHERWISE SPECIFIED	UNITS: -UNITS ARE INCHES -ALTERNATE UNITS ARE MILLIMETERS IN [BRACKETS] -REF DIMS IN (PARENTHESES)
TOLERANCES	DECIMAL: X ± .03, XX ± .01, XXX ± .005 ANGULAR: X° ±1°, .X° ± 5°

DRAWING / SHEET INFORMATION			
Georgia Institute of Technology		DO NOT SCALE DRAWING	
		DRAWN	M. KIRKA
		DATE	6 JUNE 2013
DWG NAME	LOCATOR PLATE	CHECKED	
NAME	LOCATOR PLATE	DATE	
CFG NAME		APPROVED	
PART NO		DATE	
REVISION	PROTOTYPE	SHEET	SHEET 1 OF 1
SIZE	B	SHEET SCALE	1:1
THIRD ANGLE PROJECTION			

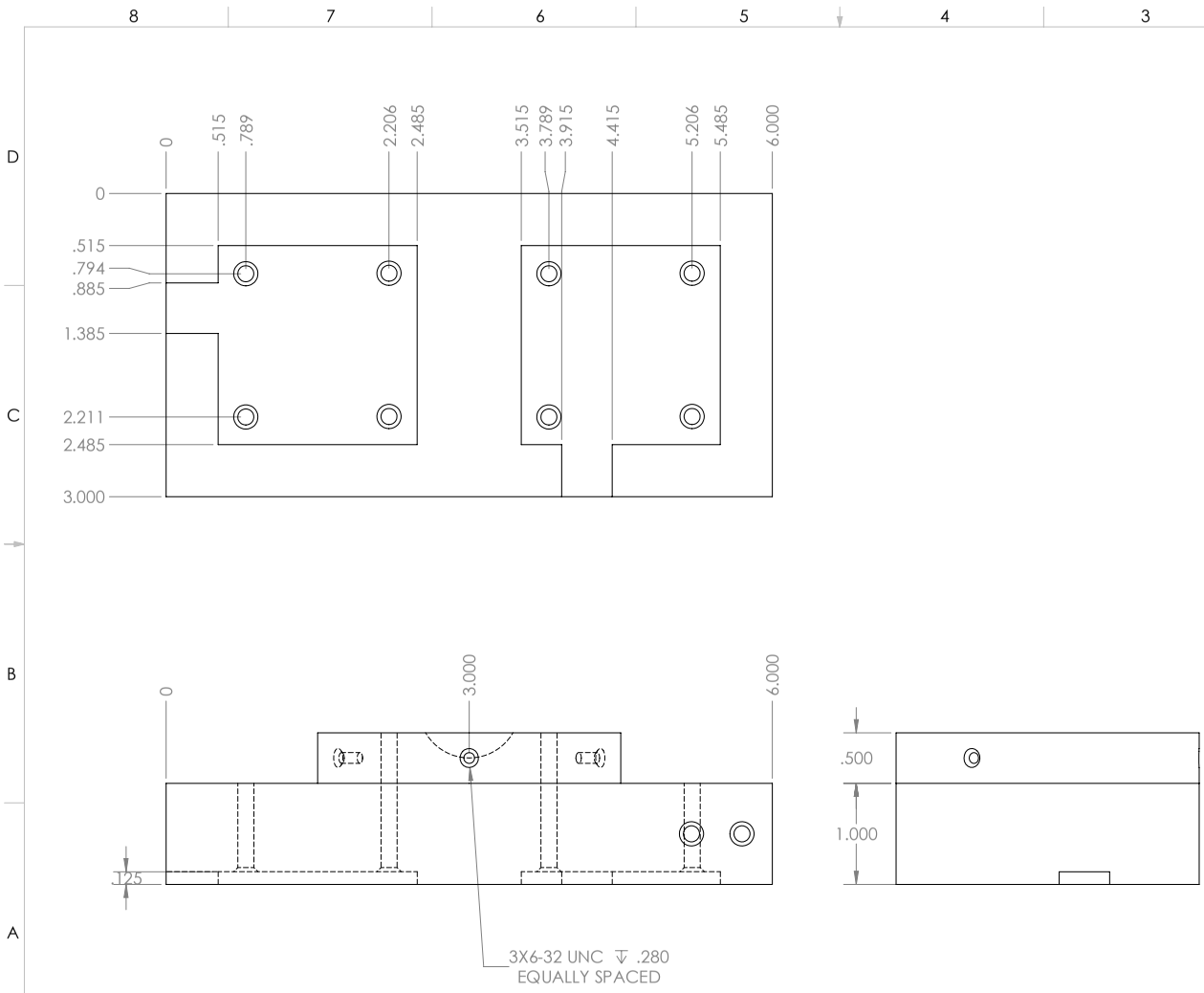

MATERIAL INFORMATION	
MATERIAL	4140 STEEL
SPECIFICATIONS	NONE
FINISH / COND	NONE
SPECIAL NOTES	

DIM / TOLERANCE INFORMATION	
UNLESS OTHERWISE SPECIFIED	UNITS: -UNITS ARE INCHES -ALTERNATE UNITS ARE MILLIMETERS IN [BRACKETS] -REF DIMS IN (PARENTHESES)
TOLERANCES	DECIMAL: X ± .03, XX ± .01, XXX ± .005 ANGULAR: X° ± 1°, X° ± 5°

DRAWING / SHEET INFORMATION		
Georgia Institute of Technology		DO NOT SCALE DRAWING
DWG NAME	HYDRAULIC CYLINDER BASE	DRAWN: M. KIRKA
NAME	HYDRAULIC CYLINDER BASE	DATE: 11 APRIL 2013
CFG NAME		CHECKED
PART NO		DATE
REVISION: PROTOTYPE	SHEET: SHEET 1 OF 2	APPROVED
SIZE: B	SHEET SCALE: 1:1	DATE
THIRD ANGLE PROJECTION		

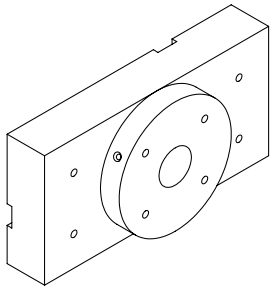

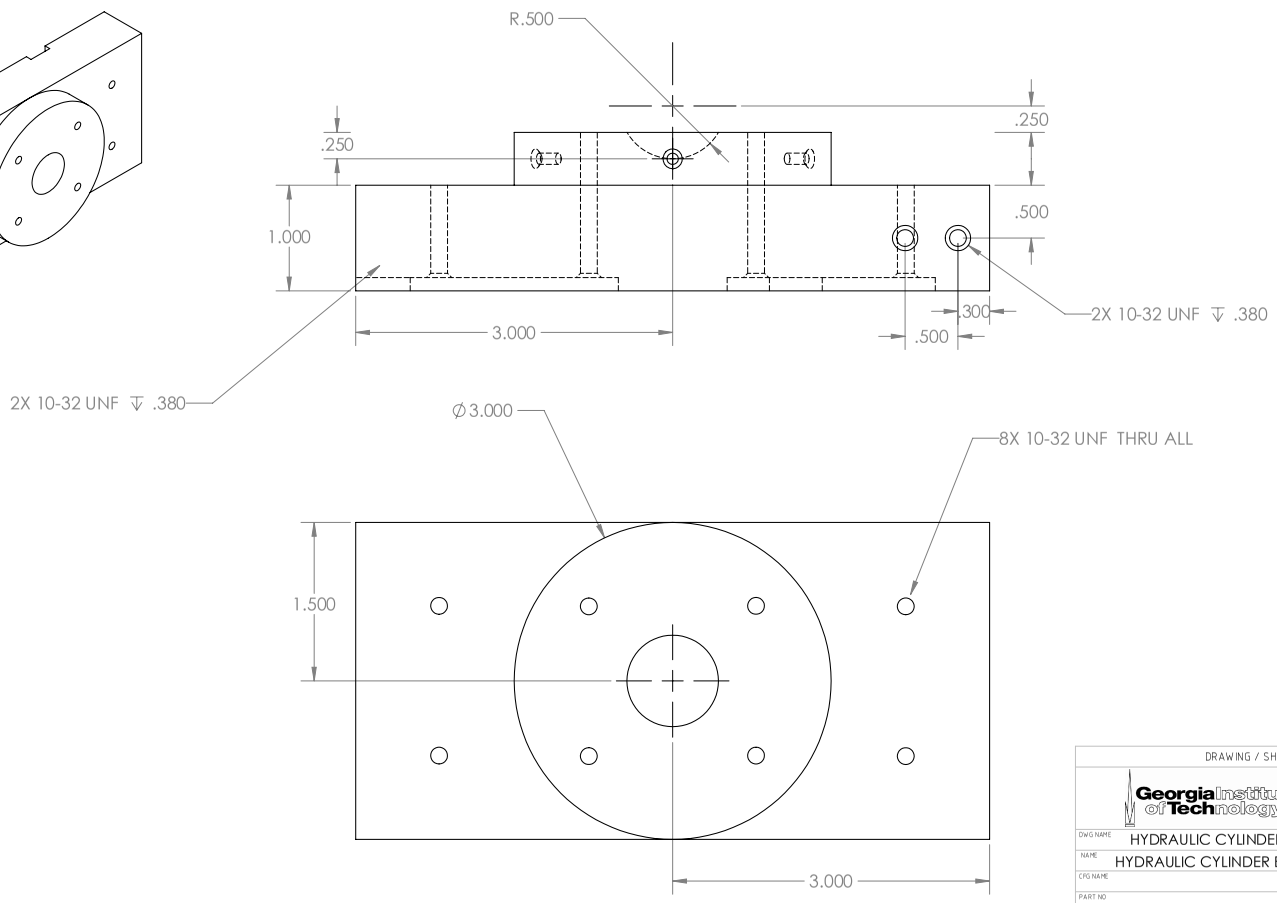

MATERIAL INFORMATION	
MATERIAL	4140 STEEL
SPECIFICATIONS	NONE
FINISH / COND	NONE
SPECIAL NOTES	

DIM / TOLERANCE INFORMATION		
UNLESS OTHERWISE SPECIFIED	UNITS	-UNITS ARE INCHES -ALTERNATE UNITS ARE MILLIMETERS IN [BRACKETS] -REF DIMS IN (PARENTHESES)
	TOLERANCES	DECIMAL: X ± .03, XX ± .01, XXX ± .005 ANGULAR: X° ±1°, .X° ± 5°

DRAWING / SHEET INFORMATION			
Georgia Institute of Technology		DO NOT SCALE DRAWING	
		DRAWN	M. KIRKA
		DATE	11 APRIL 2013
DWG NAME	HYDRAULIC CYLINDER BASE	CHECKED	
NAME	HYDRAULIC CYLINDER BASE	DATE	
CFG NAME		APPROVED	
PART NO		DATE	
REVISION	PROTOTYPE	SHEET	SHEET 2 OF 2
SIZE	B	SHEET SCALE	1:1
THIRD ANGLE PROJECTION			

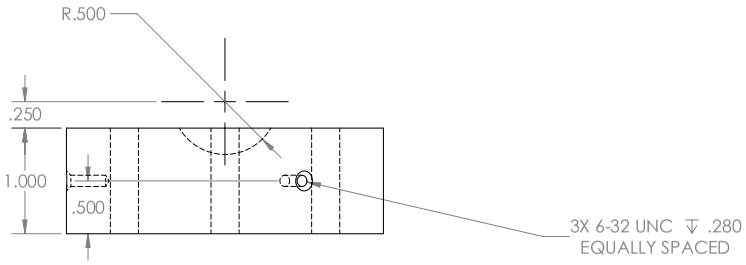

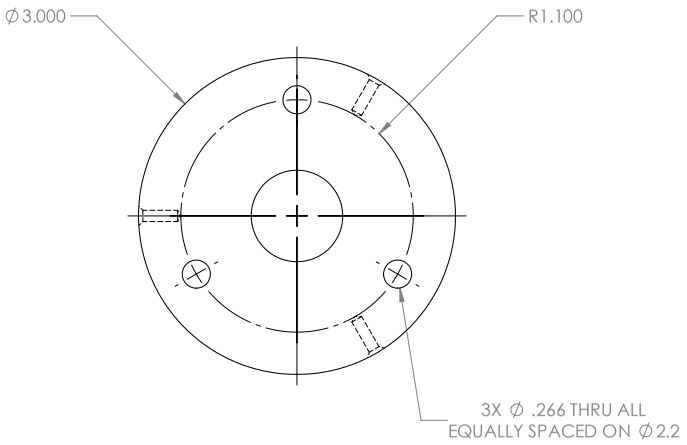

MATERIAL INFORMATION	
MATERIAL	4140 STEEL
SPECIFICATIONS	NONE
FINISH / COND	NONE
SPECIAL NOTES	

DIM / TOLERANCE INFORMATION		
UNLESS OTHERWISE SPECIFIED	UNITS	-UNITS ARE INCHES -ALTERNATE UNITS ARE MILLIMETERS IN [BRACKETS] -REF DIMS IN (PARENTHESES)
	TOLERANCES	DECIMAL: X ± .03, XX ± .01, XXX ± .005 ANGULAR: X° ±1°, X.X° ± 5°

DRAWING / SHEET INFORMATION			
Georgia Institute of Technology			DO NOT SCALE DRAWING
		DRAWN	M. KIRKA
		DATE	10 APRIL 2013
DWG NAME	BALL JOINT	CHECKED	
NAME	BALL JOINT	DATE	
CFG NAME		APPROVED	
PART NO		DATE	
REVISION	PROTOTYPE	SHEET	SHEET 1 OF 1
SIZE	B	SHEET SCALE	1:1
THIRD ANGLE PROJECTION			

APPENDIX B

EXPERIMENTAL DATA

Table B.1: Experimental data for IP fatigue tests conducted on CM247LC-DS in the as-heat treated state.

Specimen ID	IP/OP	L/T	R	T_{min}[°C]	T_{max} [°C]	$\Delta\epsilon_{mech}$ [%]	Cycle Time [sec]	Dwell [min]	$\Delta\epsilon_{plas}$[%]	σ_{min} [MPa]	σ_{max} [MPa]	$\Delta\sigma$ [MPa]	σ_{mean} [MPa]	N_i
S7L-15	IP	L	-1	500	950	1.2	180	0	0.052	471	-739	1210	-134	155
S8L-7	IP	L	-1	500	950	1	180	0	0.006	241	-750	991	-255	914
S4L-12	IP	L	0	100	950	0.8	600	0	0.023	200	-752	952	-276	933
1L2-19	IP	L	0	100	950	1	360	0	0.016	414	-663	1077	-125	183
S7L-6	IP	L	0	100	950	1	600	0	0.072	379	-734	1112	-178	146
S7L-23	IP	L	0	100	950	0.9	600	0	0.006	258	-702	960	-222	544
S6L-3	IP	L	0	100	850	1	400	0	0.005	463	-692	1155	-114	1035
S4L-20	IP	L	0	100	850	1.1	600	0	0.01	407	-741	1149	-167	389
S4L-4	IP	L	0	100	750	1.2	240	0	0.017	528	-799	1327	-136	1116
S7L-9	IP	L	0	100	950	1	360	20	0.242	409	-719	1128	-155	37
S5L-10	IP	L	0	100	850	1.1	360	20	0.03	406	-840	1246	-217	127
S5L-14	IP	L	0	100	750	1.2	240	20	0.013	597	-786	1383	-94	213
S7L-24	IP	L	0	100	950	0.8	600	20	0.022	209	-693	902	-242	210
S6L-1	IP	L	0	500	950	1	180	0	0.005	247	-751	998	-252	1000
S4L-19	IP	L	0	500	950	1	180	0	0.009	712	-304	1016	204	824
S7L-10	IP	L	0	500	950	1	180	0	0.001	229	-763	991	-267	1446
S7L-5	IP	L	0	500	950	0.85	180	0	0.067	195	-662	857	-234	4579
S7L-7	IP	L	0	500	950	1.2	180	0	0.029	373	-729	1102	-178	257
S4L-17	IP	L	0	500	850	1	140	0	0.005	395	-592	987	-99	3827
S5L-17	IP	L	0	500	850	1.1	140	0	0	386	-725	1111	-170	1707
S4L-9	IP	L	0	500	750	1.2	120	0	0.01	605	-668	1273	-31	4392
S7T-2	IP	T	0	100	950	0.55	400	0	0.006	268	-672	940	-202	558
S9T-11	IP	T	0	100	950	0.8	600	0	0.114	412	-701	1114	-144	63
S7T-7	IP	T	0	100	950	0.75	600	0	0.075	401	-738	1138	-168	90
S5T-11	IP	T	0	100	750	0.75	360	0	0.008	567	-565	1132	1	2460
S5T-13	IP	T	0	100	750	0.95	480	0	0.029	686	-762	1448	-38	825
S2T-3	IP	T	0	100	950	0.55	400	20	0.041	228	-667	895	-220	87
S7L-2	Isothermal	L	-1	20	20	1.3	60	0	0.042	834	-848	1682	-7	4832

Table B.2: Experimental data for OP fatigue tests conducted on CM247LC-DS in the as-heat treated state.

Specimen ID	IP/OP	L/T	R	T_{min}[°C]	T_{max} [°C]	$\Delta\epsilon_{mech}$ [%]	Cycle Time [sec]	Dwell [min]	$\Delta\epsilon_{plas}$[%]	σ_{min} [MPa]	σ_{max} [MPa]	$\Delta\sigma$ [MPa]	σ_{mean} [MPa]	N_i
S7L-3	OP	L	$-\infty$	100	950	1.1	600	0	0.065	797	-341	1138	228	661
S4l-7	OP	L	$-\infty$	100	950	0.8	420	0	0.005	734	-265	999	234	2099
S8L-9	OP	L	$-\infty$	100	950	0.9	600	0	0.021	797	-216	1012	290	1423
S9L-8	OP	L	$-\infty$	100	950	0.8	600	0	0.003	747	-165	912	291	0.25
S4L-1	OP	L	$-\infty$	100	950	1	600	0	0.046	780	-327	1107	226	552
S7L-14	OP	L	$-\infty$	100	850	1.1	360	0	0.01	744	-607	1351	68	1919
S6L-2	OP	L	$-\infty$	100	750	1.2	330	0	0.024	784	-695	1479	44	3558
S8L-2	OP	L	$-\infty$	100	950	0.8	600	20	0.045	706	-205	911	251	480
S5L-18	OP	L	$-\infty$	500	950	0.8	180	0	0.009	631	-177	808	227	3753
1L2-4	OP	L	$-\infty$	500	950	1	180	0	0.009	742	-257	999	242	1990
S4L-13	OP	L	$-\infty$	500	950	1	180	0	0.005	788	-256	1043	266	921
S7L-16	OP	L	$-\infty$	500	950	1.2	180	0	0.013	828	-362	1190	233	576
1L2-20	OP	L	$-\infty$	500	850	1.1	140	0	0.023	681	-516	1197	82	1859
S4L-18	OP	L	$-\infty$	500	950	0.8	240	20	0.081	713	-101	814	306	451
S1L-4	OP	L	-1	500	950	1.1	180	0	0.015	766	-336	1101	215	733
S9L-3	OP	L	-1	500	950	1	180	0	0.006	820	-230	1049	295	815
S5T-6	OP	T	$-\infty$	100	950	0.55	480	0	0.006	653	-226	879	214	2037
S7T-4	OP	T	$-\infty$	100	950	0.8	600	0	0.077	731	-384	1116	174	473
S3T-1	OP	T	$-\infty$	100	950	0.55	360	20	0.294	628	-191	819	219	790
S5T-10	OP	T	$-\infty$	500	950	0.8	180	0	0.072	722	-335	1057	193	317
S5T-7	OP	T	$-\infty$	500	950	0.55	180	0	0.018	621	-112	734	255	2563
S5T-4	OP	T	$-\infty$	500	950	0.55	240	20	0.067	574	-149	723	212	530
S2T-1	OP	T	-1	500	950	0.7	180	0	0.006	680	-254	934	213	539

Table B.3: Experimental data for fatigue tests conducted on CM247LC-DS in the stress-free coarsened state.

Specimen ID	IP/OP	L/T	R	T_{min}[°C]	T_{max} [°C]	$\Delta\epsilon_{mech}$ [%]	Cycle Time [sec]	Dwell [min]	$\Delta\epsilon_{plas}$[%]	σ_{min} [MPa]	σ_{max} [MPa]	$\Delta\sigma$ [MPa]	σ_{mean} [MPa]	N_i
S4L-5	IP	L	0	500	750	1.2	120	0	0.001	709	-528	91	1237	715
S5L-1	IP	L	0	100	750	1.2	360	0	0.002	730	-593	69	1323	474
S5L-13	IP	L	0	100	750	1.2	540	20	0.045	626	-703	-39	1329	216
S4T-5	IP	T	0	100	750	0.95	480	0	0.059	763	-592	85	1355	16
S5L-7	Isothermal	L	-1	20	20	1.3	60	0	0.002	800	-793	3	1593	6266
1SL-5	Isothermal	L	-1	20	20	1.3	60	0	0.006	832	-785	24	1617	6904
S2L-12	OP	L	-1	500	950	0.8	180	0	0.002	680	-150	184	991	2955

Table B.4: Experimental data for fatigue tests conducted on CM247LC-DS with a N-raft microstructure.

Specimen ID	IP/OP	L/T	R	T_{min}[°C]	T_{max} [°C]	$\Delta\epsilon_{mech}$ [%]	Cycle Time [sec]	Dwell [min]	$\Delta\epsilon_{plas}$[%]	σ_{min} [MPa]	σ_{max} [MPa]	$\Delta\sigma$ [MPa]	σ_{mean} [MPa]	N_i
S2L-6	IP	L	0	500	850	1	140	0	0.008	428	-569	-70	998	1004
S2L-2	IP	L	0	500	850	1.1	140	0	0.007	458	-631	-87	1089	832
S5L-6	IP	L	0	100	950	0.8	400	0	0.016	284	-628	-172	911	527
S5L-4	IP	L	0	100	950	1	600	0	0.055	319	-701	-191	1020	179
S2L-3	IP	L	0	100	850	1.1	600	0	0.081	522	-692	-85	1214	81
S2L-7	IP	L	0	100	850	1.1	400	20	0.163	401	-670	-134	1072	139
S5L-3	IP	L	0	100	950	0.8	600	20	0.045	182	-678	-248	860	205
S7T-3	IP	T	0	100	950	0.55	600	0	0.002	221	-629	-204	850	534
S3T-11	IP	T	0	100	950	0.8	600	0	0.067	145	-613	-234	758	20
S3L-12	Isothermal	L	-1	20	20	1.3	60	0	0.001	854	-772	41	1627	5049
S3L-14	OP	L	-1	500	950	1	180	0	0.018	705	-293	206	998	924
S1L-3	OP	L	-1	500	950	1.2	180	0	0.027	776	-382	197	1159	542
S3L-16	OP	L	$-\infty$	500	950	1	180	0	0.018	724	-335	195	1059	514
S3L-3	OP	L	0	500	950	1	180	0	0.011	719	-258	230	977	849
S1L-2	OP	L	-1	500	950	0.8	180	0	0.008	674	-220	227	894	1888
S3T-9	OP	T	-1	500	950	0.55	180	0	0.001	655	-198	228	853	543

Table B.5: Experimental data for fatigue tests conducted on CM247LC-DS with a P-raft microstructure.

Specimen ID	IP/OP	L/T	R	T_{min}[°C]	T_{max} [°C]	$\Delta\epsilon_{mech}$ [%]	Cycle Time [sec]	Dwell [min]	$\Delta\epsilon_{plas}$[%]	σ_{min} [MPa]	σ_{max} [MPa]	$\Delta\sigma$ [MPa]	σ_{mean} [MPa]	N_i
S7L-4	Isothermal	L	-1	20	20	1.3	60	0	0.01	831	-831	0	1662	3728
S8L-6	OP	L	$-\infty$	500	950	0.8	180	0	0.003	530	-281	124	812	1613
S8L-18	OP	L	-1	500	950	0.8	180	0	0	664	-166	249	831	1852
S7L-21	OP	L	$-\infty$	100	950	0.8	400	0	0.019	673	-263	205	936	1118
S7L-22	OP	L	$-\infty$	100	950	0.7	600	0	0.015	656	-145	255	802	2411
S7L-12	OP	L	$-\infty$	500	950	0.8	180	20	0.046	662	-139	262	801	916
S7L-8	OP	L	$-\infty$	100	950	0.8	600	20	0.043	691	-189	251	881	729
1T2-7	OP	T	$-\infty$	500	950	0.55	180	0	0.006	547	-250	149	797	1250
S4T-6	OP	T	-1	500	950	0.7	180	0	0	644	-283	180	927	599
S4T-2	OP	T	$-\infty$	500	950	0.7	180	0	0.022	574	-213	181	787	766
S4T-15	OP	T	$-\infty$	100	950	0.55	600	0	0.006	573	-228	173	801	945
1T2-6	OP	T	$-\infty$	100	950	0.55	600	20	0.103	601	-230	186	831	644

REFERENCES

[1] Claire, S., *Gas turbines a Handbook of Air, Land, and Sea Applications*. Butterworth-Heinemann, 2008.

[2] Schilke tech. rep., General Electric Corporation, 2004.

[3] Konter, M. and Thumann, M., Materials and Manufacturing of Advanced Industrial Gas Turbine Components *Journal of Materials Processing Technology*, vol. 117, no. 3, pp. 386 – 390, 2001.

[4] Wahl, J. B. and Harris, K., New Single Crystal Superalloys, CMSX-7 and CMSX-8 in *Superalloys 2012* (Huron, E., Reed, R., Hardy, M., Mills, M., Montero, R., Portella, P., and Telesman, J., eds.), pp. 179–188, 2012.

[5] Reed, R., Moverare, J., Sato, A., Karlsson, F., and Hasselqvist, M., A New Single Crystal Superalloy for Power Generation Applications in *Superalloys 2012* (Huron, E., Reed, R., Hardy, M., Mills, M., Montero, R., Portella, P., and Telesman, J., eds.), pp. 491–500, 2012.

[6] Koul, A., Immarigeon, J., Dainty, R., and Patnaik, P., Degradation of High Performance Aero-Engine Turbine Blades in *Advanced Materials and Coatings for Combustion Turbines* (Swaminathan, V. and Cheruvu, N., eds.), pp. 69–75, ASM International, ASM International, 1993.

[7] Arrell, D., Hasselqvist, M., Sommer, C., and Moverare, J., On TMF Damage, Degradation Effects, and the Associated T_{min} Influence on TMF Test Results in γ/γ' prime Alloys in *Superalloys 2004*, pp. 291–294, 2004.

[8] Schafrik, R. and Walston, S., Challenges for High Temperature Materials in the New Millennium in *Superalloys 2008* (Reed, R. C., Green, K. A., Caron, P., Gabb, T. P., Fahrmann, M. G., Huron, E. S., and Woodard, S. A., eds.), pp. 3–9, TMS, 2008.

[9] Gostic, W., Application of Materials and Process Modeling to the Design, Development and Sustainment of Advanced Turbine Engines in *Superalloys 2012* (Huron, E., Reed, R., Hardy, M., Mills, M., Montero, R., Portella, P., and Telesman, J., eds.), pp. 3–12, 2012.

[10] McDowell, D. L., Viscoplasticity of Heterogeneous Metallic Materials *Materials Science and Engineering: R: Reports*, vol. 62, no. 3, pp. 67 – 123, 2008.

[11] National Science and Technology Council, Materials Genome Initiative for Global Competitiveness 2011.

[12] Committee on Accelerating Technology Transition, N. R. C., *Accelerating Technology Transition: Bridging the Valley of Death for Materials and Processes in Defense Systems*. The National Academies Press, 2004.

[13] Cowles, B., Backman, D., and Dutton, R., Verification and Validation of ICME Methods and Models for Aerospace Applications *Integrating Materials and Manufacturing Innovation*, vol. 1, pp. 1–16, 2012.

[14] Durand-Charee, M., *The Microstructure of Superalloys*. CRC Press, 2000.

[15] Sims, C., *The Superalloys*. John Wiley and Sons, 1972.

[16] Reed, R. C., *The Superalloys Fundamentals and Applications*. Cambridge University Press, 2006.

[17] Ricks, R., Porter, A., and Ecob, R., The Growth of γ' Precipitates in Nickel-base Superalloys *Acta Metallurgica*, vol. 31, no. 1, pp. 43 – 53, 1983.

[18] K. Harris, G. E. and Schwer, R., MAR-M247 Derivative-CM247LC-DS Alloy CMSX Single Crystal Alloys Properties and Performance in *Superalloys 1984*, pp. 221–230, 1984.

[19] McLean, M., *Directionally Solidified Materials for High temperature Service*. The Metals Society, 1983.

[20] Hasebe, T., Sakane, M., and Ohnami, M., Elastic Anisotropy of Directionally Solidified Superalloy *Journal of Engineering Materials and Technology*, vol. 114, pp. 141–146, 1992.

[21] Kurz, W. and Fisher, D. J., *Fundamentals of Solidification*. Trans Tech Publications, 3rd ed., 1992.

[22] Tewari, S. and Sriramamurthy, A., Dendrite Spacing in a Directionally Solidified Superalloy *Metallurgical Transactions A*, vol. 12, no. 1, pp. 137–138, 1981.

[23] Bhambri, A., Kattamis, T., and Morral, J., Cast Microstructure of Inconel 713C and its Dependence on Solidification Variables *Metallurgical Transactions B*, vol. 6, no. 4, pp. 523–537, 1975.

[24] Safari, J. and Nategh, S., On the Heat Treatment of Rene-80 Nickel-base Superalloy *Journal of Materials Processing Technology*, vol. 176, no. 1–3, pp. 240 – 250, 2006.

[25] Gordon, A., *Crack Initiation Modeling of a Directionally-Solidified Nickel-Base Superalloy*. PhD thesis, Georgia Institute of Technology, 2006.

[26] Trexler, M. D., *The Relationship of Microstructure to Fracture and Corrosion Behavior of a Directionally Solidified Superalloy*. PhD thesis, Georgia Institute of Technology, 2007.

[27] Lvov, G., Levit, V., and Kaufman, M., Mechanism of Primary MC Carbide Decomposition in Ni-base Superalloys *Metallurgical and Materials Transactions A*, vol. 35, no. 6, pp. 1669–1679, 2004.

[28] Koul, A. and Castillo, R., Assessment of Service Induced Microstructural Damage and its Rejuvenation in Turbine Blades *Metallurgical Transactions A*, vol. 19, no. 8, pp. 2049–2066, 1988.

[29] Liu, L., Jin, T., Zhao, N., Sun, X., Guan, H., and Hu, Z., Formation of Carbides and Their Effects on Stress Rupture of a Ni-base Single Crystal Superalloy *Materials Science and Engineering: A*, vol. 361, pp. 191–197, 2003.

[30] Ges, A., Fornaro, O., and Palacio, H., Long Term Coarsening of γ' Precipitates in a Ni-base Superalloy *Journal of Materials Science*, vol. 32, pp. 3687–3691, 1997.

[31] Footner, P. K. and Richards, B. P., Long-term Growth of Superalloy γ' Particles *Journal of Materials Science*, vol. 17, no. 7, pp. 2141–2153, 1982.

[32] MacKay, R. and Nathal, M., γ' Coarsening in High Volume Fraction Nickel-base Alloys *Acta Metallurgica et Materialia*, vol. 38, no. 6, pp. 993–1005, 1990.

[33] Nathal, M., MacKay, R., and Garlick, R., Lattice Parameter Variations During Aging in Nickel-base Superalloys *Scripta Metallurgica*, vol. 22, no. 9, pp. 1421–1424, 1988.

[34] Nathal, M. V. and MacKay, R. A., The Stability of Lamellar γ-γ' Structures *Materials Science and Engineering*, vol. 85, pp. 127–138, 1987.

[35] Gabb, T., Draper, S., Hull, D., Mackay, R., and Nathal, M., The Role of Interfacial Dislocation Networks in High Temperature Creep of Superalloys *Materials Science and Engineering: A*, vol. 118, pp. 59–69, 1989.

[36] Hadjiapostolidou, D. and Shollock, B., Long Term Coarsening of René 80 Ni-Base Superalloy in *Superalloys 2008* (Reed, R., Green, K., P Caron, T. G., Fahrmann, M., Huron, E., and Woodard, S., eds.), pp. 733–739, TMS, 2008.

[37] Moshtaghin, R. S. and Asgari, S., Growth Kinetics of γ' Precipitates in Superalloy IN-738LC During Long Term Aging *Material & Design*, vol. 24, pp. 325–330, 8 2003.

[38] Lifshitz, I. and Slyozov, V., The Kinetics of Precipitation From Supersaturated Solid Solutions *Journal of Physics and Chemistry of Solids*, vol. 19, no. 1-2, pp. 35 – 50, 1961.

[39] Brailsford, A. D. and Wynblatt, P., The Dependence of Ostwald Ripening Kinetics on Particle Volume Fraction *Acta Metallurgica*, vol. 27, pp. 489–497, 3 1979.

[40] Voorhees, P. W. and Glicksman, M. E., Solution to the Multi-Particle Diffusion Problem With Applications to Ostwald Ripening-II. Computer Simulations *Acta Metallurgica*, vol. 32, pp. 2013–2030, 11 1984.

[41] Jayanth, C. S. and Nash, P., Factors Affecting Particle-coarsening Kinetics and Size Distribution *Journal of Materials Science*, vol. 24, no. 9, pp. 3041–3052, 1989.

[42] McLean, D., Predicting Growth of γ' in Nickel Alloys *Metal Science*, vol. 18, no. 5, pp. 249–256, 1984.

[43] Pollock, T. and Argon, A., Directional Coarsening in Nickel-base Single Crystals with High Volume Fractions of Coherent Precipitates *Acta Metallurgica et Materialia*, vol. 42, no. 6, pp. 1859–1874, 1994.

[44] Buffiere, J. and Ignat, M., A Dislocation Based Criterion for the Raft Formation in Nickel-based Superalloys Single Crystals *Acta Metallurgica et Materialia*, vol. 43, no. 5, pp. 1791–1797, 1995.

[45] Tien, J. K. and Copley, S. M., Effects of Stress Coarsening on Coherent Particle Strengthening *Metallurgical Transactions*, vol. 3, pp. 2157–2162, 1972.

[46] Tien, J. K., On the Celestial Limits of Nickael-base Superalloys in *Superalloys 1972*, pp. W1–W16, TMS, 1972.

[47] Ohe, J. and Wakita, S., Practical Method of Thermal Histroy Analysis by Gamma Prime Morphology in *Superalloys 1984*, pp. 93–101, 1984.

[48] Epishin, A., Link, T., Klingelhöffer, H., Fedelich, B., and Portella, P., Creep Damage of Single-crystal Nickel base Superalloys: Mechanisms and Effect on Low Cycle Fatigue *Materials at High Temperatures*, vol. 27, no. 1, pp. 53 – 59, 2010.

[49] Tinga, T., Brekelmans, W., and Geers, M., Directional Coarsening in Nickel-base Superalloys and its Effect on the Mechanical Properties *Computational Materials Science*, vol. 47, no. 2, pp. 471–481, 2009.

[50] Nabarro, F., Rafting in Superalloys *Metallurgical and Materials Transactions A*, vol. 27, no. 3, pp. 513–530, 1996.

[51] Pollock, T. and Argon, A., Creep Resistance of CMSX-3 Nickel base Superalloy Single Crystals *Acta Metallurgica et Materialia*, vol. 40, no. 1, pp. 1–30, 1992.

[52] Ohashi, T., *Microstructural Evolution in Single Crystal Nickel-based Superalloys During High Temperature Creep*. Taylor & Francis, 2001.

[53] Beardmore, P., Davies, R. G., and Johnston, T. L., On the Temperature Sependence of the Flow Stress of Nickel-base Alloys *Transactions of the Metallurgical Society of AIME*, vol. 245, pp. 1537–1545, 1969.

[54] Reppich, B., Some New Aspects Concerning Particle Hardening Mechanisms in γ' Precipitating Ni-base Alloys-I Theoretical Concept *Acta Metallurgica*, vol. 30, no. 1, pp. 87–94, 1982.

[55] Reppich, B., Schepp, P., and Wehner, G., Some New Aspects Concerning Particle Hardening Mechanisms in γ' Precipitating Nickel-base Alloys-II Experiments *Acta Metallurgica*, vol. 30, no. 1, pp. 95 – 104, 1982.

[56] Copley, S. M. and Kear, B. H., Temperature and Orientation Dependence of the Flow Stress in Off-Stoichiometric Ni_3AI (γ' Phase) *Transactions of the Metallurgical Society of AIME*, vol. 239, pp. 977–984, 1967.

[57] Nembach, E. and Neite, G., Precipitation Hardening of Superalloys by Ordered γ'-Particles *Progress in Materials Science*, vol. 29, no. 3, pp. 177–319, 1985.

[58] Ardell, A., Precipitation Hardening *Metallurgical Transactions A*, vol. 16, pp. 2131–2165, 1985.

[59] Hull, D. and Bacon, D. J., *Introduction to Dislocations*. Butterworth-Heinemann, 4th ed., 2001.

[60] Betteridge, W. and Heslop, J., *The Nimonic Alloys*. Crane, Russak and Company, Inc, 1974.

[61] Kear, B. H. and Piearcey, B. J., Tensile and Creep Properties of Single Crystals of the Nickel-Base Superalloy Mar-M200 *Transactions of the Metallurgical Society of AIME*, vol. 239, pp. 1209–1215, 1967.

[62] VerSnyder, F. and Guard, R. *Transactions of ASM*, vol. 52, p. 485, 1960.

[63] Pollock, T. and Field, R., *Dislocations and High-Temperature Plastic Deformation of Superalloy Single Crystals*, vol. 11 of *Dislocations in Solids*. Elsevier Science, 2002.

[64] Leverant, G. and Kear, B., The Mechanism of Creep in Gamma Prime Precipitation-hardened Nickel-base Alloys at Intermediate Temperatures *Metallurgical and Materials Transactions B*, vol. 1, pp. 491–498, 1970.

[65] Feller-Kniepmeier, M. and Link, T., Correlation of Microstructure and Creep Stages in the $\langle 100 \rangle$ Oriented Superalloy SRR 99 at 1253 K *Metallurgical and Materials Transactions A*, vol. 20, pp. 1233–1238, 1989.

[66] Chin, G. Y. and Mammel, W. L., A Theoretical Examination of the Plastic Deformation of Ionic Crystals: II. Analysis of Uniaxial Deformation and Axisymmetric Flow for Slip on $\{110\}$ $\langle 110 \rangle$ and $\{110\}$ $\langle 110 \rangle$ Systems *Metallurgical Transactions*, vol. 4, no. 1, pp. 335–340, 1973.

[67] Langdon, T., Dislcoations and Creep in *Dislocation and Properties of Real Materials* (Loretto, M., ed.), pp. 221–238, The Institute of Metals, 1985.

[68] Tien, J. and Caulfield, T., eds., *Superalloys, Supercomposites, and Superceramics*. Academic Press, 1989.

[69] MacKay, R. and Ebert, L., The development of - lamellar structures in a nickel-base superalloy during elevated temperature mechanical testing *Metallurgical and Materials Transactions A*, vol. 16, pp. 1969–1982, 1985.

[70] Matan, N., Cox, D., Carter, P., Rist, M., Rae, C., and Reed, R., Creep of CMSX-4 Superalloy Single Crystals: Effects of Misorientation and Temperature *Acta Materialia*, vol. 47, no. 5, pp. 1549–1563, 1999.

[71] Epishin, A. and Link, T., Mechanisms of High Temperature Creep of Nickel-Base Superalloys Under Low Applied Stress in *Superalloys 2004* (Green, K., Pollock, T., Harada, H., Howson, T., Reed, R., Schirra, J., and Walston, S., eds.), pp. 137–143, TMS, 2004.

[72] Matan, N., Cox, D., Rae, C., and Reed, R., On the kinetics of rafting in CMSX-4 superalloy single crystals *Acta Materialia*, vol. 47, no. 7, pp. 2031 – 2045, 1999.

[73] Nabarro, F. R. N. and de Villiers, F., *Physics of Creep and Creep Resistant Alloys*. CRC Press, 1995.

[74] Caron, P., Ramusat, C., and Diologent, F., Influence of the γ' Fraction on the γ/γ' Topological Inversion During High Temperature Creep of Single Crystal Superalloys in *Superalloys 2008* (Reed, R., Green, K., P Caron, T. G., Fahrmann, M., Huron, E., and Woodard, S., eds.), pp. 159–167, TMS, 2008.

[75] Shyam, A. and Milligan, W., Effects of Deformation Behavior on Fatigue Fracture Surface Morphology in a Nickel-base Superalloy *Acta Materialia*, vol. 52, no. 6, pp. 1503 – 1513, 2004.

[76] Segersall, M., Moverare, J. J., Simonsson, K., and Johansson, S., Deformation and Damage MechanismsDuring Thermomechanical Fatigue of a Single Crystal Superalloy in the$\langle 001 \rangle$ and $\langle 011 \rangle$ Directions in *Superalloys 2012* (Huron, E., Reed, R., Hardy, M., Mills, M., Montero, R., Portella, P., and Telesman, J., eds.), pp. 215–223, 2012.

[77] Liu, F., Wang, Y. C., Zhang, H., Ai, S. H., and Wang, Z. G., Evolutionary Stress Cycle Behaviour and Damage Mechanisms in Nickel Based Superalloy Under Thermomechanical Fatigue *Materials Science and Technology*, vol. 19, pp. 853–858, 2003.

[78] Chieragatti, R. and Remy, L., Influence of Orientation on the Low Cycle Fatigue of MAR-M 200 Single Crystals at 650°C I: Fatigue Life Behaviour *Materials Science and Engineering: A*, vol. 141, no. 1, pp. 1–9, 1991.

[79] Chieragatti, R. and Remy, L., Influence of Orientation on the Low Cycle Fatigue of MAR-M 200 Single Crystals at 650°C II: Cyclic Stress-strain Behaviour *Materials Science and Engineering: A*, vol. 141, no. 1, pp. 11–22, 1991.

[80] Fleury, E. and Rémy, L., Behavior of Nickel-base Superalloy Single Crystals Under Thermal-mechanical Fatigue *Metallurgical and Materials Transactions A*, vol. 25, no. 1, pp. 99–109, 1994.

[81] Marchionni, M., Osinkolu, G. A., and Maldini, M., High Temperature Cyclic Deformation of a Directionally Solidified Ni-Base Superalloy *Fatigue and Fracture of Engineering Materials and Structures*, vol. 19, no. 8, pp. 955–962, 1996.

[82] Wright, P. and Anderson, A., The Influence of Orientation on the Fatigue of Directionally Solidified Superalloys in *Superalloys 1980*, pp. 689–698, 1980.

[83] Embley, G. and Russell, E., Thermal-Mechanical Fatigue of Gas Turbine Bucket Alloys in *First Parsons International Turbine Conference, Dublin*, pp. 157–164, Parsons Press, 1984.

[84] Pineau, A. and Antolovich, S. D., High Temperature Fatigue of Nickel-base Superalloys - A Review with Special Emphasis on Deformation Modes and Oxidation *Engineering Failure Analysis*, vol. 16, no. 8, pp. 2668–2697, 2009.

[85] Kraft, S., Zauter, R., and Mughrabi, H., Aspects of High-Temperature Low-Cyle Thermomechanical Fatigue of a Single Crystal Nickel-base Superalloy *Fatigue and Fracture of Engineering Materials and Structures*, vol. 16, no. 2, pp. 237–253, 1993.

[86] Sehitoglu, H. and Boismier, D. A., Thermo-Mechanical Fatigue of Mar-M247: Part 2-Life Prediction *Journal of Engineering Materials and Technology*, vol. 112, no. 1, pp. 80–89, 1990.

[87] Vasseur, E. and Remy, L., High Temperature Low Cycle Fatigue and Thermal-mechanical Fatigue Behaviour of an Oxide-dispersion-strengthened Nickel-base Superalloyatigue behaviour of an oxide-dispersion-strengthened Nickel-base Superalloy *Materials Science and Engineering A*, vol. 184, pp. 1–5, 1994.

[88] Antolovich, S., Domas, P., and Strudel, J., Low cycle fatigue of René 80 as affected by prior exposure *Metallurgical and Materials Transactions A*, vol. 10, pp. 1859–1868, 1979.

[89] Ott, M. and Mughrabi, H., Dependence of the high-temperature low-cycle fatigue behaviour of the monocrystalline nickel-base superalloys CMSX-4 and CMSX-6 on the γ/γ' morphology *Materials Science and Engineering: A*, vol. 272, no. 1, pp. 24 – 30, 1999.

[90] Neuner, F. C., Tetzlaff, U., and Mughrabi, H., Enhancement of Thermomechanical Fatigue Resistance of a Monocrystalline Nickel-base Superalloy by Pre-rafting in *Thermomechanical Fatigue Behavior of Materials* (McGaw, A., Kalluri, S., Bressers, J., and Peteves, S. D., eds.), vol. 4 of *ASTM STP 1428*, ASTM International, 2002.

[91] Beck, T., Lang, K.-H., Pitz, G., and Löhe, D., The Influence of Superimposed Creep Loadings on the Thermal-Mechanical Fatigue Behaviour of the Ni-Base Superalloy IN 792 CC *Mechanics of Time-Dependent Materials*, vol. 6, no. 3, pp. 271–282, 2002.

[92] Veon, M., Brechet, Y., and Louchet, F., Directional Coarsening of Nickel Based Superalloys: Driving Force and Kinetics in *Superalloys 1996* (Veron, M., Brechet, Y., and Louchet, F., eds.), pp. 181–190, TMS, 1996.

[93] ASTM E606-12 Standard Practice for Strain-Controlled Fatigue Testing tech. rep., ASTM International.

[94] ASTM E139-11 Standard Test Methods for Conducting Creep, Creep-Rupture, and Stress-Rupture Tests of Metallic Materials tech. rep., ASTM International.

[95] Standard Practice for Strain Controlled Thermomechanical Fatigue Testing

[96] Körner, T. W., *Fourier Analysis*. Cambridge University Press, 1989.

[97] Voort, G. F. V., Manilova, E. P., and Lucas, G. M., Metallographic Techniques for Superalloys.

[98] Fernandez-Zelaia, P., Thermomecanical Fatigue Formation in Nickel-Base Superalloys at Notches Master's thesis, Georgia Institute of Technology, 2012.

[99] JMat Pro

[100] Sujata, M., Madan, M., Raghavendra, K., Venkataswamy, M., and Bhaumik, S., Identification of Failure Mechanisms in Nickel Base Superalloy Turbine Blades Through Microstructural Study *Engineering Failure Analysis*, vol. 17, no. 6, pp. 1436–1446, 2010.

[101] Private Communication with Siemens Energy

[102] Grosdidier, T., Hazotte, A., and Simon, A., Precipitation and Dissolution Processes in γ/γ Single Crystal Nickel-based Superalloys *Materials Science and Engineering: A*, vol. 256, pp. 183–196, 1998.

[103] Gao, X., Przybyla, C., and Adams, B., Methodology for Recovering and Analyzing Two-point Pair Correlation Functions in Polycrystalline Materials *Metallurgical and Materials Transactions A*, vol. 37, pp. 2379–2387, 2006.

[104] Fullwood, D. T., Niezgoda, S. R., Adams, B. L., and Kalidindi, S. R., Microstructure Sensitive Design for Performance Optimization *Progress in Materials Science*, vol. 55, pp. 477–562, 2010.

[105] Niezgoda, S., Fullwood, D., and Kalidindi, S., Delineation of the Space of 2-point Correlations in a Composite Material System *Acta Materialia*, vol. 56, pp. 5285–5292, 2008.

[106] Adams, B. L., Kalidinid, S. R., and Fullwood, D. T., *Microstructure-Sensitive Design for Performance Optimization*. Butterworth-Heinemann, 2013.

[107] Fedelich, B., Epishin, A., Link, T., Klingelhöffer, H., Künecke, G., and Portella, P. D., Rafting During High Temperature Deformation in a Single Crystal Superalloy: Experiments and Modeling in *Superalloys 2012* (Huron, E., Reed, R., Hardy, M., Mills, M., Montero, R., Portella, P., and Telesman, J., eds.), pp. 491–500, 2012.

[108] Epishin, A., Link, T., Nazmy, M., Staubli, M., Klingelhoffer, H., and Nolze, G., Microstructural Degradation of CMSX-4: Kinetics and Effect on Mechanical Properties in *Superalloys 2008*, pp. 725–731, The Minerals, Metals and Materials Society, 2008.

[109] Carry, C. and Strudel, J. L., Apparent and Effective Creep Parameters in Single Crystals of a Nickel Base Superalloy-I Incubation Period *Acta Metallurgica*, vol. 25, pp. 767–777, 7 1977.

[110] Carry, C. and Strudel, J. L., Apparent and Effective Creep Parameters in Single Crystals of a Nickel Base Superalloy-II Secondary Creep *Acta Metallurgica*, vol. 26, pp. 859–870, 1978.

[111] Mughrabi, H., Ott, M., and Tetzlaff, U., New Microstructural Concepts to Optimize the High-temperature Strength of γ'-hardened Monocrystalline Nickel-based Superalloys *Materials Science and Engineering: A*, vol. 234-236, pp. 434–437, 1997.

[112] Tetzlaff, U. and Mughrabi, H., Can High Temperature Tensile Strength of Nickel-base Superalloys be Improved by Pre-Rafting? in *Intermetallics and Superalloys,* (Morris, D. G. and Gareth, D., eds.), vol. 10, (Weinheim ; Chichester ; New York), pp. 22–27, EUROMAT 1999, Wiley-VCH, 2000.

[113] Caron, P., Henderson, P., Khan, T., and McLean, M., On the Effects of Heat Treatments on the Creep Behaviour of a Single Crystal Superalloy *Scripta Metallurgica*, vol. 20, pp. 875–880, 1986.

[114] Garimella, L., Liaw, P., and Klarstrom, D., Fatigue behavior in nickel-based superalloys: A literature review *JOM Journal of the Minerals, Metals and Materials Society*, vol. 49, pp. 67–71, 1997. 10.1007/BF02914771.

[115] Shah, D. and Duhl, D., The Effect of Orientation, Tempeerature and Gamma Prime Size on the Yield Strength of a Single Crystal Nickel Base Superalloy in *Superalloys 1984*, pp. 105–114, 1984.

[116] Pessah-Simonetti, Caron, M. P., and Khan, T., Effect of a Long-Term Prior Aging on the Tensile Behaviour of a High-Performance Single Crystal Superalloy 1998.

[117] Hasselqvist, M. and Moverare, J., Constitutive Behaviour of IN738LC Under TMF Cycling With and Without Intermediate Ageing in *ASME Turbo Expo 2007*, 2007.

[118] Kupkovits, R., Thermomechanical Fatigue Behavior of the Directionally-Solidified Nickel-Base Superalloy CM247 Master's thesis, Georgia Institute of Technology, 2008.

[119] Gordon, A. P., Neu, R. W., and McDowell, D. L., Effect of pre-exposure on crack initiation life of a directionally solidified Ni-base superalloy *International Journal of Fatigue*, vol. 31, no. 2, pp. 393 – 401, 2009.

[120] Viswanathan, R., *Damage Mechanisms and Life Assesment of High-Temperature Components*. ASM International, 1989.

[121] Boismier, D. A. and Sehitoglu, H., Thermo-Mechanical Fatigue of Mar-M247: Part 1-Experiments *Journal of Engineering Materials and Technology*, vol. 112, no. 1, pp. 68–79, 1990.

[122] Jacobsson, L., Persson, C., and Melin, S., Thermo-mechanical fatigue crack propagation experiments in Inconel 718 *International Journal of Fatigue*, vol. 31, no. 8-9, pp. 1318 – 1326, 2009.

[123] Saxena, A., *Nonlinear Fracture Mechanics for Engineers*. CRC Press, 1998.

[124] Gell, M. and Leverant, G. R., The Fatigue of the Nickel-Base Superalloy, Mar-M200, in Single-Crystal and Columnar-Grained Forms at Room Temperature *Transactions of the Metallurgical Society of AIME*, vol. 242, no. 367-369, 1968.

[125] Leverant, G. R. and M.Gell, The Elevated Temperature Fatigue of a Nickel-Base Superalloy, MAR-M200, in Conventually-Cast and Directionally-Solidified Forms *Transactions of the Metallurgical Society of AIME*, vol. 245, pp. 1167–1173, 1969.

[126] Trexler, M. D. and Jr., T. H. S., Quantitative Characterization of Features Affecting Crack Path in a Directionally Solidified Superalloy in *Superalloys 2008*, 2008.

[127] Karamched, P. S. and Wilkinson, A. J., High Resolution Electron Backscatter Diffraction Analysis of Thermally and Mechanically Induced Strains Near Carbide Inclusions in a Superalloy *Acta Materialia*, vol. 59, no. 1, pp. 263–272, 2011.

[128] McHugh, S., Modelling the Thermo-mechanical bBhavior of a Carbide Inclusion in a Nickel Superalloy Including Residual Stress Effects with a Simple Finite-element Model *Mathematical and Computer Modelling*, vol. 14, no. 0, pp. 933–941, 1990.

[129] Yu-ichi, K., Hidenori, T., and Xinfang, Z., Hybrid System for In-situ Observation of Microstructure Evolution in Steel Materials *Transactions of JWRI*, vol. 41, no. 2, pp. 412–418, 2012.

[130] Kamaraj, M., Rafting in Single Crystal Nickel-base Superalloys- An Overview *Sadhana*, vol. 28, pp. 115–128, 2003. 10.1007/BF02717129.

[131] Antolovich, S. D., Baur, R., and Liu, S., A Mechanistically Based Model for high Temperature LCF of Ni Base Superalloys in *Superalloys 1980*, pp. 605–613, TMS, 1980.

[132] Ghosh, R., Curtis, R., and McLean, M., Creep Deformation of Single Crystal Superalloys-Modelling the Crystallographic Anisotropy *Acta Metallurgica et Materialia*, vol. 38, no. 10, pp. 1977–1992, 1990.

[133] *Strengthening Mechanisms in Crystal Plasticity*. Oxford University Press, USA, 2011.

[134] Engler-Pinto, C., Noseda, C., Nazmy, M., and Rezai-Aria, F., Interaction Between Creep and Thermo-mechanical Fatigue of CM247LC-DS in *Superalloys 1996* (Deye, R. K. D., Anton, D., and Cetel, A., eds.), pp. 319–325, TMS, 1996.

[135] Bettge, D. and Ã-sterle, W., "Cube Slip" in Near-[111] Oriented Specimens of a Single-crystal Nickel-base Superalloy *Scripta Materialia*, vol. 40, no. 4, pp. 389–395, 1999.

[136] Mughrabi, H., Microstructural Aspects of High Temperature Deformation of Monocrystalline Nickel Base Superalloys: Some Open Problems *Materials Science and Technology*, vol. 25, no. 2, pp. 191–204, 2009.

[137] Bilby, B. A., Bullough, R., and Smith, E., Continuous Distributions of Dislocations: A New Application of the Methods of Non-Riemannian Geometry *Proceedings of the Royal Society of London. Series A, Mathematical and Physical Sciences*, vol. 231, no. 1185, pp. pp. 263–273, 1955.

[138] Sheh, M. Y. and Stouffer, D. C., Anisotropic Constitute Modeling for Nickel-base Single Crystal Superalloys Tech. Rep. CR-182157, NASA Report, 1988.

[139] Srikanth, A. and Zabaras, N., A Computational Model for the Finite Element Analysis of Thermoplasticity Coupled with Ductile Damage at Finite Strains *International Journal for Numerical Methods in Engineering*, vol. 45, pp. 1569–1605, 1999.

[140] Lee, E. H., Elastic-Plastic Deformation at Finite Strains *Journal of Applied Mechanics*, vol. 36, no. 1, pp. 1–6, 1969.

[141] Khan, A. S. and Huang, S., *Continuum Theory of Plasticity*. Wiley-Interscience, 1995.

[142] Shenoy, M. M., Gordon, A. P., McDowell, D. L., and Neu, R. W., Thermomechanical Fatigue Behavior of a Directionally Solidified Ni-Base Superalloy *Journal of Engineering Materials and Technology*, vol. 127, pp. 325–336, 2005.

[143] McDowell, D. L., A Nonlinear Kinematic Hardening Theory for Cyclic Thermoplasticity and Thermoviscoplasticity *International Journal of Plasticity*, vol. 8, no. 6, pp. 695 – 728, 1992.

[144] McDowell, D., Antolovich, S., and Oehmke, R., Mechanistic Considerations for TMF Life Prediction of Nickel-base Superalloys *Nuclear Engineering and Design*, vol. 133, pp. 383–399, 1992.

[145] Zerilli, F. J. and Armstrong, R. W., Dislocationmechanicsbased Constitutive Relations for Material Dynamics Calculations *Journal of Applied Physics*, vol. 61, pp. 1816–1825, 1987.

[146] Paidar, V., Pope, D., and Vitek, V., A Theory of the Anomalous Yield Behavior in $L1_2$ Ordered Alloys *Acta Metallurgica*, vol. 32, no. 3, pp. 435 – 448, 1984.

[147] Qin, Q. and Bassani, J. L., Non-Schmid Yield Behavior in Single Crystals *Journal of the Mechanics and Physics of Solids*, vol. 40, no. 4, pp. 813 – 833, 1992.

[148] Hirsch, P. B., A New Theory of the Anomalous Yield Stress in $L1_2$ Alloys *Philosophical Magazine A*, vol. 65, no. 3, pp. 569–612, 1992.

[149] Stouffer, D. C. and Sheh, M. Y., Anisotropic Constitute Modeling of a Single Crystal Superalloy at Elevated Temperature *Applied Mechanics Review*, vol. 43, pp. S345–S352, 1990.

[150] Roebuck, B., Cox, D., and Reed, R., The Temperature Dependence of γ' Volume Fraction in a Ni-based Single Crystal Superalloy from Resistivity Measurements *Scripta Materialia*, vol. 44, pp. 917–921, 2001.

[151] Fossum, A. F., Parameter Estimation for an Internal Variable Model Using Nonlinear Optimization and Analytical/Numerical Response Sensitivities *Journal of Engineering Materials and Technology*, vol. 119, pp. 337–345, 1997.

[152] McGinty, R., *Multiscale Representation of Polycrystalline Ineleasticity*. PhD thesis, Georgia Institute of Technology, 2001.

[153] Shenoy, M., *Constitutive Modeling and Life Prediction in Ni-Base Superalloys*. PhD thesis, Georgia Institute of Technology, 2006.

[154] Chapra, S. and Canale, R., *Numerical Methods for Engineers*. McGraw-Hill Science/Engineering/Math, 2009.

[155] Cuitino, A. M. and Ortiz, M., Computational Modelling of Single Crystals *Modelling and Simulation in Materials Science and Engineering*, vol. 1, p. 225, 1993.

[156] Roters, F., Eisenlohr, P., Hantcherli, L., Tjahjanto, D., Bieler, T., and Raabe, D., Overview of constitutive laws, kinematics, homogenization and multiscale methods in crystal plasticity finite-element modeling: Theory, experiments, applications *Acta Materialia*, vol. 58, no. 4, pp. 1152 – 1211, 2010.

[157] Sachs, G. *Zur ableilung einer Fleissbedingung VDIZ*, vol. 72, p. 734, 1928.

[158] Taylor

[159] *Acta Materialia*, vol. 33, pp. 923–953, 1985.

[160] Kocks, U. F., Tomé, C. N., Wenk, H. R., and Mecking, H., *Texture and Anisotropy: Preferred Orientations in Polycrystals and their Effect on Materials Properties*. Cambridge University Press, 2000.

[161] Butler, G. C. and McDowell, D. L., Polycrystal Constraint and Grain Subdivision *International Journal of Plasticity*, vol. 14, no. 8, pp. 703 – 717, 1998.

[162] Moore, Z. J. and Neu, R. W., Creep Fatigue of a Directionally Solidified Ni-base Superalloy – Smooth and Cylindrically Notched Specimens *Fatigue and Fracture of Engineering Materials and Structures*, vol. 34, no. 1, pp. 17–31, 2011.

[163] Nye, J. F., *Physical Properties of Crystals: Their Representation by Tensors and Matrices*. Oxford University Press, USA, 1957.

[164] Kuhn, H. A. and Sockel, H. G., Comparison Between Experimental Determination and Calculation of Elastic Properties of Nickel-Base Superalloys between 25 and 1200°C *Phys. Stat. Sol. (a)*, vol. 110, pp. 449–458, 1988.

[165] Kuhn, H. A. and Sockel, H. G., Elastic Properties of Textured and Directionally Solidified Nickel-based Superalloys Between 25 and 1200°C *Materials Science and Engineering A*, vol. 112, pp. 117–126, 1989.

[166] Kocks, U., The Relation Between Polycrystal Deformation and Single-crystal Deformation *Metallurgical and Materials Transactions B*, vol. 1, pp. 1121–1143, 1970.

[167] Daleo, J., Ellison, K., and Woodford, D., Application of Stress Relaxation Testing in Metallurgical Life Assessment Evaluations of GTD111 Alloy Turbine Buckets *Journal of Engineering for Gas Turbines and Power*, vol. 121, pp. 129–137, 1999.

[168] Gaubert, A., Bouar, Y. L., and Finel, A., Coupling Phase Field and Viscoplasticity to Study Rafting in Ni-based Superalloys *Philosophical Magazine*, vol. 90, no. 1, pp. 375–404, 2010.

[169] Zhou, N., Shen, C., Mills, M., and Wang, Y., Phase Field Modeling of Channel Dislocation Activity and γ Rafting in Single Crystal Ni–Al *Acta Materialia*, vol. 55, no. 16, pp. 5369 – 5381, 2007.

[170] Bensch, M., Preuflner, J., Httner, R., Obigodi, G., Virtanen, S., Gabel, J., and Glatzel, U., Modelling and Analysis of the Oxidation Influence on Creep Behaviour of Thin-walled Structures of the Single-crystal Nickel-base Superalloy Rene N5 at 980C *Acta Materialia*, vol. 58, pp. 1607–1617, 2010.

[171] Neal, S. D. and Neu, R. W., Reduced-order Constitutive Modeling of Directionally-solidified Ni-base Superalloys *Journal of Engineering for Gas Turbines and Power*, vol. 136, 2013.